THE MINISTRY OF SCIENCE AND HIGHER EDUCATION OF THE RUSSIAN FEDERATION

ST. PETERSBURG STATE POLYTECHNICAL UNIVERSITY JOURNAL

Physics and Mathematics

VOLUME 19, No.1.1, 2026

Peter the Great St. Petersburg
Polytechnic University
2026

ST. PETERSBURG STATE POLYTECHNICAL UNIVERSITY JOURNAL.
PHYSICS AND MATHEMATICS

JOURNAL EDITORIAL COUNCIL

A.I. Borovkov – vice-rector for perspective projects;
A.I. Rudskoy – full member of RAS;
A.E. Zhukov – corresponding member of RAS.

JOURNAL EDITORIAL BOARD

V.K. Ivanov – Dr. Sci. (phys.-math.), prof., SPbPU, St. Petersburg, Russia, – editor-in-chief;
A.E. Fotiadi – Dr. Sci. (phys.-math.), prof., SPbPU, St. Petersburg, Russia, – deputy editor-in-chief;
V.M. Kapralova – Candidate of Phys.-Math. Sci., associate prof., SPbPU, St. Petersburg, Russia, – executive secretary;
V.I. Antonov – Dr. Sci. (phys.-math.), prof., SPbPU, St. Petersburg, Russia;
I.B. Bezprozvanny – Dr. Sci. (biology), prof., The University of Texas Southwestern Medical Center, Dallas, TX, USA;
A.V. Blinov – Dr. Sci. (phys.-math.), prof., SPbPU, St. Petersburg, Russia;
A.S. Cherepanov – Dr. Sci. (phys.-math.), prof., SPbPU, St. Petersburg, Russia;
D.V. Donetski – Dr. Sci. (phys.-math.), prof., State University of New York at Stony Brook, NY, USA;
V.V. Dubov – Dr. Sci. (phys.-math.), prof., SPbPU, St. Petersburg, Russia;
D.A. Firsov – Dr. Sci. (phys.-math.), prof., SPbPU, St. Petersburg, Russia;
P.A. Karaseov – Dr. Sci. (phys.-math.), prof., SPbPU, St. Petersburg, Russia;
A.S. Kheifets – Ph.D., prof., Australian National University, Canberra, Australia;
O.S. Loboda – Candidate of Phys.-Math. Sci., associate prof., SPbPU, St. Petersburg, Russia;
J.B. Malherbe – Dr. Sci. (physics), prof., University of Pretoria, Republic of South Africa;
V.M. Ostryakov – Dr. Sci. (phys.-math.), prof., SPbPU, St. Petersburg, Russia;
V.E. Privalov – Dr. Sci. (phys.-math.), prof., SPbPU, St. Petersburg, Russia;
E.M. Smirnov – Dr. Sci. (phys.-math.), prof., SPbPU, St. Petersburg, Russia;
A.V. Solov'yov – Dr. Sci. (phys.-math.), prof., MBN Research Center, Frankfurt am Main, Germany;
A.K. Tagantsev – Dr. Sci. (phys.-math.), prof., Swiss Federal Institute of Technology, Lausanne, Switzerland;
I.N. Toptygin – Dr. Sci. (phys.-math.), prof., SPbPU, St. Petersburg, Russia.

The journal is included in the List of leading peer-reviewed scientific journals and other editions to publish major findings of theses for the research degrees of Doctor of Sciences and Candidate of Sciences.

The publications are presented in the VINITI RAS Abstract Journal and Ulrich's Periodical Directory International Database.

The journal is published since 2008 as part of the periodical edition 'Nauchno-tekhnicheskie vedomosti SPb-GPU'.

The journal is registered with the Federal Service for Supervision in the Sphere of Telecom, Information Technologies and Mass Communications (ROSKOMNADZOR). Certificate ПИ № ФС77-52144 issued December 11, 2012.

The journal is distributed through the CIS countries catalogue, the «Press of Russia» joint catalogue and the «Press by subscription» Internet catalogue. The subscription index is 71823.

The journal is in the **Web of Science** (Emerging Sources Citation Index), **Scopus,** the **Russian Science Citation Index** (RSCI) and the **Directory of Open Access Journals** (DOAJ) databases.

© Scientific Electronic Library (http://www.elibrary.ru).

No part of this publication may be reproduced without clear reference to the source.

The views of the authors may not represent the views of the Editorial Board.

Address: 195251 Politekhnicheskaya St. 29, St. Petersburg, Russia.

Phone: 8 (812) 552-62-16.

http://ntv.spbstu.ru/physics

© Peter the Great St. Petersburg Polytechnic University, 2026

PREFACE

27th Russian Youth Conference on Physics of Semiconductors and Nanostructures, Opto- and Nanoelectronics (RYCPS-2025)/ 27 Всероссийская молодежная конференция по физике полупроводников и наноструктур, полупроводниковой опто- и наноэлектронике

The 27th Russian Youth Conference on Physics of Semiconductors and Nanostructures, Opto- and Nanoelectronics (RYCPS-2025) was held in Saint Petersburg at Alferov University from November 24 to November 28, 2025. The conference was organized by Peter the Great St. Petersburg Polytechnic University, Alferov University, St. Petersburg State University, Ioffe Institute and Russian-Armenian University (Yerevan).

The conference program covered semiconductor technology, heterostructures with quantum wells, quantum dots and other low-dimensional systems, bulk properties of semiconductors, as well as opto- and nanoelectronic devices and new materials. The conference was held in an in-person format, providing an excellent opportunity for fruitful discussions among participants and experienced scientists.

The conference featured two invited lectures by leading scientists, addressing current challenges and recent advances in physics and engineering. The keynote speakers were *Alexey Toropov* (*Ioffe Institute, Saint Petersburg*) with the presentation "Deterministic photon sources: achievements and challenges" and *Vladislav Malyshkin* (*Ioffe Institute, Saint Petersburg*) with the presentation "Machine learning and artificial intelligence in physics". Young researchers, including undergraduate, graduate and postgraduate students, presented their results in plenary and poster sessions. A total of 98 abstracts, published in Russian (the official conference language), were accepted. In this volume, 27 selected papers are published in English.

In accordance with conference traditions, the participants took part in a competition for the best presentations. Certificates and cash prizes were awarded to several participants whose contributions were selected by the Program Committee. *Alexey Zibinskiy* (Alferov University, St. Petersburg) received the award for the best student presentation for his report "Spin dynamics of an ensemble of localized electrons under quantum measurements". *Anna Razova* (Institute for Physics of Microstructures, RAS, Nizhny Novgorod) received the award for the best postgraduate presentation for her report "Distributed feedback laser based on HgCdTe quantum well heterostructures". *Mikhail Sotnichuk*, a student at Moscow State University, was awarded the Evgeni Gross Prize for the best presentation in semiconductor optics for his report "Residual photoconductivity in InAs/GaInSb heterostructures".

The conference was supported by the Ministry of Science and Higher Education of the Russian Federation (state assignment No. 075-03-2025-256/7) and Tydex LLC (St. Petersburg).

The official conference website is: http://www.semicond.ru/conf2025

Editors
D.A. Firsov
V.A. Shalygin
H.A. Sarkisyan

© Peter the Great St. Petersburg Polytechnic University, 2026

Contents

Bulk properties of semiconductors

Balashov V.S., Ruzhevich M.S., Chumanov I.V., Firsov D.D., Komkov O.S., Mynbaev K.D., Remesnik V.G., Varavin V.S., Mikhailov N.N. *Photoluminescence and photoreflectance of annealed HgCdTe films with high CdTe content* 6

Ustimenko R.V., Shalygin V.A., Karaulov D.A., Norvatov I.A., Melentev G.A., Vinnichenko M. Ya., Firsov D.A. *Electric field-induced anisotropy of absorption and refraction of terahertz radiation in n-InSb* 12

Isakov I.D., Verbitskaya E.M., Eremin I.V., Fadeeva N.N., Eremin V.K. *Lifetimes of electrons and holes in pure Si at temperature 40 mK* 21

Yakovleva V.V., Likhachev K.V., Muzafarova M.V., Babunts R.A., Baranov P.G. *The influence of diamond origin on the properties of NV centers* 27

Heterostructures, superlattices, quantum wells

Kirilenko I.D., Mynbaev K.D., Romanov V.V., Bazhenov N.L., Moiseev K.D. *Radiative recombination in InAs/InAsSb/InAsSbP heterostructures* 33

Lakuntsova O.E., Klimko G.V., Sedova I.V., Myasoedov A.V., Semenov A.N., Prasolov N.D., Sorokin S.V. *Heterostructures with ultrathin $In_xGa_{1-x}As$/GaAs(001) metamorphic buffer layers and InAs/InGaAs QDs grown by molecular beam epitaxy* 39

Chumanov I.V., Firsov D.D., Kolyada D.V., Komkov O.S., Skvortsov I.V., Mashanov V.I., Loshkarev I.D., Timofeev V.A. *Temperature-dependent infrared photoluminescence study of GeSn/Si and GeSiSn/Si multiple quantum wells* 45

Ruzhevich M.S., Mynbaev K.D., Firsov D.D., Chumanov I.V., Komkov O.S., Varavin V.S., Mikhailov N.N. *Photoluminescence and photoreflectance of long-wavelength HgTe/CdHgTe heterostructure* 51

Quantum wires, quantum dots, and other low-dimensional systems

Nikolaeva A.V., Anikina M.A., Pavlov D.V., Maksimov F.M., Kuznetsov A., Kondratev V.M., Sharov V.A., Kuchmizhak A.A., Bolshakov A.D. *Photoluminescence control of WSe_2 monolayers integrated with plasmon nanobumps via strain engineering* 56

Mashinsky K.V., Popov V.V., Fateev D.V. *Hybridization between the plasmonic modes of a graphene square screened by a metal gate and the Fabry-Pérot resonances in barrier layer* 64

Gevorgyan D.G., Gavalajyan S.P., Vinnichenko M.Ya., Kazaryan E.M. *Interband absorption and photoluminescence in lens-shaped quantum dots: an adiabatic approach* 69

Lutsevich M.A., Sharov V.A., Kaveev A.K., Fedorov V.V., Mukhin I.S. *Role of the buffer layer on the mechanical strength of nanowire-substrate interface* 75

Tatarinov D.A., Sapozhnikova E.V., Semenov D.A., Pushkarev A.P. *Perovskite microwires generating red laser emission* 81

Optoelectronic and nanoelectronic devices

Nekrasov A.S., Zolotarev V.V., Oreshko I.V., Slipchenko S.O., Pikhtin N.A. *Beam divergence of surface-emitting semiconductor laser with resonator based on two-dimensional photonic crystal* 86

Yashkin Z.M., Zakharchenko M.V., Glinskii G.F. *Band structure of PT-symmetric phononic crystals* 92

Babichev A.V., Kovach Ya.N., Dragunova A.S., Makhov I.S., Kryzhanovskaya N.V., Zadiranov Yu.M., Salii Yu.A., Kulagina M.M., Bobrov M.A., Vasiliev A.P., Blokhin S.A., Maleev N.A., Karachinsky L.Ya., Novikov I.I., Egorov A.Yu. *Room temperature microlasers based on quasi-planar geometry* 98

Bobrov M.A., Blokhin S.A., Kovach Ya.N., Blokhin A.A., Maleev N.A., Kuzmenkov A.G., Marchiy M.N., Vasil'ev A.P. *Analysis of the low-frequency noise of 89X nm-range single-mode VCSELs* 105

Kornienko P.D., Epoletov V.S., Levina S.A., Larionov V.R., Mintairov M.A., Nakhimovich M.V., Shvarts M.Z. *Illumination and temperature dependence of optical interactions in multijunction solar cells* 111

Prudchenko K.K., Kontrosh E.V., Tolkachev I.A., Abolmasov S.N., Kalinovskii V.S., Terukov E.I. *Prospects of hybrid bifacial four-junction solar cell for concentrating photovoltaics* 117

Malevskaya A.D., Mintairov M.A., Evstropov V.V., Malevsky D.A., Malevskaya A.V., Mintairov S.A., Kalyuzhnyy N.A. *Modeling the current-voltage characteristics and optimizing the laser-powered photovoltaic converters with a spot-type rear contact* 123

Arteev D.S., Sakharov A.V., Nikolaev A.E., Zavarin E.E., Rodin S.N., Tsatsulnikov A.F. *Optimization of AlGaN/GaN heterostructures for high-electron mobility transistors* 129

Safonov I.V., Svintsov D.A. *Response times of two-dimensional photodetectors limited by intrinsic resistance and capacitance* 134

Vassilyev S.Ya., Khrapai V.S., Tikhonov E.S. *Time-resolved measurement of resistance* 141

Novel materials

Kalantaevskii I.E., Gorelkina T.D., Kravtsov V.A. *Investigation of self-hybridized waveguide exciton-polaritons in the two-dimensional antiferromagnet CrSBr at room temperature* 146

Sapozhnikova E.V., Semyonov D.A., Anoshkin S.S., Tatarinov D.A., Verkhogliadov G.A., Pushkarev A.P. *Second harmonic generation in iodine quasi-2D halide perovskite crystals* 151

Ekgardt A.A., Marunchenko A.A., Sapozhnikova E.V., Verkhogliadov G.A., Pushkarev A.P. *The role of charge carrier diffusion in halide perovskite luminophores with memory for optical computing* 156

Kolesnikova A.R., Sinelnik A.D., Litvinov D.A. *Switching of Kerker effect from single Sb_2Se_3 nanoparticles* 162

Conference Organizers and Sponsors..... 168

Bulk properties of semiconductors

Conference paper
UDC 538.91
DOI: https://doi.org/10.18721/JPM.191.101

Photoluminescence and photoreflectance of annealed HgCdTe films with high CdTe content

V.S. Balashov [1]✉, M.S. Ruzhevich [1], I.V. Chumanov [2], D.D. Firsov [2], O.S. Komkov [2], K.D. Mynbaev [1,3], V.G. Remesnik [4], V.S. Varavin [4], N.N. Mikhailov [4]

[1] ITMO University, St. Petersburg, Russia;
[2] St. Petersburg Electrotechnical University "LETI", St. Petersburg, Russia;
[3] Ioffe Institute, St. Petersburg, Russia;
[4] Rzhanov Institute of Semiconductor Physics Siberian Branch of RAS, Novosibirsk, Russia
✉ vovan.balashov@niuitmo.ru

Abstract. The results of a study of photoluminescence and photoreflectance of $Hg_{1-x}Cd_xTe$ films with CdTe molar fraction $x = 0.5 - 0.7$ are presented. The films were grown by molecular beam epitaxy and annealed under mercury deficiency conditions to convert them to hole-type conductivity by generating intrinsic acceptors, mercury vacancies. Annealing resulted in the significant blue-shift of both the photoluminescence and photoreflectance spectra. Energy levels within the bandgap with ionization energies from 44 to 125 meV were detected in the films, and their nature is discussed.

Keywords: HgCdTe, annealing, photoluminescence, photoreflectance

Citation: Balashov V.S., Ruzhevich M.S., Chumanov I.V., Firsov D.D., Komkov O.S., Mynbaev K.D., Remesnik V.G., Varavin V.S., Mikhailov N.N. Photoluminescence and photoreflectance of annealed HgCdTe films with high CdTe content, St. Petersburg State Polytechnical University Journal. Physics and Mathematics. 19 (1.1) (2026) 6–11. DOI: https://doi.org/10.18721/JPM.191.101

This is an open access article under the CC BY-NC 4.0 license (https://creativecommons.org/licenses/by-nc/4.0/)

Конференционная статья
УДК 538.91
DOI: https://doi.org/10.18721/JPM.191.101

Фотолюминесценция и фотоотражение отожженных пленок HgCdTe с большим содержанием CdTe

В.С. Балашов [1], М.С. Ружевич [1]✉, И.В. Чуманов [2], Д.Д. Фирсов [2], О.С. Комков [2], К.Д. Мынбаев [1,3], В.Г. Ремесник [4], В.С. Варавин [4], Н.Н. Михайлов [4]

[1] Университет ИТМО, Санкт-Петербург, Россия;
[2] Санкт-Петербургский государственный электротехнический университет «ЛЭТИ» им. В.И. Ульянова (Ленина), Санкт-Петербург, Россия;
[3] Физико-технический институт им. А.Ф. Иоффе РАН, Санкт-Петербург, Россия
[4] Институт физики полупроводников им. А.В. Ржанова Сибирского отделения РАН, г. Новосибирск, Россия
✉ vovan.balashov@niuitmo.ru

Аннотация. В статье представлены результаты исследования фотолюминесценции и фотоотражения пленок $Hg_{1-x}Cd_xTe$ с мольной долей CdTe $x = 0.5 - 0.7$. Пленки были выращены методом молекулярно-лучевой эпитаксии и подвергнуты отжигу в условиях дефицита ртути, что позволило преобразовать их в дырочный тип проводимости за счет генерации собственных акцепторов – вакансий ртути.

© Balashov V.S., Ruzhevich M.S., Chumanov I.V., Firsov D.D., Komkov O.S., Mynbaev K.D., Remesnik V.G., Varavin V.S., Mikhailov N.N., 2026. Published by Peter the Great St. Petersburg Polytechnic University.

Показано, что отжиг привел к существенному высокоэнергетическому сдвигу спектров и фотолюминесценции, и фотоотражения. В запрещенной зоне пленок обнаружены энергетические уровни с энергией ионизации от 44 до 125 мэВ и обсуждается природа выявленных уровней.

Ключевые слова: HgCdTe, отжиг, фотолюминесценция, фотоотражение

Ссылка при цитировании: Балашов В.С., Ружевич М.С., Чуманов И.В., Фирсов Д.Д., Комков О.С., Мынбаев К.Д., Ремесник В.Г., Варавин В.С., Михайлов Н.Н. Фотолюминесценция и фотоотражение отожженных пленок HgCdTe с большим содержанием CdTe // Научно-технические ведомости СПбГПУ. Физико-математические науки. 2026. Т. 19. № 1.1. С. 6–11. DOI: https://doi.org/10.18721/JPM.191.101

Статья открытого доступа, распространяемая по лицензии CC BY-NC 4.0 (https://creativecommons.org/licenses/by-nc/4.0/)

Introduction

$Hg_{1-x}Cd_xTe$ (MCT) solid solutions with a high ($x \geq 0.5$) CdTe content ("composition") are required in the development of near-infrared (IR) photodetectors for astronomical observations [1], and for fabrication of barrier layers in lasers [2] and *nBn* photodetectors [3]. For the fabrication of both photodetectors and injection lasers, a hole-type conductivity material is required; however, approaches to acceptor doping of MCT with $x \geq 0.5$ are just being sought [4, 5]. An obvious (as in the case of MCT with $x < 0.5$) option there could be the introduction of intrinsic acceptors, mercury vacancies V_{Hg}, by annealing the material under mercury deficiency conditions. We carried out such annealing at temperatures T from 330 to 440 °C for a series of MCT films with $x = 0.5 - 0.7$, and in [6], the results of the studies of the structural properties of the films, their optical transmittance at $T = 294$ K, and photoluminescence (PL) at $T = 103$ K and $T = 294$ K were reported. In the present paper, we report the results of the detailed studies of the optical properties of the annealed films carried out with PL and photoreflectance (PR) methods in a wide temperature range, 30 to 300 K.

Materials and Methods

The 3 to 4 μm-thick films were grown by Molecular Beam Epitaxy (MBE) on (013)GaAs substrates [7] and had a constant composition (determined with *in situ* ellipsometry) across their thickness. Optical studies were performed using the setup described in [8] and based on a VERTEX 80 Fourier-transform IR spectrometer with cooled InGaAs, InSb or HgCdTe photodetector. PL/PR studies were carried out under excitation/modulation with an 809 nm cw laser diode with 2.5 kHz modulation frequency, which provided power density up to 4.0 W/cm^2. During the measurements, the films were placed in a Janis CCS-150 closed-cycle cryostat.

Results and Discussion

Fig. 1, *a* shows low-temperature ($T = 30$ K) PL spectra of the films before and after annealing. With x increasing, a shift in the PL spectra towards higher energies was observed. All spectra generally consisted of two bands: an intense narrow high-energy (HE) peak and a less intense broad low-energy (LE) band. For the as-grown films, the full widths at half maximum (FWHM) of the HE peaks were 22, 31, and 34 meV for films with $x = 0.50$, 0.60, and 0.70, respectively; these values and the increase in FWHM with increasing x were consistent with the PL data obtained earlier at $T = 103$ K [6]. For the as-grown films with $x = 0.50$ and 0.60, the broad LE bands were weakly pronounced and separated from the HE peaks by ~111 meV ($x = 0.50$) and ~76 meV ($x = 0.60$), respectively. For the as-grown film with $x = 0.70$, the LE band was separated from the HE peak by ~115 meV.

As a result of annealing, the HE peaks for the films with $x = 0.50$, $x = 0.60$ and $x = 0.70$ narrowed to 17 meV, 20 meV and 22 meV and shifted towards higher energies by 6 meV, 37 meV and 40 meV, respectively. For a film with $x = 0.50$, a LE peak with FWHM ~79 meV appeared, separated from the HE peak by ~44 meV. A broad, low-intensity LE feature was observed in the spectra of the annealed films at a distance of ~128 meV from the HE peak for the film with $x = 0.60$ and ~105 meV for the film with $x = 0.70$, respectively.

© Балашов В.С., Ружевич М.С., Чуманов И.В., Фирсов Д.Д., Комков О.С., Мынбаев К.Д., Ремесник В.Г., Варавин В.С., Михайлов Н.Н., 2026. Издатель: Санкт-Петербургский политехнический университет Петра Великого.

Fig. 1, *b* shows the PL spectra of the annealed film with $x = 0.70$ recorded at excitation laser power $P_{las} = 81.2$ mW at different temperatures. It is seen that the PL signal intensity for both the main HE peak and the LE band decreased with T increasing.

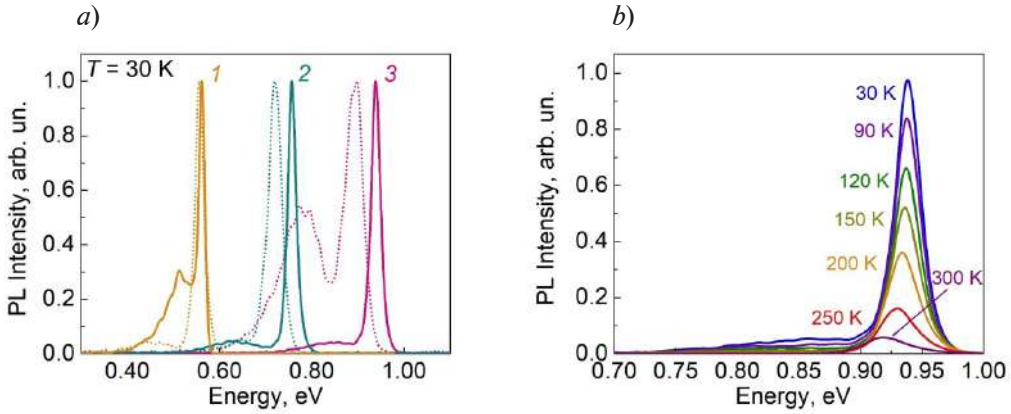

Fig. 1. Normalized PL spectra of the films with $x = 0.50$ (*1*), 0.60 (*2*) and 0.70 (*3*) at $T = 30$ K (dots, as-grown films; solid curves, annealed films) (*a*), and PL spectra of the film with $x = 0.70$ at different temperatures (*b*)

Fig. 2 shows the PL spectra of the film with $x = 0.70$ at $T = 30$ K and different values of P_{las}. For all the as-grown films including this one (Fig. 2, *a*), with P_{las} increasing the intensity of the HE peaks increased more rapidly than that of the LE bands. A similar effect was observed for the annealed film with $x = 0.70$ (Fig. 2, *b*). The energy of the HE peaks and their FWHM changed with P_{las} insignificantly.

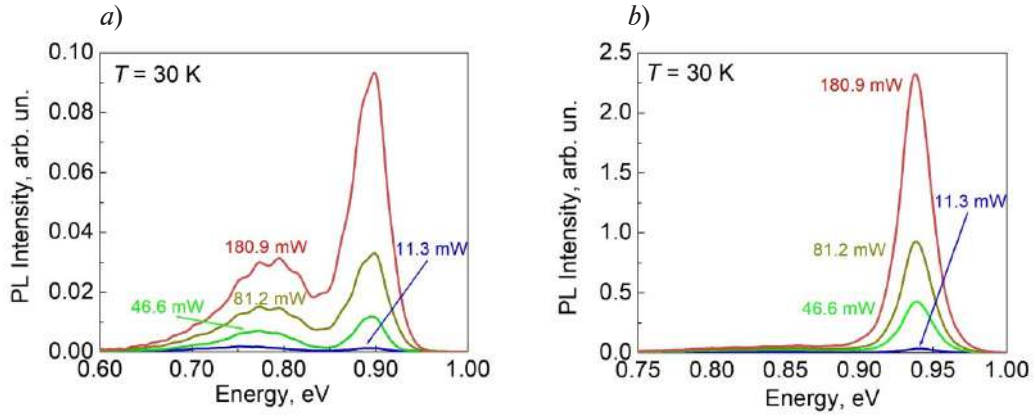

Fig. 2. PL spectra of the film with $x = 0.70$ recorded at $T = 30$ K under different excitation power values: as-grown film (*a*), annealed film (*b*)

The temperature dependence of the HE PL peak positions for the studied films (see Fig. 3, *a* for the detailed data for the film with $x = 0.70$ and Fig. 3, *b* for the data for all films) did not follow the temperature dependence of the bandgap $E_g(T)$. The latter was calculated using the well-known empirical formula from [9]. A similar effect was previously observed for MCT films with $x = 0.6 - 0.7$ grown both by MBE and liquid-phase epitaxy, and is believed to be caused by the effect of carrier localization in potential wells induced by compositional fluctuations [10].

Fig. 4, *a* shows PR spectra of the film with $x = 0.70$ recorded at $T = 300$ K before and after annealing. Both spectra exhibited a superposition of the Fabry–Pérot interference and the differential signal near the interband transition. The energy of the latter, i.e., the optical bandgap E_g' was extracted from the spectra using the approach developed in [11]. However, the overlap of the signal from the interband transition and the interference in the PR spectra limits the accuracy of determining E_g'. It is seen that the spectrum shifted after annealing towards higher energies by ~31 meV, similar to the shift of the PL HE peaks. A similar effect was observed for the PR

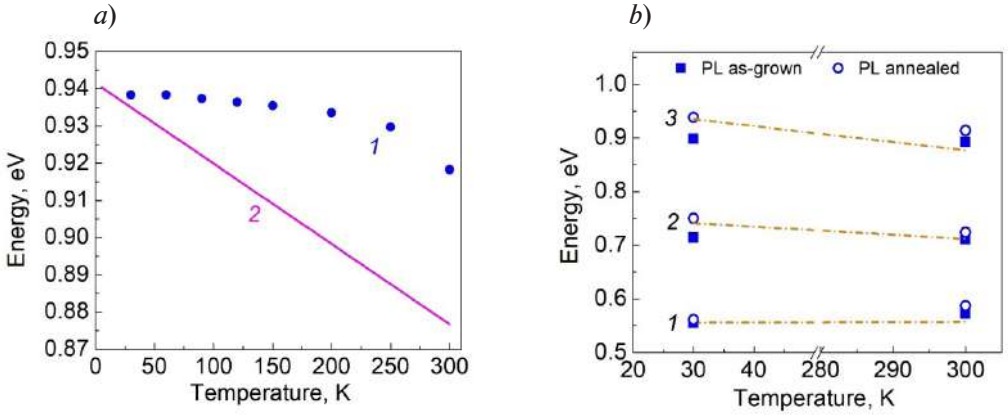

Fig. 3. Temperature dependence of the position of the HE peak in the PL spectra of the film with $x = 0.70$ (symbols *1*) and calculated $E_g(T)$ dependence for MCT with $x = 0.70$ (curve *2*) (*a*), and a review of the positions of the HE peaks for the films with $x = 0.50$ (*1*), 0.60 (*2*) and 0.70 (*3*) in respect to the calculated $E_g(T)$ dependences (lines) (*b*)

spectra of the film with $x = 0.60$. Considering the accuracy of determining the values of E_g' from the PR spectra, they reasonably corresponded to the positions of the HE peaks of the PL for all the films. Since the PR method is sensitive only to interband transitions, it could be concluded that the HE peaks in the PL spectra, including those at low temperatures, also reflected the value of E_g' and were not associated with transitions to energy states within the bandgap.

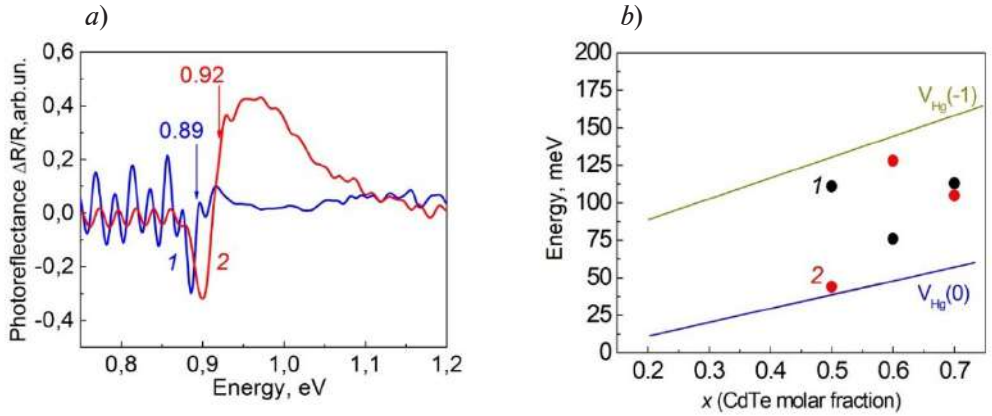

Fig. 4. PR spectra of the film with $x = 0.70$ before (*1*) and after (*2*) annealing, with arrows showing the optical bandgap (*a*), and the values of acceptor ionization energy E_a according to our PL data (symbols: *1*, as-grown films, *2*, annealed ones) and the extrapolation of empirical $E_a(T)$ dependences from [5] to large x values (*b*)

The latter gave us a reference point, allowing to proceed to the analysis of energy levels in the bandgap. According to the data of the Hall effect study performed at $T = 77$ K, the as-grown films had n-type conductivity with electron concentration $(3 - 60)\cdot10^{14}$ cm^{-3}; as a result of annealing, the films were converted into p-type with hole concentration $(2 - 7)\cdot10^{15}$ cm^{-3} [6]. Results of carrier lifetime measurements also suggested that annealed films were converted into p-type conductivity: the lifetime dropped ~1000 times in the annealed films with respect to its value of ~50 μs in the as-grown ones. According to these data, we could expect to observe band(s) related to V_{Hg}-induced energy states in the PL spectra of the annealed films. At the same time, as follows from Fig. 1 and 2, the PL spectra of these films already contained a number of LE features related to levels in the bandgap. We plotted the experimental data on the tentative positions of the LE band maxima in Fig. 4, *b* along with the composition dependences of the ionization energies of neutral and single-charged V_{Hg} as adapted from [5]. It is seen in Fig. 4, *b* that our experimental data do not exactly follow the dependences for the two charge states of V_{Hg}. Still, for the annealed film with $x = 0.50$ ionization energy E_a ~ 44 meV can be related to the energy level formed by the neutral V_{Hg}. The experimental value E_a ~ 113 meV for

the as-grown film with $x = 0.50$ is in good agreement with a similar value measured for a vacancy-doped MCT sample with the same x in [5] (115 meV). For the films with $x = 0.60$ and $x = 0.70$, however, the observed energy levels could not be directly associated with V_{Hg} as a point defect. Extrapolation of the extrinsic acceptor ionization energy $E_a(x)$ from [12] towards $x = 0.70$ yields a maximum value $E_a \approx 20$ meV. The energy of donor levels in MCT with $x = 0.70$ according to the hydrogen-like model is even lower, ~7 meV [12]. Thus, the observed energy levels should be attributed to native acceptors, or to deep centers that are not described by the hydrogen-like model. For example, a strong LE band in the as-grown film with $x = 0.70$, which disappeared after annealing, was similar in behavior to the band with $E_a = 25$ meV observed in films with $x = 0.30$, where, according to the findings in [13], it was associated with defects caused by the presence of excess tellurium [14]. All these observations suggested the presence of a number of intrinsic defects/complexes in the studied films with the evolution of the defect pattern under annealing. Possibly, V_{Hg} manifestation in the PL spectra of vacancy-doped MCT films with $x > 0.5$ is not as straightforward as in the low-x material.

Conclusion

Using photoluminescence and photoreflectance, we studied optical properties of $Hg_{1-x}Cd_xTe$ films with a high ($x = 0.5 - 0.7$) CdTe content before and after thermal annealing. The annealing resulted in a shift of the spectra towards higher energies, which was indicative of the increase in the CdTe molar fraction of the films, possibly due to the reduction in the compositional fluctuations. Despite the fact that electrical and lifetime measurements showed conversion of conductivity type from n- to p- in all the annealed films, the photoluminescence studies revealed clear signatures of generated mercury vacancies only in the film with $x = 0.5$. Still, clear signs of the changes in the defect pattern of all the films were observed after annealing. Further studies are required for the clear identification of optical signatures of mercury vacancies in $Hg_{1-x}Cd_xTe$ films with $x > 0.5$.

REFERENCES

1. **Friess T., Pichon T., Le Goff T., et al.,** Proton Radiation Effects on Low-Flux P-on-N Short-Wavelength Infrared HgCdTe Focal Plane Array, IEEE Transactions on Nuclear Science. 72 (4) (2025) 1191–1197.

2. **Razova A.A., Rumyantsev V.V., Mazhukina K.A., et al.,** Microdisk HgCdTe lasers operating at 22–25 μm under optical pumping, Applied Physics Letters. 126 (12) (2025) 121102.

3. **Vallone M., Alasio M., Tibaldi A., et al.,** Exploring Optimal Dark Current Design in HgCdTe Infrared Barrier Detectors, IEEE Photonics Journal. 16 (1) (2024) 6800208.

4. **Umana-Membreno G.A., Kala H., Bainsy S., et al.,** Hole Transport in Arsenic-Doped $Hg_{1-x}Cd_xTe$ with $x > 0.5$, Journal of Electronic Materials. 45 (9) (2016) 4686–4691.

5. **Majkowycz K., Murawski K., Kopytko M.,** New insight into defect energy levels in HgCdTe, Infrared Physics & Technology. 137 (2024) 105126.

6. **Ruzhevich M.S., Mynbaev K.D., Bazhenov N.L., et al.,** Thermal annealing of CdTe-rich HgCdTe: structural and optical studies, Physics of the Solid State. 67 (1) (2025) 22–27.

7. **Varavin V.S., Vasiliev V.V., Dvoretsky S.A., et al.,** HgCdTe epilayers on GaAs: growth and devices, Opto-Electronics Review. 11 (2) (2003) 99–111.

8. **Firsov D.D., Komkov O.S., Solov'ev V.A., Kop'ev P.S., Ivanov S.V.,** Temperature- dependent photoluminescence of InSb/InAs nanostructures with InSb thickness in the above-monolayer range, Journal of Physics D: Applied Physics. 49 (28) (2016) 285108.

9. **Hansen G.L., Schmit J.L., Casselman T.N.,** Energy gap versus alloy composition and temperature in $Hg_{1-x}Cd_xTe$, Journal of Applied Physics. 53 (10) (1982) 7099–7101.

10. **Mynbaev K.D., Smirnov A.M., Bazhenov N.L., Mikhailov N.N., Remesnik V.G., Yakushev M.V.,** Optical Studies of Molecular-Beam Epitaxy-Grown $Hg_{1-x}Cd_xTe$ with $x = 0.7 - 0.8$, Journal of Electronic Materials. 49 (8) (2020) 4642–4646.

11. **Hosea T.J.C.,** Estimating Critical-Point Parameters of Modulated Reflectance Spectra, physica status solidi B. 189 (2) (1995) 531–542.

12. **Shaw D., Capper P.,** Extrinsic Doping, In: Mercury Cadmium Telluride: Growth, Properties, and Applications, ed. by Capper P., Garland J., John Wiley & Sons, Ltd. Chichester. (2010) 297–316.

13. **Chen W., Rignanese G.-M., Liu J., Hautier G.,** Native point defects in HgCdTe infrared detector material: Identifying deep centers from first principles, Journal of Applied Physics. 135 (11) (2024) 114502.

14. **Ruzhevich M.S., Mynbaev K.D., Firsov D.D., Chumanov I.V., Komkov O.S., Marin D.V., Varavin V.S., Yakushev M.V.,** Arsenic-doped HgCdTe: FTIR photoluminescence and photoreflectance spectroscopy study, Solid State Communications. 394 (2024) 115720.

THE AUTHORS

BALASHOV Vladimir S.
vovan.balashov@niuitmo.ru
ORCID: 0009-0000-8288-8215

CHUMANOV Ivan V.
chumanov2000@yandex.ru
ORCID: 0009-0009-2564-6100

KOMKOV Oleg S.
oskomkov@yahoo.com
ORCID: 0000-0002-8999-1175

REMESNIK Vladimir G.
remesnik@isp.nsc.ru
ORCID: 0009-0003-7495-929X

MIKHAILOV Nikolay N.
mikhailov@isp.nsc.ru
ORCID: 0009-0007-7474-102X

RUZHEVICH Maxim S.
max.ruzhevich@niuitmo.ru
ORCID: 0000-0002-4513-6345

FIRSOV Dmitrii D.
ddfirsov@etu.ru
ORCID: 0000-0001-7608-9580

MYNBAEV Karim D.
mynkad@mail.ioffe.ru
ORCID: 0000-0002-9853-8874

VARAVIN Vasiliy S.
varavin@isp.nsc.ru
ORCID: 0000-0001-7722-6428

Received 16.12.2025. Approved after reviewing 14.01.2026. Accepted 14.01.2026.

© Peter the Great St. Petersburg Polytechnic University, 2026

Conference paper
UDC 535.34
DOI: https://doi.org/10.18721/JPM.191.102

Electric field-induced anisotropy of absorption and refraction of terahertz radiation in *n*-InSb

R.V. Ustimenko, V.A. Shalygin, D.A. Karaulov, I.A. Norvatov, G.A. Melentev, M.Ya. Vinnichenko ✉, D.A. Firsov

Peter the Great St. Petersburg Polytechnic University, St. Petersburg, Russia
✉ mvin@spbstu.ru

Abstract. The effect of an electric field on the optical characteristics of bulk *n*-InSb in the terahertz spectral range (wavelength of 119 μm) at a temperature of 78 K was experimentally studied. The observed changes in the absorption coefficient and refractive index are explained by an increase in the average energy of electrons in an electric field, which is accompanied by a change in the average inverse effective mass of electrons due to the non-parabolicity of the conduction band. Along with the isotropic change in the optical characteristics in electric field, a dependence of the absorption and refraction of terahertz radiation on the direction of the polarization vector was revealed: the measurement results are different for electromagnetic radiation linearly polarized parallel and perpendicular to the field. A comparison of the experimental results with the results of theoretical modeling showed that the observed anisotropy of absorption and refraction is associated with the combined action of two factors: the non-parabolicity of the conduction band and the anisotropy of the nonequilibrium distribution function of electrons over states in momentum space.

Keywords: distribution function anisotropy, electron heating, electron drift, radiation absorption, radiation refraction, polarization of radiation, InSb

Funding: The reported study was funded by Russian Science Foundation (Grant No. 23-12-00036), https://rscf.ru/project/23-12-00036/.

For citation: Ustimenko R.V., Shalygin V.A., Karaulov D.A., Norvatov I.A., Melentev G.A., Vinnichenko M.Ya., Firsov D.A., Electric field-induced anisotropy of absorption and refraction of terahertz radiation in *n*-InSb, St. Petersburg State Polytechnical University Journal. Physics and Mathematics. 19 (1.1) (2026) 12–20. DOI: https://doi.org/10.18721/JPM.191.102

This is an open access article under the CC BY-NC 4.0 license (https://creativecommons.org/licenses/by-nc/4.0/)

Конференционная статья
УДК 535.34
DOI: https://doi.org/10.18721/JPM.191.102

Индуцированная электрическим полем анизотропия поглощения и преломления терагерцового излучения в *n*-InSb

Р.В. Устименко, В.А. Шалыгин, Д.А. Караулов, И.А. Норватов, Г.А. Мелентьев, М.Я. Винниченко ✉, Д.А. Фирсов

Санкт-Петербургский политехнический университет Петра Великого, Санкт-Петербург, Россия
✉ mvin@spbstu.ru

Аннотация. Экспериментально исследовано влияние электрического поля на оптические характеристики объемного *n*-InSb в терагерцовом спектральном диапазоне (длина волны 119 мкм) при температуре 78 K. Обнаруженные изменения коэффициента поглощения и показателя преломления объясняются увеличением средней энергии электронов в электрическом поле, что сопровождается

Ustimenko R.V., Shalygin V.A., Karaulov D.A., Norvatov I.A., Melentev G.A., Vinnichenko M.Ya., Firsov D.A., 2026. Published by Peter the Great St. Petersburg Polytechnic University.

изменением средней обратной эффективной массы электронов вследствие непараболичности зоны проводимости. Наряду с изотропным изменением оптических характеристик в электрическом поле обнаружена зависимость поглощения и преломления терагерцового излучения от направления вектора поляризации: параллельно или перпендикулярно полю. Сравнение результатов эксперимента с результатами теоретического моделирования показало, что обнаруженная анизотропия поглощения и преломления связана с совместным действием двух факторов: непараболичности зоны проводимости и анизотропии неравновесной функции распределения электронов по состояниям в импульсном пространстве.

Ключевые слова: анизотропия функции распределения, разогрев электронов, дрейф электронов, поглощение излучения, преломление излучения, поляризация излучения, InSb

Финансирование: Работа выполнена при финансовой поддержке Российского научного фонда (грант № 23-12-00036), https://rscf.ru/project/23-12-00036/.

Для цитирования: Устименко Р.В., Шалыгин В.А., Караулов Д.А., Норватов И.А., Мелентьев Г.А., Винниченко М.Я., Фирсов Д.А. Индуцированная электрическим полем анизотропия поглощения и преломления терагерцового излучения в *n*-InSb // Научно-технические ведомости СПбГПУ. Физико-математические науки. 2026. Т. 19. № 1.1. С. 12–20. DOI: https://doi.org/10.18721/JPM.191.102

Статья открытого доступа, распространяемая по лицензии CC BY-NC 4.0 (https://creativecommons.org/licenses/by-nc/4.0/)

Introduction

Electro-optical effects are widely used to modulate electromagnetic radiation. Due to the rapid development of terahertz (THz) optoelectronics and photonics, the study of electro-optical effects in this spectral region is of great current interest [1, 2]. The aim of this work is to experimentally investigate the anisotropy of THz radiation absorption and refraction that occurs in an optically isotropic semiconductor when exposed to an electric field.

The object of our study is donor-doped indium antimonide single crystals. The experiment directly measures the modulation of the sample's optical transmission when exposed to electric field pulses. The microscopic mechanism of the observed modulation can be associated with a field-induced change in the free electron contribution to the permittivity of *n*-InSb. The peculiarity of indium antimonide is that this semiconductor has a non-parabolic conduction band. The effect of an electric field in this case is accompanied by a change in the dielectric constant, which is different for radiation with linear polarization along the field (extraordinary wave) and perpendicular to it (ordinary wave). Previously, such an effect was experimentally observed in *n*-InSb in the mid-IR range ($\lambda = 10.6$ μm) [3]. In the cited work, the wavelength was significantly shorter than the wavelengths of the plasmon-phonon resonance, the absorption of radiation by free electrons was negligible, and the effect was entirely reduced to a change in the refractive index, which was different for ordinary and extraordinary waves.

In this work, experiments were conducted in the THz range. The radiation wavelength ($\lambda \approx 119$ μm) is an order of magnitude longer than in [3] and is close to the wavelength of the low-frequency plasmon-phonon mode in the samples studied. In this case, the situation is more complex: there is noticeable absorption by free electrons, and the modulation of the sample transmission by the electric field is associated with two factors, namely, a change in the refractive index and a change in the absorption coefficient. Moreover, the change in the absorption coefficient also turns out to be different for ordinary and extraordinary waves. Theoretical modeling of the electric field-induced anisotropy of absorption and refraction of terahertz radiation in *n*-InSb was previously performed in [4].

The aim of this work is to obtain experimental data on the field dependence of the refractive index and absorption coefficient, as well as their polarization anisotropy in the THz spectral range for indium antimonide. For this purpose, an original research method was developed and tested, based on parallel measurements of the electro-optical modulation of laser radiation under

© Устименко Р.В., Шалыгин В.А., Караулов Д.А., Норватов И.А., Мелентьев Г.А., Винниченко М.Я., Фирсов Д.А., 2026. Издатель: Санкт-Петербургский политехнический университет Петра Великого.

conditions of multipath interference and in its absence. The obtained experimental data were compared with model calculations.

Experimental technique

All samples were fabricated from the same *n*-InSb single crystal with a free electron concentration of $N_e = 3.5 \cdot 10^{15}$ cm^{-3} and a low-field mobility of $\mu(0) = 1.2 \cdot 10^5$ cm^2/(V·s) (at a temperature of $T_0 = 78$ K). The samples were dumbbell-shaped (see the inset in Fig. 1, *a*). First, plane disks of about a millimeter thickness were cut from the single crystal using an electrical discharge machine. The disks were subjected to mechanical grinding and polishing, as a result of which the thickness was reduced to 0.6–0.7 mm. Then, dumbbells were cut from the polished disks, also using an electrical discharge machine. The dumbbell shape of the samples helps to create a uniform electric field in the working region and reduces the current density through the contacts.

In the neck of a dumbbell with a small cross-section $w \times d$ and length $L >> w, d$, a uniform electric field was created by applying a pulsed voltage V to the contacts of the sample. The contact regions of the sample were 6 – 7 times wider than the width of the dumbbell neck w, and their length was 4 – 5 times shorter than L. Therefore, the resistance of the contact regions was negligible, and the electric field strength E in the dumbbell neck can be calculated using the formula $E = V / L$. Ohmic contacts on the ends of the sample were created by electrolytic deposition of nickel from a Ni_2SO_4 solution.

A continuous gas laser with optical pumping by CO_2 laser radiation, namely, a methanol vapor laser FIRL-100 (Edinburgh Instruments) with an operating wavelength of $\lambda = 118.8$ μm, was used as a source of THz radiation. The laser beam was focused onto the polished face of the dumbbell neck using an off-axis parabolic mirror, and the beam aperture was limited by a diaphragm. The beam path length in the sample was equal to d. Switching of radiation polarization from the **e** ∥ **E** state to the **e** ⊥ **E** state was carried out using a half-wave quartz plate (here **e** and **E** denote the unit polarization vector and vector of applied electric field, respectively). The sample was mounted in a flooded nitrogen cryostat with TPX windows and had a temperature of $T_0 = 78$ K. The radiation transmitted through the sample was focused using two parabolic mirrors onto a Ge:Ga detector (QMC Instruments), cooled to 4.2 K in a closed-cycle cryostat. Photoresponse signals were measured with a TDS 2014B oscilloscope (Tektronix).

In the first series of samples (samples PP), the polished surfaces were plane-parallel (the deviation from plane-parallelism did not exceed 1 μm within the laser beam probing region). Multiple reflections of the laser beam from the input and output surfaces of the sample were

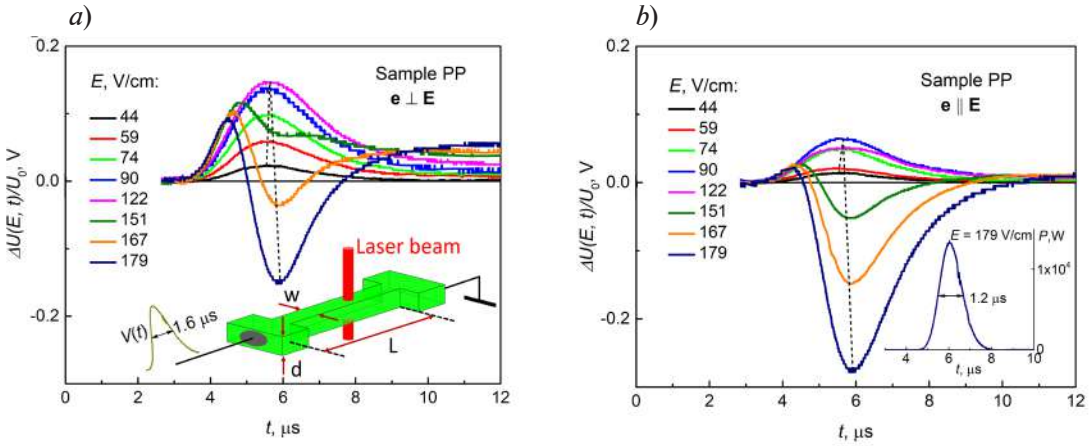

Fig. 1. Transmission modulation in sample PP with pulsed electric field (experiment): oscillograms of photoresponse signal pulse $\Delta U(E, t)$ for an ordinary wave (**e** ⊥ **E**), (*a*), and an extraordinary wave (**e** ∥ **E**), (*b*), normalized to the amplitude of the periodic photoresponse signal at the chopper frequency U_0.

In the legend, E denotes the amplitude of the electric field pulse.

Inset to (*a*): sample configuration for the electrooptical measurements, $V(t)$ shows shape of the voltage pulse.

Inset to (*b*): power pulse shape

accompanied by multipath Fabry–Pérot interference. The optical transmittance of the sample in this case is described by the Airy formula:

$$T = \frac{(1-r)^2 e^{-\alpha d}}{1 - 2re^{-\alpha d}\cos(\delta) + r^2 e^{-2\alpha d}}, \quad (1)$$

where

$$r = \frac{(1-n)^2 + k^2}{(1+n)^2 + k^2}, \quad (2)$$

is the intensity reflection coefficient of the *n*-InSb/vacuum interface under normal incidence of a beam of monochromatic electromagnetic radiation, $\alpha = 4\pi k/\lambda$ is the absorption coefficient, n and k denote the refractive index and extinction coefficient of the *n*-InSb, respectively, and $\delta = 4\pi nd/\lambda$ is the interference phase (the phase shift during double passage of radiation through the sample). When the electric field E varied in the range of 0–180 V/cm, the interference phase changed significantly, which made a noticeable contribution to the modulation of the sample's transmission, along with the field-induced change in the absorption coefficient.

In the second series of samples (samples C), the output surface of the dumbbell neck had a *cylindrical* shape, with its thickness being greatest at the center and gradually decreasing toward its edges. This surface shape was achieved by additional grinding and polishing of the dumbbell neck. As a result, the interference phase δ took on different values at different points of the probing laser spot, and Fabry–Pérot interference was suppressed. In this case, the optical transmittance of the sample can be described by the formula:

$$T = \frac{(1-r)^2 e^{-\alpha d}}{1 - r^2 e^{-2\alpha d}}. \quad (3)$$

The geometric dimensions of the two samples, the experimental data for which are presented in this paper, are given in Table.

Table

Dimensions of the samples

Sample	*L*, mm	*w*, mm	*d*, mm
Sample PP	10	0.8	0.613
Sample C	16	1.2	0.699

The laser beam was modulated by a chopper at a frequency of 160 Hz. Bell-shaped electric field pulses of 1.6 μs duration (see inset in Fig. 1, *a*) were synchronized with the chopper and had a frequency 80 times lower, ensuring negligible Joule heating of the sample's crystal lattice when exposed to periodic pulses. Experiments were conducted in pre-breakdown electric fields ($E \leq 180$ V/cm), where the free electron concentration remains constant.

The magnitude of the field-induced modulation of the sample transmission M was determined as follows:

$$M(E) = \frac{T(E) - T(0)}{T(0)}, \quad (4)$$

where $T(E)$ denotes the transmittance of the sample in the field E.

Results and discussion

The oscillograms of the photoresponse signal pulses in sample PP (Fig. 1) and sample C (Fig. 2) differ qualitatively. In sample C, for both radiation polarizations (**e** ∥ **E** and **e** ⊥ **E**), the photoresponse signal remains positive over the entire range of the studied electric fields, which corresponds to a field-induced increase in the sample transmittance. Sample PP exhibits bipolar photoresponse signals in strong fields: when the supplied electric power approaches the peak value, the photoresponse signal becomes negative, indicating a decrease in the sample transmittance. In Fig. 1 and 2, the time dependences of the photoresponse signal $\Delta U(E, t)$, induced by the electric field, are normalized to the amplitude U_0 of the periodic photoresponse signal at the chopper frequency.

Note that the pulse of supplied electric power had a duration of 1.2 μs (see inset in Fig. 1, *b*) and with increasing field the pulse peak shifted by +0.2 μs. The photodetector had a time constant

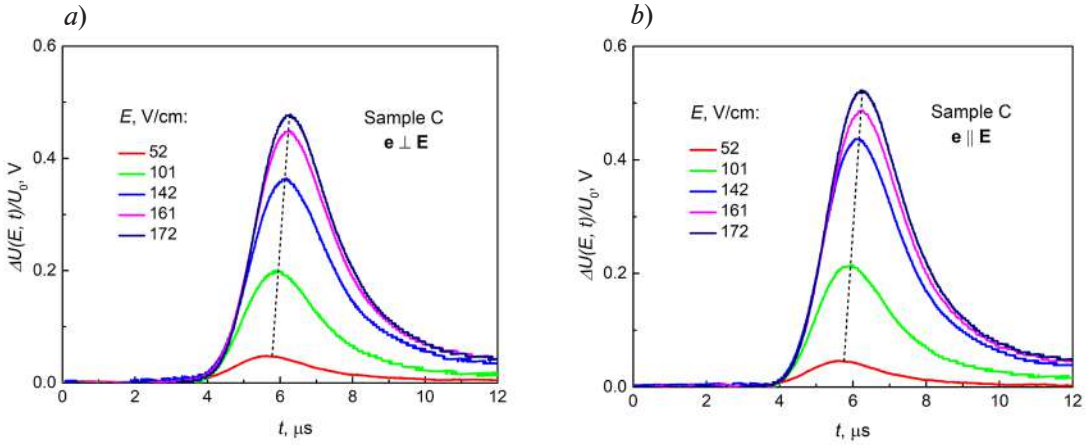

Fig. 2. Modulation of sample transmission with electric field pulses (experiment): oscillograms of photoresponse signal pulse for an ordinary wave (*a*) and an extraordinary wave (*b*), normalized to the amplitude of the periodic photoresponse signal at the chopper frequency

of ~1.3 μs, while the photoresponse pulse duration was ~2.5 μs, and with increasing field its peak shifted by +0.4 μs. In Fig. 1 and 2, the shift of the photoresponse signal peak is shown by dashed lines. In each oscillogram, the dashed line indicates the value of the ratio $\Delta U(E, t)/U_0$, which coincides with the modulation value $M(E)$, defined by Eq. (4).

The experimental field dependences of the transmission modulation for both samples are shown in Fig. 3. Their joint analysis allows us to determine the electric field-induced changes in the absorption coefficient and refractive index for the single crystal from which the samples are made.

As noted in the previous section, in sample C the Fabry–Pérot interference is suppressed, and its transmittance can be described by Eq. (3). Then, in the approximation $r \approx \text{const}(E)$ (which is satisfied with an accuracy of 1% for the sample under study), the field-induced change in the absorption coefficient can be found from the value of M using the equation:

$$\Delta\alpha(E) = -\frac{1}{d}\ln\left[M(E)+1\right], \tag{5}$$

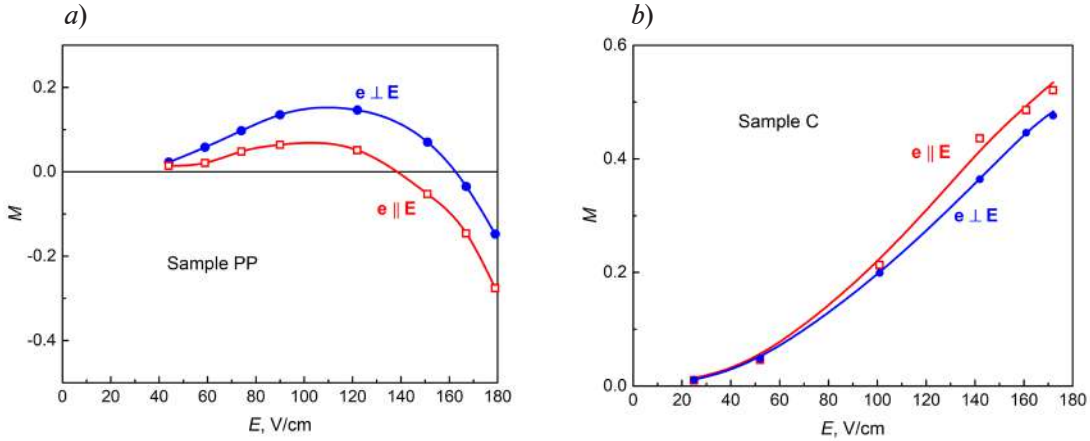

Fig. 3. Experimental field dependences of transmission modulation for ordinary (circles) and extraordinary (squares) waves: sample PP (*a*), sample C (*b*).
Solid lines are a guide for the eye

The resulting field dependences of the electric-field-induced change in the absorption coefficient of *n*-InSb, $\Delta\alpha_P(E)$, for radiation of two mutually orthogonal linear polarizations (P = ⊥, ∥) are shown in Fig. 4, *a*. Note that for both polarizations the electric field induces negative changes in transmission, and at a given field $|\Delta\alpha_{\parallel}(E)| > |\Delta\alpha_{\perp}(E)|$. In the maximum field (172 V/cm), the average change in the absorption coefficient $[\Delta\alpha_{\parallel}(E) + \Delta\alpha_{\perp}(E)]/2$ reaches a value of -6 cm^{-1}, and the polarization anisotropy reaches a value of $|\alpha_{\parallel}(E) - \Delta\alpha_{\perp}(E)| = 0.45$ cm^{-1}.

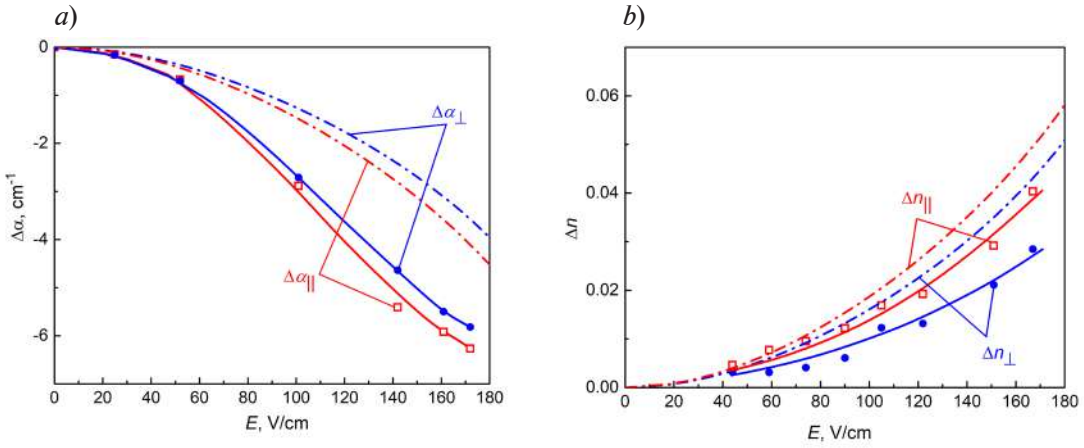

Fig. 4. Electric-field-induced change in the absorption coefficient of *n*-InSb, $\Delta\alpha_p(E)$, for radiation of two mutually orthogonal linear polarizations (P = ⊥, ∥) (*a*); circles and squares show the experimental values obtained from the transmittance modulation analysis in sample C, dash-dotted lines represent the results of theoretical modeling. Electric-field-induced change in the refractive index of *n*-InSb $\Delta n_p(E)$ for radiation of two linear polarizations (*b*); circles and squares show the experimental values obtained from the transmittance modulation analysis in sample PP, dash-dotted lines represent the simulation results. Solid lines in both panels are a guide for the eye

The analysis of transmittance modulation in sample PP is, generally speaking, a more complex task. In this sample, due to multipath Fabry–Pérot interference, a significant contribution to the modulation comes from the change in the interference phase δ [see Eq. (1)], caused by the electric field-induced change in the refractive index $\Delta n_p(E)$, P = ⊥, ∥.

Let us write the nonequilibrium absorption coefficient for polarized light as $\alpha_p(E) = \alpha(0)+\Delta\alpha_p(E)$, and the nonequilibrium refractive index as $n_p(E) = n(0)+\Delta n_p(E)$, where α(0) and $n(0)$ are the equilibrium values of the absorption coefficient and refractive index ($E = 0$). Then, for a given polarization, using Eqs. (1) and (4), we can express the electric field-induced modulation M through α(0), $\Delta\alpha_p(E)$, $n(0)$ and $\Delta n_p(E)$. Since $\Delta\alpha_p(E)$ is already known from the experiment (Fig. 4, *a*), an analysis of the experimental field dependence of the transmittance modulation for this polarization allows us to find α(0), $n(0)$ and $\Delta n_p(E)$. We used the parameters α(0) and $n(0)$ as fitting parameters. Note that α(0) determines the contrast of the interference pattern, and $n(0)$ determines the number of the interference pattern period within which the phase δ changes under the effect of electric field.

When α(0) and $n(0)$ are specified, the magnitude of Δn_p can be uniquely found from the experimental modulation value. The optimal values of α(0) and $n(0)$ were found by an iterative procedure aimed at obtaining the value of $n(0)$ as close as possible to the model value of this parameter (the modeling procedure is described in the paper [4]). As a result of the analysis of the experimental field dependence of the transmittance modulation (Fig. 1), the dependences $\Delta n_p(E)$ (see Fig. 4, *b*) and the equilibrium optical parameters of *n*-InSb were found: $\alpha(0) = 19$ cm^{-1} (theoretical modeling gives a value of 26 cm^{-1}) and $n(0) = 3.975$ (theoretical modeling gives a value of 3.968). Accordingly, for sample PP in zero field the interference phase is $\delta \approx 41\cdot(2\pi)$, which corresponds to the 41st interference maximum. In a field of 167 V/cm $\Delta n_{\parallel}(E) = 0.040$ and $\Delta n_{\perp}(E) = 0.028$ (see Fig. 4, *b*), which corresponds to a significant increase in the interference phase (by 0.81π and 0.56π, respectively) and leads to a change in the modulation sign in Fig. 1, *a*. In this case, the refractive index anisotropy reaches a magnitude of $n_{\parallel}(E) - n_{\perp}(E) = 0.012$.

We also performed theoretical modeling of the dependences $\Delta\alpha_p(E)$ and $\Delta n_p(E)$ for two linear polarizations (P = ⊥, ∥). The calculation algorithm and the main calculation parameters were published in [4]. The calculation is based on a nonequilibrium stationary electron distribution function in the form of a shifted Fermi–Dirac distribution:

$$f(\mathbf{k}_c) = \frac{1}{\exp\left[\dfrac{\varepsilon(\mathbf{k}_c) - \hbar\mathbf{k}_c\mathbf{v}_{dr} - \varepsilon_F}{k_B T_e}\right] + 1}, \quad (6)$$

where $\mathbf{k}_c$ is the electron wave vector, $\varepsilon(\mathbf{k}_c)$ is the dispersion law for the conduction band, and k_B is the Boltzmann constant. The parameters of this function are the nonequilibrium electron temperature T_e, which exceeds the lattice temperature T_0, the electron drift velocity $\mathbf{v}_{dr}$, and the Fermi energy ε_F; all three parameters depend on the electric field E.

We determined the dependence $\mathbf{v}_{dr}(E) = -\mu(E)\mathbf{E}$ from the experimental current-voltage characteristic (CVC). Studies in pulsed operation mode showed that the dependences of the current density j on the field strength E for samples PP and C coincide within the experimental error (see Fig. 5, *a*). Over the entire range of electric fields, the CVC remains linear; therefore, $\mu(E) = \text{const} = \mu(0)$.

The temperature of nonequilibrium electrons T_e at a given electric field strength can be determined using the power balance equation:

$$q_e\mu(E)E^2 = \left\langle \frac{d\varepsilon}{dt} \right\rangle, \quad (7)$$

where q_e is the electron charge, and $\left\langle \dfrac{d\varepsilon}{dt} \right\rangle$ denotes the electron energy loss rate averaged over an ensemble of electrons with a given concentration. When calculating the energy loss rate, the scattering of electrons with optical phonons was considered, taking into account the electron-electron interaction [5]. The Coulomb logarithm required for the calculation was obtained on the basis of the work [6]. The dependence of the energy loss rate on the electron temperature, obtained at $N_e = 3.5 \cdot 10^{15}$ cm^{-3} and $T_0 = 78$ K, is shown in the inset to Fig. 5, *b*. Using this dependence, as well as the experimental data on $\mu(E)$, we determined the field dependence of the temperature of nonequilibrium electrons T_e (the algorithm of this procedure is described in detail in the paper [7]). The degree of heating of free electrons $\Delta T_e = T_e - T_0$ depending on the electric field is shown in Fig. 5, *b*. Under the conditions of our experiment, the field dependence of ΔT_e is close to quadratic (the relative deviation does not exceed 10%), which corresponds to a linear dependence on the supplied electric power. The maximum heating of electrons was 102 K (in a field of 180 V/cm).

The position of the Fermi level ε_F at the electron temperature T_e was determined by normalizing the distribution function (6) to the electron concentration N_e.

A comparison of the results of theoretical modeling of the dependences $\Delta\alpha_p(E)$ and $\Delta n_p(E)$ for two linear polarizations with the experimental results is shown in Fig. 4 *a*, *b*. The model

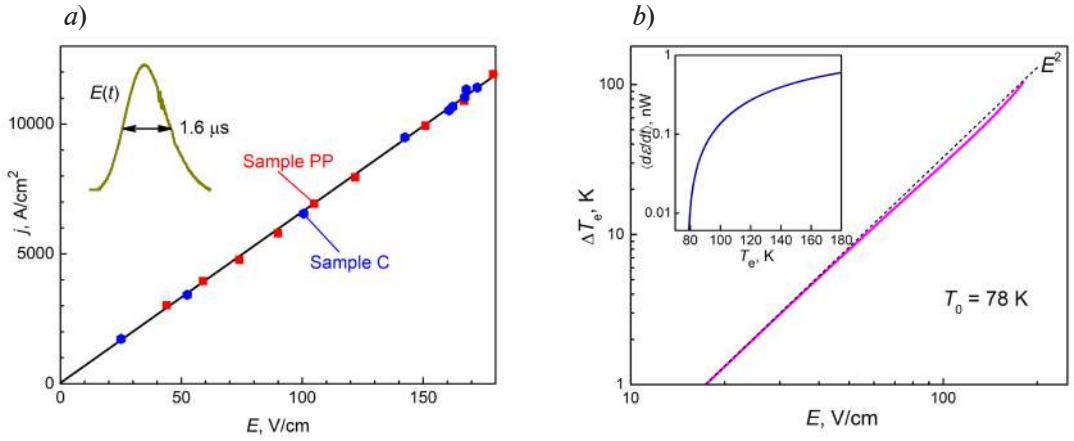

Fig. 5. Experimental current–voltage characteristics for two samples (*a*), inset: electric field pulse shape. Field dependence of electron temperature (*b*), obtained from the current–voltage characteristics using the power balance equation, inset: energy loss rate per electron vs. the nonequilibrium electron temperature T_e (theoretical simulation)

field dependences are in qualitative agreement with the experimental ones: (*i*) the absorption coefficients for both polarizations decrease with the field, (*ii*) the anisotropy $\alpha_{\parallel} - \alpha_{\perp}$ is negative and increases in absolute value with increasing field, (*iii*) the refractive indices for both polarizations increase with field, (*iv*) the anisotropy $n_{\parallel} - n_{\perp}$ is positive and increases with increasing field.

A quantitative comparison shows that the model calculation yields an anisotropy of the absorption coefficient $\alpha_{\parallel}(E) - \alpha_{\perp}(E)$ that coincides with the experiment with an accuracy of 10%, while the simulation yields a weaker average decrease in the absorption coefficient $[\alpha_{\parallel}(E) + \alpha_{\perp}(E)]/2$ in strong fields compared to the experiment (by approximately 40%).

The simulated anisotropy of the refraction coefficient $n_{\parallel}(E) - n_{\perp}(E)$ is approximately two times smaller than that observed in the experiment, while the simulation yields a stronger average increase in the refractive index $[n_{\parallel}(E) + n_{\perp}(E)]/2$ in strong fields compared to the experiment (by approximately 30%).

This quantitative difference between the experimental and theoretical modeling results may be due in part to experimental imperfections and in part to the approximate nature of the model. Specifically, the experiment utilized bell-shaped electric field pulses with a duration comparable to the photodetector time constant, and no correction for the photodetector's dynamic error was made when analyzing the photoresponse waveform. Theoretical calculations of the change in the absorption coefficient and refractive index of *n*-InSb in an electric field were based on a model dependence of the energy loss rate $\left\langle \frac{d\varepsilon}{dt} \right\rangle$ on the electron temperature, obtained without taking into account non-parabolicity of the conduction band.

Summary

Electric-field-induced changes in the absorption coefficient and refractive index for terahertz radiation in *n*-InSb were experimentally detected and studied. The studies were conducted in the pre-breakdown electric field region (less than 180 V/cm), where the free electron concentration remains constant. Polarization anisotropy of both effects was revealed. The current-voltage characteristics of the samples used for electro-optical studies were also measured. In the studied electric field region, the current-voltage characteristics are linear. It was found that the maximum electron heating reached ~100 K, and the maximum drift velocity was approximately $2.2 \cdot 10^7$ cm/s.

Theoretical modeling of the studied effects was performed. It was shown that they are caused by the combined effect of the non-parabolicity of the indium antimonide conduction band and the anisotropy of the electron distribution function over states in momentum space, associated with electron heating and drift.

The research results can be used in the development of high-speed modulators of terahertz radiation.

Acknowledgments

The work was supported by the Russian Science Foundation (grant № 23-12-00036).

REFERENCES

1. **Ma Z.T., Geng Z.X., Fan Z.Y., Liu J., Chen H.D.,** Modulators for Terahertz Communication: The Current State of the Art, Research. 2019 (2019) 6482975.

2. **Huang Y., Shen Y., Wang J.,** From terahertz imaging to terahertz wireless communications, Engineering. 22 (2023) 106–124.

3. **Vorobjev L.E., Stafeev V.I., Firsov D.A.,** Influence of heating and drift of electrons on the refractive index of *n*-type InSb determined allowing for band-band transitions, Soviet Physics: Semiconductors. 18 (3) (1984) 317–320.

4. **Karaulov D.A., Vinnichenko M.Ya., Shalygin V.A., Firsov D.A.,** The effect of electron heating and drift in an electric field on the absorption and refraction of terahertz radiation in *n*-InSb, St. Petersburg State Polytechnical University Journal. Physics and Mathematics. 18 (4) (2025) (to be published).

5. **Gelmont V.L., Lyagushchenko R.I., Yassievich I.N.,** Distribution function and energy loss of hot electrons under interaction with optical phonons, Fizika tverdogo tela. 14 (2) (1972) 533 (in Russian).
6. **Kramers H.A.,** The stopping power of a metal for alpha-particles, Physica. 13 (6-7) (1947) 401.
7. **Shalygin V.A., Makhov I.S., Adamov R.B., Vinnichenko M.Ya., Khvostikov V.P., Firsov D.A.,** Electric-field-induced polarization anisotropy of interband photoluminescence in GaAs, Journal of Applied Physics. 136 (19) (2024) 195703.

THE AUTHORS

USTIMENKO Ratmir V.
ratmirustimenko@yandex.ru
ORCID: 0000-0003-4123-4375

MELENTEV Grigorii A.
gamelen@spbstu.ru
ORCID: 0000-0002-1680-333X

SHALYGIN Vadim A.
vadim_shalygin@mail.ru
ORCID: 0000-0001-6728-7286

VINNICHENKO Maxim Ya.
mvin@spbstu.ru
ORCID: 0000-0002-6118-0098

KARAULOV Danila A.
donil793@yandex.ru
ORCID: 0009-0002-1608-3659

FIRSOV Dmitry A.
dmfir@rphf.spbstu.ru
ORCID: 0000-0003-3947-4994

NORVATOV Ilya A.
norv2@mail.ru
ORCID: 0000-0002-0048-7514

Received 17.11.2025. Approved after reviewing 24.11.2025. Accepted 03.12.2025.

© Peter the Great St. Petersburg Polytechnic University, 2026

Conference materials
UDC 621.315.592.2
DOI: https://doi.org/10.18721/JPM.191.103

Lifetimes of electrons and holes in pure Si at temperature 40 mK

I.D. Isakov [1,2]✉, E.M. Verbitskaya [1], I.V. Eremin [1], N.N. Fadeeva [1], V.K. Eremin [1]

[1] Ioffe Institute, St. Petersburg, Russia;
[2] St. Petersburg Electrotechnical University "LETI", St. Petersburg, Russia
✉ isakov-ivan.2016@yandex.ru

Abstract. The paper presents the study of experimental current responses of Si p^+-n-n^+ 3 mm thick structure operated at 40 mK. Analysis of the data showed reduction of carrier lifetimes in silicon to 50–70 ns for electrons and 350 ns for holes, which is the most critical factor for restriction of the internal thermal gain in bolometric detectors based on the Joule-Lenz effect and should be accounted for in the optimization of detector design.

Keywords: silicon, current response, carrier trapping, bolometric detector

Funding: The research was supported by the Ministry of Science and Higher Education of the Russian Federation (Project No. 4G24).

Citation: Isakov I.D., Verbitskaya E.M., Eremin I.V., Fadeeva N.N., Eremin V.K., Lifetimes of electrons and holes in pure Si at temperature 40 mK, St. Petersburg State Polytechnical University Journal. Physics and Mathematics. 19 (1.1) (2026) 21–26. DOI: https://doi.org/10.18721/JPM.191.103

This is an open access article under the CC BY-NC 4.0 license (https://creativecommons.org/licenses/by-nc/4.0/)

Конференционная статья
УДК 621.315.592.2
DOI: https://doi.org/10.18721/JPM.191.103

Время жизни электронов и дырок в чистом Si при температуре 40 мК

И.Д. Исаков [1,2]✉, Е.М. Вербицкая [1], И.В. Еремин [1], Н.Н. Фадеева [1], В.К. Еремин [1]

[1] Физико-технический институт им. А.Ф. Иоффе РАН, Санкт-Петербург, Россия;
[2] Санкт-Петербургский государственный электротехнический университет «ЛЭТИ» им. В.И. Ульянова (Ленина), Санкт-Петербург, Россия
✉ isakov-ivan.2016@yandex.ru

Аннотация. В статье представлены результаты исследования экспериментальных токовых откликов кремниевой p^+-n-n^+-структуры толщиной 3 мм, работающей при температуре 40 мК. Анализ данных показал уменьшение времени жизни носителей заряда в кремнии до 50–70 нс для электронов и 350 нс для дырок, что является наиболее критичным фактором для ограничения внутреннего теплового усиления в болометрических детекторах, основанных на эффекте Джоуля-Ленца, и должно учитываться при оптимизации конструкции детектора.

Ключевые слова: кремний, токовый отклик, захват носителей, болометрический детектор

Финансирование: Работа выполнена в рамках Государственного задания [Проект № 4г24].

© Isakov I.D., Verbitskaya E.M., Eremin V.K., Fadeeva N.N., Eremin I.V., 2026. Published by Peter the Great St. Petersburg Polytechnic University.

Ссылка при цитировании: Исаков И.Д., Вербицкая Е.М., Еремин И.В., Фадеева Н.Н., Еремин В.К., Время жизни электронов и дырок в чистом Si при температуре 40 мК // Научно-технические ведомости СПбГПУ. Физико-математические науки. 2026. Т. 19. № 1.1. С. 21–26. DOI: https://doi.org/10.18721/JPM.191.103

Статья открытого доступа, распространяемая по лицензии CC BY-NC 4.0 (https://creativecommons.org/licenses/by-nc/4.0/)

Introduction

Bolometric radiation detectors (BDs), in which the signal is a change in the temperature of the semiconductor sensitive element (SE) due to the energy deposition by the detected particle, attract growing interest owing to the possibility to achieve unique sensitivity. Development of BD on high purity Ge and high resistivity Si is motivated by the search for dark matter particles (CDMS and EDELWEISS collaborations [1, 2]) and measuring the characteristics of neutrinos. In particular, the latter is planned within the scope of program No. 8 at the National Center for Physics and Mathematics, Sarov, aimed at building a silicon massive BD up to 10 kg operating at a temperature of tens of mK [3]. A productive idea was to record the change in the SE temperature arising from released particle energy instead of electrical signal generated at the contacts of semiconductor sensor acting as a sensitive element (SE) of BD. The factor in favor of achieving higher internal thermal gain (ITG) is that the heat capacity of Si decreases with temperature as T^3, so, for example, reducing the operational temperature of a SE from 10 K to 10 mK should increase the temperature signal by a factor of 10^9.

The ITG implementation is based on generation of the additional thermal energy ΔE_{dr} in the SE via the drift of nonequilibrium electrons and holes created by the particle, expressed as

$$\Delta E_{dr} = Q_e(t) \cdot \Delta V_e + Q_h(t) \cdot \Delta V_h, \quad (1)$$

where $Q_e(t)$, $Q_h(t)$ are respectively the charges of nonequilibrium electrons and holes, depending on time t, and ΔV_e, ΔV_h are the fractions of applied voltage V passed by electrons and holes that follows from the Shockley–Ramo theorem [4]. The drift energy ΔE_{dr} can be raised up to hundreds of times by applying the proper voltage, accordingly increasing the BD signal. The maximum gain is achieved if Q_e and Q_h remain constant during the drift due to the absence of carrier trapping. However, at temperatures < 100 mK this currently has no experimental confirmation.

Carrier trapping was earlier studied in Si SE with a thickness d of 300 μm and 1 mm [5, 6]. Here we extend this task to the sample with a 3 mm thickness using the same approach for obtaining experimental data and their processing.

Experimental results and analysis

The p^+-n-n^+ structure was processed on the 3 mm thick wafer of pure n-type silicon with a resistivity of ~ 40 kΩ·cm (concentration of phosphorus atoms < 10^{11} cm^{-3}) using planar technology. The measurements of the responses were performed in a closed-loop dilution cryostat at T = 40 mK. The sample was mounted on a copper holder ensuring its thermal connection to the cryostat plate. The holder and sample were screened by aluminum foil from the cryostat warmer component radiation. The measurements of the current response, whose procedure was described in [5, 6], were carried out using the Transient Current Technique with electron-hole pairs generation by illuminating the sample contacts with a 670 nm, 47 ps laser pulse. Current signals were recorded by a digital oscilloscope with an analog bandwidth of 2 GHz and an input impedance of 50 Ω. Negative bias voltage V was applied to the p^+-contact while the n^+-contact was grounded.

In the measurements the current responses originated from the drift of carriers (either electrons or holes) to the contact opposite to the illuminated one. Fig. 1, *a* shows examples of the responses arising from electron drift from the p^+- to the n^+-contact. The pulse shapes observed at $V \leq 160$ V exhibit the following regions: a small narrow peak adjacent to the sharp pulse front, a smooth signal growth to the maximal current, clearly defined descending pulse tops and gradual

© Исаков И.Д., Вербицкая Е.М., Еремин В.К., Фадеева Н.Н., Еремин И.В., 2026. Издатель: Санкт-Петербургский политехнический университет Петра Великого.

signal decay. The current in the narrow peak near the front (oval in Fig. 1, *a*) and the region of slow current growth are presumably due to the space charge limited current (SCLC) process [6], which forms an extended cloud of drifting electrons. Narrow peak disappears at $V > 240$ V. Within the time range of slow current reduction on the pulse top the current occurs as the drift of the extended electron cloud between the p^+-n-n^+ structure contacts. At $V \geq 140$ V the pulse tops demonstrate a slope close to a linear increase with the voltage, and a sharp drop of the signals. Transition of the final gradual current decay to a sharp drop is the evidence that electrons reach the n^+-contact.

For the responses from holes (Fig. 1, *b*) the signal appeared at $V = 40$ V and at higher voltages displayed a clearly defined sharp front and abrupt decay. No peak was observed near the pulse front. The pulse tops showed a superlinear increase in the current at $V = 40$–300 V and a nearly linear rise at $V \geq 300$ V.

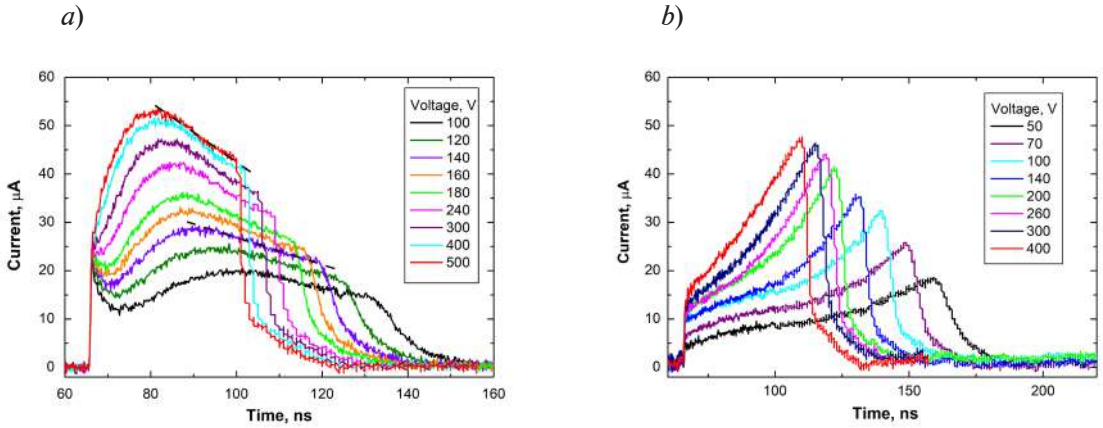

Fig. 1. Current pulse responses of Si p^+-n-n^+ structure to electron drift (*a*) and hole drift (*b*). Dashed lines in (*a*) show linear top slopes at $V = 140$ and 500 V

Drift of nonequilibrium carriers in the Si SE occurs in the electrically neutral material due to low operational temperature, at which thermal activation of charge carriers even from shallow energy levels of boron and phosphorus with an activation energy of about 46 meV is impossible. Thus, in the external circuit of the sample the current originated from the drift of charge cloud acts as the displacement current arising from a change in the charge position in the volume between the contacts. The depth δ of carrier generation near the contacts at temperatures of a few mK is ~ 10 μm [6], which enables considering the process of charge collection as the drift of a flat carrier layer in a 1D-geometry. Then, the resulting drift current i when the charge q moves at the coordinate x at the time t is described by the Shockley-Ramo expression [4]:

$$i(x) = q(t) F_w(x) \mu(F,T) F(x), \qquad (2)$$

where μ is the mobility of drifting carriers depending on the electric field F and T, and F_w is the weighting electric field, which determines the efficiency of charge induction on the contacts, and in plane-parallel geometry is $1/d$.

Generally, the current shape may not have a flat top if it is controlled by the non-uniform $F(x)$ profile and the $q(t)$ reduction due to the capture of carriers on electrically active centers. However, according to [5], $F(x)$ distribution in a p^+-n-n^+ structure is uniform at $T < 800$ mK since the energy levels of shallow impurities of phosphorus and boron (positively charged donors and negatively charged acceptors respectively) in silicon at F up to $3 \cdot 10^4$ V/cm cannot be thermally activated. Cooling of the sample at zero bias voltage freezes electrical neutrality of the silicon bulk and maintains this state in the range of electric field corresponding to the SE operation, and $F(x)$ profile still holds its uniformity. In turn, reduction of $q(t)$ due to trapping and its kinetics are dependent on the carrier capture probability $1/\tau_{tr} = \sigma v_{th} N_{tr}$ (where τ_{tr} is the trapping time constant (carrier lifetime), σ and v_{th} are carrier capture cross section and thermal velocity respectively, and N_{tr} is the trap concentration), which violates the flat pulse shape.

Two approaches, both based on the trapping phenomenon of the drifting carriers, were used to determine τ_{tr}.The first is fitting the current response tops using the relationship $i(t) \infty \exp(-t_{col}/\tau_{tr})$ (where tcol is the carrier collection time), which is only possible for electron pulses with decay in the top. The exponential fits of the current response tops at low (140 V) and high (500 V) bias voltage, at which the SCLC effect is negligible, are illustrated in Fig. 1, *a* by dashed lines. Reduction of the current on the pulse top is well fitted, which proves the interpretation of its origin. The result of the analysis in the full range of bias is presented in Fig. 2 as the dependence of τ_{tr} on the average electric field in the sample determined as $F = V/d$. The obtained τ_{tr} values for electrons are in the range 60–80 ns, rising only insignificantly with the electric field increase at $F > 0.7$ kV/cm. It should be noted here that the applied approach was based on the analysis of carrier package drift and required the knowledge of the electric field distribution inside the sample bulk.

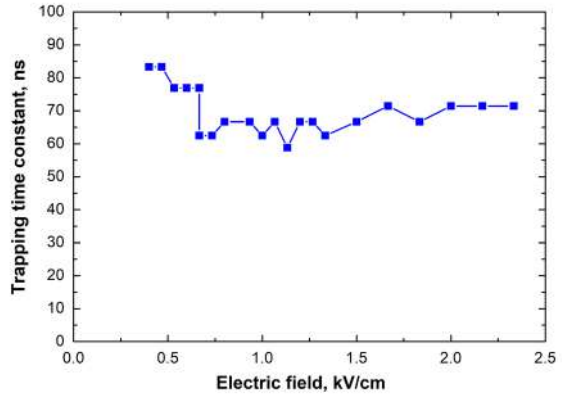

Fig. 2. Dependence of the electron trapping time constant on the average electric field

The second approach to evaluation of τ_{tr} is based on the relation between the collected charge and carrier collection time. According to the Shockley-Ramo expression that considers induction of the current on the sample contacts by drifting charge changing in time, the charge was determined by integrating the current response over t_{col}. This parameter was estimated as the duration between the time points at half of the pulse front and half of the decay. The experimental dependences for electrons and holes as well as their fits are shown in Fig. 3 as normalized charge $Q_{col\text{-}n}$ vs. $t_{çol}$. For electrons, using simple proportionality between $Q_{col\text{-}n}$ and $\exp(-t_{col}/\tau_{tr})$ fails fails to properly fit the experimental data in the total range of tcol. Therefore $Q_{col\text{-}n}$ vs. t_{col} dependence was treated by using the Hecht equation [7, 8], which is only correct in the case of significant trapping and expressed as

$$Q_{col} = \frac{\tau_{tr}}{t_{col}}\left[1 - \exp\left(\frac{t_{col}}{\tau_{tr}}\right)\right]. \quad (3)$$

The fit shows reasonable agreement with the experimental data at $\tau_{tr_e} \approx 50$ ns. It should be noted that disagreement between the curves at $t_{col} \geq 100$ ns ($V \leq 60$ V) may be due to the influence of space charge limited current; however, the trends of the experimental data and the fit well correlate. The matching results obtained with different approaches for data treatment give a clear indication of the distribution of electric field through the entire thickness of the sample and the efficient charge drift between the p^+- and n^+-contacts.

The last note is the argument to use only the $Q_{col}(t_{col})$ approach for evaluating the trapping time constant for holes when the impact of the charge trapping on the current pulse shapes is not resolved. The current responses corresponding to the hole collection (Fig. 1, *b*) have specific shapes with intensively rising current, which can be explained based on the model of carrier drift in an electric field strongly disturbed by the carrier cloud itself [6]. In the case of non-intensive trapping of drifting carriers, the mechanism of the electric field distortion can dominate, and analysis of the current responses becomes insensitive to trapping. Thus, the $Q_{col_p}(t_{col})$ approach was used for fitting experimental data for holes, and the result is presented in Fig. 3 (black dashed line). The fit with the Hecht function matches the experimental data and yields $\tau_{tr_h} \approx 350$ ns. In toto, in the range of smaller tcol the fits for electrons and holes nicely match the experimental data, whereas at $t_{col} > 100$ ns coincidence is observed with large errors, although the trend in the change of the experimental Q_{col} values corresponds to the calculation.

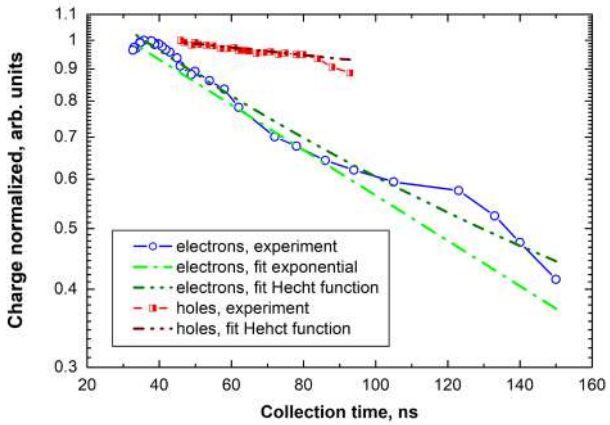

Fig. 3. Dependences of normalized collected charge of electrons and holes on collection time

Going back to estimated τ_{tr}, it should be emphasized that the determined values are 4–5 orders of magnitude smaller than the values of several milliseconds typical for pure high-resistivity silicon at room temperature. Such intensive trapping might be related to the high probability of shallow impurity levels of boron and phosphorus with an activation energy of about 46 meV to capture charge carriers at a temperature of tens of mK, since the time of carrier emission to the corresponding energy band drastically increases. The problem is to resolve the individual contribution of Ntr and □, which is hardly possible at the moment due to the lack of □(T) dependences at a temperature of a few K and below. This issue is the subject for further study.

Conclusion

1. The determined electron lifetimes were obtained using two methods of processing the experimental results: the current pulse kinetics and the dependence of the collected charge on the collection time. Therefore, the fact that the electron lifetime decreases by up to 5 orders of magnitude compared to room temperature has a high degree of reliability.

2. The decrease in the hole trapping time by 4 orders of magnitude confirms the trend of significant carrier lifetime drop, which requires physical understanding and additional study.

3. The measured trapping times should be taken into account when developing bolometric detectors with internal thermal gain.

REFERENCES

1. **Albakry M.F. et al.,** Light dark matter constraints from SuperCDMS HVeV detectors operated underground with an anticoincidence event selection. Phys. Rev. D. 111 (2025) 012006.

2. **Cebrián S.,** Review on dark matter searches. J. Phys.: Conf. Ser. 2502 (2023) 012004.

3. **Yukhimchuk A.A. et al.,** Physics of hydrogen isotopes. FIZMAT. 1 (1) (2023) 5–19 (in Russian).

4. **Ramo S.,** Currents induced by electron motion. Proc. IRE. 27 (9) (1939) 584–585.

5. **Verbitskaya E.M., Eremin I.V., Podoskin A.A., Zbrozhek V.O., Slipchenko S.O., Fadeeva N.N., Yablokov A.A., Eremin V.K.,** Drift transport of charge carriers in silicon p^+-n-n^+ structures at temperatures ≤ 100 mK. Semicond. 58 (8) (2024) 381–388.

6. **Verbitskaya E.M., Eremin I.V., Fadeeva N.N., Eremin V.K., Zbrozhek V.O., Yablokov A.A., Isakov I.D.,** Charge collection in silicon p^+-n-n^+-structures at temperature 40 mK. Semicond. 59 (3) (2025) 168–175.

7. **Eremin V., Shepelev A., Verbitskaya E., Zamantzas C., Galkin A.,** Paradox of characteristics of Si detectors operated at liquid helium temperature, J. Appl. Phys. 123 (2018) 204501.

8. **Glenn G.E.,** Radiation detection and measurement, 3rd edition, John Wiley & Sons, Inc. 2000.

THE AUTHORS

ISAKOV Ivan D.
isakov-ivan.2016@yandex.ru

VERBITSKAYA Elena M.
elena.verbitskaya@mail.ioffe.ru
ORCID: 0000-0002-2313-1789

EREMIN Vladimir K.
vladimir.eremin@mail.ioffe.ru

FADEEVA Nadezda N.
fadeevanadezda@gmail.com
ORCID: 0000-0002-1282-4619

EREMIN Igor V.
Igor.Pti@mail.ioffe.ru

Received 14.12.2025. Approved after reviewing 24.02.2026. Accepted 04.03.2026.

© Peter the Great St. Petersburg Polytechnic University, 2026

Conference paper
UDC 535.3
DOI: https://doi.org/10.18721/JPM.191.104

The influence of diamond origin on the properties of NV centers

V.V. Yakovleva ✉, K.V. Likhachev, M.V. Muzafarova, R.A. Babunts, P.G. Baranov

Ioffe Institute, St. Petersburg, Russia
✉ v.yakovleva@mail.ioffe.ru

Abstract. Diamond samples of various origins containing NV centers were studied using optically detected magnetic resonance (ODMR) and photoluminescence (PL) methods. It is shown that various impurities and deformation-induced defects can significantly influence the crystal environment and properties of NV centers. This influence is reflected in such characteristics as the distribution of NV centers throughout the crystal volume, their charge state (the ratio of neutral to negatively charged NV centers), mechanical stresses and strains in their crystalline environment, interaction with a nitrogen donor, which affects their coherent properties, and their orientation within the diamond lattice.

Keywords: diamond, photoluminescence, optically detected magnetic resonance, NV center, scanning confocal microscopy

Funding: The research was carried out within the state assignment of the Ministry of Science and Higher Education of the Russian Federation (theme No. FFUG-2024-0046).

Citation: Yakovleva V.V., Likhachev K.V., Muzafarova M.V., Babunts R.A., Baranov P.G., The influence of diamond origin on the properties of NV centers, St. Petersburg State Polytechnical University Journal. Physics and Mathematics. 19 (1.1) (2026) 27–32. DOI: https://doi.org/10.18721/JPM.191.104

This is an open access article under the CC BY-NC 4.0 license (https://creativecommons.org/licenses/by-nc/4.0/)

Конференционная статья
УДК 535.3
DOI: https://doi.org/10.18721/JPM.191.104

Влияние происхождения алмаза на свойства NV-центров

В.В. Яковлева ✉, К.В. Лихачев, М.В. Музафарова, Р.А. Бабунц, П.Г. Баранов

Физико-технический институт им. А.Ф. Иоффе РАН, Санкт-Петербург, Россия
✉ v.yakovleva@mail.ioffe.ru

Аннотация. Методами оптически детектируемого магнитного резонанса (ОДМР) и фотолюминесценции (ФЛ) были исследованы образцы алмазов различного происхождения, содержащих NV-центры. Было показано, что различные примеси и деформационные дефекты могут оказывать значительное влияние на кристаллическое окружение и свойства NV-центров. Это влияние отражается в таких характеристиках, как распределение NV-центров по объему кристалла, их зарядовое состояние (соотношение нейтральных NV-центров к отрицательно заряженным), механические напряжения и деформации их кристаллического окружения, взаимодействие с донором азота, влияющим на их когерентные свойства, и их ориентация в алмазной решетке.

Ключевые слова: алмаз, фотолюминесценция, оптически детектируемый магнитный резонанс, NV-центр, сканирующая конфокальная микроскопия

Финансирование: Исследование выполнено в рамках государственного задания Министерства Науки и Высшего Образования Российской Федерации (тема № FFUG 2024 0046).

© Yakovleva V.V., Likhachev K.V., Muzafarova M.V., Babunts R.A., Baranov P.G., 2026. Published by Peter the Great St. Petersburg Polytechnic University.

Ссылка при цитировании: Яковлева В.В., Лихачев К.В., Музафарова М.В., Бабунц Р.А., Баранов П.Г., Влияние происхождения алмаза на свойства NV-центров // Научно-технические ведомости СПбГПУ. Физико-математические науки. 2026. Т. 19. № 1.1. С. 27–32. DOI: https://doi.org/10.18721/JPM.191.104

Статья открытого доступа, распространяемая по лицензии CC BY-NC 4.0 (https://creativecommons.org/licenses/by-nc/4.0/)

Introduction

Diamond is a highly promising mineral with a wide range of industrial and technological uses. Particular attention is paid to the well-known NV center, one of its paramagnetic defects. It represents a negatively charged center consisting of a substitutional nitrogen atom bound to a carbon vacancy. Optical excitation of NV centers leads to optically induced alignment of the electron populations of the spin sublevels of the ground triplet state, resulting in the filling of the spin sublevel with $M_S = 0$, opening the possibility of spin manipulation using ODMR [1–3].

The spin Hamiltonian describing the NV center ODMR spectrum (excluding quadrupole interactions with nitrogen and hyperfine interaction with ligands of ^{13}C) has the form [4]:

$$H = \mu_B g_e \mathbf{S}\cdot\mathbf{B} + D\left[S_Z^2 - \frac{1}{3}S(S+1)\right] + E\left(S_{1X}^2 - S_{1Y}^2\right) + \mathbf{S}\cdot\mathbf{A}_{\mathbf{NV}}\cdot\mathbf{I}_{\mathbf{N}}, \quad (1)$$

where the first term describes the electronic Zeeman interaction, the second and the third terms describe the NV^- center zero field splitting (ZFS), $S = 1$ is the spin of the NV^- center, S_X, S_Y, S_Z are the projections of the spin S onto the coordinate axes X, Y, and Z, respectively; the parameter $D = 2870$ MHz describes the axial part of ZFS; the parameter $E = 0$–20 MHz describes the non-axial part of ZFS and depends on stress and strain in the diamond sample; $\mathbf{A}_{\mathbf{NV}}$ is the anisotropic ^{14}N hyperfine structure interaction parameter for the NV^- center, which is axially symmetric with respect to the symmetry axis of the NV^- center, that is directed along one of the four ⟨111⟩ axes of a diamond. The spin Hamiltonian parameters are key for the for the interpretation of the experiments, since they directly influence the ODMR spectrum shape, which allows extracting information about the NV^- centers local environment, which depends on the diamond sample origin and treatment.

Since the NV center is sensitive to changes in external conditions, such as magnetic and electric fields, temperature, pressure, stresses and strains, it can be used as a probe for local visualization and diagnostics of diamond properties in its environment. Therefore, the aim of this work is to study the diamonds of different origin, containing NV centers, in order to investigate their internal structure and the effect of the crystalline environment on the properties of NV centers.

Materials and Methods

In this study a home-made ODMR spectrometer equipped with a confocal optical circuit (NT-MDT SI) was used [5, 6]. It allows registration of PL and ODMR signals in the region of ~1 μm in diameter at room temperature. It is possible to reveal the spatial distribution of PL and ODMR signals using confocal 3D (X, Y, Z) scanning with a micron resolution. The following instrumental setup was used: objectives (×100 and ×10) and pinhole with diameter from 100 μm, lock-in detector, low-frequency generator, microwave generator working in the range of 2–4 GHz with an antenna for feeding of resonant microwave power to the sample, CCD camera for recording the PL spectra, PMT for ODMR registration. The PL was excited by a laser with a wavelength of 532 nm and a power of $P = 5$ mW. The ODMR spectra of NV^- centers were obtained by lock-in detection of changes in the PL intensity under conditions of magnetic resonance with microwave frequency sweep at the frequency of amplitude modulation of microwave power 680 Hz. ODMR was recorded in the zero-phonon line (ZPL) and phonon sideband (PSB) regions of the NV^- center.

© Яковлева В.В., Лихачев К.В., Музафарова М.В., Бабунц Р.А., Баранов П.Г., 2026. Издатель: Санкт-Петербургский политехнический университет Петра Великого.

Studies were carried out on six samples belonging to the different groups of diamonds, containing NV centers [4], at room and liquid nitrogen temperature:

1) Natural plastically deformed cubic diamond of the variety II [7] (sample *1*), belonging to type IaA + Ib.

2) Treated natural type IIa diamond (~1 ppm of N impurity) (sample *2*). NV centers were artificially created via fast neutron irradiation (~10^{18} cm^{-2}) and annealing at 800 °C for 1 hour.

3) Synthetic HPHT diamond with high nitrogen (~300 ppm of N impurity) (sample *3*), irradiated by either electrons or neutrons (10^{18} cm^{-2}) and annealed at 800 °C to form NV centers.

4) Natural diamond cryptocrystalline aggregate (Orlov's variety X–carbonado [7]) (sample *4*) of micron-sized grains.

5) Natural diamond cryptocrystalline aggregate, carbonado (sample *5*), similar to sample *4* but containing native metal inclusions.

6) HPHT sintered aggregate of detonation nanodiamonds (6 GPa, 800 °C) (sample *6*).

The choice of research methods for each sample was determined by the objectives. Confocal photoluminescence (PL) scanning was performed for samples *1*, *2*, and *4*, as it is most effective for visualizing the spatial distribution of NV centers depending on the crystallization conditions of the diamond, as well as post-crystallization processes. PL spectra were measured for samples *2*, *4*, and *5*, demonstrating differences in the charge state of the centers, which is important for analyzing the influence of impurities. The ODMR study focused on the samples most representative for studying the influence of nitrogen concentration (samples *2* and *3*) and the textural features of the aggregates (samples *4* and *6*). This approach allowed for the most efficient identification of key patterns linking the origin of the diamond to the properties of the NV centers.

Results and Discussion

Distribution of NV centers in diamond crystals. The results of a natural plastically deformed diamond single crystal (sample *1*) study showed that NV centers are predominantly formed in dislocation slip planes (Fig. 1, *a*). In the treated diamond (sample *2*), NV centers are fairly uniformly distributed, without any patterns (Fig. 1, *b*). In natural cryptocrystalline diamond aggregate (sample *4*) NV centers distribution has the form of halo clusters (Fig. 1, *c*).

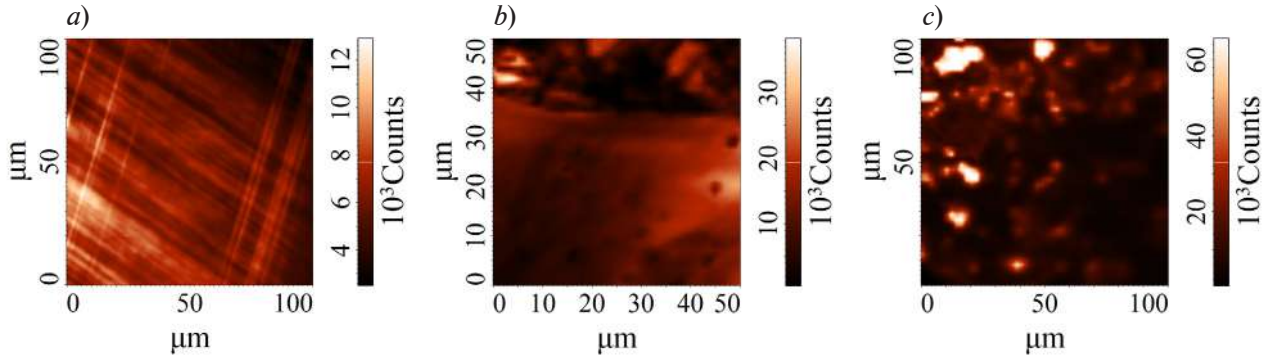

Fig. 1. PL scans of samples *1* (*a*), *2* (*b*) and *4* (*c*)

Fig. 2 shows the PL spectra of treated diamond and two carbonado samples (samples *2*, *4* and *5*, respectively). It can be seen that sample *4* has the lowest NV^0/NV^- ratio, less than 10%. This ratio can be measured by approximating the PL spectrum with a weighted sum of the reference spectra of NV^0 and NV^- centers. Furthermore, the PL spectrum of sample *4* does not contain any additional lines in contrast with PL spectra of samples *2* and *5*. Other defects in diamond can convert the negatively charged NV center into a neutral state [8].

Fig. 3 shows the ODMR spectra of samples *2* and *3*. Sample *2* has an extremely low nitrogen donor concentration, which can be seen in the ODMR spectrum, which has weak satellite lines and additional splitting of the central line caused by the NV center hyperfine structure. The local nitrogen donor concentration can be measured by calculating the intensity ratio of the satellite line to the central line [9]. For comparison, the ODMR spectrum of HPHT diamond (sample *3*), which has a high concentration of nitrogen donors (~300 ppm), is

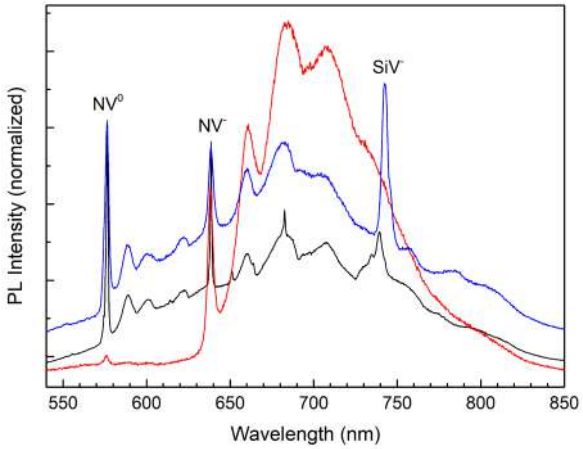

Fig. 2. PL spectra of samples *2* (black line), *4* (red line) and *5* (blue line), recorded at $T = 77$ K

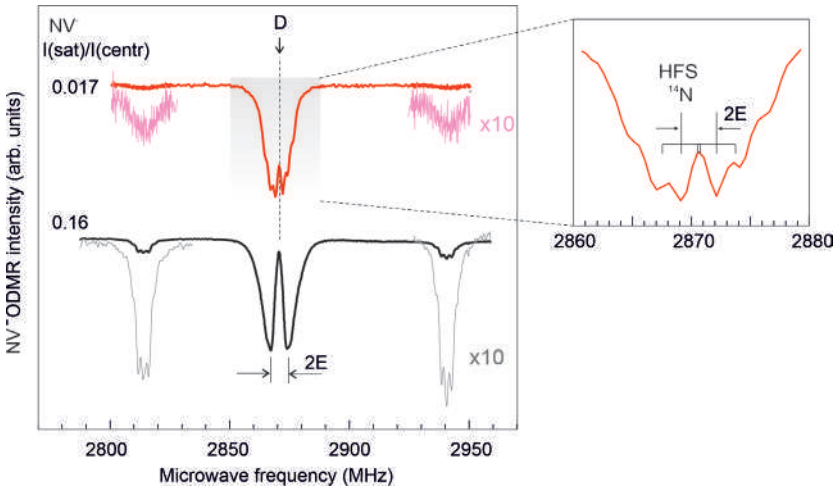

Fig. 3. ODMR spectra of samples *2* (red line) and *3* (black line); the inset shows an enlarged fragment of the sample *2* ODMR spectrum, where additional splitting of the central line can be seen

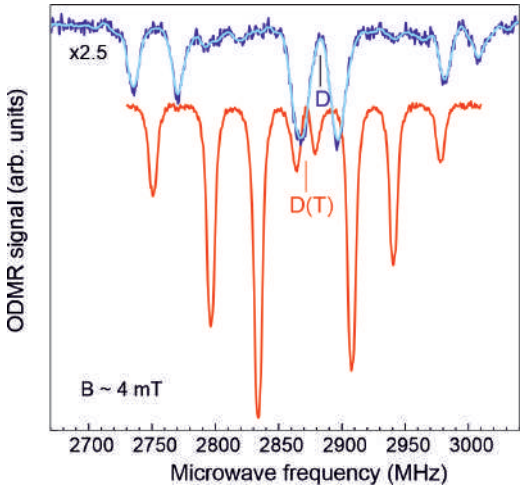

Fig. 4. ODMR spectra of samples *4* (blue line) and *6* (red line) with an additional magnetic field of ~ 4 mT directed at an arbitrary angle

shown. The intensity ratio of the satellite and central lines is more than 10%. The satellite lines also exhibit additional splitting due to the weak hyperfine interaction between the substitutional nitrogen atom and the nitrogen nucleus in the NV center.

Fig. 4 shows the ODMR spectra of carbonado and diamond aggregate obtained by HPHT sintering (samples *4* and *6*) with an additional magnetic field of ~4 mT directed at an arbitrary angle. It can be seen that the ODMR lines of sample 6 are better resolved, which can be explained by the same orientation of diamond crystals in the composition of sample *6*. The shift of its spectrum is associated with a temperature difference between samples *4* and *6*.

Conclusion

The characteristics of diamonds containing NV centers, such as the distribution of NV centers, their charge state, their interaction with nitrogen donors and their orientation in diamond, are highly dependent on the nature of each diamond origin and the way of NV centers formation.

In natural single crystals (sample *1*), the centers are localized along dislocation slip planes, reflecting their plastic deformation. In artificially irradiated crystals (sample *2*), the distribution is uniform, while in cryptocrystalline aggregates (sample *4*), it has a clustered character, reflecting their polycrystalline nature. The predominance of the negatively charged state of the NV centers over the neutral state is most pronounced in samples with minimal impurity and defect content (sample *4*). The presence of foreign defects, either naturally occurring (sample *5*) or by irradiation (sample *3*), facilitates the transition of the centers to the neutral state. The contrast and shape of the ODMR lines respond to the concentration of paramagnetic nitrogen (samples *2* and *3*), as confirmed by hyperfine structure analysis. The orientational ordering of crystallites in sintered aggregates (sample *6*) results in better resolution of the ODMR spectra compared to unoriented ones in natural aggregates (sample *4*).

Thus, the origin of the diamond and its treatment determine the morphology, charge state and spectral properties of NV centers, which allows them to be used not only as quantum sensors, but also as effective probes for diagnosing the internal structure and history of diamond materials of various natures.

Acknowledgments

The research was carried out within the state assignment of the Ministry of Science and Higher Education of the Russian Federation (theme No. FFUG-2024-0046).

REFERENCES

1. **Gruber A., Drabenstedt A., Tietz C., Ludovic F., Wrachtrup J., von Borczyskowski C.,** Scanning Confocal Optical Microscopy and Magnetic Resonance on Single Defect Centers, Science. 276 (5321) (1997) 2012–2014.

2. **Drabenstedt A., Ludovic F., Tietz C., Jelezko F., Kilin S.Y., Nizovtzev A., Wrachtrup J.,** Low-temperature microscopy and spectroscopy on single defect centers in diamond, Physical Review B. 60 (16) (1999) 11503.

3. **Baranov P.G., von Bardeleben H.J., Jelezko F., Wrachtrup J.,** Magnetic resonance of semiconductors and their nanostructures: Basic and advanced applications, Springer, Vienna. (2017).

4. **Yakovleva V.V., Likhachev K.V., Ilyin I.V., Muzafarova M.V., Bundakova A.P., Babunts R.A., Titkov S.V., Baranov P.G.,** Micron scale scanning imaging and diagnostics of natural and treated diamond with nitrogen-vacancy centers as a probe, Physica B: Condensed Matter. 713 (2025) 417374.

5. **Babunts R.A., Muzafarova M.V., Anisimov A.N., Solmatov V.A., Baranov P.G.,** Diagnostics of NV defect structure orientation in diamond using optically detected magnetic resonance with a modulated magnetic field, Tech. Phys. Lett. 41 (6) (2015) 583–586.

6. **Baranov P.G., Soltamov V.A., Anisimov A.N., Muzafarova M.V., Babunts R.A.,** Method for determining the orientation of the NV defects in a crystal, Patent of the Russian Federation No. 2570471 (2015).

7. **Orlov Y.L.,** The Mineralogy of the Diamond, John Wiley & Sons. (1977).

8. **Baranov P.G., Soltamova A.A., Tolmachev D.O., Romanov N.G., Babunts R.A., Shakhov F.M., Kidalov S.V., Vul A., Mamin G., Orlinskii S., Silkin N.I.,** Enormously High Concentrations of Fluorescent Nitrogen-Vacancy Centers Fabricated by Sintering of Detonation Nanodiamonds, Small. 7 (11) (2011) 1533–1537.

9. **Babunts R.A., Breev I.D., Kramushchenko D.D., Bundakova A.P., Muzafarova M.V., Anisimov A.N., Baranov P.G.,** Interaction between NV centers and substituting nitrogen complexes in diamond as a diagnostic probe of the local nitrogen concentration, J. Appl. Phys. 132 (17) (2022) 175705.

THE AUTHORS

YAKOVLEVA Valentina V.
v.yakovleva@mail.ioffe.ru
ORCID: 0000-0003-1040-5362

LIKHACHEV Kirill V.
Likhachevkv@mail.ioffe.ru
ORCID: 0000-0001-5038-2535

MUZAFAROVA Marina V.
Marina.Muzafarova@mail.ioffe.ru
ORCID: 0000-0003-3227-5220

BABUNTS Roman A.
roman.babunts@gmail.com
ORCID: 0000-0001-8434-9020

BARANOV Pavel G.
Pavel.Baranov@mail.ioffe.ru
ORCID: 0000-0003-1955-9245

Received 15.12.2025. Approved after reviewing 16.02.2026. Accepted 20.02.2026.

© Peter the Great St. Petersburg Polytechnic University, 2026

Heterostructures, superlattices, quantum wells

Conference materials
UDC 535.3
DOI: https://doi.org/10.18721/JPM.191.105

Radiative recombination in InAs/InAsSb/InAsSbP heterostructures

I.D. Kirilenko [1]✉, K.D. Mynbaev [1,2], V.V. Romanov [2], N.L. Bazhenov [2], K.D. Moiseev [2]

[1] ITMO University, St. Petersburg, Russia;
[2] Ioffe Institute, St. Petersburg, Russia
✉ idkirilenko@itmo.ru

Abstract. Comprehensive studies of electroluminescence of InAs/InAsSb/InAsSbP heterostructures with different fractions of Sb in narrow-gap InAsSb layers were performed. Electroluminescent properties of the heterostructures were investigated in a wide range of both forward and reverse biases at temperature $T = 77$ K. It was found that in the different parts of the heterostructures, radiative recombination proceeds via interband and interface mechanisms, which manifests in the presence of two emission bands at different wavelengths in the electroluminescence spectra recorded under the forward bias. The recombination mechanisms were explained using schematic band diagrams of the heterostructures calculated for $T = 77$ K and both directions of the external bias.

Keywords: solid solutions, InAsSb, heterostructures, interface recombination, electroluminescence

Citation: Kirilenko I.D., Mynbaev K.D., Romanov V.V., Bazhenov N.L., Moiseev K.D., Radiative recombination in InAs/InAsSb/InAsSbP heterostructures, St. Petersburg State Polytechnical University Journal. Physics and Mathematics. 19 (1.1) (2026) 33–38. DOI: https://doi.org/10.18721/JPM.191.105

This is an open access article under the CC BY-NC 4.0 license (https://creativecommons.org/licenses/by-nc/4.0/)

Конференционная статья
УДК 535.3
DOI: https://doi.org/10.18721/JPM.191.105

Излучательная рекомбинация в гетероструктурах InAs/InAsSb/InAsSbP

Я.Д. Кириленко [1]✉, К.Д. Мынбаев [1, 2], В.В. Романов [2], Н.Л. Баженов [2], К.Д. Моисеев [2]

[1] Университет ИТМО, Санкт-Петербург, Россия;
[2] Физико-технический институт им. А.Ф. Иоффе, Санкт-Петербург, Россия
✉ idkirilenko@itmo.ru

Аннотация. Всесторонне исследована электролюминесценция гетероструктур InAs/InAsSb/InAsSbP с различным содержанием Sb в узкозонном слое InAsSb. Электролюминесцентные свойства гетероструктур исследовались при приложении смещения как в прямом, так и в обратном направлениях при температуре $T = 77$ K. Установлено, что в различных частях гетероструктур реализуются межзонный и интерфейсный механизмы излучательной рекомбинации, что проявляется в наличии двух полос излучения с разной длиной волны в спектрах электролюминесценции при прямом смещении. Механизмы рекомбинации объяснены с использованием зонных диаграмм гетероструктур, рассчитанных для $T = 77$ K и обоих направлений внешнего смещения.

Ключевые слова: твердые растворы, InAsSb, гетероструктуры, интерфейсная рекомбинация, электролюминесценция

© Kirilenko I.D., Mynbaev K.D., Romanov V.V., Bazhenov N.L., Moiseev K.D., 2026. Published by Peter the Great St. Petersburg Polytechnic University.

Ссылка при цитировании: Кириленко Я.Д., Мынбаев К.Д., Романов В.В., Баженов Н.Л., Моисеев К.Д. Излучательная рекомбинация в гетероструктурах InAs/InAsSb/InAsSbP // Научно-технические ведомости СПбГПУ. Физико-математические науки. 2026. Т. 19. № 1.1. С. 33–38. DOI: https://doi.org/10.18721/JPM.191.105

Статья открытого доступа, распространяемая по лицензии CC BY-NC 4.0 (https://creativecommons.org/licenses/by-nc/4.0/)

Introduction

Heterostructures (HS) featuring an active layer made of $InAs_{1-y}Sb_y$ solid solution are widely incorporated in optoelectronic devices operating in the mid-wavelength infrared (IR) spectrum. By adjusting the antimony content in this layer, it is possible to cover a spectral range from 3.4 μm to 11.0 μm. The above-mentioned IR optoelectronic devices mostly find applications in gas and molecule spectroscopy, environmental monitoring systems, industrial and safety solutions, and medical diagnosis [1 – 5]. However, the efficiency of InAsSb-based devices operating at near-room temperatures (T = 25 °C) is hindered by the dominance of non-radiative recombination. Consequently, the studies of fundamental recombination processes occurring via different mechanisms, particularly dominating spectral properties of HSs of various designs and active layer compositions, remain highly relevant. In order to investigate this effect, comprehensive studies of electroluminescence (EL) of n-InAs/n-$InAs_{1-y}Sb_y$/p-InAsSbP (y = 0.06–0.10) HSs under both forward and reverse bias at T = 77 K were carried out in this work.

Materials and Methods

HSs were grown by metal-organic vapor-phase epitaxy in a horizontal reactor at atmospheric pressure; the detailed growth procedure is discussed elsewhere [6]. Undoped (001)InAs wafers with the electron concentration $n = 3 \cdot 10^{16}$ cm^{-3} at T = 300 K were used as substrates. Epitaxial layers of the ternary $InAs_{1-y}Sb_y$ solid solution (y = 0.06–0.10) had the thickness of ~3.0 μm and were not doped intentionally, having n-type conductivity. The ~1.2 μm-thick barrier layers represented the quaternary $InAs_{1-x-y'}Sb_{y'}P_x$ solid solution with the composition set during the growth as y' = 0.22 and x = 0.47. P-type conductivity in the barrier layers was achieved by doping them with Zn during growth. The composition of the active layers in HSs is listed in Table.

Table

Studied heterostructures

#	Heterostructure design
1	n^0-InAs/n^0-$InAs_{0.94}Sb_{0.06}$/p^+-InAsSbP:Zn
2	n^0-InAs/n^0-$InAs_{0.91}Sb_{0.09}$/p^+-InAsSbP:Zn
3	n^0-InAs/n^0-$InAs_{0.90}Sb_{0.10}$/p^+-InAsSbP:Zn

Light-emitting diode chips were fabricated from the HSs and mounted substrate-side down onto TO-18 housings. EL studies were carried out under pulse excitation (f = 1 kHz, τ = 2 μs) and both forward and reverse bias at T = 77 K with the use of computer-controlled setup employing a grating monochromator MDR-23 (LOMO) and a lock-in amplifier. A cooled (T = 77 K) InSb photodiode was used as a detector.

Results and Discussion

EL spectra of structures *2* and *3* under forward bias contained two distinct emission bands (Fig. 1): a low-energy band ($h\nu_1$) related to radiative transitions involving the InAsSb/InAsSbP heterointerface and a high-energy band ($h\nu_2$) attributed to near-interband transitions with the assistance of impurity states in the substrate. The spectral position of the peak intensity of the $h\nu_1$ band varied with the change of Sb fraction in the active layer, while that of the $h\nu_2$ band remained constant ($h\nu_2$ = 0.393 eV) and close to the band gap energy of the bulk InAs at the same temperature ($E_{g,\,InAs}$ = 0.408 eV). The photon energy difference of ~15 meV allowed us to attribute this band to donor-acceptor recombination involving a shallow acceptor state, which is typical of the undoped InAs [7,8].

© Кириленко Я.Д., Мынбаев К.Д., Романов В.В., Баженов Н.Л., Моисеев К.Д., 2026. Издатель: Санкт-Петербургский политехнический университет Петра Великого.

High-energy band $h\nu_2$ dominated independently of injection levels, and its intensity increased throughout the whole range of voltages, whereas the intensity of the $h\nu_1$ band gradually decreased with the injection level increasing. This phenomenon can be explained by the lowering of the potential barrier at the heterointerface between the ternary and quaternary solid solutions as the forward bias increased. Under these conditions, holes with increasing probability could overcome the barrier, reaching first the narrow-gap layer and then the n^0-InAs substrate. That redistribution of charge carriers led to increasing recombination probability in the substrate, resulting in the increase of the high-energy band intensity in the EL spectra.

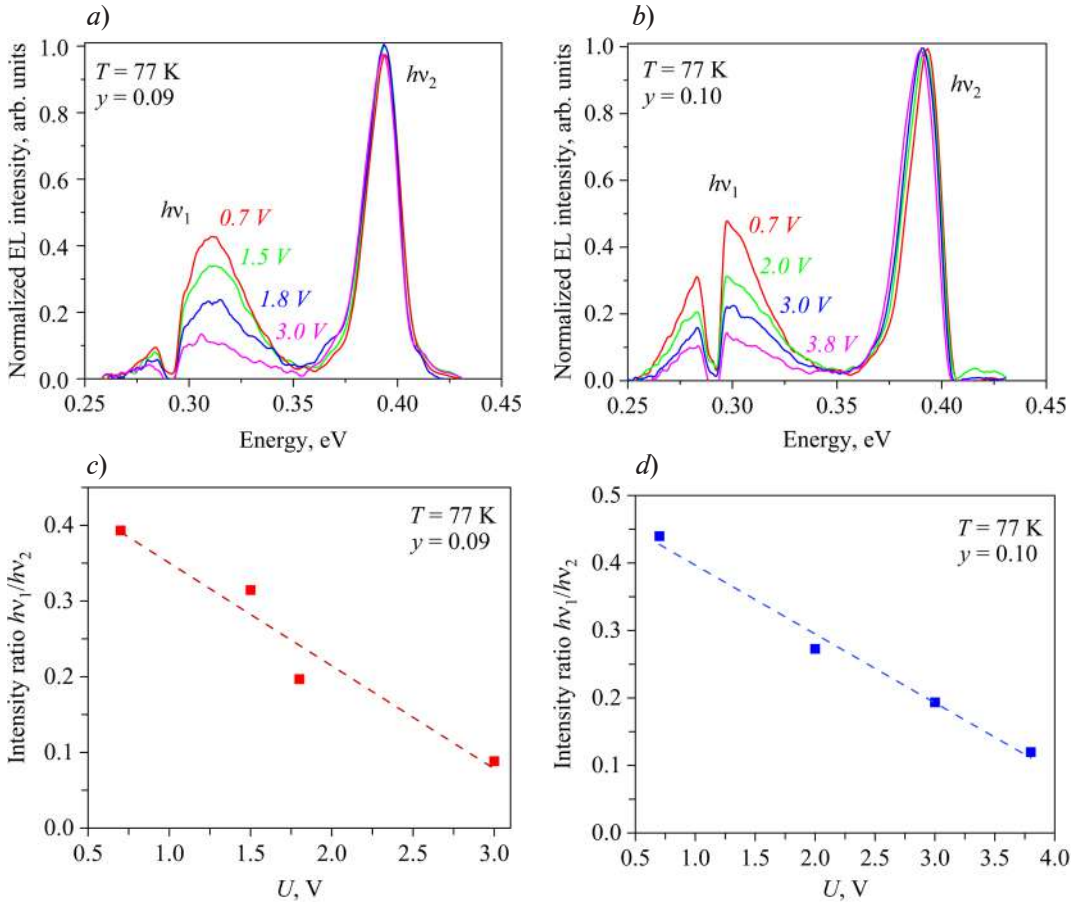

Fig. 1. Electroluminescence spectra under the forward bias applied to structures *2* (*a*) and *3* (*b*), and dependence of the ratio of EL band intensities $h\nu_1/h\nu_2$ on the applied bias (*c*, *d*)

EL under reverse bias was studied to determine whether the energy gaps alignment at the InAsSb/InAsSbP heterointerface was resulting from the specifics of chemical processes occurring during precursor decomposition at the stage of structure growth, or the offset forming the type-II heterojunction was caused just by the applied forward bias. EL spectra of structures *1* and *3* under the reverse bias $-U$ at $T = 77$ K are shown in Fig. 2. For comparison, Fig. 2 also shows corresponding EL spectra of the structures under the forward bias +U of the about the same value.

In the EL spectrum recorded with the reverse bias applied to structure *2*, both bands of luminescence were present, similarly to the situation under the forward bias. This observation is indicative of the fact that the energy band structure of InAsSb/InAsSbP heterojunction is not the result of an applied external bias, but an inherent feature of HS governed by the technological mode at the stage of fabrication (Fig. 2, *a*). In case of structure *3*, under both forward and reverse bias band $h\nu_2$ resulting from radiative recombination in the InAs substrate was observed, unlike band $h\nu_1$, which was solely present in EL spectra recorded under the forward bias. The latter observation is also indicative of the fact that the long-wavelength EL of HSs at low temperatures originates at the interface rather than in the 'bulk' of the active layer.

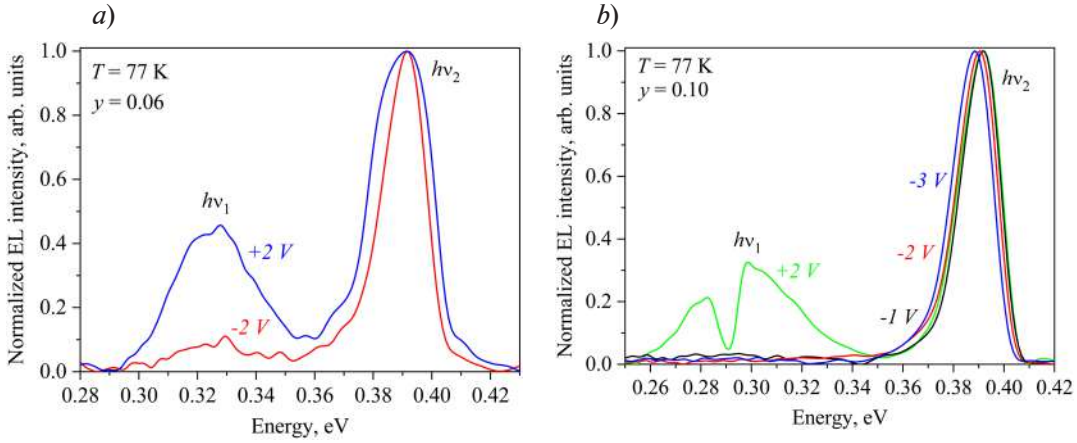

Fig. 2. Electroluminescence spectra under the reverse bias applied to structures *2* (*a*) and *3* (*b*) compared to that under the forward bias with close absolute value

The studied HSs featured noticeably high potential barriers for electrons in the conduction band at the InAsSb/InAsSbP heterointerface. The presence of such barriers strongly affects the electrical and luminescent properties of HSs. Fig. 3 (*a*, *d*) schematically shows band diagrams of structures *2* and *3* at $T = 77$ K, calculated in accordance to experimental data discussed in the work [9]. In that case, ternary and quaternary solid solutions form heterojunctions of type-II featuring high conduction band offsets ΔE_c and comparably low valence band offsets ΔE_v [10].

Under forward bias $U = 0.35$ V the potential barrier for electrons (holes) at the InAsSb/InAsSbP heterointerface was estimated to be $\Delta E_c = 0.19$ eV ($\Delta E_v = 0.05$ eV) and $\Delta E_c = 0.22$ eV ($\Delta E_v = 0.08$ eV) for structures *2* and *3*, respectively. An increase of free charge carriers concentration in the appropriate layers of the HSs results in localization of carriers in self-consistent potential wells formed on the opposite sides of the type-II heterointerface under the forward bias. This situation leads to an increase in the probability of radiative transitions at the interface (Fig. 3, *b*, *e*).

Fig. 3 (*c*, *f*) shows energy band diagrams similar to that under reverse bias −0.22 V with voltage drops at the InAs/InAsSb and InAsSb/InAsSbP barriers taken as −0.02 V and −0.20 V,

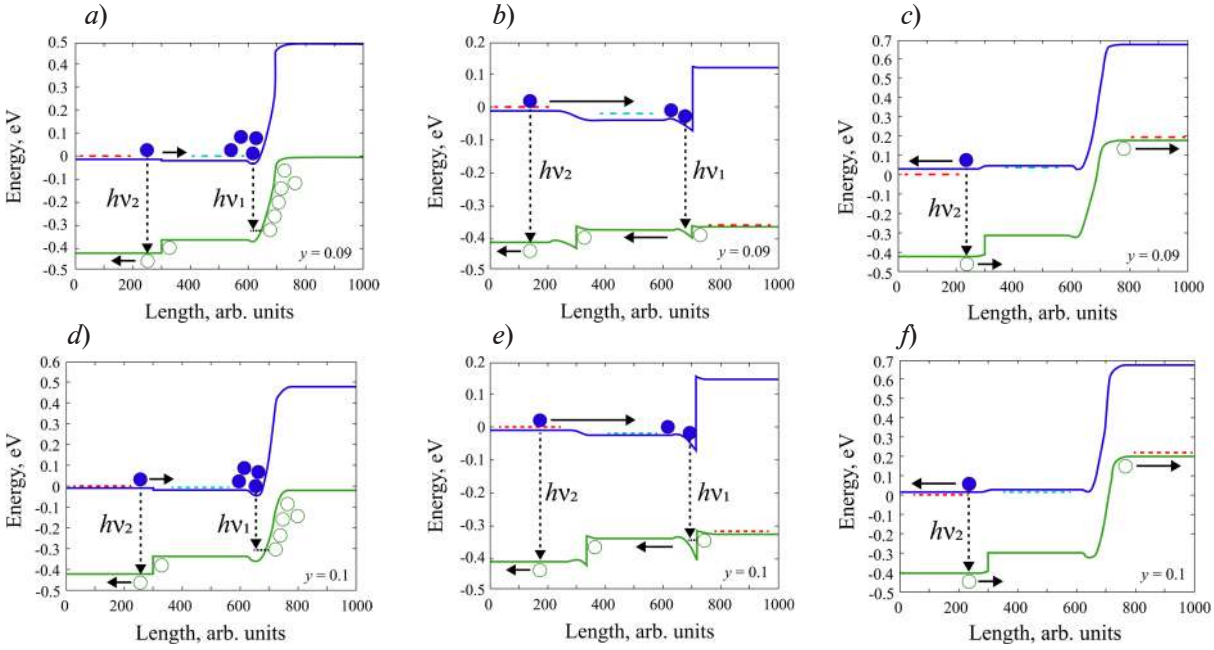

Fig. 3. Schematic band diagrams of structures *2* and *3*, respectively: under minimal forward bias (*a*, *d*); under forward bias of 0.35 V (*b*, *e*); under reverse bias of −0.22 V and corresponding voltage drops at the InAs/InAsSb and InAsSb/InAsSbP barriers estimated as −0.02 V and −0.20 V, respectively (*c*, *f*)

respectively. Since in this situation there are no potential barriers for charge carriers, they are free to move throughout the structure and radiative recombination occurs in the substrate, which corresponds to the EL spectra shown in Fig. 2. The interface EL band recorded under reverse bias applied to structure *1* ($y = 0.06$) is presumably associated with peculiarities of InAsSb / InAsSbP heterointerface of that particular structure. Note that for simplicity, transitions in the substrate are shown in Fig. 3 as interband ones; in reality they occur via shallow levels in the bandgap, as discussed above.

Conclusion

Our studies of electroluminescence at low temperature ($T = 77$ K) under both forward and reversed biases showed that in different parts of InAs / InAsSb / InAsSbP heterostructures radiative recombination occurs via interband or interface mechanisms. The intensity of the interface EL band decreases with the increase of the external bias in the forward direction due to the redistribution of charge carriers with decreasing of the potential barrier at the InAsSb/InAsSbP heterointerface. Observation of electroluminescence under a bias applied to the HSs in the reverse direction indicated that energy band alignment at the InAsSb/InAsSbP type II heterointerfaces is the result of epitaxial growth conditions rather than the applied bias.

The presence of two radiative recombination channels in the studied HSs and the dependence of the intensity ratio of the corresponding electroluminescence bands on the applied forward bias shows possibilities to control output wavelength via adjustment of the bias. These HSs are promising for development of differential detection devices used in optical spectroscopy.

REFERENCES

1. **Rangel G. F., de Leon Martínez L. D., Walter L. S., Mizaikoff B.,** Recent advances and trends in mid-infrared chem/bio sensors, TrAC Trends in Analytical Chemistry. 180 (2024) 117916.

2. **Tang Y., Zhao Y., Liu H.,** Room-Temperature Semiconductor Gas Sensors: Challenges and Opportunities, ACS Sensors. 7 (12) (2022) 3582–3597.

3. **Hlavatsch M., Mizaikoff B.,** Advanced mid-infrared lightsources above and beyond lasers and their analytical utility, Analytical Science. 38 (2022) 1125–1139.

4. **Gawron W., Madejczyk P., Martyniuk P., Krishna S.,** Infrared Barrier Detectors With Metamorphic InAsSb Absorbers on GaAs Substrates, IEEE Sensors Journal. 24 (9) (2024) 14151–14158.

5. **Fujita H., Yasuda D., Ota S., Geka H., Gomes Camargo E., Isshiki S., Fukunaka T., Kuze N.,** Hydrofluoroolefins Leakage Detection by Nondispersive Infrared Gas Sensor Using InAsSb Light Emitting Diodes and Photodiodes, IEEE Sensors Letters. 7 (9) (2023) 3502004.

6. **Romanov V.V., Moiseev K.D.,** Features of the Energy Band Structure of the InAsSbP Epilayer Deposited on a Surface of the $InAs_{1-y}Sb_y$ Solid Solution, Physics of the Solid State. 65 (10) (2023) 1634–1641.

7. **Lacroix Y., Tran C.A., Watkins S.P., Thewalt M.L.W.,** Low temperature photoluminescence of epitaxial InAs, Journal of Applied Physics. 80 (11) (1996) 6416–6424

8. **Sumikura H., Shinya A., Notomi M.,** Time-resolved mid-infrared photoluminescence spectroscopy of an undoped InAs substrate, Applied Physics Letters. 124 (5) (2024) 052105.

9. **Moiseev K.D., Romanov V.V.,** Band Diagram of the $InAs_{1-y}Sb_y$/InAsSbP Heterojunction in the Composition Range $y < 0.2$, Physics of the Solid State. 63 (4) (2021) 595–602.

10. **Grigoryev M.M., Ivanov E.V., Moiseev K.D.,** Interfacial luminescence in an InAs/InAsSbP isotype type II heterojunction at room temperature, Semiconductors. 45 (10) (2011) 1334–1338.

THE AUTHORS

KIRILENKO Iaroslav D.
idkirilenko@itmo.ru
ORCID: 0009-0007-1056-5100

MYNBAEV Karim D.
mynkad@mail.ioffe.ru
ORCID: 0000-0002-9853-8874

ROMANOV Viacheslav V.
romanovvv@mail.ioffe.ru
ORCID: 0000-0002-9989-3843

BAZHENOV Nikolay L.
bazhnil.ivom@mail.ioffe.ru
ORCID: 0000-0002-3019-2280

MOISEEV Konstantin D.
mkd@iropt2.ioffe.ru
ORCID: 0000-0002-6306-0129

Received 12.12.2025. Approved after reviewing 09.02.2026. Accepted 09.02.2026.

© Peter the Great St. Petersburg Polytechnic University, 2026

Conference paper
UDC: 538.911
DOI: https://doi.org/10.18721/JPM.191.106

Heterostructures with ultrathin $In_xGa_{1-x}As$/GaAs(001) metamorphic buffer layers and InAs/InGaAs QDs grown by molecular beam epitaxy

O.E. Lakuntsova ✉, G.V. Klimko, I.V. Sedova, A.V. Myasoedov, A.N. Semenov, N.D. Prasolov, S.V. Sorokin

Ioffe Institute, Saint Petersburg, Russia
✉ o.e.lakuntsova@mail.ioffe.ru

Abstract. The heterostructures with ultrathin (~220 nm) $In_xGa_{1-x}As$/GaAs(001) metamorphic buffer layers with a convex indium composition profile were grown by molecular beam epitaxy and studied using structural characterization techniques. Analysis of atomic force microscopy images revealed a relationship between the surface roughness and the growth conditions of the graded layer. The density of threading dislocations in the structures with a ultra-thin graded layer was estimated as ~10^7 cm^{-2}, which is consistent with the high average grading rate of ~90% In/μm. The reciprocal space maps of high-resolution X-ray diffraction measured for both symmetric (004) and asymmetric (224) reflections in grazing exit geometry are presented.

Keywords: Metamorphic buffer layers, convex compositional profile, molecular beam epitaxy, $In_xGa_{1-x}As$, heterostructures, reciprocal space mapping, atomic force microscopy, energy-dispersive X-ray spectroscopy, transmission electron microscopy

Funding: The work was carried out within the framework of the State Assignment No. FFUG-2024-0043.

Citation: Lakuntsova O.E., Klimko G.V., Sedova I.V., Myasoedov A.V., Semenov A.N., Prasolov N.D., Sorokin S.V., Heterostructures with ultrathin $In_xGa_{1-x}As$/GaAs(001) metamorphic buffer layers and InAs/InGaAs QDs grown by molecular beam epitaxy, St. Petersburg State Polytechnical University Journal. Physics and Mathematics. 19 (1.1) (2026) 39–44. DOI: https://doi.org/10.18721/JPM.191.106

This is an open access article under the CC BY-NC 4.0 license (https://creativecommons.org/licenses/by-nc/4.0/)

Конференционная статья
УДК 538.911
DOI: https://doi.org/10.18721/JPM.191.106

Гетероструктуры со сверхтонкими метаморфными буферными слоями $In_xGa_{1-x}As$/GaAs(001) и КТ InAs/InGaAs, выращенные методом молекулярно-пучковой эпитаксии

О.Е. Лакунцова ✉, Г.В. Климко, И.В. Седова, А.В. Мясоедов, А.Н. Семенов, Н.Д. Прасолов, С.В. Сорокин

Физико-технический институт им. А.Ф. Иоффе РАН, Санкт-Петербург, Россия
✉ o.e.lakuntsova@mail.ioffe.ru

Аннотация. Гетероструктуры со сверхтонкими (~220 нм) метаморфными буферными слоями $In_xGa_{1-x}As$/GaAs(001) с корневым профилем изменения состава по индию выращены методом молекулярно-пучковой эпитаксии и исследованы с использованием методов структурной характеризации. Из анализа изображений атомно-силовой микроскопии установлена взаимосвязь между шероховатостью поверхности и условиями роста градиентного слоя. Оценена плотность прорастающих дислокаций в структурах со сверхтонким градиентным слоем ~10^7 $см^{-2}$, что согласуется с высокой средней скоростью изменения содержания In ~90% In/мкм.

© Lakuntsova O.E., Klimko G.V., Sedova I.V., Myasoedov A.V., Semenov A.N., Prasolov N.D., Sorokin S.V., 2026. Published by Peter the Great St. Petersburg Polytechnic University.

Представлены карты обратного пространства высокоразрешающей рентгеновской дифрактометрии, измеренные для симметричных (004) и асимметричных (224) отражений в геометрии скользящего отражения.

Ключевые слова: Метаморфные буферные слои, корневой профиль изменения состава, молекулярно-пучковая эпитаксия, $In_xGa_{1-x}As$, гетероструктуры, картирование обратного пространства, атомно-силовая микроскопия, энергодисперсионная рентгеновская спектроскопия, просвечивающая электронная микроскопия

Финансирование: Работа выполнена в рамках Государственного задания № FFUG-2024-0043.

Ссылка при цитировании: Лакунцова О.Е., Климко Г.В., Седова И.В., Мясоедов А.В., Семенов А.Н., Прасолов Н.Д., Сорокин С.В. Гетероструктуры со сверхтонкими метаморфными буферными слоями $In_xGa_{1-x}As$/GaAs(001) и КТ InAs/InGaAs, выращенные методом молекулярно-пучковой эпитаксии // Научно-технические ведомости СПбГПУ. Физико-математические науки. 2026. Т. 19. № 1.1. С. 39–44. DOI: https://doi.org/10.18721/JPM.191.106

Статья открытого доступа, распространяемая по лицензии CC BY-NC 4.0 (https://creativecommons.org/licenses/by-nc/4.0/)

Introduction

One of the key requirements in growing heterostructures for device applications is a small lattice mismatch between the structure layers and the substrate to provide the conditions of pseudomorphic growth, since strain relaxation with the formation of misfit dislocations (MDs) also leads to the appearance of numerous threading dislocations (TDs), which can significantly degrade the characteristics of semiconductor devices. If the growth of pseudomorphic structures is not possible, an approach based on metamorphic buffer layers (MBLs) with graded composition profiles is widely used. In this case, MBL provide a smooth transition from the substrate lattice constant to the specified lattice constant. One of the possible ways for implementing a single-photon source emitting in the telecom O-band or C-band (λ = 1.3 and 1.55 μm, respectively) is also associated with the use of $In_xGa_{1-x}As$/GaAs(001) MBL followed by the formation of InAs quantum dots (QDs) in an InGaAs matrix [1 – 3]. The advantage of this approach is the ability to use $Al_{0.9}Ga_{0.1}As$/GaAs distributed Bragg reflectors, which potentially allows the fabrication of micropillars using photolithography and ion etching.

Reducing the thickness of the MBL is extremely important for the fabrication of microcavity structures with a small mode volume, as it leads to an increase in the Purcell factor and, consequently, to an increase in the rate of spontaneous radiative recombination from QDs. The key challenges are the selection of a suitable MBL design, as well as finding the optimal growth conditions that ensure both a sufficiently smooth surface morphology and low TDs density in the active region of the structure.

In this work, we study the structural properties of heterostructures with InAs/InGaAs QDs grown on top of ultrathin $In_xGa_{1-x}As$/GaAs(001) MBL with a square-root (“convex”) indium composition profile. Transmission electron microscopy (TEM), energy-dispersive X-ray spectroscopy (EDS), atomic force microscopy (AFM), X-ray diffraction both in 2θ-ω- scanning mode and reciprocal space mapping (RSM) mode were used as characterization techniques.

Materials and Methods

The heterostructures with ultrathin $In_xGa_{1-x}As$/GaAs(001) MBL were grown by molecular beam epitaxy (MBE) on semi-insulating GaAs(001) epi-ready substrates and contain $In_xGa_{1-x}As$ MBL layer, a QD layer and an inverse layer. Standard Ga and In effusion cells, as well as an As valve cracker cell were used as molecular beam sources. The growth of all heterostructures began with the deposition of a homoepitaxial GaAs buffer layer (d_{GaAs} ~ 0.2 μm) at a temperature of T_S ~ 590–600°C. The thickness of the $In_xGa_{1-x}As$ MBL with a convex composition profile was as low as d_{MBL} ~ 220 nm with initial In step of x_{min} = 0.18 and maximum In content at the end

© Лакунцова О.Е., Климко Г.В., Седова И.В., Мясоедов А.В., Семенов А.Н., Прасолов Н.Д., Сорокин С.В., 2026. Издатель: Санкт-Петербургский политехнический университет Петра Великого.

of graded layer x_{max} = 0.38. In this case the average In composition grading rate is as high as ~90% In/μm. The variable parameters during MBE of the graded layer were both the substrate temperature and the V/III flux ratio: the substrate temperature varied from ~380 to 470°C, while the J_V/J_{III} flux ratio varied correspondingly in the range of ~2–6.5. InAs/InGaAs QDs were deposited directly on top of the graded layer using the Stranski-Krastanov growth mode followed by the deposition of a uniform composition layer with a thickness ~200 nm at a temperature of T_S ~ 420°C [4]. The indium content in this so-called "inverse" layer (x_{inv}) is lower than x_{max}, since this layer reduces the residual strain accumulated in the upper part of the graded layer. The thickness of the inverse layer is d_{inv} ~ 200 nm, and the indium content in this layer is $x_{inv} \approx 0.28$. The parameters of the heterostructures under study, as well as the MBE growth conditions of the graded layer are listed in Table.

Table

Parameters of the studied heterostructures

Type of structure	d_{MBL}, μm	d_{inv}, μm	x_{min}	x_{max}	x_{inv}	J_V/J_{III}	$T_{S(MBL)}$, °C	$T_{S(inv)}$, °C
#1	0.22	0.2	0.18	0.38	~0.28	2	380	420
#2						4	420	
#3						6.5	470	

Notations: d_{MBL} is the thickness of graded layer, d_{inv} is the thickness of inverse layer, x_{min} and x_{max} are the minimum and maximum In content in the $In_xGa_{1-x}As$ MBL with square-root profile, x_{inv} is In content in the inverse layer, J_V/J_{III} is V/III flux ratio during MBE growth of the graded layer, $T_{S(MBL)}$ and $T_{S(inv)}$ is the substrate temperature during MBE growth of the graded and inverse layer, respectively.

TEM measurements were performed using a JEOL-2100F electron microscope at an accelerating voltage of 200 kV. The specimen was prepared using a standard technique, including mechanical grinding and polishing to a thickness of ~10 μm and subsequent Ar^+ ion milling. A cross section was prepared to study the heterostructure in the vicinity of zone axis ⟨110⟩. Microanalysis of the composition of heterostructures with MBL was carried out by EDS technique using a Bruker XFlash 6TI30 solid-state energy-dispersive X-ray detector. A DRON-8 (Bourevestnik, Russia) X-ray diffractometer was used for high-resolution X-ray diffraction measurements. The surface morphology of the metamorphic heterostructures was explored using an AFM Dimension 3100 (Veeco) microscope.

Results and Discussion

Fig. 1, *a* shows a bright-field TEM image of the structure #2. The cross-section in the image corresponds to the {110} crystallographic plane. The image demonstrates that the dense array of MDs is shifted towards the GaAs substrate presumably due to efficient strain relaxation at the initial growth stages of $In_xGa_{1-x}As$ MBL with a large initial indium step (x_{min} = 0.18) and a high grading rate (~90% In/μm) of the graded layer with convex compositional profile.

The sheet of InAs/InGaAs QDs is clearly visible due to the strain contrast. The TDs density in heterostructure #2 can be estimated at a level of $\rho_{TD} \sim 10^7$ cm^{-2}. The In composition profile in structure #2 measured using EDS technique is close to the technologically specified profile (see Fig. 1, *b*). The step in the thickness between points of the profile is as low as ~ 6 nm. To improve the accuracy of the analysis, the specimen was mounted so that its surface, (001) plane, was perpendicular to the first (longitudinal) axis of the TEM double-tilt specimen holder. The holder was tilted at an angle of approximately 15° towards the detector, and a second tilt was used to achieve an orientation at which the (002) and (00-2) reflections were observed with equal intensity in the electron diffraction pattern. This configuration allows for an increase in the level of X-ray signal reaching the detector while still providing sharp boundaries between the layers during measurement. The experimentally measured MBL profile exhibits extended tails near the interfaces with GaAs and inverse layer, which are presumably caused by local overlapping of the regions during measurements.

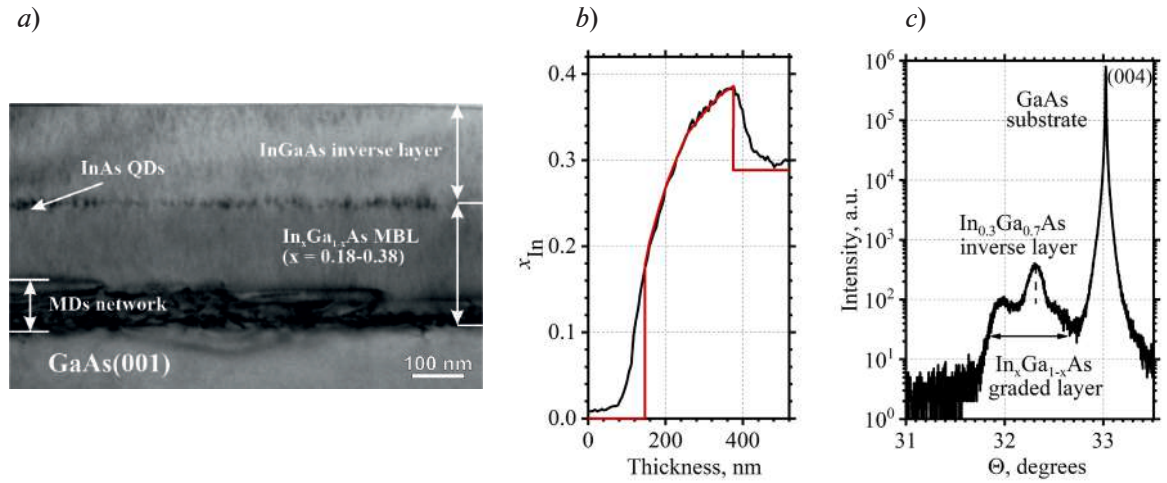

Fig. 1. Bright-field cross-sectional TEM image of the heterostructure #2 obtained in a two-beam diffraction contrast mode with strong excitation of reflection **g** = 2–20 (*a*). In composition profile measured using the EDS technique (black curve) and the technologically specified one (red curve) in structure #2 (*b*). 2θ-ω X-ray diffraction curve around GaAs (004) symmetric reflection (*c*)

Fig. 1, *c* shows the diffraction curve measured around the GaAs (004) reflection for the same structure. The narrow peak near $\theta \approx 33.03°$ corresponds to the (004) reflection of GaAs, while the broad peak at smaller angles originates from the $In_xGa_{1-x}As$ MBL. The asymmetric shape of this peak is a direct indication of a non-linear composition profile of the graded layer [5]. The intense peak at $\theta \approx 32.3°$ corresponds to the inverse layer.

The surface morphology and roughness of the samples were characterized by AFM. Surface roughness is one of the main criteria for the optimization of MBL because it has a significant impact on InAs QDs growth. The AFM topographical images for all the studied structures with a surface area of 100×100 μm are shown in Fig. 2. It can be seen that all structures are characterized by a "cross-hatch" morphology with surface corrugations along the ⟨110⟩ directions. This morphology is a sign of a two-dimensional growth mode and is usually associated with the formation of a network of MDs, since the average period of surface undulations corresponds to the separation of MDs projected into the interface [6]. A.M. Andrews et al. proposed a model according to which the cross-hatch is associated with the formation of an array of MDs and, accordingly, with the appearance of steps on the growth surface due to the gliding of TDs [7]. The asymmetric character of the surface undulations reflects the asymmetric distribution of MDs and is caused by the anisotropic surface migration of In adatoms in two mutually perpendicular directions [110] and [1–10]. The root mean square (RMS) surface roughness exhibits a rise from 2.89 nm to 4.23 nm with increasing substrate temperature, which agrees well with previous works showing that the surface roughness associated with cross-hatch may be reduced by low-temperature growth [8]. In segregation is important even at a growth temperature of T_S = 380 °C. To reduce the effect of In segregation on the surface, the V/III flux ratio should be increased with increasing T_S.

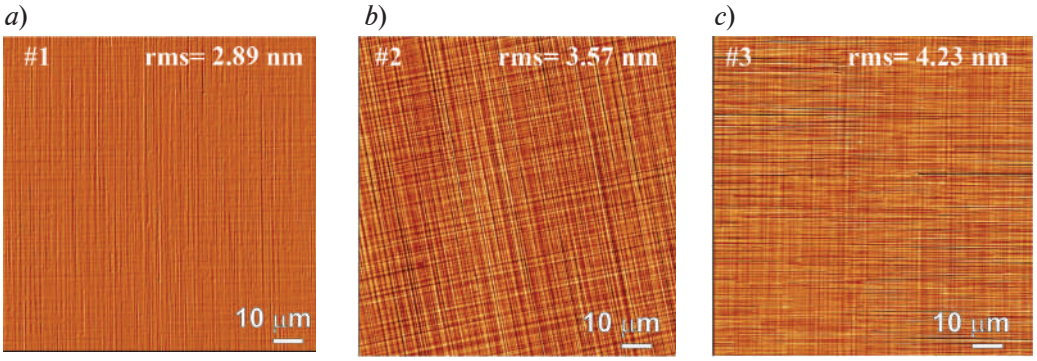

Fig. 2. AFM topographical images for structures #1 (*a*), #2 (*b*) and #3 (*c*).
The dimensions of the surface area are 100×100 μm

RSMs are commonly used to estimate the state of strain and crystallographic tilt in heterostructures with MBLs. Fig. 3 demonstrates the X-ray diffraction reciprocal space maps measured for both symmetric (004) and asymmetric (224) reflections in grazing exit geometry for the structure #2. The symmetric (004) RSMs were measured for two orthogonal azimuth angles perpendicular to ⟨110⟩ directions designated here as $\Phi = 0°$ and $\Phi = 90°$.

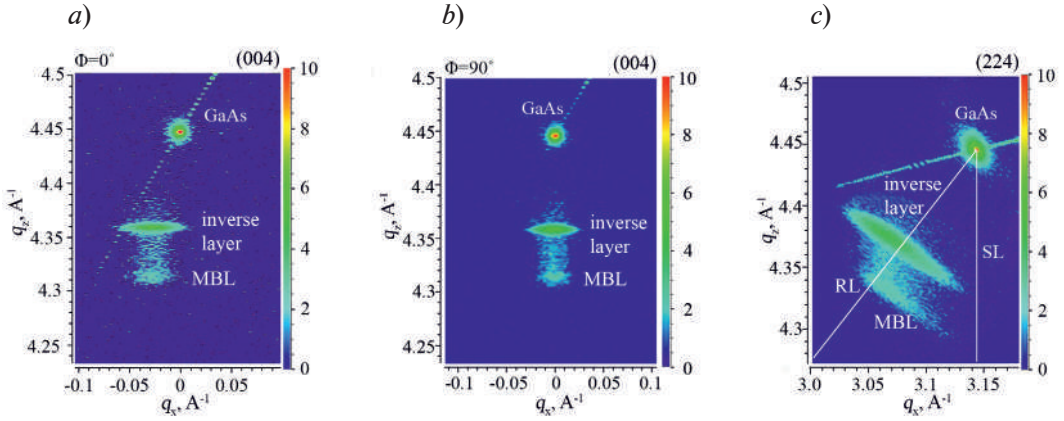

Fig. 3. The reciprocal space maps for both symmetric (004) (*a*, *b*) and asymmetric (224) reflections (*c*) measured in grazing exit geometry for the structure #2

RSMs demonstrate three clearly resolved peaks. The peak with the highest qz coordinate corresponds to the GaAs substrate, and the second most intense peak corresponds to the inverse InGaAs layer. The graded layer in Fig. 3, *a* and Fig. 3, *b* appears as a less intense band extending along the q_z axis. The peak with the lowest q_z coordinate is associated with the upper part of the graded layer due to the lower grading rate in the upper part of the MBL with a convex composition profile. The shift of the peaks from inverse and MBL layers along the q_x axis in symmetrical RSMs reflects the crystallographic tilt of these layers with respect to the GaAs substrate. The tilt arises due to an imbalance of MDs with positive and negative tilt components because of an imbalance in the dislocation populations on the various slip systems [9]. The broadening of the peaks in the direction perpendicular to the scattering vector (i.e., perpendicular to the vertical line) is associated with the mosaicity of the crystal.

The asymmetric (224) RSM is shown in Fig. 3, *c*. The RL denotes the relaxation line, which shows the positions of fully relaxed $In_xGa_{1-x}As$ alloys with different lattice constants in reciprocal space. The SL line shows a set of elastically strained alloys with in-plane lattice constants equal to the lattice constant of GaAs. The center of the peak corresponding to the MBL is close to the RL line, indicating the lattice relaxation around 90–95%. The q_x coordinate of the MBL and inverse layers are the same, indicating that the in-plane lattice constants of these layers are equal. In other words, the inverse layer is coherently grown on the relaxed MBL layer.

Conclusions

To summarize, heterostructures with ultrathin $In_xGa_{1-x}As$/GaAs(001) MBLs with a convex composition profile were grown by MBE and studied using structural characterization techniques. AFM images of all studied structures reveal a cross-hatch morphology, confirming the two-dimensional growth mode during MBE. The RMS surface roughness increases with increasing substrate temperature, indicating that low-temperature MBL growth is preferable for the subsequent deposition of InAs/InGaAs QDs to create single photon emitters in the telecom O-band or C-band. RSM maps show that strain relaxation in ultrathin $In_xGa_{1-x}As$/GaAs(001) MBL layers is partially achieved by layer tilting. The inverse layer is well matched to the upper part of the MBL.

Acknowledgments

TEM and AFM studies were carried out using the equipment of the Federal Center for Collective Use "Materials Science and Diagnostics in Advanced Technologies".

REFERENCES

1. **Sorokin S.V., et al.,** High-resolution X-ray diffractometry and topography of metamorphic buffers for III–V quantum well heterostructures, JETP Letters. 121 (1) (2025) 35–40.

2. **Scaparra B., et al.,** Compositionally graded InAlGaAs buffers for mid-infrared photonic devices, Materials for Quantum Technology. 3 (2023) 035004.

3. **Sittig R. et al.,** Strain engineering of optical properties in metamorphic nanophotonic structures, Nanophotonics. 11 (6) (2022) 1109–1116.

4. **Sorokin S.V., et al.,** Structural and transport characteristics of metamorphic InAlAs/InGaAs quantum wells, JETP Letters. 120 (9) (2024) 668–674.

5. **Bowen D.K., Tanner B.K.,** High Resolution X-Ray Diffractometry and Topography, 1st edition, CRC Press, London. (1998).

6. **Capotondi F., et al.,** Strain induced effects on the transport properties of metamorphic InAlAs/InGaAs quantum wells, Thin Solid Films. 484 (1–2) (2005) 400–407.

7. **Andrews A.M., et al.,** Modeling crosshatch surface morphology in growing mismatched layers. Part II: Periodic boundary conditions and dislocation groups, Journal of Applied Physics. 95 (11) (2004) 6032–6047.

8. **Choy H.K.H., Fonstad C.G.Jr.,** Effects of substrate temperature on the growth of InGaAs compositionally graded buffers and on quantum well structures grown above them, Journal of Vacuum Science & Technology B. 23 (5) (2005) 2109–2113.

9. **Kumar R., Biswas D.,** Strain relaxation and dislocation phenomena in metamorphic semiconductor buffers, Crystal Research and Technology. 51 (2016) 723–731.

THE AUTHORS

LAKUNTSOVA Olga E.
o.e.lakuntsova@mail.ioffe.ru
ORCID: 0009-0003-4202-9514

SEMENOV Alexey N.
semenov@beam.ioffe.ru
ORCID: 0000-0002-0719-0236

KLIMKO Grigorii V.
Klimko@beam.ioffe.ru
ORCID: 0000-0001-8893-7751

PRASOLOV Nikita D.
nikpras@mail.ioffe.ru
ORCID: 0000-0002-7519-9208

SEDOVA Irina V.
irina@beam.ioffe.ru
ORCID: 0000-0002-9540-0933

SOROKIN Sergey V.
sorokin@beam.ioffe.ru
ORCID: 0000-0003-0320-2233

MYASOEDOV Alexander V.
a.v.myasoedov@mail.ioffe.ru
ORCID: 0000-0003-2706-7240

Received 15.12.2025. Approved after reviewing 09.02.2026. Accepted 20.02.2026.

© Peter the Great St. Petersburg Polytechnic University, 2026

Conference paper
UDC 538.958
DOI: https://doi.org/10.18721/JPM.191.107

Temperature-dependent infrared photoluminescence study of GeSn/Si and GeSiSn/Si multiple quantum wells

I.V. Chumanov [1] ✉, D.D. Firsov [1], D.V. Kolyada [1], O.S. Komkov [1], I.V. Skvortsov [2], V.I. Mashanov [2], I.D. Loshkarev [2], V.A. Timofeev [2]

[1] St. Petersburg Electrotechnical University "LETI", St. Petersburg, Russia;
[2] Rzhanov Institute of Semiconductor Physics Siberian Branch of RAS, Novosibirsk, Russia
✉ chumanov2000@yandex.ru

Abstract. The study of the luminescence properties of multiple $Ge_{0.53}Sn_{0.47}$/Si and $Ge_{0.3}Si_{0.56}Sn_{0.14}$/Si quantum wells allowed the energies of interband transitions between the electron Δ subband in silicon and the hole level in the quantum well to be estimated. Temperature studies revealed an initial increase in photoluminescence intensity between 8 and 30 K, followed by a decrease at higher temperatures. Approximation of the obtained results allowed the activation energies of the processes responsible for the temperature quenching of luminescence to be determined.

Keywords: photoluminescence, multiple quantum wells, germanium, silicon, tin, semiconductors, solid solutions, FTIR spectroscopy

Funding: The study was funded by the Russian Science Foundation grant № 25-19-00742.

Citation: Chumanov I.V., Firsov D.D., Kolyada D.V., Komkov O.S., Skvortsov I.V., Mashanov V.I., Loshkarev I.D., Timofeev V.A., Temperature-dependent infrared photoluminescence study of GeSn/Si and GeSiSn/Si multiple quantum wells, St. Petersburg State Polytechnical University Journal. Physics and Mathematics. 19 (1.1) (2026) 45–50. DOI: https://doi.org/10.18721/JPM.191.107

This is an open access article under the CC BY-NC 4.0 license (https://creativecommons.org/licenses/by-nc/4.0/)

Конференционная статья
УДК 538.958
DOI: https://doi.org/10.18721/JPM.191.107

Исследование температурной зависимости инфракрасной фотолюминесценции множественных квантовых ям GeSn/Si и GeSiSn/Si

И.В. Чуманов [1] ✉, Д.Д. Фирсов [1], Д.В. Коляда [1], О.С. Комков [1], И.В. Скворцов [2], В.И. Машанов [2], И.Д. Лошкарев [2], В.А. Тимофеев [2]

[1] Санкт-Петербургский государственный электротехнический университет «ЛЭТИ» им. В.И. Ульянова (Ленина), Санкт-Петербург, Россия;
[2] Институт физики полупроводников им. А.В. Ржанова Сибирского отделения РАН, г. Новосибирск, Россия
✉ chumanov2000@yandex.ru

Аннотация. Изучение люминесцентных свойств множественных квантовых ям $Ge_{0.53}Sn_{0.47}$/Si и $Ge_{0.3}Si_{0.56}Sn_{0.14}$/Si позволило оценить энергии межзонных переходов между электронной Δ-подзоной в кремнии и дырочным уровнем в квантовой яме. Температурные исследования выявили изначальный рост интенсивности фотолюминесценции от 8 до 30 K, а затем – её снижение при дальнейшем нагреве. Аппроксимация полученных результатов позволила определить энергии активации процессов, ответственных за температурное гашение люминесценции.

© Chumanov I.V., Firsov D.D., Kolyada D.V., Komkov O.S., Skvortsov I.V., Mashanov V.I., Loshkarev I.D., Timofeev V.A., 2026. Published by Peter the Great St. Petersburg Polytechnic University.

Ключевые слова: фотолюминесценция, множественные квантовые ямы, германий, кремний, олово, полупроводники, твердые растворы, Фурье-спектроскопия

Финансирование: Исследование выполнено за счет гранта Российского научного фонда № 25-19-00742.

Ссылка при цитировании: Чуманов И.В., Фирсов Д.Д., Коляда Д.В., Комков О.С., Скворцов И.В., Машанов В.И., Лошкарев И.Д., Тимофеев В.А. Исследование температурной зависимости инфракрасной фотолюминесценции множественных квантовых ям GeSn/Si и GeSiSn/Si // Научно-технические ведомости СПбГПУ. Физико-математические науки. 2026. Т. 19. № 1.1. С. 45–50. DOI: https://doi.org/10.18721/JPM.191.107

Статья открытого доступа, распространяемая по лицензии CC BY-NC 4.0 (https://creativecommons.org/licenses/by-nc/4.0/)

Introduction

Semiconductor materials based on Group IV elements of the Periodic Table are actively studied in modern micro- and nanoelectronics. Solid solutions of silicon, germanium, and tin are of particular interest. Their key advantage is in compatibility with modern CMOS technology, paving the way for the creation of new optoelectronic devices. Such devices can operate effectively in a wide spectral range, including near (1.5–3 μm), mid (3–8 μm), and long-wavelength (8–14 μm) infrared. This makes them promising for use in optical communication lines, gas analysis, environmental monitoring systems and other applications [1].

One such material is the $Ge_{1-x}Sn_x$ solid solution, which, at a certain Sn content over 6–10 at. % for unstrained layers, exhibits a direct band gap structure [2, 3]. The introduction of additional strains can lead to a shift in the boundary of the direct band gap for tin, either upward or downward [4, 5]. Optoelectronic devices operating in the near and mid-infrared ranges have already been demonstrated using this solid solution [6, 7].

The growth technology for this material faces a number of challenges that affect the achievement of high-quality layers. The significant difference in the lattice parameters of Sn and Ge (Si) leads to low tin solubility (< 1% in Ge and < 0.1% in Si) and other undesirable processes, such as tin segregation during structure growth, defect formation, and elastic mechanical stresses in the layers [8].

A new stage in the development of this area is the study of ternary $Ge_{1-x-y}Si_xSn_y$ solid solutions, in which independent control of the band gap and lattice parameter becomes possible by adjusting the composition. The possibility of forming thin layers of these materials, forming multiple quantum wells (MQWs), has previously been demonstrated [9].

This paper presents the results of a photoluminescence (PL) study of multiple GeSn and GeSiSn quantum wells with an increased tin content and silicon barriers.

Materials and Methods

The studied samples were grown using molecular beam epitaxy at the Institute of Semiconductor Physics. Initially, a 150 nm-thick silicon buffer layer was formed on silicon (100) wafers. Ten periods of multiple quantum wells were then formed on top of this layer: $Ge_{0.3}Si_{0.56}Sn_{0.14}$/Si in the first sample and $Ge_{0.53}Sn_{0.47}$/Si in the second sample. To minimize undesirable tin segregation, silicon barriers were grown in two stages: at 150 °C, the well layer was coated with 2 nm of silicon, and at 500 °C, the layer thickness was further increased by 5 nm. Upon completion of the structure growth, a 10 nm-thick silicon capping layer was formed.

In addition to differences in the composition of the QW layer, the samples differ in the nominal well thickness and the growth temperature. For the first sample, the $Ge_{0.3}Si_{0.56}Sn_{0.14}$ layer thickness was 1 nm, and the growth temperature was 150 °C. The well layer of the second sample has a thickness of 0.17 nm (~1 monolayer), but it was grown at room temperature. The samples were also subjected to high-temperature annealing in a quartz furnace under an argon atmosphere. Annealing of each structure was performed for several samples at different temperatures

© Чуманов И.В., Фирсов Д.Д., Коляда Д.В., Комков О.С., Скворцов И.В., Машанов В.И., Лошкарев И.Д. Тимофеев В.А., 2026. Издатель: Санкт-Петербургский политехнический университет Петра Великого.

(600, 625, 650, 675, and 700 °C) for 10 minutes. The samples that demonstrated the most intense photoluminescence signal were selected for the studies: $Ge_{0.3}Si_{0.56}Sn_{0.14}$/Si after annealing at 625 °C and $Ge_{0.53}Sn_{0.47}$/Si at a temperature of 650 °C.

Photoluminescence spectra were recorded on a Vertex 80 FTIR spectrometer equipped with a liquid-nitrogen-cooled InSb photovoltaic detector. Luminescence was excited by a 405 nm diode laser with a power of up to 140 mW. Samples were cooled in a Janis CCS-150 closed-cycle helium cryostat, capable of achieving temperatures as low as 8 K. Luminescence signal recording was performed using gated integration with short laser pulses [10]. This approach minimized sample surface heating during the study.

Results and Discussion

At low temperatures, the $Ge_{0.53}Sn_{0.47}$/Si and $Ge_{0.3}Si_{0.56}Sn_{0.14}$/Si MQW samples exhibit an intense photoluminescence signal in the energy range of ~0.87 eV and ~0.76 eV, respectively. Fig. 1 shows the PL spectra for each sample, measured at 8 K. The shape of the spectra indicates the presence of several radiative recombination processes. The nature of the most intense high-energy peak is explained by interband optical transitions between the electron Δ subband in silicon and the hole level in the QW layer of the solid solution. This was further confirmed by calculating the band diagram for quantum wells of similar composition [11]. In the lower energy region, a broad shoulder is observed, which is explained by the luminescence signal from defects in the crystal structure of the sample [12].

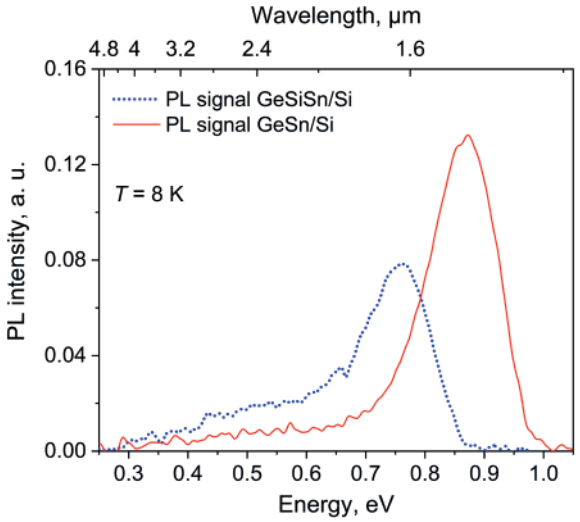

Fig. 1. Comparison of PL spectra of $Ge_{0.53}Sn_{0.47}$/Si and $Ge_{0.3}Si_{0.56}Sn_{0.14}$/Si MQW samples at 8 K

A comparison of the spectra of the samples shown in Fig. 1 shows that the sample with the $Ge_{0.53}Sn_{0.47}$/Si MQW has a higher ratio of the PL signal from interband transitions to the signal in the defect region. At the same time, in the sample with the $Ge_{0.3}Si_{0.56}Sn_{0.14}$/Si MQW, defects produce more intense luminescence, while the signal from optical transitions involving QWs is noticeably weaker.

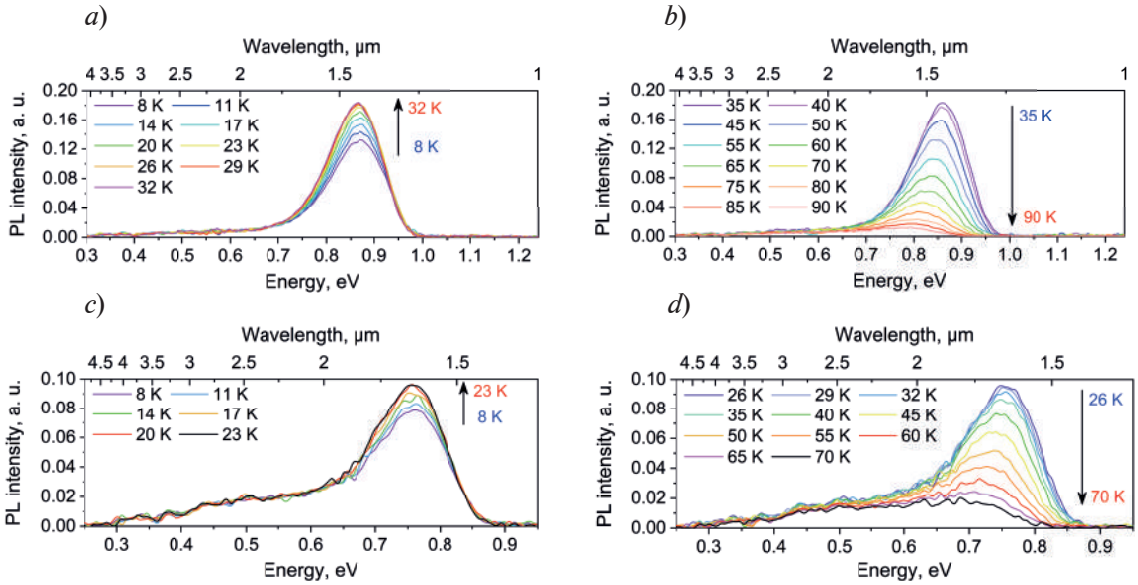

Fig. 2. PL spectra of $Ge_{0.53}Sn_{0.47}$/Si (*a*, *b*) and $Ge_{0.3}Si_{0.56}Sn_{0.14}$/Si (*c*, *d*) MQW samples at different temperatures

Arrows show the shift of the PL peak with increasing temperature for clarity

A comparison of the PL spectra at different temperatures for the sample with the $Ge_{0.53}Sn_{0.47}$/Si MQW (Fig. 2, *a*, *b*) reveals that the PL signal intensity increases with increasing temperature up to 29–32 K and then decreases, starting from 35 K. The second sample, containing the $Ge_{0.3}Si_{0.56}Sn_{0.14}$/Si MQW, exhibits similar behavior with increasing temperature (see Fig. 2, *c*, *d*). This behavior can presumably be explained by a combination of several factors. As the sample heats, the number of phonons required for the observed (indirect) radiative transitions increases. Another process may be the thermal activation of photogenerated charge carriers trapped by defect levels in the band gap. Thus, up to a certain critical temperature, an enhancement of the interband transition signal is observed due to the release of trapped charge carriers [13].

With increasing temperature, both samples exhibit a 'red' shift in peak position, which is typical for materials of this class. Fig. 3, *a* shows the temperature dependence of the transition energy for each sample.

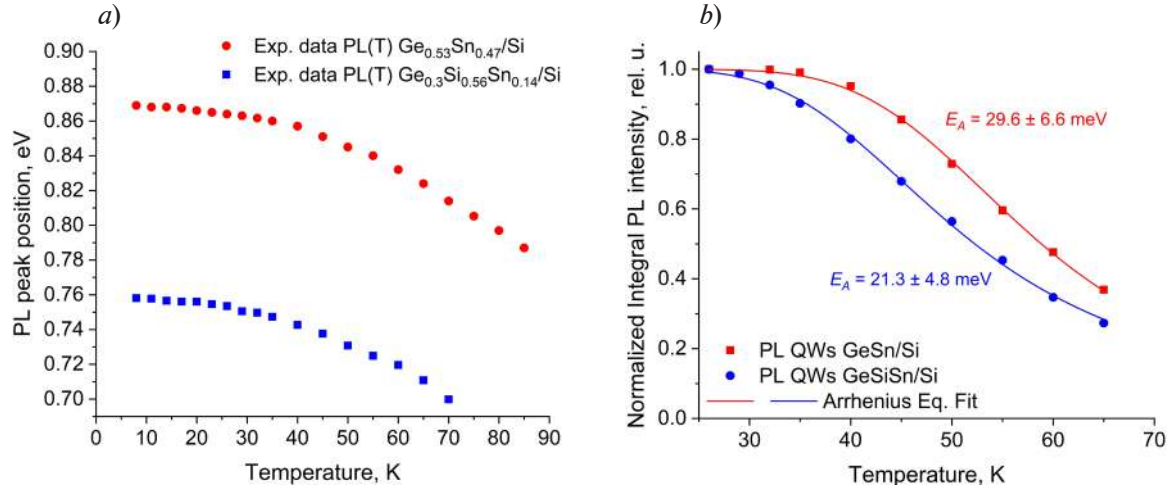

Fig. 3. Temperature dependences of the peak position (*a*) and the integral of the PL intensity (*b*)

It should be noted that the 'red' shift for the studied samples reaches ~60 meV and ~80 meV with temperature increases of 62 K and 72 K, respectively (see Fig. 3, *a*). We suggest that the strong temperature dependence in the low-temperature region may be due to charge carriers localized in the minima of the spatial inhomogeneity of multiple quantum wells [9].

Fig. 3, *b* shows the temperature dependences of the integrated photoluminescence intensity of the interband transition. An approximation was performed for each sample using the Arrhenius equation:

$$I = \frac{I_0}{1 + C\exp\left(-\frac{E_A}{k_B T}\right)}, \quad (1)$$

where I_0 is the intensity at a temperature of 0 K, C is the ratio of radiative to nonradiative carrier lifetimes, and E_A is the activation energy of the process that leads to quenching of photoluminescence.

The approximation used allowed us to determine the activation energies of the nonradiative process leading to luminescence decay in the structures with increasing temperature, and obtain the C coefficients corresponding to the relation between the nonradiative and radiative recombination lifetimes. The value of the C coefficient is approximately three times higher for the sample with GeSn layers. With increasing temperature, this is manifested in a steeper slope of the dependence and a rapid quenching of luminescence (see Fig. 3, *b*). The values of the obtained energies are significantly (an order of magnitude) lower than the energy of thermal emission of holes from the quantum well. Excluding Auger recombination mechanisms, since for thin QWs they are of a thresholdless and quasi-thresholdless nature [14], the most probable scenario for the temperature quenching of PL is presumably the Shockley–Read–Hall (SRH) mechanism.

Conclusion

This paper presents the results of a study of the temperature dependence of photoluminescence in $Ge_{0.53}Sn_{0.47}$/Si and $Ge_{0.3}Si_{0.56}Sn_{0.14}$/Si samples with MQWs, measured by FTIR spectroscopy using gated integration. The spectra contained a signal from interband transitions involving hole levels in the QWs and an electron Δ subband in the silicon barriers. Luminescence from defects in the sample structure was also observed. The interband PL intensity initially increases with sample heating, which is explained by the increase in the phonon number and the thermal activation of charge carriers localized at defect levels in the band gap. Further heating of the sample leads to a decrease in the PL intensity, which we associate with the process of nonradiative recombination by the SRH mechanism; the activation energy of the process was ~21 and ~30 meV for samples with MQW $Ge_{0.3}Si_{0.56}Sn_{0.14}$/Si and $Ge_{0.53}Sn_{0.47}$/Si, respectively. In conclusion, we note that the sample with GeSn layers demonstrates better temperature stability of luminescence due to the higher activation energy.

REFERENCES

1. **Moutanabbir O., Assali S., Gong X., O'Reilly E., Broderick C.A., Marzban B., Witzens J., Du W., Yu S.-Q., Chelnokov A., Buca D., Nam D.,** Monolithic infrared silicon photonics: The rise of (Si)GeSn semiconductors. Applied Physics Letters. 118 (11) (2021) 110502.

2. **Ghetmiri S.A., Du W., Margetis J., Mosleh A., Cousar L., Conley B.R., Domulevicz L., Nazzal A., Sun G., Soref R. A., Tolle J., Li B., Naseem H.A., Yu S.-Q.,** Direct-bandgap GeSn grown on silicon with 2230 nm photoluminescence. Applied Physics Letters. 105 (15) (2014) 151109.

3. **Wirths S., Geiger R., von den Driesch N., Mussler G., Stoica T., Mantl S., Ikonic Z., Luysberg M., Chiussi S., Hartmann J. M., Sigg H., Faist J., Buca D., Grützmacher D.,** Lasing in direct-bandgap GeSn alloy grown on Si. Nature Photonics. 9 (2) (2015) 88–92.

4. **Elbaz A., Buca D., von den Driesch N., Pantzas K., Patriarche G., Zerounian N., Herth E., Checoury X., Sauvage S., Sagnes I., Foti A., Ossikovski R., Hartmann J.-M., Boeuf F., Ikonic Z., Boucaud P., Grützmacher D., El Kurdi M.,** Ultra-low-threshold continuous-wave and pulsed lasing in tensile-strained GeSn alloys. Nature Photonics. 14 (6) (2020) 375–382.

5. **Chen R., Lin H., Huo Y., Hitzman C., Kamins T.I., Harris J.S.,** Increased photoluminescence of strain-reduced, high-Sn composition $Ge_{1-x}Sn_x$ alloys grown by molecular beam epitaxy. Applied Physics Letters. 99 (18) (2011) 181125.

6. **Marzban B., Seidel L., Liu T., Wu K., Kiyek V., Zoellner M. H., Ikonic Z., Schulze J., Grützmacher D., Capellini G., Oehme M., Witzens J., Buca D.,** Strain engineered electrically pumped SiGeSn microring lasers on Si. ACS Photonics. 10 (1) (2022) 217–224.

7. **Zhang D., Hu X., Liu D., Lin X., Wang W., Ding Z., Wang Z., Cheng B., Xue C.,** GeSn on Si avalanche photodiodes for short wave infrared detection. In Optical Sensing and Imaging Technologies and Applications. 10846 (2018) 327–334.

8. **Lin G., Qian K., Cai H., Zhao H., Xu J., Chen S., Li C., Hickey R., Kolodzey J., Zeng Y.,** Enhanced photoluminescence of GeSn by strain relaxation and spontaneous carrier confinement through rapid thermal annealing. Journal of Alloys and Compounds. 915 (2022) 165453.

9. **Timofeev V.A., Mashanov V.I., Nikiforov A.I., Skvortsov I.V., Loshkarev I.D., Kolyada D.V., Firsov D.D., Komkov O.S.,** Features of optical transitions in GeSiSn/Si multiple quantum wells. Optoelectronics, Instrumentation and Data Processing. 58 (6) (2022) 571–578.

10. **Luferau A.I., Firsov D.D., Komkov O.S.,** Measurement of infrared photoluminescence spectra by gated integration with active baseline subtraction. Optics and Spectroscopy. 128 (1) (2020) 131–136.

11. **Timofeev V.A., Skvortsov I.V., Mashanov V.I., Gayduk A.E., Bloshkin A.A., Kirienko V.V., Utkin D.E., Nikiforov A.I., Kolyada D.V., Firsov D.D., Komkov O.S.,** Excitation of hybrid modes in plasmonic nanoantennas coupled with GeSiSn/Si multiple quantum wells for the photoresponse enhancement in the short-wave infrared range. Applied Surface Science. 659 (2024) 159852.

12. **Timofeev V., Skvortsov I., Mashanov V., Nikiforov A., Kolyada D., Firsov D., Komkov O., Samadov S., Sidorin A., Orlov O.,** Effects of high-temperature annealing on vacancy complexes and luminescence properties in multilayer periodic structures with elastically strained GeSiSn layers. Journal of Vacuum Science & Technology B. 42 (3) (2024) 030601.

13. **Pezzoli F., Giorgioni A., Patchett D., Myronov M.,** Temperature-dependent photoluminescence characteristics of GeSn epitaxial layers. ACS Photonics. 3 (11) (2016) 2004–2009.

14. **Zegrya G.G., Polkovnikov A.S.,** Mechanisms of Auger recombination in quantum wells. Journal of Experimental and Theoretical Physics. 86 (1998) 815–832.

THE AUTHORS

CHUMANOV Ivan V.
chumanov2000@yandex.ru
ORCID: 0009-0009-2564-6100

FIRSOV Dmitrii D.
d.d.firsov@gmail.com
ORCID: 0000-0001-7608-9580

KOLYADA Dmitry V.
kolyada.dima94@mail.ru

KOMKOV Oleg S.
oleg_sergeevich@mail.ru
ORCID: 0000-0002-8999-1175

SKVORTSOV Ilya V
i.skvortsov@isp.nsc.ru
ORCID: 0000-0002-2153-1615

MASHANOV Vladimir I.
mash@isp.nsc.ru
ORCID: 0000-0003-4420-6695

LOSHKAREV Ivan D.
idl@isp.nsc.ru
ORCID: 0000-0003-4771-3705

TIMOFEEV Vyacheslav A.
Vyacheslav.t@isp.nsc.ru
ORCID: 0000-0003-4093-7802

Received 15.12.2025. Approved after reviewing 18.02.2026. Accepted 27.02.2026.

© Peter the Great St. Petersburg Polytechnic University, 2026

Conference paper
UDC 538.91
DOI: https://doi.org/10.18721/JPM.191.108

Photoluminescence and photoreflectance of long-wavelength HgTe/CdHgTe heterostructure

M.S. Ruzhevich [1]✉, K.D. Mynbaev [1,2], D.D. Firsov [3], I.V. Chumanov [3], O.S. Komkov [3], V.S. Varavin [4], N.N. Mikhailov [4]

[1] ITMO University, St. Petersburg, Russia

[2] Ioffe Institute, St. Petersburg, Russia

[3] St. Petersburg Electrotechnical University "LETI", St. Petersburg, Russia

[4] Rzhanov Institute of Semiconductor Physics Siberian Branch of RAS, Novosibirsk, Russia

✉ max.ruzhevich@niuitmo.ru

Abstract. This paper presents the results of optical studies of a long-wavelength HgTe/CdHgTe heterostructure performed using photoluminescence and photoreflectance methods. Optical transitions involving several electron and hole levels were observed, with the dominant levels switching with changes in temperature. Using the photoreflectance method, optical transitions not detectable by the photoluminescence were observed. It is demonstrated that the combination of the methods allows for the most detailed evaluation of optical transitions in the HgTe/CdHgTe quantum wells.

Keywords: CdHgTe, heterostructures, photoluminescence, photoreflectance

Citation: Ruzhevich M.S., Mynbaev K.D., Firsov D.D., Chumanov I.V., Komkov O.S., Varavin V.S., Mikhailov N.N. Photoluminescence and photoreflectance of long-wavelength HgTe/CdHgTe heterostructure, St. Petersburg State Polytechnical University Journal. Physics and Mathematics. 19 (1.1) (2026) 51–55. DOI: https://doi.org/10.18721/JPM.191.108

This is an open access article under the CC BY-NC 4.0 license (https://creativecommons.org/licenses/by-nc/4.0/)

Конференционная статья
УДК 538.91
DOI: https://doi.org/10.18721/JPM.191.108

Фотолюминесценция и фотоотражение длинноволновой гетероструктуры HgTe/CdHgTe

М.С. Ружевич [1]✉, К.Д. Мынбаев [1,2], Д.Д. Фирсов [3], И.В. Чуманов [3], О.С. Комков [3], В.С. Варавин [4], Н.Н. Михайлов [4]

[1] Университет ИТМО, Санкт-Петербург, Россия;

[2] Физико-технический институт им. А.Ф. Иоффе РАН, Санкт-Петербург, Россия;

[3] Санкт-Петербургский государственный электротехнический университет «ЛЭТИ» им. В.И. Ульянова (Ленина), Санкт-Петербург, Россия;

[4] Институт физики полупроводников им. А.В. Ржанова Сибирского отделения РАН, г. Новосибирск, Россия

✉ max.ruzhevich@niuitmo.ru

Аннотация. В работе представлены результаты оптических исследований длинноволновой гетероструктуры HgTe/CdHgTe, выполненных методами фотолюминесценции и фотоотражения. Обнаружены оптические переходы с участием нескольких электронных и дырочных уровней, причем доминирующие уровни переключались с изменением температуры. Методом фотоотражения обнаружены переходы, не детектируемые методом фотолюминесценции. Показано, что сочетание использованных методов позволяет наиболее детально оценить оптические переходы в квантовых ямах HgTe/CdHgTe.

© Ruzhevich M.S., Mynbaev K.D., Firsov D.D., Chumanov I.V., Komkov O.S., Varavin V. S., Mikhailov N.N., 2026. Published by Peter the Great St. Petersburg Polytechnic University.

Ключевые слова: CdHgTe, гетероструктуры, фотолюминесценция, фотоотражение

Ссылка при цитировании: Ружевич М.С., Мынбаев К.Д., Фирсов Д.Д., Чуманов И.В., Комков О.С., Варавин В.С., Михайлов Н.Н. Фотолюминесценция и фотоотражение длинноволновой гетероструктуры HgTe/CdHgTe // Научно-технические ведомости СПбГПУ. Физико-математические науки. 2026. Т. 19. № 1.1. С. 51–55. DOI: https://doi.org/10.18721/JPM.191.108

Статья открытого доступа, распространяемая по лицензии CC BY-NC 4.0 (https://creativecommons.org/licenses/by-nc/4.0/)

Introduction

Mercury cadmium telluride (HgCdTe, MCT) is a semiconductor solid solution that occupies a dominant position in infrared (IR) optoelectronics due to its small bandgap and high charge carrier mobility. In addition to classical structures based on bulk MCT of various compositions (mole fraction CdTe x), interest is growing in MCT-based heterostructures (HSs) with quantum wells (QWs). These HSs are used in fabrication of lasers for the mid-IR range (wavelengths $\lambda = 3 - 6$ μm) [1] and long-IR range ($\lambda > 10$ μm) [2]. They are also used in the production of photodetectors [3] and structures with topological insulators [4]. The energies of optical transitions in such structures depend on the width of the QW and on x in the wells and barrier layers. Careful selection of these parameters allows one not only to obtain a structure with emission at the desired wavelength, but also to suppress Auger recombination processes [5]. Growth of an 'ideal' HS, however, using the widespread method of molecular beam epitaxy (MBE), is limited by the impossibility of an instant transition from growing CdTe to HgTe and back, as well as by the difference in the optimal growth temperatures of HgTe and CdTe by more than 100 °C [6]. Therefore, a complete characterization of 'real' structures with HgTe/CdHgTe QWs is a very relevant task. In this paper, we report the results of optical studies of a HS with HgTe/CdHgTe QWs, where in addition to the 'classical' photoluminescence (PL) method, the modulation Fourier-transform infrared (FTIR) spectroscopy, photoreflectance (PR), was used. This method has been successfully used in the studies of III–V semiconductors [7], however, its application to MCT has been limited to just a few works performed solely on epitaxial films [8–11].

Materials and Methods

The HS was grown by MBE on a (013)GaAs substrate with ZnTe and CdTe buffer layers [12]. The structure contained 11 QWs with a thickness $w = 7.1$ nm with composition in the wells set during the growth as corresponding to pure HgTe ($x = 0$), and composition in the barriers, $x_b = 0.62$. The waveguide layers (spacers) in the HS with a thickness $d \approx 4–5$ μm had a composition $x_s \approx 0.7$; a layer of pure CdTe with a thickness of 30 nm was grown *in situ* on the HS surface.

The PL and PR studies were carried out using a setup based on a Vertex 80 FTIR spectrometer operating in step scan mode [13]. A diode laser ($\lambda = 809$ nm) was used to excite the PL signal and as a source of modulating radiation when recording the PR spectra. Lock-in signal amplification was used to eliminate the influence of background thermal radiation. The laser emission was mechanically modulated at a frequency $f = 2.5$ kHz. The PL and PR spectra were recorded in the temperature range $T = 12 - 294$ K using a Janis CCS-150 closed-cycle helium cryostat. The signal was recorded with an MCT photoconductive detector.

Results and Discussion

Several peaks were observed in the PL spectra of the HS (Fig. 1); changes in their intensity and energy with temperature are described below. With an increase in temperature to $T \approx 90$ K, a 'blue' shift of line A was observed, and its intensity decreased (Fig. 1, *a*). Along with that, a 'blue' shift of another, low-energy peak (line *B*) was observed, the intensity of which increased due to a gradual transition of the signal into the working range of the photodetector (~ 75 meV and higher). Its energy reached a value of ~ 92 meV at $T \approx 90$ K. Also, at $T \approx 90$ K, this peak exhibited a noticeable high-energy shoulder in the energy range of 115–118 meV (line *C*).

© Ружевич М.С., Мынбаев К.Д., Фирсов Д.Д., Чуманов И.В., Комков О.С., Варавин В.С., Михайлов Н.Н., 2026. Издатель: Санкт-Петербургский политехнический университет Петра Великого.

A further increase in temperature (Fig. 1, *b*) led to a shift of *B* and *C* lines into the high-energy region; a simultaneous decrease in the intensity of line *B* and an increase in the intensity of line *C* were observed. At $T \approx 150$ K, line *D* appeared, representing a shoulder with a higher energy of 133 – 135 meV. At $T \approx 180$ K, a signal with an energy of ~160 meV (line *E*) appeared. Heating the structure to $T \approx 210$ K made it possible to obtain the most intense PL signal, where the largest contribution came from lines *C* and *D*, which represented a peak with a shoulder in the high-energy region. A further increase in the temperature up to room temperature led to a decrease in the intensity of lines *C* and *D*, as well as an increase in the intensity of line *E*. At room temperature, the spectrum represented a broad band with several energy lines, among which the most intense lines *C* and *E* could clearly be distinguished. According to the energy range of these peaks, they obviously corresponded to the long-wavelength (up to 15 μm) IR emission from the QWs. In the case of PL, most likely, we observed optical transitions involving levels closest to the ground states in the QWs.

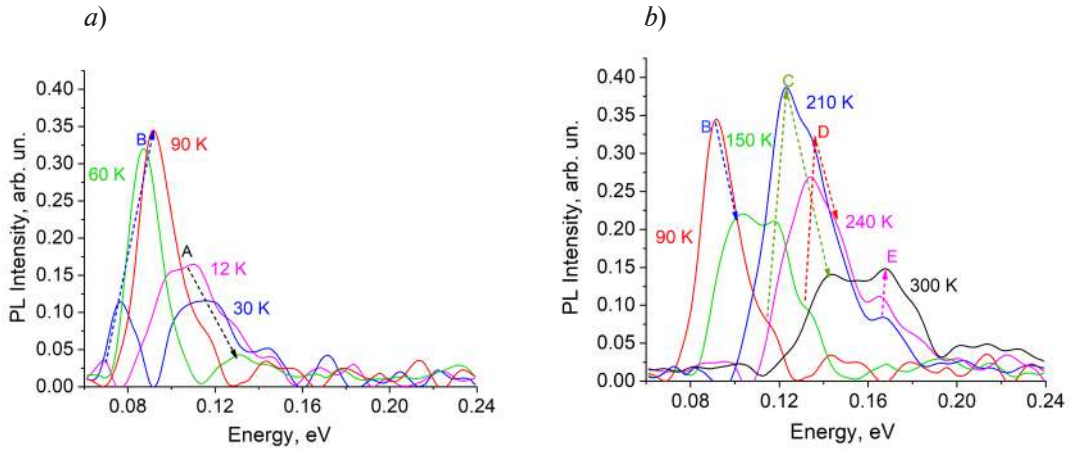

Fig. 1. PL spectra of the HS at different temperatures

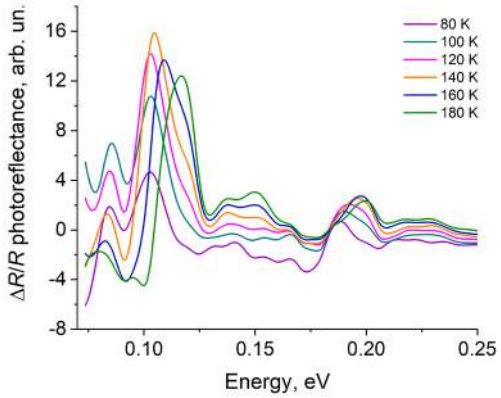

Fig. 2. PR spectra of the HS at different temperatures

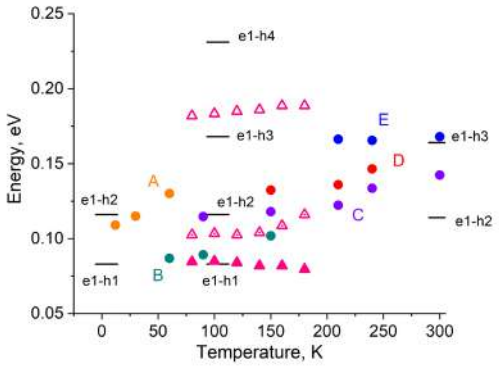

Fig. 3. Temperature dependence of the energies of optical transitions detected with PL (circles) and PR (triangles), and the calculated values of possible transitions in the QWs (dashes)

The optical signal from the QWs was also obtained with the PR method (Fig. 2). Using the technique described in [14], the energies of three PR peaks were obtained at $T = 80$ K: ~84 meV, ~102 meV, and ~180 meV. The first two peaks were likely associated with the *e*1-*h*1 (representing the first levels of quantization for electrons and holes), and *e*1-*h*2 transitions, respectively. The positions of the peaks remained virtually unchanged with varying temperature. The peak with the energy ~180 meV (at $T = 80$ K) in the PR spectra was not previously observed in the PL spectra. Thus, it can be concluded that PR allows one to detect transitions involving deeper levels in MCT-based HSs, which is promising for the comprehensive characterization of such structures.

Fig. 3 presents the summary data on the PL and PR energies for the HS with temperature variation. Also, the transition energies in the QWs estimated using [15] are presented. It should be noted that the estimates at this stage were very rough, in particular, due to the non-obvious choice of calculation parameters, such as the exact value of the bandgap in the wells as well as the electron effective mass. However, it can still be concluded that the PL and PR methods detected transitions between the states closest to the ground ones. The energy of all PL peaks also increased with increasing temperature.

Conclusion

A long-wavelength HgTe/CdHgTe-based QW heterostructure was studied using PL and PR methods. It is demonstrated that these methods can be used to determine the energy of optical transitions in the QWs. PL detected transitions involving levels closest to the ground states, and with increasing temperature, the dominance of various transitions was observed. Using the PR method, transitions with energies of ~180 meV were additionally detected. Thus, a comprehensive study of the optical properties of MCT-based heterostructures using PL and PR methods enabled the most accurate determination of the energies of optical transitions in the QWs.

REFERENCES

1. **Kudryavtsev K.E., Rumyantsev V.V., Dubinov A.A., Aleshkin V.Y., Zholudev M.S., Mikhailov N.N., Dvoretsky S.A., Gavrilenko V.I., Morozov S.V.,** Hot phonon effect in mid-infrared HgTe/CdHgTe quantum wells evaluated by quasi-steady-state photoluminescence, Applied Physics Letters. 125 (22) (2024) 223505.

2. **Razova A.A., Rumyantsev V.V., Mazhukina K.A., Utochkin V.V., Fadeev M.A., Dubinov A.A., Aleshkin V.Ya., Mikhailov N.N., Dvoretsky S.A., Shengurov D.V., Gusev N.S., Morozova E.E., Gavrilenko V.I., Morozov S.V.,** Microdisk HgCdTe lasers operating at 22–25 μm under optical pumping, Applied Physics Letters. 126 (12) (2025) 121102.

3. **Aleshkin V.Ya., Dubinov A.A., Morozov S.V., Ryzhii M., Otsuji T., Mitin V., Shur M.S., Ryzhii V.,** Interband infrared photodetectors based on HgTe–CdHgTe quantum-well heterostructures, Optical Materials Express. 8 (5) (2018) 1349.

4. **Sengupta P., Kubis T., Tan Y., Povolotskyi M., Klimeck G.,** Design principles for HgTe-based Topological Insulator Devices, Journal of Applied Physics. 114 (4) (2013) 043702.

5. **Fadeev M.A., Dubinov A.A., Aleshkin V.Ya., Rumyantsev V.V., Utochkin V.V., Gavrilenko V.I., Teppe F., Hübers H.-W., Mikhailov N.N., Dvoretskii S.A.,** Effect of Cd content in barriers on the threshold energy of Auger recombination in waveguide structures with HgTe/Cd_xHg_{1-x}Te quantum wells, emitting at a wavelength of 18 μm, Quantum Electronics. 49(6) (2019) 556–558.

6. **Becker C.R., Casselman T.N., Grein C.H., Sivananthan S.,** Molecular Beam Epitaxy of HgCdTe Materials and Detectors. In: P. Bhattacharya, R. Fornari, H. Kamimura (eds.), Comprehensive Semiconductor Science and Technology. 6 (2011) 128–159.

7. **Komkov O.S.,** Infrared Photoreflectance of III–V Semiconductor Materials (Review), Physics of the Solid State. 63 (8) (2021) 991–1014.

8. **Komkov O.S., Yakushev M.V.,** Photomodulation optical spectroscopy of CdHgTe graded band gap heterostructures, Semiconductors. 57 (6) (2023) 425–430.

9. **Ruzhevich M.S., Mynbaev K.D., Firsov D.D., Chumanov I.V., Komkov O.S., Marin D.V., Varavin V.S., Yakushev M.V.,** Arsenic-doped HgCdTe: FTIR photoluminescence and photoreflectance spectroscopy study, Solid State Communications. 394 (2024) 115720.

10. **Motyka M., Sęk G., Janiak F., Misiewicz J., Kłos K., Piotrowski J.,** Fourier-transformed photoreflectance and fast differential reflectance of HgCdTe layers. The issues of spectral resolution and Fabry–Perot oscillations, Measurement Science and Technology. 22 (12) (2011) 125601.

11. **Shao J., Chen L., Zha F.-X., Lu W., Lü X., Guo S., He L., Chu J.,** Modulation mechanism of infrared photoreflectance in narrow-gap HgCdTe epilayers: A pump power dependent study, Journal of Applied Physics. 108 (2) (2010) 023518.

12. **Dvoretsky S., Mikhailov N., Sidorov Y., Shvets V., Danilov S., Wittman B., Ganichev S.,** Growth of HgTe Quantum Wells for IR to THz Detectors, Journal of Electronic Materials. 39 (2010) 918–923.

13. **Firsov D.D., Komkov O.S., Solov'ev V.A., Kop'ev P.S., Ivanov S.V.,** Temperature-dependent photoluminescence of InSb/InAs nanostructures with InSb thickness in the above-monolayer range, Journal of Physics D: Applied Physics. 49 (28) (2016) 285108.

14. **Hosea T.J.C.,** Estimating Critical-Point Parameters of Modulated Reflectance Spectra. Physica Status Solidi B. 189 (2) (1995) 531–542.

15. MatProp. URL: http://www.matprop.ru/levels/ Accessed Dec. 16, 2025.

THE AUTHORS

RUZHEVICH Maxim S.
max.ruzhevich@niuitmo.ru
ORCID: 0000-0002-4513-6345

KOMKOV Oleg S.
okomkov@yahoo.com
ORCID: 0000-0002-8999-1175

MYNBAEV Karim D.
mynkad@mail.ioffe.ru
ORCID: 0000-0002-9853-8874

VARAVIN Vasiliy S.
varavin@isp.nsc.ru
ORCID: 0000-0001-7722-6428

FIRSOV Dmitrii D.
d.d.firsov@gmail.com
ORCID: 0000-0001-7608-9580

MIKHAILOV Nikolay N.
mikhailov@isp.nsc.ru
ORCID: 0009-0007-7474-102X

CHUMANOV Ivan V.
chumanov2000@yandex.ru
ORCID: 0009-0009-2564-6100

Received 15.12.2025. Approved after reviewing 19.01.2026. Accepted 22.01.2026.

© Peter the Great St. Petersburg Polytechnic University, 2026

Quantum wires, quantum dots, and other low-dimensional systems

Conference paper
UDC 535.372
DOI: https://doi.org/10.18721/JPM.191.109

Photoluminescence control of WSe_2 monolayers integrated with plasmon nanobumps via strain engineering

A.V. Nikolaeva [1,2]✉, M.A. Anikina [1,2], D.V. Pavlov [3], F.M. Maksimov [1,4], A. Kuznetsov [1], V.M. Kondratev [1,2], V.A. Sharov [2,5], A.A. Kuchmizhak [3,6], A.D. Bolshakov [1,2,7]

[1] Moscow Institute of Physics and Technology (National Research University), Moscow, Russia;
[2] Alferov University, St. Petersburg, Russia;
[3] Institute of Automation and Control Processes FEB RAS, Vladivostok, Russia;
[4] Russian Quantum Center, Moscow, Russia;
[5] Ioffe Institute, St. Petersburg, Russia;
[6] Far Eastern Federal University, Vladivostok, Russia;
[7] St. Petersburg State University, St. Petersburg, Russia
✉ nikalex2000@bk.ru

Abstract. This work presents a hybrid system for photoluminescence control, consisting of a tungsten diselenide monolayer (1L-WSe_2) integrated with an array of plasmonic gold nanobumps fabricated by femtosecond laser printing. This technique allows precise tuning of the plasmonic resonance in these structures by controlling their geometry. It is shown that this integration provides a dual mechanism for enhancing and controlling photoluminescence (PL). First, the plasmonic resonance significantly amplifies the PL emission near the nanobump due to exciton-plasmon interaction. Second, the deformation of the WSe_2 monolayer on the nanobump leads to a red shift of the PL peak, resulting from modification of the bandgap. A key feature of this system is the ability to control the spectrum by selecting the pump wavelength: changing the excitation energy affects the correlation between the neutral exciton (X^0) and the low-energy dark exciton/trion ($X^{D/T}$) states. Low-temperature microspectroscopy further revealed a deformation-induced redistribution of intensity from the neutral exciton (X^0) to low-energy states, including the dark exciton/trion complex ($X^{D/T}$). These results establish a foundation for a platform of spectrally tunable light sources based on hybrid exciton-plasmon-strain interactions, which offers a pathway for the advancement of nanophotonics and the development of next-generation optoelectronic devices.

Keywords: WSe_2, emitter, nanobump, photoluminescence

Funding: Ministry of Science and Higher Education of the Russian Federation (Grant FSRM-2026-0004, project FSMG-2025-0005); Saint-Petersburg State University (research project 122040800254-4).

Citation: Nikolaeva A.V., Anikina M.A., Pavlov D.V., Maksimov F.M., Kuznetsov A., Kondratev V.M., Sharov V.A., Kuchmizhak A.A., Bolshakov A.D., Photoluminescence control of WSe_2 monolayers integrated with plasmon nanobumps via strain engineering, St. Petersburg State Polytechnical University Journal. Physics and Mathematics. 19 (1.1) (2026) 56–63. DOI: https://doi.org/10.18721/JPM.191.109

This is an open access article under the CC BY-NC 4.0 license (https://creativecommons.org/licenses/by-nc/4.0/)

© Nikolaeva A.V., Anikina M.A., Pavlov D.V., Maksimov F.M., Kuznetsov A., Kondratev V.M., Sharov V.A., Kuchmizhak A.A., Bolshakov A.D., 2026. Published by Peter the Great St. Petersburg Polytechnic University.

Конференционная статья
УДК 535.372
DOI: https://doi.org/10.18721/JPM.191.109

Управление фотолюминесценцией монослоев WSe_2, интегрированных с плазмонными нанобампами, методом деформационной инженерии

А.В. Николаева [1,2]✉, М.А. Аникина [1,2], Д.В. Павлов [3], Ф.М. Максимов [1,4], А. Кузнецов [1], В.М. Кондратьев [1,2], В.А. Шаров [2,5], А.А. Кучмижак [3,6], А.Д. Большаков [1,2,7]

[1] Московский физико-технический институт (национальный исследовательский университет), Москва, Россия;

[2] Академический университет им. Ж.И. Алфёрова РАН, Санкт-Петербург, Россия;

[3] Институт автоматики и процессов управления ДВО РАН, г. Владивосток, Россия;

[4] Российский квантовый центр, Москва, Россия;

[5] Физико-технический институт им. А.Ф. Иоффе РАН, Санкт-Петербург, Россия;

[6] Дальневосточный федеральный университет, г. Владивосток, Россия;

[7] Санкт-Петербургский государственный университет, Санкт-Петербург, Россия

✉ nikalex2000@bk.ru

Аннотация. В данной работе представлена гибридная система для управления фотолюминесценцией, состоящая из монослоя диселенида вольфрама (WSe_2), интегрированного с массивами плазмонных золотых нанобампов, изготовленных методом фемтосекундной лазерной печати, позволяющей точно настраивать плазмонный резонанс таких структур путём контроля их геометрии. Показано, что такая интеграция обеспечивает двойной механизм усиления и управления фотолюминесценцией (ФЛ). Во-первых, плазмонный резонанс значительно усиливает излучение ФЛ в области нанобампа за счёт экситон-плазмонного взаимодействия. Во-вторых, деформация монослоя WSe_2 на нанобампе приводит к смещению пика в спектре ФЛ, что является следствием модификации ширины запрещённой зоны. Ключевой особенностью системы является возможность активного управления спектром путём выбора длины волны накачки: изменение энергии возбуждения влияет на соотношение между состояниями нейтрального экситона (X^0) и низкоэнергетического тёмного экситона/триона ($X^{D/T}$). Низкотемпературная микроспектроскопия дополнительно выявила вызванное деформацией перераспределение интенсивности от нейтрального экситона (X^0) к низкоэнергетическим состояниям, включая комплекс тёмного экситона/триона ($X^{D/T}$). Полученные результаты создают основу для платформы спектрально перестраиваемых источников света на базе гибридных экситон-плазмон-деформационных взаимодействий, что имеет значение для развития нанофотоники и разработки оптоэлектронных устройств нового поколения.

Ключевые слова: WSe_2, эмиттер, фотолюминесценция

Финансирование: Министерство науки и высшего образования Российской Федерации (грант FSRM-2026-0004, проект FSMG-2025-0005); Санкт-Петербургский государственный университет (исследовательский проект 122040800254-4).

Ссылка при цитировании: Николаева А.В., Аникина М.А., Павлов Д.В., Максимов Ф.М., Кузнецов А., Кондратьев В.М., Шаров В.А., Кучмижак А.А., Большаков А.Д. Управление фотолюминесценцией монослоев WSe_2, интегрированных с плазмонными нанобампами, методом деформационной инженерии // Научно-технические ведомости СПбГПУ. Физико-математические науки. 2026. Т. 19. № 1.1. С. 56–63. DOI: https://doi.org/10.18721/JPM.191.109

Статья открытого доступа, распространяемая по лицензии CC BY-NC 4.0 (https://creativecommons.org/licenses/by-nc/4.0/)

© Николаева А.В., Аникина М.А., Павлов Д.В., Максимов Ф.М., Кузнецов А., Кондратьев В.М., Шаров В.А., Кучмижак А.А., Большаков А.Д., 2026. Издатель: Санкт-Петербургский политехнический университет Петра Великого.

Introduction

Two-dimensional materials, particularly monolayer transition metal dichalcogenides (TMDC) like MoS_2, WS_2, $MoSe_2$ are ideal for optoelectronics due to their direct bandgap and strong excitonic effects [1 – 3]. The strategy for enhancing material functionality through hybridization with nanostructures is well-established in fields such as sensor technology, which widely employs carbon nanomaterials for signal transduction [4].

A promising approach to overcome the inherent limitations of two-dimensional materials is their integration with nanostructured surfaces. Of particular interest in this context are metallic nanostructures that support plasmonic resonances, the spectral position of which can be precisely tuned by tailoring their geometry. A significant advancement in this field is the development of the femtosecond laser printing method for such plasmonic elements fabrication [5, 6]. In contrast to nanostructured surfaces obtained via complex and costly lithography and etching techniques, laser printing offers a pathway to produce similar structures using an accessible and scalable technology.

This work presents a study of a hybrid system based on a tungsten diselenide monolayer (1L-WSe_2) integrated with gold plasmonic nanobumps (Au-nanobumps). This configuration not only provides significant photoluminescence enhancement through resonant exciton-plasmon interaction but also enables control over the spectral characteristics of the system achieved by modifying the bandgap of the two-dimensional material via its deformation on the nanoscale relief of the nanostructure.

Materials and Methods

In our work, WSe_2 monolayers were obtained using a mechanical exfoliation method and transferred to a target substrate with Au-nanobumps using a custom transfer system based on tsc2 h_q graphene (HQ Graphene, Netherlands). In this transfer method, crystal layers are exfoliated onto the surface of adhesive tape and then deposited onto a polydimethylsiloxane (PDMS) polymer film supported by a glass substrate. Subsequently, the monolayers are transferred from this "stamp" to the target substrate using a dry transfer technique: the polymer film is brought into contact with the substrate and then peeled away, leaving the layers on the substrate surface. During this process, the target substrate is heated to a temperature between 60°C and 100°C, and the contact time between the crystalline monolayers on the polymer film and the substrate is maintained for 2–4 minutes.

The Au-nanobumps metasurface was fabricated by a combination of inexpensive and scalable magnetron sputtering of thin Au films with a direct fs-laser printing technique. First, a gold film with a thickness of 50 nm was coated over a glass substrate using magnetron deposition. Then, laser patterning of the glass-supported Au films was carried out using $\approx$ 200 fs second-harmonic (λ = 515 nm) pulses generated by a regeneratively amplified Yb:KGW laser system (Pharos, Light Conversion) at 50 kHz repetition rate. A computer-driven nanopositioning platform (ANT130XY, Aerotech) ensured precise movement of the sample surface with respect to the laser focal spot, allowing each pulse to form isolated nanobumps arranged into a square-shaped lattice with a period (Λ) defined by the sample scanning speed.

The nanobump arrays fabricated under these conditions are shown in Fig. 1, *a*, with each row corresponding to a specific laser pulse power, expressed as a percentage of the maximum (100% = 2 nJ). Fig. 1, *b* quantifies the empirical linear dependence between laser pulse power and nanobump height, demonstrating that increased energy produces taller nanostructures. Furthermore, each periodic array (with periods of 3, 5, and 10 μm) exhibits a distinct plasmonic resonance, the spectral position of which depends on the bump height, as shown in Fig. 1, *c*.

Using these techniques, we successfully fabricated a hybrid sample consisting of a monolayer WSe_2 integrated with an array of Au nanobumps.

Results and Discussion

Optical characterization of the hybrid structure was performed via Raman and photoluminescence (PL) microspectroscopy using a Horiba LabRAM HR 800 spectrometer (Horiba Scientific, Japan) equipped with a 532 nm diode-pumped solid-state laser.

Fig. 2, *a* shows an optical image of a WSe_2 flake transferred onto a substrate patterned with a periodic array of Au-nanobumps (mean height: 147 nm, base diameter: 364 nm), fabricated

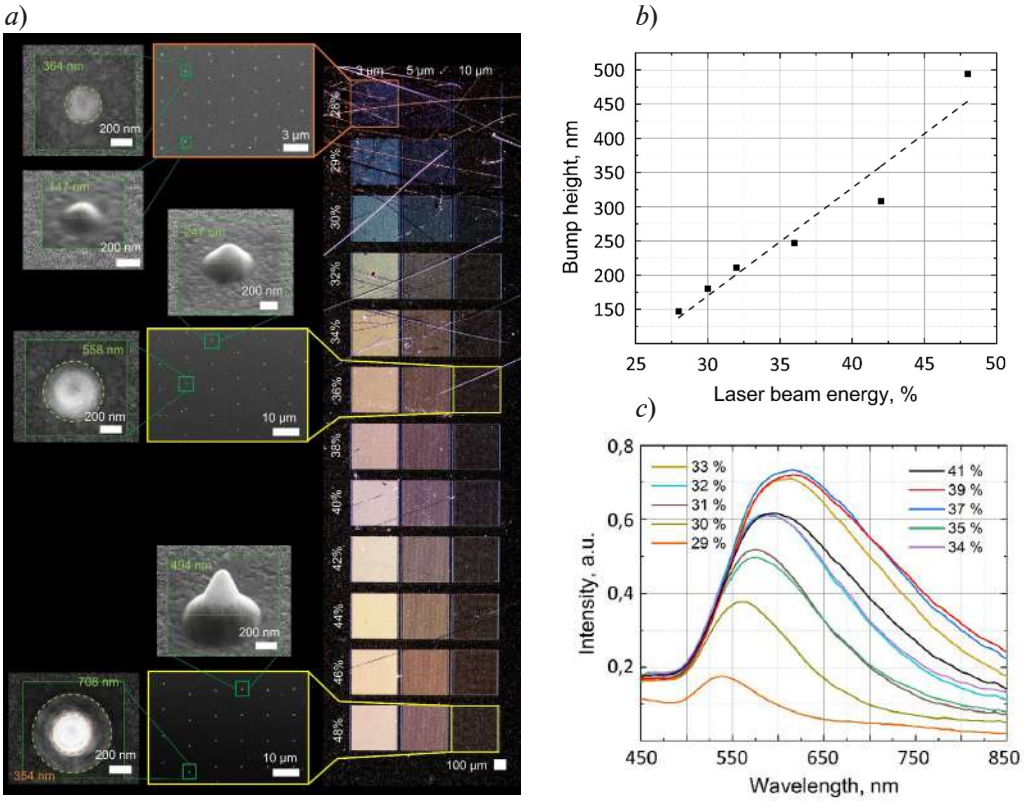

Fig. 1. Au-nanobumps: SEM (left) and optical (right) images of nanobump arrays with periods of 3, 5 and 10 μm (*a*); dependence of the Au-nanobump height on the laser pulses of different output, expressed as a percentage, where 100% corresponds to 2 nJ (*b*); dark-field scattering spectra of Au-nanobump arrays as a function of laser pulses of different output, expressed as a percentage (*c*)

via femtosecond laser printing at a pulse energy of 0.58 nJ (29% of maximum output). The corresponding atomic force microscopy (AFM) topography of this region is presented in Fig. 2, *b*. The flake comprises two distinct thickness domains: a monolayer (1L) and a bilayer (2L) region. AFM analysis demonstrates conformal coverage of the nanostructures, with the flake adopting a tensile, tent-like morphology over each nanobump. Notably, the formation of pronounced folds in the inter-bump regions is enhanced within the bilayer region. The substrate also exhibits a distribution of polydisperse golden nanoparticles (Au-nanoparticles), which are byproducts of the laser fabrication process.

Raman mapping of area *R* (Fig. 2, *a*, *c*) was performed to distinguish the mono- and bilayer regions of WSe_2. The bilayer (2L-WSe_2) region shows a significantly enhanced integrated Raman intensity compared to the monolayer (1L-WSe_2) (Fig. 2, *d*). Furthermore, the spatial boundary is corroborated by a systematic shift in the A'_1 peak position, where the bilayer region exhibits a distinct downshift of several cm^{-1} (Fig. 2, *c*). In the 2L-WSe_2 region, particularly at folds and in the deformed area under the nanobump, a significant enhancement of the integrated Raman scattering intensity is observed. Specifically, in addition to the primary optical modes (A'_1, E′) the intensity of the second-order modes at 311 cm^{-1}, 376 cm^{-1}, and 397 cm^{-1} increases. In contrast, these modes are indistinguishable from the noise level in the undeformed monolayer region.

PL mapping across the 1L-WSe_2 region, from the planar area to the Au-nanobump apex (Fig. 3, *b*), along with the AFM map (Fig. 3, *a*) and corresponding spectra (Fig. 3, *d*), reveals two primary strain-dependent effects. First, the PL intensity increases significantly near the Au-nanobump. This enhancement results from a combination of exciton localization, which suppresses non-radiative recombination pathways, and the plasmonic nanoantenna effect of the gold nanostructure, which amplifies the local electromagnetic field. Moreover, the PL peak exhibits a red shift of several nanometers under tensile strain, consistent with a reduction in the direct bandgap of the deformed WSe_2 lattice.

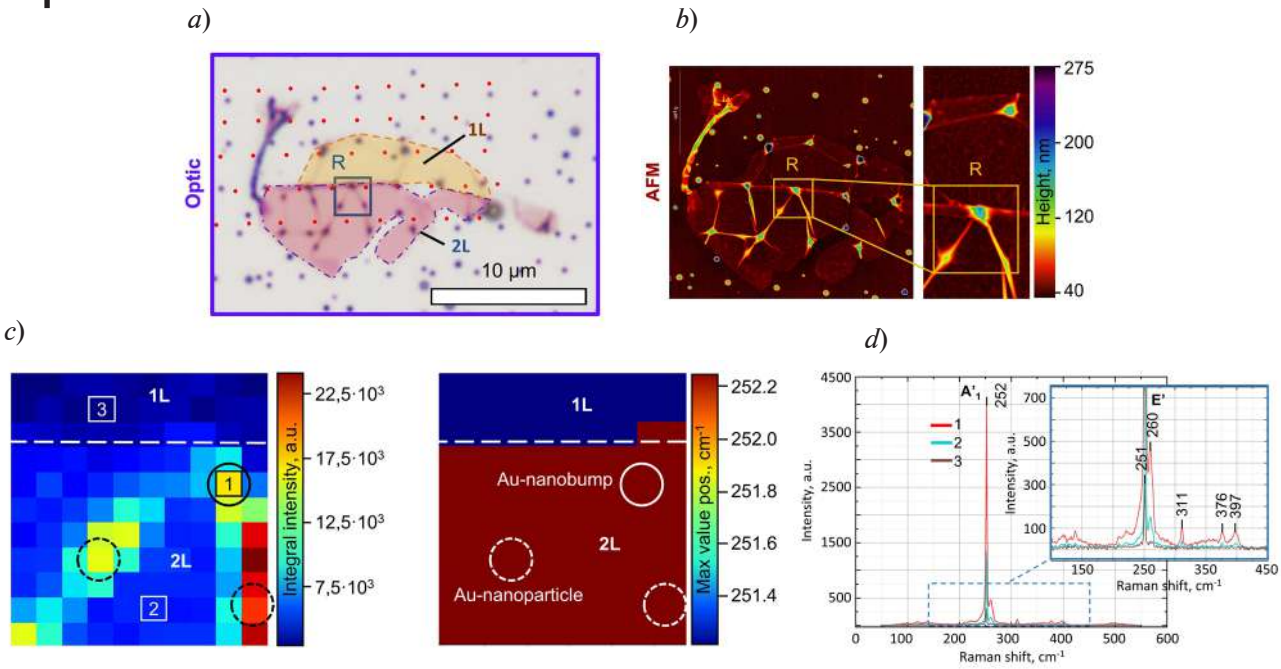

Fig. 2. WSe_2 on Au-nanobumps (29%): optical image of 1L-WSe_2 and 2L-WSe_2 flakes on Au-nanobumps indicated by red dots (*a*) and AFM-map (*b*) with the selected Raman mapping area *R*; Raman mapping of the area *R* representing integral intensity and the primary peak position of Raman spectra, in cm^{-1} (*c*); Raman spectra of the dots 1, 2 and 3 represented on the integral intensity map (*d*)

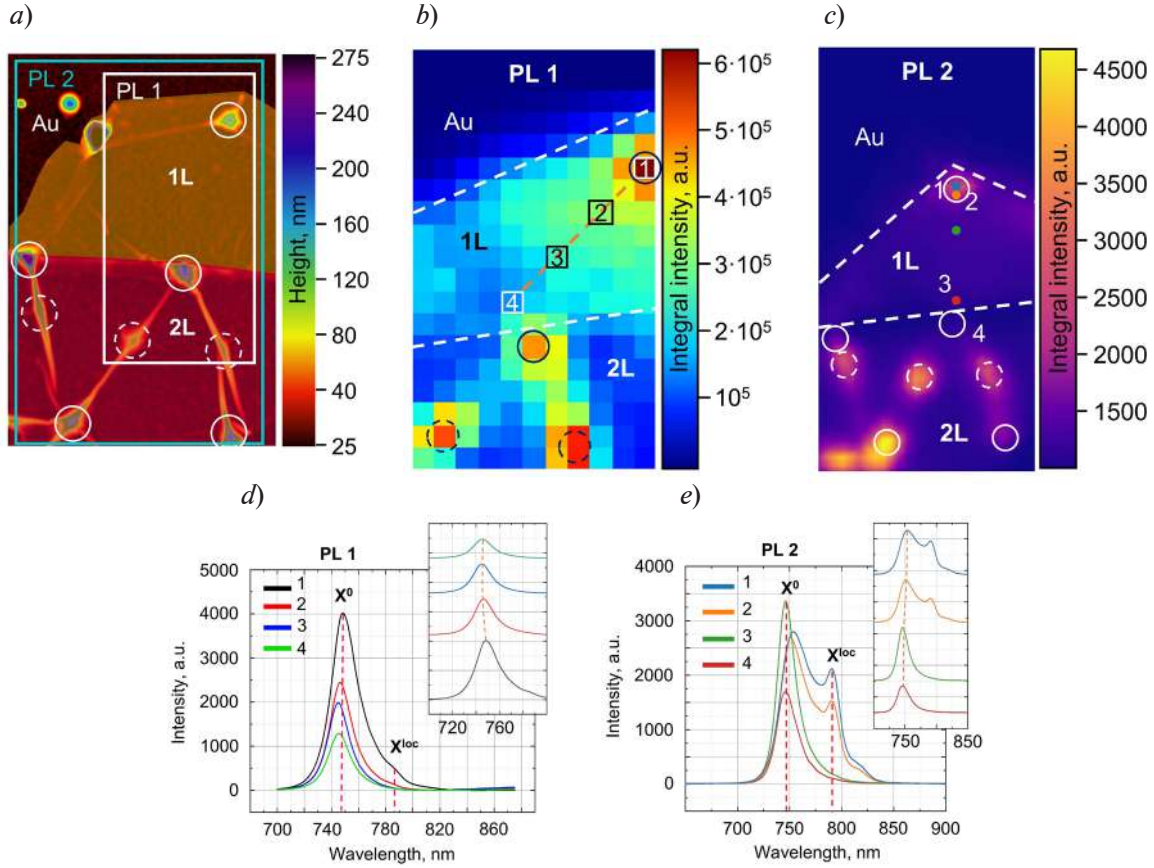

Fig. 3. AFM map (*a*) and photoluminescence map PL 1 at 532 nm (*b*) and PL 2 at 473 nm (*c*) excitation and the corresponding spectra (*d*, *e*). The locations of Au-nanobumps and Au-nanoparticles on all maps are highlighted with solid and dashed circles, respectively

The photoluminescence (PL) spectra of area 1 (Fig. 3, *d*) exhibit a low-energy shoulder at 785 nm alongside the neutral exciton X^0 peak at 750 nm. This feature can likely be attributed to a strain-localized exciton (X^{loc}) as shown in the work on WS_2 [7]. Localized excitons in transition metal dichalcogenide (TMDC) monolayers typically arise from structural defects or spatially confined strain. The concept of localized excitons is further substantiated by the ability to deterministically create nanoscale potential wells through precisely induced deformation at predefined sites, which effectively funnel excitons and give rise to strain localized excitonic states. Mapping of the same area under 473 nm laser excitation (Ntegra Spectra II system, NT-MDT) revealed a significant alteration of the spectral profile near the nanobump (Fig. 3, *e*): the low-energy state at 788 nm appears as a distinct, intense peak rather than a shoulder. Concurrently, the X^0 peak shows no enhancement. This observation can be interpreted from two perspectives: firstly, in terms of energy transfer between the two states (X^0/X^{loc}), and secondly, considering the disparity in excitation power at 532 nm (3.9 mW/μm²) versus 473 nm (5 μW/μm²). At lower power levels, the low-energy state becomes more prominent, emerging against a backdrop of diminished neutral exciton photoluminescence intensity. Moreover, the more pronounced enhancement of the neutral exciton (X^0) under 532 nm excitation can be attributed to the spectral overlap between the pump energy and the maximum of the nanobumps' plasmon resonance (Fig. 1, *c*).

To investigate this spectral feature further, low-temperature photoluminescence measurements at 10 K were performed using a customized setup. The micro-PL system for low-temperature measurements comprised a Hubner C-Wave tunable continuous-wave (CW) laser with a radiation wavelength of 512 nm. The sample was mounted in a Montana Instruments Cryostation S50 with optical access. The photoluminescence signal was collected and analyzed using a HORIBA Jobin Yvon iHR320 spectrometer equipped with a Horiba SynapsePlus detector.

Fig. 4, *a* presents the photoluminescence (PL) intensity map integrated around 1.617 eV state, acquired at 10 K. Within this selected spectral window, the integrated PL intensity reaches its maximum near the nanobump. For reference, the corresponding AFM topography is provided on the same panel, indicating the 1L-WSe_2 and 2L-WSe_2 regions, as well as the specific points of PL spectra shown in Fig. 4, *c*.

The low-temperature PL spectra of WSe_2 contain, in addition to the primary neutral exciton (X^0) and trion (X^T) states in accordance with the work [8], an ensemble of low-energy features commonly interpreted in the literature as localized excitonic states [9]. Both the neutral exciton and the trion exhibit a red shift on the nanobump compared to the flat region: 1.8 meV for X^0 and 4.3 meV for XT. The pronounced peak at 1.617 eV, corresponding to the maximum photoluminescence intensity in the deformed WSe_2 region beneath the nanobump, can be interpreted as a potential low energy strain-localized state, which is also observed in room temperature spectra.

This spectral reorganization demonstrates the pronounced effect of strain and plasmonic enhancement on the optoelectronic properties of 1L-WSe_2. It highlights the potential for actively tuning the photoluminescence in hybrid plasmonic nanostructure/2D material systems, which is highly relevant for developing nanolasers, highly sensitive sensors, and nanophotonic components.

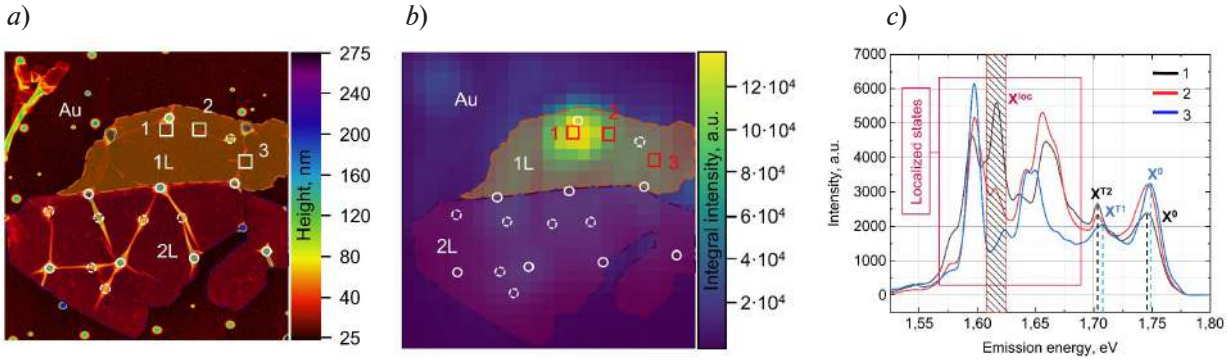

Fig. 4. AFM map (*a*) and photoluminescence map (*b*) at 10 K and 512 nm excitation and the corresponding spectra (*c*). The locations of Au-nanobumps and Au-nanoparticles on all maps are highlighted with solid and dashed circles, respectively

Conclusion

In summary, we demonstrated the integration of a WSe_2 monolayer with a plasmonic Au-nanobumps surface, fabricated via simple and cost-effective femtosecond laser printing and dry transfer. This hybrid system leverages a dual mechanism combining resonant plasmonic enhancement with strain-induced bandgap engineering. The observed pump-strain-driven spectral redistribution, characterized by a red shift and controlled correlation between intensity of neutral exciton and low-energy excitonic features, confirms the decisive role of nanoscale deformation in modulating optoelectronic properties. This study presents a versatile platform for spectrally tunable light emission, advancing the development of nanoscale light sources and strain-sensitive nanophotonic components.

Acknowledgments

A.V.N. thanks the Ministry of Science and Higher Education of the Russian Federation (Grant FSRM-2026-0004) for supporting the processing. M.A.A. thanks the Ministry of Science and Higher Education of the Russian Federation (project FSMG-2025-0005) for support of the PL mapping. A.D.B. acknowledges Saint-Petersburg State University for a research project 122040800254-4 supporting the paper preparation.

REFERENCES

1. **Kuznetsov A., Anikina M.A., Toksumakov A.N., Abramov A.N., Dremov V.V., Zavyalova E.G., Kondratev V.M., Fedorov V.V., Mukhin I.S., Kravtsov V., Novoselov K.S., Arsenin A.V., Volkov V.S., Ghazaryan D.A., Bolshakov A.D.,** In-Plane Directional MoS_2 Emitter Employing Dielectric Nanowire Cavity, Small Structures. (2025).

2. **Nikolaeva A.V., Anikina M.A., Kondratev V.M., Sharov V.A., Barulina E.Yu., Gridchin V.O., Khrebtov A.I., Kuchmizhak A.A., Bolshakov A.D.,** Hybrid emitters based on two-dimensional WSe_2 and ordered plasmonic nanobumps, St. Petersburg State Polytechnical University Journal. Physics and Mathematics. 18 (3.1) (2025) 30–35.

3. **Uymina P.G., Anikina M.A., Speshilova A.B., Kondratev V.M., Karaseva E.P., Shmakov S.V., Kuznetsov A., Syuy A.V., Osipov A.A., Mishin M.V., Bolshakov A.D.,** Blossoming layers: Morphological engineering of vertically aligned MoS_2 sheets, Materials Science in Semiconductor Processing. 200 (2025) 109906.

4. **Nikolaeva A.V., Kondratev V.M., Kadinskaya S.A., Kolesina D.E., Zubov F.I., Anikina M.A., Dvoretckaia L.N., Lendyashova V.V., Gridchin V.O., Monastyrenko A.O., Krasnikov D.V., Nasibulin A.G., Kochetkov F.M., Bolshakov A.D.,** ZnO nanowire-based flexible sensors for pressure and temperature monitoring, Materials Science in Semiconductor Processing. 189 (2025) 109253.

5. **Lapidas V., Cherepakhin A., Storozhenko D., Gurevich E.L., Zhizhchenko A., Kuchmizhak A.A., Lapidas V., Cherepakhin A., Storozhenko D., Gurevich E.L., Zhizhchenko A., Kuchmizhak A.A.,** Surface coloring and plasmonic information encryption at 50000 dpi enabled by direct femtosecond laser printing, Nano Letters. 24 (40) (2025) 12590–12596.

6. **Sergeeva K.A., Pavlov D.V., Seredin A.A., Mitsai E.V., Sergeev A.A., Modin E.B., Sokolova A.V., Tsz Chun Lau, Baryshnikova K.V., Petrov M.I., Kershaw S.V., Kuchmizhak A.A., Kam Sing Wong, Rogach A.L.,** Laser-printed plasmonic metasurface supporting bound states in the continuum enhances and shapes infrared spontaneous emission of coupled HgTe quantum dots, Advanced Functional Materials. 33 (44) (2023) 2307660.

7. **Feng S., Cong H., Kholid F.N., Zhang J., Liu X., Li Y., Liu Z., Yu T., Wang G., Mohib-Ul-Kabir M., Liu Y., Lou J., Huang J., Chen Y., Ma C., Su F., Feng M., Cao Y., Liu B., He R., Du W., Dresselhaus M.S., Yang R.,** Direct observations of the rotation and translation of anisotropic nanoparticles adsorbed at a liquid-solid interface, ACS Nano. 16 (6) (2022) 9217–9228.

8. **Robert C., Lagarde D., Cadiz F., Wang G., Lassagne B., Amand T., Balocchi A., Renucci P., Tongay S., Urbaszek B., Marie X.,** Exciton radiative lifetime in transition metal dichalcogenide monolayers, Physical Review B. 93 (20) (2016) 205423.

9. **Wang G., Bouet L., Lagarde D., Vidal M., Balocchi A., Amand T., Marie X., Urbaszek B.,** Valley dynamics probed through charged and neutral exciton emission in monolayer WSe_2, Physical Review B. 90 (7) (2014) 075413.

THE AUTHORS

NIKOLAEVA Aleksandra V.
nikalex2000@bk.ru
ORCID: 0009-0008-4344-4863

ANIKINA Maria A.
mari.a.nikina@yandex.ru
ORCID: 0000-0002-5522-5026

PAVLOV Dmitrii V.
pavlov.dim@mail.ru
ORCID: 0000-0001-8726-5615

MAKSIMOV Fedor M.
maksimov.fm@phystech.edu
ORCID: 0000-0002-2845-5061

KUZNETSOV Alexey
alkuznetsov1998@gmail.com
ORCID: 0000-0001-7143-6686

KONDRATEV Valeriy M.
kvm_96@mail.ru
ORCID: 0000-0002-3469-5897

SHAROV Vladislav A.
vl_sharov@mail.ru
ORCID: 0000-0001-9693-5748

KUCHMIZHAK Aleksandr A.
ku4mijak@iacp.dvo.ru
ORCID: 0000-0002-5376-5555

BOLSHAKOV Alexey D.
acr1235@mail.ru
ORCID: 0000-0001-7223-7232

Received 14.12.2025. Approved after reviewing 10.02.2026. Accepted 03.03.2026.

© Peter the Great St. Petersburg Polytechnic University, 2026

Conference paper
UDC 538.958
DOI: https://doi.org/10.18721/JPM.191.111

Interband absorption and photoluminescence in lens-shaped quantum dots: an adiabatic approach

D.G. Gevorgyan [1]✉, S.P. Gavalajyan [1, 2], M.Ya. Vinnichenko [3], E.M. Kazaryan [1]

[1] Russian-Armenian University, Yerevan, Armenia;
[2] Quantum Materials and Nanophotonics Laboratory,
A.B. Nalbandyan Institute of Chemical Physics, Yerevan, Armenia;
[3] Peter the Great St. Petersburg Polytechnic University, St. Petersburg, Russia
✉ davitgevorgyan2000@gmail.com

Abstract. We present an analytic-numerical framework for carriers and excitons in lens-shaped (semi-ellipsoidal) quantum dots within the effective-mass and envelope-function approximations, assuming hard-wall confinement. Exploiting the geometry, we use an adiabatic separation of fast (axial) and slow (planar) motion to obtain closed-form single-particle states and energies. The exciton binding energy is evaluated numerically in first-order perturbation theory using the analytic envelopes. Interband absorption follows from bright-state selection rules, and photoluminescence is obtained from absorption via the van Roosbroeck–Shockley relation with Lorentzian broadening. It is shown that single-particle confinement energies are much more sensitive to the dot height than to the lateral size, states with higher axial quantum number lie well above the lowest branch, the Coulomb binding decreases with increasing size, exhibiting comparable fractional sensitivity to both the axial and planar semi-axes and grouping primarily by radial quantum number. The framework yields compact formulas, transparent scaling trends, and interpretable spectra for the design and analysis of lens-shaped quantum dots.

Keywords: Quantum dots, lens-shaped quantum dots, exciton, photoluminescence

Funding: This work was supported by the Science Committee of the Republic of Armenia (Research project № 24AA-1C047). M.Y.V. acknowledges support from the Ministry of Science and Higher Education of the Russian Federation (State Assignment FSEG-2023-0016).

Citation: Gevorgyan D.G., Gavalajyan S.P., Vinnichenko M.Ya., Kazaryan E.M., Interband absorption and photoluminescence in lens-shaped quantum dots: an adiabatic approach, St. Petersburg State Polytechnical University Journal. Physics and Mathematics. 19 (1.1) (2026) 69–74. DOI: https://doi.org/10.18721/JPM.191.111

This is an open access article under the CC BY-NC 4.0 license (https://creativecommons.org/licenses/by-nc/4.0/)

Конференционная статья
УДК 538.958
DOI: https://doi.org/10.18721/JPM.191.111

Межзонное поглощение и фотолюминесценция в линзообразных квантовых точках: адиабатический подход

Д.Г. Геворгян [1]✉, С.П. Гаваладжян [1, 2], М.Я. Винниченко [3], Э.М. Казарян [1],

[1] Российско-Армянский университет, г. Ереван, Армения;
[2] Лаборатория квантовых материалов и нанофотоники, Институт химической физики им. А.Б. Налбандяна, г. Ереван, Армения;
[3] Санкт-Петербургский политехнический университет Петра Великого, Санкт-Петербург, Россия
✉ davitgevorgyan2000@gmail.com

© Gevorgyan D.G., Gavalajyan S.P., Vinnichenko M.Ya., Kazaryan E.M., 2026. Published by Peter the Great St. Petersburg Polytechnic University.

Аннотация. Представлен аналитико-численный подход к описанию носителей и экситонов в линзовидных (полуэллипсоидальных) квантовых точках в рамках приближений эффективной массы и огибающей функции при предположении бесконечного потенциального ограничения. Используя геометрию системы, мы применяем адиабатическое разделение быстрых (аксиальных) и медленных (плоских) движений, что позволяет получить аналитические выражения для одночастичных состояний и энергий. Энергия связи экситона рассчитывается численно в первом порядке теории возмущений с использованием аналитических огибающих функций. Межзонное поглощение определяется правилами отбора для светлых состояний, а фотолюминесценция получается из спектра поглощения с помощью соотношения ван Роосбрука–Шокли с лоренцевским уширением. Показано, что одночастичные энергии значительно более чувствительны к высоте квантовой точки, чем к ширине; состояния с более высоким аксиальным квантовым числом располагаются значительно выше нижней ветви спектра; кулоновская энергия связи уменьшается с ростом размеров структуры, демонстрируя сопоставимую относительную чувствительность как к аксиальной, так и к плоской полуосям и группируясь преимущественно по радиальному квантовому числу. Предложенный подход приводит к компактным формулам, наглядным закономерностям масштабирования и физически интерпретируемым спектрам, что делает его удобным инструментом для анализа и проектирования линзовидных квантовых точек.

Ключевые слова: квантовые точки, линзообразные квантовые точки, экситон, фотолюминесценция

Финансирование: Работа выполнена при поддержке Комитета по науке Республики Армения (научный проект № 24AA-1C047). М. Я. В. выражает благодарность Министерству науки и высшего образования Российской Федерации за поддержку в рамках государственного задания FSEG-2023-0016.

Ссылка при цитировании: Геворгян Д.Г., Гаваладжян С.П., Винниченко М.Я., Казарян Э.М. Межзонное поглощение и фотолюминесценция в линзообразных квантовых точках: адиабатический подход // Научно-технические ведомости СПбГПУ. Физико-математические науки. 2026. Т. 19. № 1.1. С. 69–74. DOI: https://doi.org/10.18721/JPM.191.111

Статья открытого доступа, распространяемая по лицензии CC BY-NC 4.0 (https://creativecommons.org/licenses/by-nc/4.0/)

Introduction

Semiconductor quantum dots (QDs) are often described as “artificial atoms” because quantum confinement yields discrete energy spectra and size-tunable optical properties with broad impact across imaging, sensing, and optoelectronics. Recent surveys and application-driven studies highlight both the technological progress and remaining challenges in materials, devices, and integration [1]. In bioimaging and biodiagnostics, QDs offer bright, photostable labels with multiplexing capabilities [2]. Together, these works underscore the central role of QDs in modern photonics and the importance of tractable theoretical models that connect geometry to spectra.

Beyond composition and overall size, shape is a powerful design parameter for tailoring selection rules, oscillator strengths, and polarization characteristics. Ellipsoidal families – including oblate and prolate spheroids – have been analyzed in detail for their electronic states and interband absorption [3, 4], as well as for related ellipsoidal/lens-like nanostructures with strong shape anisotropy [5 – 7]. In epitaxial systems, lens-shaped (semi-ellipsoidal) QDs arise naturally. Related work on asymmetric biconvex lens-shaped dots mapped the influence of external fields on interband and intraband optical properties [8].

Against this backdrop, the present paper develops a minimal effective-mass, envelope-function description for carriers and excitons in lens-shaped (semi-ellipsoidal) QDs with hard-wall confinement. We derive closed-form single-particle states in an adiabatic (fast/slow) separation, compute first-order Coulomb corrections to exciton energies using analytic envelopes, and obtain interband absorption together with photoluminescence (PL) via the van Roosbroeck–Shockley

© Геворгян Д.Г., Гаваладжян С.П., Винниченко М.Я., Казарян Э.М., 2026. Издатель: Санкт-Петербургский политехнический университет Петра Великого.

detailed balance relation [9]. Our goal is to provide compact formulas, transparent scaling trends, and interpretable spectra that clarify how lens geometry organizes bright transitions and Coulomb-induced splittings.

Theory

Single-Particle Energies and States. The geometry of the lens-shaped quantum dot is modeled by a cylindrically symmetric semi-ellipsoid illustrated in Fig. 1 that satisfies the condition $c << a$ where a and c denote the major and minor semi-axes of the semi-ellipsoid, respectively.

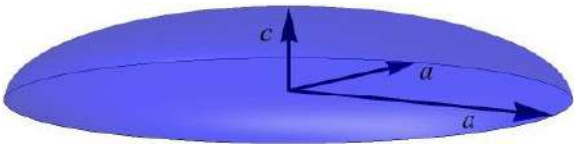

Fig. 1. Schematic representation of a semi-ellipsoid with semi-axes a, a and c

The confining potential of a particle in such a quantum dot is defined as $V(\mathbf{r}) = 0$ inside and $V(\mathbf{r}) = \infty$ outside the dot. The single-particle Hamiltonian in cylindrical coordinates then takes the form

$$\hat{H} = -\left(\frac{\partial^2}{\partial r^2} + \frac{1}{r}\frac{\partial}{\partial r} + \frac{1}{r^2}\frac{\partial^2}{\partial \varphi^2} + \frac{\partial^2}{\partial z^2} \right) + V(\mathbf{r}), \quad (1)$$

where distances and energies are expressed in effective atomic units (Bohr radius and Rydberg).

It follows from the condition $c << a$ that the motion of the particle along the OZ axis is much faster than in the OXY plane, which makes it possible to apply the adiabatic approximation. Within this approximation, the particle Hamiltonian can be separated into two components: $\hat{H}_r$ corresponds the slow planar degrees of freedom, while $\hat{H}_z$ corresponds to the fast axial one. The solution of the stationary Schrödinger equation is sought in the form

$$\psi(r, \varphi, z) = \psi_r(r)\psi_z(r, z)e^{im\varphi}. \quad (2)$$

For a fixed value of r, the fast subsystem can be represented as a potential well with an effective width $w(r) = c\sqrt{1 - r^2/a^2}$ and the solution of the Schrödinger equation yields

$$\psi_z(r, z) = \sqrt{\frac{2}{w(r)}} \sin\left(\frac{\pi n_z z}{w(r)} \right), \; \varepsilon_z(r) = \frac{\pi^2 n_z^2}{w^2(r)}, \quad (3)$$

where n_z is the axial quantum number. Here $\varepsilon_z(r)$ can be expanded in a Taylor series with respect to r/a as

$$\varepsilon_z(r) \approx \alpha n_z^2 + \beta^2 n_z^2 r^2, \; \alpha = \frac{\pi^2}{c^2}, \; \beta = \frac{\pi}{ac}. \quad (4)$$

Substituting $\varepsilon_z(r)$ into the equation for the slow subsystem as an effective potential leads to the problem of a two-dimensional harmonic oscillator. Accordingly, the radial component of the wave function $\psi_r(r)$ is given by

$$\psi_r(r) = Ar^{|m|} e^{-\beta n_z r^2/2} L_{n_r}^{|m|}(\beta n_z r^2), \quad (5)$$

where n_r and m are the radial and angular quantum numbers, respectively, $L_{n_r}^{|m|}(\cdot)$ is the associated Laguerre polynomial, and A is a normalization constant.

The corresponding single-particle energy spectrum is

$$E_{n_z, n_r, m} = \alpha n_z^2 + \beta n_z (2n_r + |m| + 1). \quad (6)$$

For the lowest longitudinal branch $n_z = 1$, the energy depends only on $N \equiv 2n_r + |m|$; all states with the same N are degenerate with multiplicity $N + 1 = 2n_r + |m| + 1$.

Exciton Energy

The Hamiltonian of the exciton is

$$\hat{H} = \hat{H}_e + \hat{H}_h - \frac{1}{|\mathbf{r}_e - \mathbf{r}_h|}, \quad (7)$$

where $\hat{H}_e$ and $\hat{H}_h$ are the single-particle Hamiltonians of the electron and hole, respectively, and the last term describes their Coulomb attraction.

When comparing with optical spectra, the relevant interband transition energy includes the band gap E_g:

$$E_{ex} = E_g + E_{eh}, E_{eh} = E_e + E_h - V_{eh}, \tag{8}$$

where E_e and E_h are the confinement (single-particle) energies of the electron and the hole measured from the band edges, and

$$V_{eh} = \int \psi_e^*(\mathbf{r}_e)\psi_h^*(\mathbf{r}_h)\frac{1}{|\mathbf{r}_e - \mathbf{r}_h|}\psi_e(\mathbf{r}_e)\psi_h(\mathbf{r}_h)d^3\mathbf{r}_e d^3\mathbf{r}_h, \tag{9}$$

where $\psi_{e,h}$ are the normalized envelopes from the previous subsection.

Interband Absorption and Photoluminescence

Interband absorption probes the allowed optical transitions in the quantum dot and is strongly shaped by excitonic effects. The absorption coefficient (up to a material-dependent prefactor) can be written as a sum over electron-hole envelope states. Taking into account the orthonormality of the modes, it can be reduced to a sum over bright transitions only ($n_z^e = n_z^h, n_r^e = n_r^h,\ m_e = -m_h$),

$$\alpha(\hbar\omega) \propto \sum_{n_r, n_z, m} \delta\left[\hbar\omega - E_{ex}(n_r, n_z, m)\right]. \tag{10}$$

Substituting the absorption spectrum into the RS relation [10] yields the PL spectrum

$$R(\hbar\omega) \propto (\hbar\omega)^2 \sum_{n_r, n_z, m} \delta\left(\hbar\omega - E_{ex}(n_r, n_z, m)\right)\frac{f_c(1 - f_v)}{f_v - f_c}. \tag{11}$$

where f_c and f_v are the Fermi-Dirac occupation probabilities of the conduction and valence band states that depend on the lattice temperature.

In practice, delta-peaks are broadened by coupling to phonons. A convenient replacement is a Lorentzian with typical half-width at half-maximum γ in the range 0.5–5 meV. The resulting broadened spectra are evaluated numerically in the next section.

Results and Discussion

Fig. 2 shows the probability density $|\psi_{n_z, n_r, m}(r, \varphi, z)|^2$ for several representative states in the lens-shaped dot. The expected nodal structure is evident: along z there are $n_z - 1$ internal nodes and n_z lobes, while in the radial direction the Laguerre part yields exactly n_r radial nodes. The angular quantum number m controls the central behavior via the $r^{|m|}$ term: for $m = 0$ the density is maximal at $r = 0$, whereas for $|m| \leq 1$ it vanishes at $r = 0$ and forms ring-like maxima whose radius grows with $|m|$. Overall, the examples show clear localization of the particle near the dot center for the lowest (n_r, m) and the emergence of additional nodes as n_z or n_r increase.

States with $n_z > 1$ have energies far above the $n_z = 1$ ones as a direct consequence of the relation $c << a$, and will be disregarded in what follows. The lowest level shows only a very weak dependence on a since the dominant α-term is controlled solely by c.

Fig. 3 presents the electron-hole Coulomb contribution V_{eh} in electron Rydbergs for several $n_z = 1$ states as a function of the dot dimensions. The range is chosen based on GaAs parameters. As either the height c (a) or the lateral semi-axis a (b) increases, the binding weakens monotonically. Notably, the sensitivity to relative changes in a and in c is comparable over the plotted ranges. An interesting systematic ordering emerges: curves group primarily by the radial quantum number n_r (across different m) and with an increasing n_r the binding energy decreases.

The calculated PL spectrum $R(\hbar\omega)$ for the representative dot is shown in Fig. 4. The sequence of peaks follows the ordering of the single-particle ladder corrected by the electron-hole attraction consistent with the selection rules. In the non-interacting limit, the states within a fixed $N \equiv 2n_r + |m|$ would be degenerate with multiplicity $N + 1$. The Coulomb term V_{eh} depends on (n_r, $|m|$) and therefore partially lifts this degeneracy.

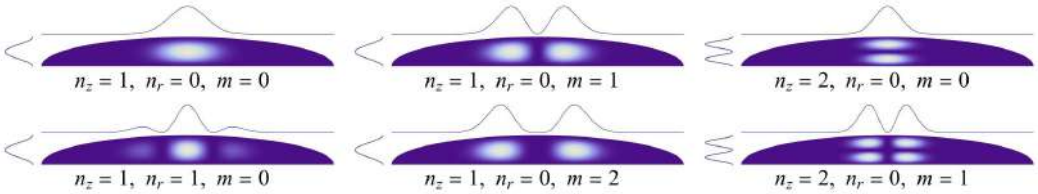

Fig. 2. Probability densities and marginals in the lens-shaped dot. Each panel displays the probability density $|\psi_{n_z,n_r,m}(r,\varphi,z)|^2$ for a representative state. For each state, curves plotted to the left and on top show the longitudinal and the radial marginal probability densities respectively

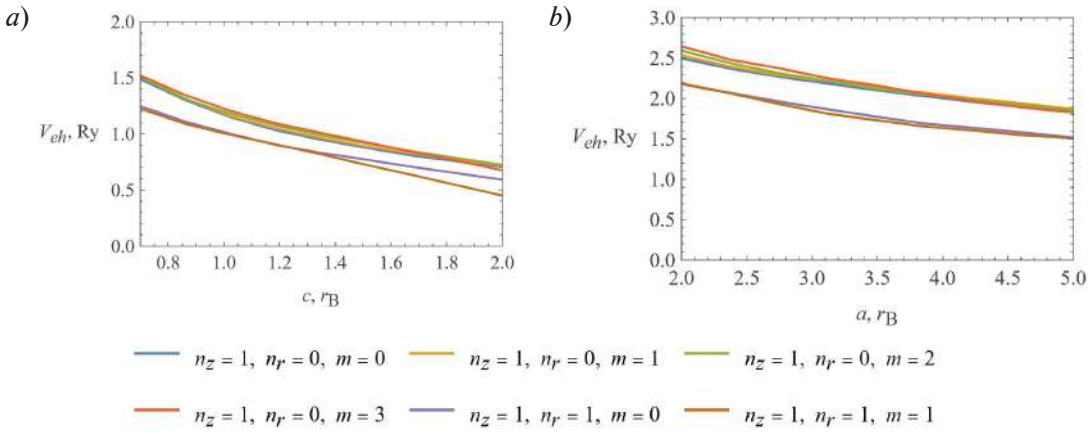

Fig. 3. Exciton Coulomb binding energy versus vertical semi-axis c at fixed $a = 5r_B$ (a) and lateral semi-axis a at fixed $c = 0.5r_B$ (b) for $n_z = 1$

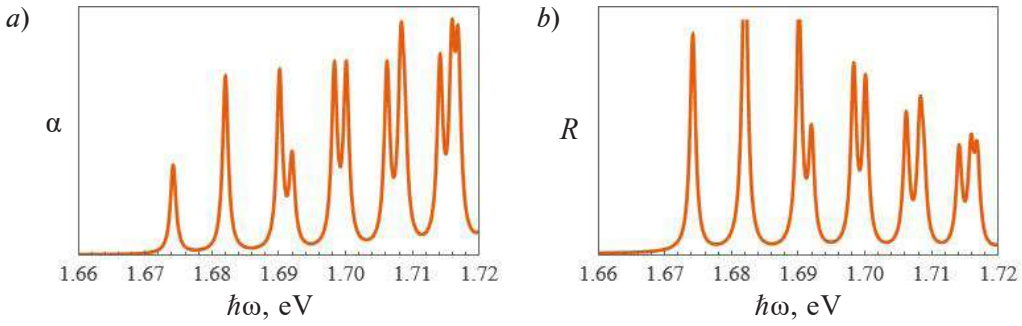

Fig. 4. Absorption (a) and photoluminescence (b) spectra for a GaAs lens-shaped dot with $a = 5r_B$ and $c = 0.5r_B$ and $T = 300$K. Both graphs use Lorentzian peak broadening with half-width $\gamma = 0.5$meV

Conclusion

We developed an analytic-numerical framework for carriers and excitons in a lens-shaped (semi-ellipsoidal) quantum dot with hard-wall confinement. Within an adiabatic separation of fast (longitudinal) and slow (in-plane) motion, we derived closed-form envelope functions and the single-particle spectrum, and established simple size dependence. Using these states, we evaluated the electron-hole interaction energy and constructed interband absorption and PL spectra.

The main findings are as follows. (i) The Coulomb binding $|V_{eh}|$ decreases monotonically with increasing a or c; over the plotted ranges, its relative sensitivity to changes in a and c is comparable, and the curves group primarily by the radial quantum number nr, reflecting the role of central localization. (ii) The absorption and PL spectra are dominated by bright transitions with matched envelope quantum numbers; electron-hole attraction lifts the non-interacting degeneracy within each $N = 2n_r + |m|$ multiplet, shifting more localized states to lower energy and producing the observed multiplet structure.

In summary, the semi-ellipsoidal model combined with adiabatic separation provides compact analytic states, clear size-dependence trends, and physically interpretable optical spectra, offering a useful baseline for both the design and analysis of lens-shaped quantum dots.

REFERENCES

1. **García de Arquer, F.P., Talapin D.V., Klimov V.I., Arakawa Y., Bayer M., Sargent E.H.,** Semiconductor quantum dots: Technological progress and future challenges, Science. 373 (6555) (2021) eaaz8541.

2. **Skolnick M.S., Mowbray D.J.,** Self-assembled semiconductor quantum dots: Fundamental physics and device applications. Annu. Rev. Mater. Res. 34 (1) (2004) 181–218.

3. **Baghdasaryan D.A., Hayrapetyan D.B., Kazaryan E.M.,** Oblate spheroidal quantum dot: electronic states, direct interband light absorption and pressure dependence, The European Physical Journal B. 88 (9) (2015) 223.

4. **Baghdasaryan D.A., Hayrapetyan D.B., Kazaryan E.M.,** Prolate spheroidal quantum dot: electronic states, direct interband light absorption and electron dipole moment, Physica B: Condensed Matter. 479 (2015) 85–89.

5. **Hayrapetyan D.B., Dvoyan K.G., Kazaryan E.M.,** Direct interband light absorption in a strongly oblated ellipsoidal quantum dot, Journal of Contemporary Physics (Armenian Academy of Sciences). 42 (4) (2007) 151–157.

6. **Baghdasaryan D.A., Hayrapetyan D.B., Kazaryan E.M.,** Optical properties of narrow band prolate ellipsoidal quantum layers ensemble, Journal of Nanophotonics. 10 (3) (2016) 033508–033508.

7. **Hayrapetyan D.B., Ohanyan G.L., Baghdasaryan D.A., Sarkisyan H.A., Baskoutas S., Kazaryan E.M.,** Binding energy and photoionization cross-section of hydrogen-like donor impurity in strongly oblate ellipsoidal quantum dot, Physica E: Low-dimensional Systems and Nanostructures. 95 (2018) 27–31.

8. **Mkrtchyan M.A., Hayrapetyan D.B., Kazaryan E.M., Sarkisyan H.A., Vinnichenko M.Y., Shalygin V.A., Firsov D.A., Petrosyan L.S.,** Effects of an external magnetic field on the interband and intraband optical properties of an asymmetric biconvex lens-shaped quantum dot, Nanomaterials. 12 (1) (2021) 60.

9. **Bhattacharya R., Pal B., Bansal B.,** On conversion of luminescence into absorption and the van Roosbroeck–Shockley relation. Applied Physics Letters. 100 (22) (2012) 222103.

THE AUTHORS

GEVORGYAN Davit G.
davitgevorgyan2000@gmail.com
ORCID: 0009-0004-0202-4396

GAVALAJYAN Sargis P.
sargis.gavalajyan@rau.am
ORCID: 0009-0002-2353-1704

VINNICHENKO Maxim Ya.
mvin@spbstu.ru
ORCID: 0000-0002-6118-0098

KAZARYAN Eduard M.
edghaz@mail.ru

Received 15.12.2025. Approved after reviewing 09.02.2026. Accepted 18.02.2026.

© Peter the Great St. Petersburg Polytechnic University, 2026

Conference paper
UDC 538.911
DOI: https://doi.org/10.18721/JPM.191.112

Role of the buffer layer on the mechanical strength of nanowire-substrate interface

M.A. Lutsevich ✉[1, 2], **V.A. Sharov** [1, 2], **A.K. Kaveev** [1, 2], **V.V. Fedorov** [1, 3], **I.S. Mukhin** [1]

[1] Alferov University, St. Petersburg, Russia;
[2] Ioffe Institute, St. Petersburg, Russia;
[3] Peter the Great St. Petersburg Polytechnic University, St. Petersburg, Russia
✉ malysh_ma@spbau.ru

Abstract. Atomic force microscopy has been utilized to study the structure and mechanical strength of the epitaxial interfaces of InAs and GaP nanowires grown on Si substrates. Measuring the elastic forces during the controlled cleavage of individual crystals carried out by lateral mechanical action of atomic force microscope probe allowed us to establish a correlation between the strength of the epitaxial interface and the level of lattice mismatch. It was shown that InAs nanowires grown on InAs buffer layer demonstrate different mechanical strength compared with the ones grown directly on Si. Meanwhile, mechanical strength of GaP nanowires grown on GaP buffer is of the same order as that of GaP nanowires grown directly on Si. Analysis of the topography after nanowire removal confirmed differences in the failure mechanisms of the interface.

Keywords: nanowires, epitaxial interface, GaP, InAs, atomic force microscopy

Funding: This study was funded by Ministry of Science and Higher Education of Russian Federation, grant number FSEG-2024-0017, FSRM-2026-0004.

Citation: Lutsevich M.A., Sharov V.A., Kaveev A.K., Fedorov V.V., Mukhin I.S., Role of the buffer layer on the mechanical strength of nanowire-substrate interface, St. Petersburg State Polytechnical University Journal. Physics and Mathematics. 19 (1.1) (2026) 75–80. DOI: https://doi.org/10.18721/JPM.191.112

This is an open access article under the CC BY-NC 4.0 license (https://creativecommons.org/licenses/by-nc/4.0/)

Конференционная статья
УДК 538.911
DOI: https://doi.org/10.18721/JPM.191.112

Влияние буферного слоя на механическую прочность интерфейса нанопровод-подложка

М.А. Луцевич ✉[1, 2], **В.А. Шаров** [1, 2], **А.К. Кавеев** [1, 2], **В.В. Федоров** [1, 3], **И.С. Мухин** [1]

[1] Академический университет им. Ж.И. Алфёрова РАН, Санкт-Петербург, Россия;
[2] Физико-технический институт им. А.Ф. Иоффе РАН, Санкт-Петербург, Россия;
[3] Санкт-Петербургский политехнический университет Петра Великого, Санкт-Петербург, Россия;
✉ malysh_ma@spbau.ru

Аннотация. Атомно-силовая микроскопия была использована для изучения структуры и механической прочности эпитаксиальных интерфейсов нанопроводов InAs и GaP, выращенных на кремниевых подложках. Измерение упругих сил во время контролируемого отщепления отдельных нанопроводов от подложки, осуществляемого латеральным механическим воздействием зонда атомно-силового микроскопа, позволило установить корреляцию между прочностью эпитаксиального интерфейса и уровнем решеточного рассогласования. Было показано, что нанопровода InAs,

© Lutsevich M.A., Sharov V.A., Kaveev A.K., Fedorov V.V., Mukhin I.S., 2026. Published by Peter the Great St. Petersburg Polytechnic University.

выращенные на буферном слое InAs, демонстрируют другую механическую прочность по сравнению с выращенными непосредственно на кремнии. В то же время, механическая прочность нанопроводов GaP, выращенных на буферном слое GaP, имеет тот же порядок, что и у выращенных непосредственно на кремнии. Кроме того, анализ топографии после удаления нанопроводов подтвердил различия в механизмах разрушения интерфейса.

Ключевые слова: нанопровода, эпитаксиальный интерфейс, GaP, InAs, атомно-силовая микроскопия

Финансирование: Работа выполнена при финансовой поддержке Министерства Науки и Высшего Образования Российской Федерации, грант номер FSEG-2024-0017, FSRM-2026-0004.

Ссылка при цитировании: Луцевич М.А., Шаров В.А., Кавеев А.К., Федоров В.В., Мухин И.С. Влияние буферного слоя на механическую прочность интерфейса нанопровод-подложка // Научно-технические ведомости СПбГПУ. Физико-математические науки. 2026. Т. 19. № 1.1. С. 75–80. DOI: https://doi.org/10.18721/JPM.191.112

Статья открытого доступа, распространяемая по лицензии CC BY-NC 4.0 (https://creativecommons.org/licenses/by-nc/4.0/)

Introduction

Semiconductor nanowires (NWs) are promising as active and passive elements for optoelectronics and nanophotonics. In particular, GaP NWs, due to their optical transparency, high refractive index, and high nonlinear coefficients, are promising for waveguides [1] and second harmonic generators [2], while InAs NWs, due to their high carrier mobility and direct bandgap, are promising for infrared light-emitting diodes and photodiodes [3]. One of the key advantages of the NW architecture over planar structures is considered to be the possibility of epitaxial growth of III-V compounds directly on silicon substrates without the use of buffer layers [4]. However, despite more than 20 years of active research, the efficiency of NW-based devices, in particular solar cells [5] and light-emitting diodes [6], still lags behind their planar counterparts. One of the reasons may be the high defect density at the NW-substrate growth interface induced by lattice mismatch, which degrades the electrophysical properties of devices despite the good crystalline quality of the NWs themselves. This work compares the mechanical properties of NWs depending on the level of lattice mismatch with the Si substrate $f_{NW} = (a_{NW} - a_{Si})$. In [7], we studied GaP NWs ($f_{GaP} = 0.37\%$) and InAs NWs ($f_{InAs} = 11.5\%$) grown directly on silicon, and experimentally demonstrated the influence of lattice mismatch on the interfacial misfit dislocations density and mechanical strength. In the present comparative study, arrays of GaP and InAs NWs grown on buffer layers are investigated in an analogous manner. The study was conducted using a previously developed methodology based on atomic force microscopy (AFM). The method involves removing individual NWs using a probe, with simultaneous recording of the elastic forces acting on the cantilever and subsequent scanning of the topography of the same area to check for the presence or absence of NW remnants (‘stumps’).

The results indicate a significant increase in the strength of the InAs/InAs interface compared to InAs/Si, while the strength of the GaP/GaP and GaP/Si interfaces differs only slightly. The results confirm the critical influence of the lattice mismatch at the NW-substrate interface on its mechanical properties, which should be taken into account when designing devices.

Materials and Methods

Arrays of NWs were grown by molecular beam epitaxy on silicon (111) substrates in the self-catalytic mode. Synthesis was carried out on Veeco Gen III system equipped with effusion cells for In and Ga, and cracker cells for P and As. A Zeiss Supra 25 system was used to obtain SEM images of the NW arrays. For the scanning probe measurements, we have utilized an NT-MDT NTegra Aura atomic force microscope (AFM) and a TipsNano HA_CNC probe.

© Луцевич М.А., Шаров В.А., Кавеев А.К., Федоров В.В., Мухин И.С., 2026. Издатель: Санкт-Петербургский политехнический университет Петра Великого.

The AFM is equipped with a standard optical system for registering probe deflection, based on reflecting a laser beam from the cantilever onto a four-segment photodiode and recording differential photocurrents. The coordinates of the NWs are determined using the regular semi-contact scanning mode. Then, the amplitude of the cantilever oscillations and the feedback gain are significantly reduced, after which a lateral displacement of the probe along a straight-line trajectory passing through the NW is performed, as shown in Fig. 1. Mechanical contact of the probe tip with the side facet of the NW leads to elastic deformations of the cantilever and the appearance of the differential photocurrent signals I_{LF} ('lateral force-induced photocurrent'). When the elastic force acting on the NW exceeds its mechanical strength during further probe displacement, the NW breaks off from the substrate, after which the cantilever deformation also disappears, and the recorded photocurrent returns to its initial zero position. Thus, a photocurrent spike is observed on the oscillogram, the amplitude of which reflects the maximum load that the NW can withstand. The ratio of the spike amplitudes, recorded by the same probe on different samples under identical conditions, allows comparison of the mechanical strength of the NW-substrate contact. The more detailed description of the method can be found in [7].

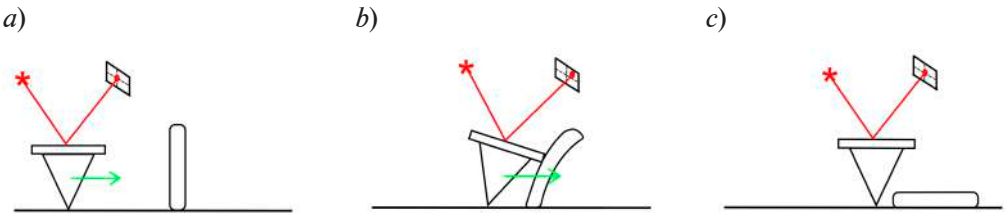

Fig.1. Schematic of the probe experiment for measuring the strength of the epitaxial NW-substrate contact

Results and Discussion

The obtained experimental data allow for a comprehensive assessment of the influence of crystallographic parameters, morphology, and epitaxial growth conditions on the mechanical strength of the NW-substrate contact. In the SEM images of all four arrays (Fig. 2), the features of the nanowire geometry are clearly distinguishable: both their lateral dimensions and the distribution in diameter and density vary. A NW with the mean geometric parameters from each array is schematically depicted above the corresponding SEM image. These differences directly affect the interaction between the probe and the NW during their removal, since the force acting on the cantilever upon contact with the side facet of the nanocrystal is determined by the lateral probe stiffness coefficient, which depends on the length from the tip base to the point of contact [7].

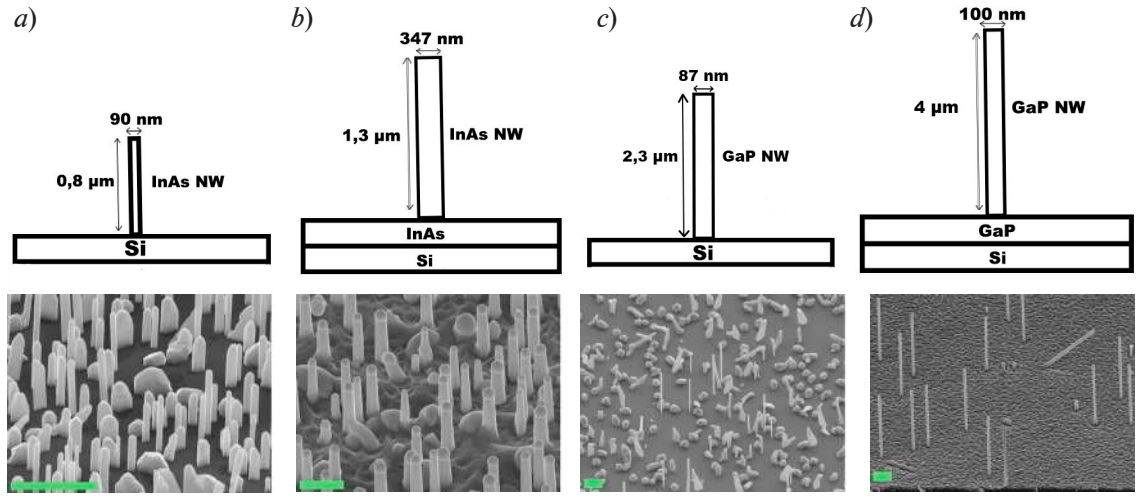

Fig. 2. SEM images of the studied samples. All scale bars are 1 μm long

Fig. 3 shows the ILF spikes amplitudes recorded on several NWs on each sample, recalculated from current units into force units using the previously developed methodology [7]. Comparison of the average amplitudes allows for a correlation between the materials of the epitaxial interface and its mechanical strength. The average values of the critical lateral elastic forces were: for InAs/Si: F_L = 813 nN, for InAs/InAs: F_L = 5195 nN, for GaP/GaP: F_L = 7109 nN, for GaP/Si: F_L = 7669 nN. Values for the GaP/Si and InAs/Si samples were taken from a previous work [7]. Significantly higher force values for both GaP NWs samples indicate greater mechanical strength of their epitaxial interface, which is explained by the low degree of lattice mismatch. It is important to note that the GaP/Si and GaP/GaP interfaces possess similar mechanical strength. In contrast, both samples with InAs NWs demonstrate lower critical forces. The high lattice mismatch between InAs and Si leads to the formation of initially highly-stressed growth interface which fully relaxes with the formation of high density of dislocations during the NW axial and radial growth. Such an interface is less robust, and therefore contact failure occurs at noticeably smaller cantilever deformations – hence the smaller I_{LF} amplitudes.

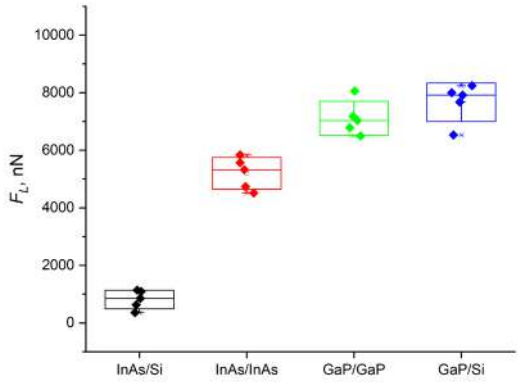

Fig. 3. Critical lateral force values corresponding to nanowire cleavage, obtained with AFM probe on several individual nanowires from each of four arrays. The boxes indicate average values, 10% and 90% percentiles

The InAs/InAs interface is approximately an order of magnitude stronger than InAs/Si, but still significantly inferior to GaP/Si and GaP/GaP. Taking into account the significantly larger lateral area of InAs/InAs interface, we normalize the measured forces to the interface area for all samples ($F^* = F/S$), obtaining for InAs/Si: F^* = 15.5 kN/cm^2, for InAs/InAs: F^* = 6.6 kN/cm^2, for GaP/GaP: F^* = 144.7 kN/cm^2, for GaP/Si: F^* = 118.2 kN/cm^2. It can be seen now that the normalized force for InAs/InAs is smaller than that for InAs/Si. Thus, the addition of a buffer layer weakens, rather than strengthens, the nanowire interface, which is counterintuitive.

To further study the nature of the NW removal, the topography of the vicinity of the growth interface of the removed crystals was investigated. The topographic features such as presence or absence of NW remains of any kind allow revealing the differences in the NW cleavage mechanism between the studied samples.

From the previous work [7] it's known that cleaved GaP/Si NWs remain certain 'stumps' up to 200 nm height while cleaved InAs/Si leave atomically-smooth surface without any stumps. From Fig. 4 we can investigate the degree of NW preservation for GaP/GaP and InAs/InAs NWs. In both cases, approximately 200 nm high stumps remain after NW removal. It can be seen that the whole lateral areas of the NW bases are preserved. Thus, GaP NWs show similar behavior both with or without GaP buffer layer. This result reflects the specificity of GaP failure mechanism, i.e., the NW body is more fragile than GaP/Si or GaP/GaP interface. At the same time, InAs NWs leave stumps only with InAs buffer layer.

Together, both groups of data, the dynamics of the I_{LF} signal and the analysis of post-removal topography, form a comprehensive picture that allows for a quantitative and qualitative assessment of the mechanical strength of NW epitaxial contacts. However, the utilized approach seems promising for further investigation of mechanical properties of nanostructures. However, the obtained results for InAs are somewhat counterintuitive. On the one hand, after removing the InAs NWs from the buffer, stumps remain, indicating that the fracture occurs within the InAs bulk, not at the growth interface. On the other hand, the assumption that the buffer would increase the strength of the InAs nanowires was not confirmed. On the contrary, a 300% reduction in the normalized critical lateral force was observed. Thus, InAs/Si interface is stronger than InAs/InAs despite potentially higher defect density.

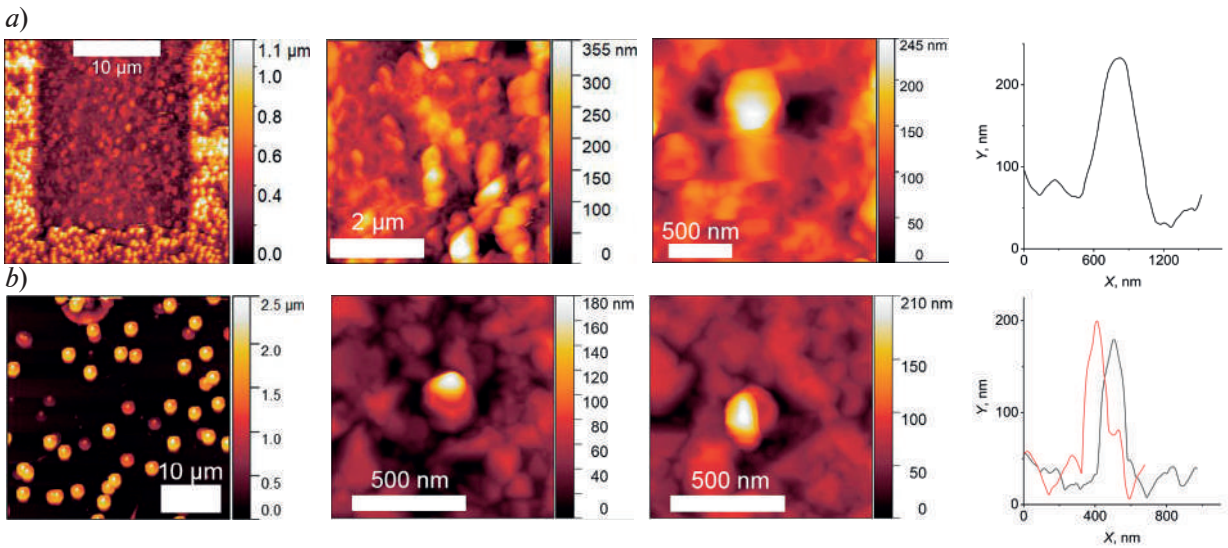

Fig. 4. Topography and topography profile of the InAs/InAs (*a*) and GaP/GaP (*b*) surface before (left pictures) and after (close-up right pictures) NW removal. The rightmost panels show 1D height profiles drawn horizontally through the stumps centers

Conclusion

Mechanical strength of individual GaP and InAs nanowires, grown on the homoepitaxial buffer layers, is investigated and compared with that of the nanowires grown directly on Si substrates.

In both cases GaP nanowires demonstrate similar strength and incomplete removal from the substrate, leaving 200 nm high stumps, indicating that both GaP/Si and GaP/GaP interfaces are stronger than the nanowire body itself. InAs nanowires demonstrate different mechanical properties with respect to the base material. The ones grown on Si are cleaving without any remains, indicating that the cleavage occurs at InAs/Si interface. The ones grown on InAs buffer are cleaving similarly to GaP nanowires, leaving stumps, but enduring 300% lower critical mechanical forces. The obtained results demonstrate the high sensitivity of the proposed methodology to structural differences between homo- and heteroepitaxial systems. Further understanding of underlying physical phenomena defining mechanical properties of nanowires requires the use of structural analysis techniques such as TEM. However, the presented approach can be used to optimize the growth conditions of nanowires and improve technologies for creating optoelectronic devices based on them.

Acknowledgments

The epitaxial growth of nanostructures was supported by the Ministry of Science and Higher Education (Project № FSEG-2024-0017). The probe experiments were supported by the Ministry of Science and Higher Education (Project № FSRM-2026-0004).

REFERENCES

1. **Kuznetsov A., Moiseev E., Abramov A.N., Fominykh N., Sharov V.A., Kondratev V.M., Khrebtov A.I., Kulagina A.S., Bolshakov A.D.,** Elastic gallium phosphide nanowire optical waveguides–versatile subwavelength platform for integrated photonics, Small. 19 (28) (2023) 2301660.

2. **Jansson M., Ishikawa F., Chen W.M., Buyanova I.A.,** Designing Semiconductor Nanowires for Efficient Photon Upconversion via Heterostructure Engineering, ACS Nano. 16 (8) (2022) 12666–12676.

3. **Li Z., Azimi Z., Li Z., Yu Y., Huang L., Jin W., Tan H. H., Jagadish C., Wong-Leung J., Fu L.,** InAs nanowire arrays for room-temperature ultra-broadband infrared photodetection, Nanoscale. 15 (2023) 10033–10041.

4. **Anyebe E.A., Kesaria M.,** Recent advances in the Van der Waals epitaxy growth of III-V semiconductor nanowires on graphene, Nano Select. 2 (4) (2021) 688–711.

5. **Mukherjee A., Ren D., Vullum P. E., Huh J., Fimland B.O., Weman H.,** GaAs/AlGaAs nanowire array solar cell grown on Si with ultrahigh power-per-weight ratio, ACS Photonics. 8 (8) (2021) 2355–2366.

6. **Lin C.C., Wu Y.R., Kuo H.C., Wong M.S., DenBaars S.P., Nakamura S., Speck J.S., Ooi B.S., He J.H., Fang Y.H.,** The micro-LED roadmap: status quo and prospects, Journal of Physics: Photonics. 5 (4) (2023) 042502.

7. **Sharov V.A., Malysh M.A., Fedorov V.V., Kaveev A.K., Kirilenko D., Mukhin I.S.,** Structure and mechanical strength of the interface between epitaxial III–V nanowires and Si substrate, Applied Surface Science. (2025) 165505.

THE AUTHORS

LUTSEVICH Marina A.
malysh_ma@spbau.ru
ORCID: 0009-0005-4691-104X

SHAROV Vladislav A.
vl_sharov@mail.ru
ORCID: 0000-0001-9693-5748

KAVEEV Andrey K.
kaveev@mail.ioffe.ru

FEDOROV Vladimir V.
fedorov_vv@spbstu.ru
ORCID: 0000-0001-5547-9387

MUKHIN Ivan S.
muhin_is@spbstu.ru

Received 15.12.2025. Approved after reviewing 16.03.2026. Accepted 26.03.2026.

© Peter the Great St. Petersburg Polytechnic University, 2026

Conference paper
UDC 53.093
DOI: https://doi.org/10.18721/JPM.191.113

Perovskite microwires generating red laser emission

D.A. Tatarinov [1,2]✉, E.V. Sapozhnikova [1,2], D.A. Semenov [1], A.P. Pushkarev [2]

[1] ITMO University, St. Petersburg, Russia;

[2] Skolkovo Institute of Science and Technology, Moscow, Russia

✉ dmitry.tatarinov@metalab.ifmo.ru

Abstract. Sources of stimulated coherent emission in all visible range are highly demanded for numerous applications in photonic and optoelectronic devices. In that regard, metal halide perovskite-based microlasers are established to be promising objects due to their low-threshold and lasing with high quality factor (more than 1000) at room temperature. However, there are still challenges in synthesis of stable and uniform crystals emitting red light. This work presents a novel sublimation synthesis method to produce mixed-anion perovskite $CsPb(Br,I)_3$ microwires that generate laser emission in red region of visible range. An increase in the iodine content in the structure contributes to a red-shift in photoluminescence from 530 nm to 680 nm. $CsPb(Br,I)_3$ microwires demonstrate multimode laser generation with threshold at 70 mJ/cm^2 and Q-factor near 1500. A uniform distribution of bromine and iodine ions in the structure is confirmed by energy dispersive x-ray analysis. Additionally, study of surface morphology by scanning electron microscopy showed core-shell like structure, which can improve long-term stability of obtained crystals. Our study reveals the sublimation as a promising synthesis method to produce low-threshold red microlasers that emit light at room temperature.

Keywords: halide perovskites, lasing, sublimation, red-shift, photoluminescence

Funding: The work was supported by the Russian Science Foundation (project 24-73-10072).

Citation: Tatarinov D.A., Sapozhnikova E.V., Semenov D.A., Pushkarev A.P., Perovskite microwires generating red laser emission, St. Petersburg State Polytechnical University Journal. Physics and Mathematics. 19 (1.1) (2026) 81–85. DOI: https://doi.org/10.18721/JPM.191.113

This is an open access article under the CC BY-NC 4.0 license (https://creativecommons.org/licenses/by-nc/4.0/)

Конференционная статья
УДК 53.093
DOI: https://doi.org/10.18721/JPM.191.113

Перовскитные нитевидные микрокристаллы, генерирующие лазерное излучение в красном диапазоне

Д.А. Татаринов [1,2]✉, Е.В. Сапожникова [1,2], Д.А. Семёнов [1], А.П. Пушкарёв [2]

[1] Университет ИТМО, Санкт-Петербург, Россия;

[2] Сколковский институт науки и технологий, Москва, Россия.

✉ dmitry.tatarinov@metalab.ifmo.ru

Аннотация. Источники стимулированного когерентного излучения во всем видимом диапазоне крайне востребованы для многочисленных применений в фотонных и оптоэлектронных устройствах. В этом отношении, микролазеры на основе металлогалогенидных перовскитов зарекомендовали себя как перспективные объекты благодаря низкопороговому и высокодобротному излучению (с показателем добротности больше 1000) при комнатной температуре. Однако до сих пор существуют проблемы с синтезом стабильных и однородных кристаллов, излучающих в красном диапазоне. В данной работе представлен новый метод сублимационного синтеза для создания нитевидных смешанно-анионных перовскитных

© Tatarinov D.A., Sapozhnikova E.V., Semenov D.A., Pushkarev A.P., 2026. Published by Peter the Great St. Petersburg Polytechnic University.

микрокристаллов $CsPb(Br,I)_3$, генерирующих лазерное излучение в красной области видимого спектра. Увеличение содержания иода в структуре способствует сдвигу фотолюминесценции в красную область спектра от 530 нм до 680 нм. Микрокристаллы $CsPb(Br,I)_3$ демонстрируют многомодовую генерацию лазерного излучения с порогом 70 мДж/см^2 и добротностью около 1500. Равномерное распределение ионов брома и иода в структуре подтверждается энергодисперсионным рентгеновским анализом. Кроме того, исследование морфологии поверхности кристалла с помощью сканирующей электронной микроскопии показывает наличие структуры типа «ядро-оболочка», что может улучшить долговременную стабильность полученных кристаллов. Наше исследование показывает, что сублимация является перспективным методом синтеза для получения низкопороговых красных микролазеров, излучающих свет при комнатной температуре.

Ключевые слова: галогендные перовскиты, лазерная генерация, сублимация, смещение в красную область, фотолюминесценция

Финансирование: Работа выполнена при поддержке Российского Научного Фонда (проект 24-73-10072).

Ссылка при цитировании: Татаринов Д.А., Сапожникова Е.В., Семёнов Д.А., Пушкарёв А.П. Перовскитные нитевидные микрокристаллы, генерирующие лазерное излучение в красном диапазоне // Научно-технические ведомости СПбГПУ. Физико-математические науки. 2026. Т. 19. № 1.1. С. 81–85. DOI: https://doi.org/10.18721/JPM.191.113

Статья открытого доступа, распространяемая по лицензии CC BY-NC 4.0 (https://creativecommons.org/licenses/by-nc/4.0/)

Introduction

Perovskite crystals possess a number of outstanding properties, such as a low concentration of lattice defects, a high optical absorption coefficient, and a high luminescence quantum yield at room temperature [1]. In addition, microstructures can be fabricated in various resonant shapes, which enables generation of lasing emission in crystals [2]. Microscale sources of stimulated emission are highly demanded for application in various optoelectronic and photonic devices. For inorganic metal halide perovskite (MHP) crystals of the $CsPbBr_3$ composition the emission spectrum may be tuned by partial replacement of the halogen ions. The introduction of Cl^- or I^- ions instead of Br^- leads to a shift in the luminescence spectrum towards the blue or red region, respectively. However, due to the high mobility of iodine ions and its interaction with oxygen and water molecules in atmosphere, mixed crystals of this composition are highly unstable [3]. That results in formation of uneven distribution of Br^--rich and I^--rich domains under prolonged optical or electrical pump. Hence it leads to the shift of luminescence spectrum or the appearance of additional emission peak [4]. Such instability of spectra is especially pronounced for mixed-iodine crystals that are synthesized at rather low temperatures (below 100 °C) through anion exchange where the source of halogen is gas [5] or another pure iodine structure [6] as the migration process mainly happens at the surface level. In this work, the new sublimation method was employed for creating microstructures that exhibit narrow and smooth photoluminescence peak at room temperature in red range. Here, the crystals are synthesized at higher temperatures which facilitates the I^- ions uniform diffusion within all crystal volume and the additional shell-like layer of PbI_2 protects perovskite from the external environment.

Materials and Methods

Two types of solutions were prepared to produce polycrystalline perovskite source-substrates. They were obtained by dissolving CsBr, $PbBr_2$ and PbI_2 powders in dimethyl sulfoxide to produce pure solutions with 0.3 M for $CsPbBr_3$ and 0.075 M for PbI_2. At the beginning, 2 types of sources for subsequent synthesis of microwires (MWs) by sublimation technique were prepared. Firstly, the $CsPbBr_3$ solution was drop-cast on a glass substrate and placed in a petri dish in isopropyl vapor at 100 °C for 10 minutes to form $CsPbBr_3$ crystals. Secondly, the same protocol was repeated

© Татаринов Д.А., Сапожникова Е.В., Семёнов Д.А., Пушкарёв А.П., 2026. Издатель: Санкт-Петербургский политехнический университет Петра Великого.

for the PbI_2 solution. In this work, glass substrates coated with $CsPbBr_3/PbI_2$ microcrystals were used as the source substrate, and a mica substrate was used as the receiver substrate. Source substrate was placed on a high-temperature plate and a receiver substrate was fixed on top of it at a 2.5 cm distance. Initially, the $CsPbBr_3$ substrate was used as a source to create microwires on the mica, and later lead iodide was evaporated onto the resulting microwires, thereby allowing the formation of mixed $CsPb(Br,I)_3$ microstructures. After that the samples were cooled down to room temperature.

The surface morphology and elemental analysis of obtained mixed-anion perovskite microwires were studied by a scanning electron microscopy (SEM) method and energy-dispersive X-ray (EDX) analysis (FEI Quanta Inspect). The bright-field and luminescent images of $CsPb(Br,I)_3$ MWs with different iodide concentration were obtained by C.Z.A Imager 2 microscope (Carl Zeiss). The photoluminescence spectra were measured on a QE-Pro spectrometer (Ocean Optics) coupled to microscope with optical fiber. Lasing properties of single microwire were studied under femtosecond laser excitation (Antaus, Avesta) with pulse width τ = 150 fs at a wavelength of 515 nm and 10 kHz repetition rate. The laser beam was focused onto the sample surface at normal incidence by a microscope objective (50×, NA = 0.42) aligned to provide uniform irradiation of the microwires (Gaussian distribution with an FWHM of ≈ 20 μm). The signal was separated from pump via long-pass dichroic mirror (cut-off wavelength of 550 nm) and registered on a spectrometer (Andor Kymera 328i, Oxford instruments) equipped with a cooled electron multiplying CCD camera. All measurements were performed at normal conditions and reproduced several times.

Results and Discussion

Arrays of synthesized microwires were visualized by bright-field images from optical microscope. The produced crystals varied in cross-section size and total length (5 to 20 microns) (Fig. 1, *a*). In addition, the fluorescent images show homogeneous luminescence of crystals (Fig. 1, *b*). The EDX mapping analysis revealed uniform distribution of elements within the crystal which indicates its structural stability (Fig. 1, *c*). The photoluminescence spectrum of the MW was 577 nm, which corresponded to 16% of iodine concentration in the structure. Notably, it was discovered that iodine deposition creates a so-called 'coat' over the obtained $CsPbBr_3$ microwires,

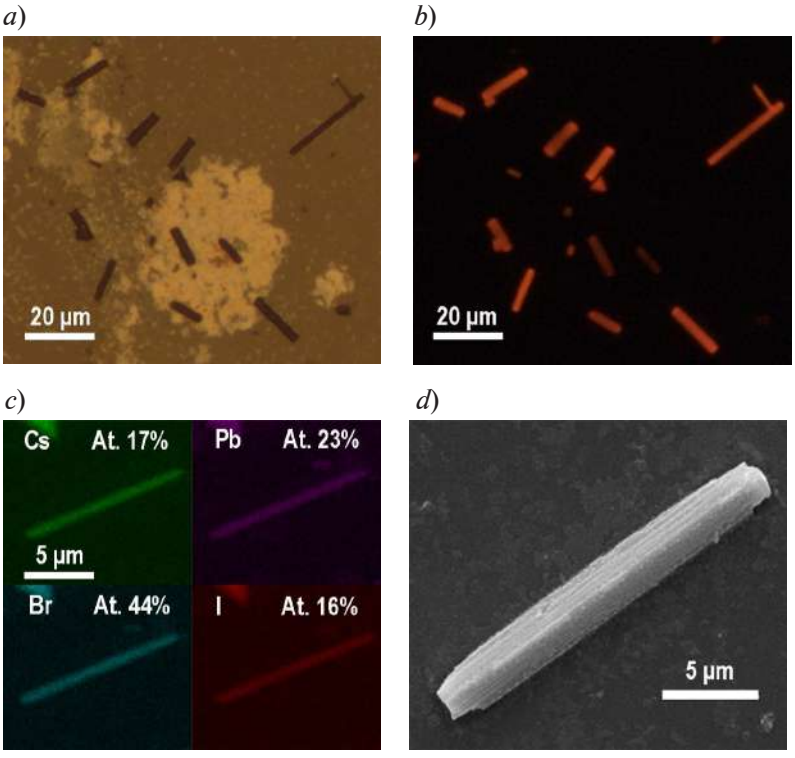

Fig. 1. Characterization of mixed-anion $CsPb(Br,I)_3$ microwires: bright-field (*a*) and fluorescent (*b*) images of obtained microwires; EDX mapping of single MW (*c*); SEM-image of a single MW (*d*)

as clearly seen in the SEM image (Fig. 1, *d*). We suggest that the produced mixed MWs possess a core-shell-like structure, where the iodine-based 'shell' protects perovskite 'core' from oxygen and moisture, thereby making them more stable over time.

A comparison of optical properties of obtained mixed-anion microwires was made by measuring photoluminescence (PL) spectra (Fig. 2, *a*). For the reference microwire without iodine, the photoluminescence peak was 530 nm. A subsequent increase of the iodine concentration in the structures allows one to observe a red shift in the photoluminescence spectra (see Fig. 2, *b* for a visual representation). At the point of maximum iodine concentration, the photoluminescence peak is located at a wavelength of 680 nm. The difference in the full width at half maximum of the measured photoluminescence spectra can be explained by the difference in the lateral dimensions of the mixed perovskite microwires.

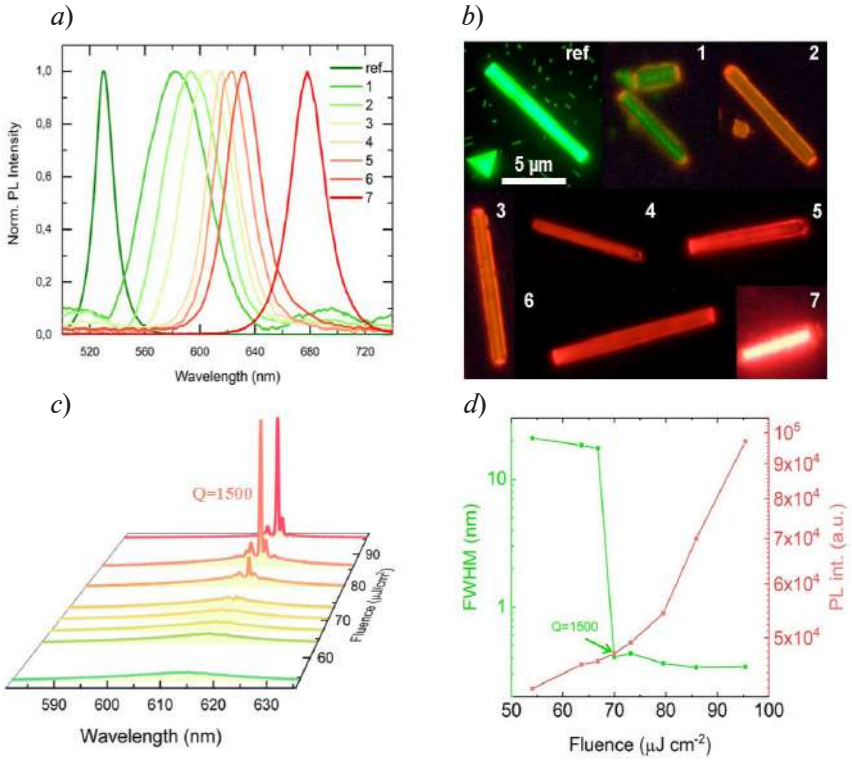

Fig. 2. Optical characterization of $CsPb(Br,I)_3$ microwires: photoluminescence spectra of isolated microwires 1–7 found at different locations on the substrate (*a*); fluorescent images of microwires 1–7, respectively (*b*); photoluminescence spectra for $CsPb(Br,I)_3$ microwire at different intensities below and after the lasing threshold (*c*); intensity and full-width-half-maximum (FWHM) of emission spectrum of the microwire at the lasing wavelength (*d*)

To demonstrate the lasing properties of MWs, they were pumped by a femtosecond laser emission. Fig. 2, *c* reveals the spectral evolution of PL with the increase of the laser pump fluence for a single mixed-anion perovskite microwire with lateral size 15 μm. It worth noting that there was no PL spectral split contributed to iodine migration, which confirms the stability of luminescence in crystals. The observed behavior demonstrates all basic lasing features: clear lasing threshold at fluence = 70 $\mu J/cm^2$ and its sharp spectral narrowing by two orders of magnitude at the red wing ($\lambda = 620–625$ nm) of excitonic PL spectra as shown in Fig. 2, *d*. Quality factor (Q) of the most intense lasing mode was estimated to be 1500 and calculated as $Q = \lambda/\Delta\lambda$, where λ is the mode center wavelength and $\Delta\lambda$ is the mode width.

Conclusion

In this work we presented a novel synthesis method of mixed-anion $CsPb(Br,I)_3$ perovskite microwires which demonstrated laser generation in red region of visible range. The obtained perovskite microwires showed a stable peak of photoluminescence without any shifts throughout

all experiments at room temperature. Lasing threshold was estimated to be 70 μJ/cm^2 with quality factor near 1500. Produced structures can be used in optoelectronic and photonic devices, which require stable photoluminescence and laser emission.

Acknowledgments

The work was supported by the Russian Science Foundation (project 24-73-10072).

REFERENCES

1. **Dey A. et al.,** State of the Art and Prospects for Halide Perovskite Nanocrystals. ACS nano. 15 (2021) 10775–10981.

2. **Shi Y., Deng X., Gan Y., Xu L., Zhang Q., Xiong Q.,** Ten Years of Perovskite Lasers. Advanced Materials. 37 (2025) 2413559.

3. **Hidalgo J. et al.,** Synergistic role of water and oxygen leads to degradation in formamidinium-based halide perovskites. Journal of the American Chemical Society. 145 (2023) 24549–24557.

4. **Brennan M.C., Draguta S., Kamat P.V., Kuno M.,** Light-Induced Anion Phase Segregation in Mixed Halide Perovskites. ACS Energy Letters. 1 (2017) 204–213.

5. **Markina D. I. et al.,** Photophysical properties of halide perovskite $CsPb(Br_{1-x}I_x)_3$ thin films and nanowires. Journal of Luminescence. 220 (2020) 116985.

6. **Li J. et al.,** Ultralong compositional gradient perovskite nanowires fabricated by source-limiting anion exchange. ACS nano. 18 (2024) 30978–30986.

THE AUTHORS

TATARINOV Dmitry A.
dmitry.tatarinov@metalab.ifmo.ru
ORCID: 0000-0002-4825-9041

SAPOZHNIKOVA Elizaveta V.
e.sapozhnikova@metalab.ifmo.ru
ORCID: 0009-0000-2732-6711

SEMENOV Dmitry A.
dmitrii.semenov@metalab.ifmo.ru

PUSHKAREV Anatoly P.
an.pushkarev@skoltech.ru
ORCID: 0000-0002-1793-6812

Received 15.12.2025. Approved after reviewing 19.01.2026. Accepted 27.01.2026.

© Peter the Great St. Petersburg Polytechnic University, 2026

Optoelectronic and nanoelectronic devices

Conference paper
UDC 621.373.826
DOI: https://doi.org/10.18721/JPM.191.114

Beam divergence of surface-emitting semiconductor laser with resonator based on two-dimensional photonic crystal

A.S. Nekrasov [1,2]✉, V.V. Zolotarev [1], I.V. Oreshko [1], S.O. Slipchenko [1], N.A. Pikhtin [1]

[1] Ioffe Institute, St. Petersburg, Russia;
[2] Peter the Great St. Petersburg Polytechnic University, St. Petersburg, Russia
✉ nekrasov.74as@gmail.com

Abstract. Theoretical calculations of the resonator modes optical characteristics of a semiconductor surface-emitting laser with a resonator based on a two-dimensional photonic crystal with a square lattice were carried out in the paper. Photonic crystal provides distributed feedback in plane of heterostructure layers and determines diffraction of radiation to the surface of the laser structure. Output beam emitted in the direction normal to the surface of such devices allows decreasing the beam divergence and increasing the output optical power. However, an increase in radiation aperture also affects the mode composition of the laser emission. The dependences of resonator modes optical losses and beam divergence on cavity size were obtained. A suggestion of the optimal cavity length to achieve single-mode operation with small output laser beam divergence angle was made.

Keywords: photonic crystal, surface-emitting laser, semiconductor laser, resonator, beam divergence

Citation: Nekrasov A.S., Zolotarev V.V., Oreshko I.V., Slipchenko S.O., Pikhtin N.A., Beam divergence of surface-emitting semiconductor laser with resonator based on two-dimensional photonic crystal, St. Petersburg State Polytechnical University Journal. Physics and Mathematics. 19 (1.1) (2026) 86–91. DOI: https://doi.org/10.18721/JPM.191.114

This is an open access article under the CC BY-NC 4.0 license (https://creativecommons.org/licenses/by-nc/4.0/)

Конференционная статья
УДК 621.373.826
DOI: https://doi.org/10.18721/JPM.191.114

Расходимость лазерного пучка вертикально-излучающего полупроводникового лазера с резонатором на основе двумерного фотонного кристалла

А.С. Некрасов [1,2]✉, В.В. Золотарев [1], И.В. Орешко [1], С.О. Слипченко [1], Н.А. Пихтин [1]

[1] Физико-технический институт им. А.Ф. Иоффе РАН, Санкт-Петербург, Россия;
[2] Санкт-Петербургский политехнический университет Петра Великого, Санкт-Петербург, Россия
✉ nekrasov.74as@gmail.com

Аннотация. В данной работе проведены теоретические расчеты оптических характеристик полупроводникового поверхностно-излучающего лазера с резонатором на основе двумерного фотонного кристалла квадратной симметрии. Фотонный кристалл обеспечивает распределенную положительную обратную связь и дифракцию излучения в направлении нормали поверхности лазерного чипа. Вывод излучения через поверхность позволяет уменьшить расходимость пучка выходного излучения, увеличение апертуры приводит к увеличению выходной оптической мощности.

© Nekrasov A.S., Zolotarev V.V., Oreshko I.V., Slipchenko S.O., Pikhtin N.A., 2026. Published by Peter the Great St. Petersburg Polytechnic University.

Однако, увеличение размеров резонатора также влияет на модовый состав излучения. Были получены зависимости оптических потерь резонаторных мод и расходимости пучка от апертуры излучения. Были подобраны оптимальные размеры резонатора для обеспечения одномодового режима работы при малой расходимости пучка выходного излучения.

Ключевые слова: фотонный кристалл, поверхностно-излучающий лазер, полупроводниковый лазер, резонатор, расходимость пучка

Ссылка при цитировании: Некрасов А.С., Золотарев В.В., Орешко И.В., Слипченко С.О., Пихтин Н.А. Расходимость лазерного пучка вертикально-излучающего полупроводникового лазера с резонатором на основе двумерного фотонного кристалла // Научно-технические ведомости СПбГПУ. Физико-математические науки. 2026. Т. 19. № 1.1. С. 86–91. DOI: https://doi.org/10.18721/JPM.191.114

Статья открытого доступа, распространяемая по лицензии CC BY-NC 4.0 (https://creativecommons.org/licenses/by-nc/4.0/)

Introduction

Ridge semiconductor lasers have a highly asymmetric wide radiation pattern and multi-mode operation [1], which complicates their application in optoelectronics since expensive collimating optics are required. This problem can be solved by outputting radiation through the surface of a laser device, which is implemented in vertical cavity surface-emitting lasers (VCSELs) [2]. However, VCSELs have a small aperture size due to the design features of the resonator, which limits the high optical output power. Because of this, photonic crystal (PC) surface-emitting lasers (SEL) are developed [3–6], which enabled single-mode high-power output laser emission with symmetrical narrow beam.

Distributed feedback and diffraction to the direction normal to the surface of the device are provided by forming two-dimensional (2D) PC in the heterostructure layers [7]. Optical characteristics of such devices depend on sizes of the resonator, therefore it is important to study this effect.

In this paper theoretical calculation of the mode composition of the resonator based on square lattice 2D-PC has been made. PC is formed by air holes in the layer of heterostructure GaAs/AlGaAs/InGaAs, emitting at a wavelength of 1005 nm. The analysis of dependences of resonator modes optical losses and directional pattern on size of the radiation aperture are carried out.

Materials and Methods

In this paper we studied the heterostructure GaAs/AlGaAs with 3 quantum wells InGaAs. Generated in active layer emission is TE polarized, that is typical for InGaAs. Square lattice PC is formed by air holes in the shape of a right isosceles triangle (RIT) in one of the heterostructure layers (Fig. 1, *a*).

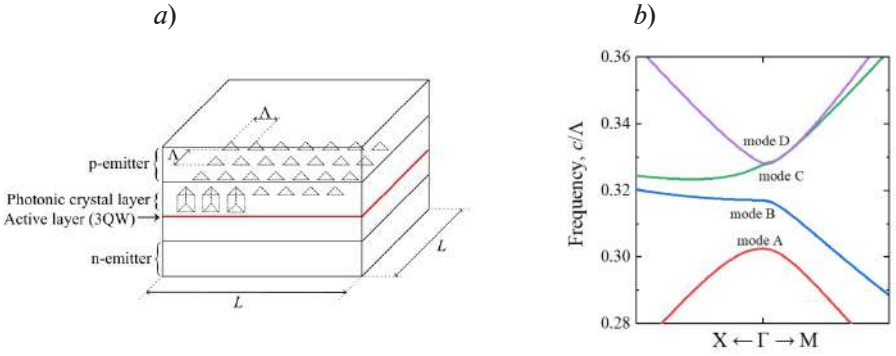

Fig. 1. Schematic structure of SEL device with resonator based on square lattice PC (*a*); typical photonic band structure for square lattice PC with RIT holes (*b*)

© Некрасов А.С., Золотарев В.В., Орешко И.В., Слипченко С.О., Пихтин Н.А., 2026. Издатель: Санкт-Петербургский политехнический университет Петра Великого.

PC lattice constant Λ = 300 nm is chosen to satisfy the second-order Bragg's condition, and the holes, whose size is characterized by fill factor $f = S_{air\,hole}/S_{u.c.}$, have f = 22.2%. Calculations of photonic band structure for infinite size square lattice PC shows that in second order Γ-point there are four band-edge modes [8]. We call these modes A, B, C, D (Fig. 1, *b*) in order of increasing frequency.

In order to make the necessary calculations of the resonator's optical characteristics, we utilized coupled-wave model [9]. We will highlight peculiarities of this method: we consider TE polarized wave, for which we have wave equation

$$\nabla \times \nabla \times \vec{E}(\vec{r}) = k_0^2 \tilde{n}^2(\vec{r}) \vec{E}(\vec{r}) \tag{1}$$

where $\tilde{n}(\vec{r})$ is the complex refractive index, k_0 is the wavevector of the light in the vacuum. The TE polarization field $\vec{E}(\vec{r}) = (E_x(\vec{r}), E_y(\vec{r}), 0)$ can be expanded in PC due to Bloch theorem:

$$E_i(z) = \sum E_{i,m,n}(z) \exp(-im\beta_0 x - in\beta_0 y),\ i = x, y, \tag{2}$$

where m, n are integers, $\beta_0 = 2\pi/\Lambda$ is the reciprocal lattice vector. The real part of the refractive index can be expanded into a Fourier sum

$$n^2(\vec{r}) = n_0^2(z) + \sum_{m \neq 0, n \neq 0} \xi_{m,n}(z) \exp(-im\beta_0 x + in\beta_0 y), \tag{3}$$

where Fourier coefficients are expressed as

$$\xi_{m,n} = \frac{1}{\Lambda^2} \iint_{PC} \Delta n^2(x, y) \exp(im\beta_0 x + in\beta_0 y) dx dy \tag{4}$$

and equal zero outside of the PC layer. Waves from expansion (2) can be classified based on their wavenumber $\sqrt{m^2 + n^2}\beta_0$: basic waves ($m^2 + n^2 = 1$), radiative waves ($m = 0$, $n = 0$) and high-order waves ($m^2 + n^2 > 1$). In the approximation of this model, is suggested that radiative and high-order waves are stimulated by basic waves. The solution of the wave equation (1) for basic waves is reduced to the problem

$$(\delta + i\alpha) \begin{pmatrix} R_x \\ S_x \\ R_y \\ S_y \end{pmatrix} = C \begin{pmatrix} R_x \\ S_x \\ R_y \\ S_y \end{pmatrix} + i \begin{pmatrix} \partial R_x / \partial x \\ -\partial S_x / \partial x \\ \partial R_y / \partial y \\ -\partial S_y / \partial y \end{pmatrix}, \tag{5}$$

where δ is the deviation of the wavevector from Bragg's wavevector, α is the optical losses, $R_x(x, y)$, $S_x(x, y)$, $R_y(x, y)$, $S_y(x, y)$ – amplitudes of the basic waves propagating in the $+x$, $-x$, $+y$, $-y$ directions accordingly, $C = C_{1D} + C_{rad} + C_{2D}$, C_{1D}, C_{rad}, C_{2D} – matrices, which correspond to one-dimensional coupling, radiative and basic waves coupling, two-dimensional optical coupling accordingly. Problem (5) can be solved using staggered grid finite-difference method with boundary conditions:

$$R_x(0, y) = S_x(L, y) = R_y(x, 0) = S_y(x, L) = 0, \tag{6}$$

where L is length of the square resonator (and, accordingly, the radiation apertures). Thereby we obtain set of optical losses of the resonator modes and relative to them values of the basic waves' amplitudes in the grid nodes. We can obtain radiation intensity distribution in near and far fields of the specific mode by utilizing amplitudes of the basic waves [9].

Results and Discussion

In case of RIT holes, modes C and D have much higher threshold losses compared with modes A and B [8], therefore we excluded them from further consideration. We calculated intensity distribution in near and far fields for resonator modes $A_1, L_{1,2}^{A_2}, A_2$ (L = 200 μm, Fig. 2) and $B_1, L_{1,2}^{B_2}, B_2$ (L = 200 μm, Fig. 3) at different cavity lengths. Fundamental modes A_1 and B_1 are characterized by the presence of a single maximum in the center (or close to the center)

of the intensity distribution (Fig. 2, *a*, *b*, Fig. 3, *a*, *b*), the smallest beam divergence in their group, and a symmetrical radiation pattern. In contrast, high-order modes have several intensity maximums, which slightly deviate from the normal to the lasing surface (Fig. 2, *c*–*h*, Fig. 3, *c*–*h*), that complicates the use of the device. Additionally, high-order modes electromagnetic fields penetrate the boundaries more than fields of fundamental modes, which correspond to higher parasitic losses.

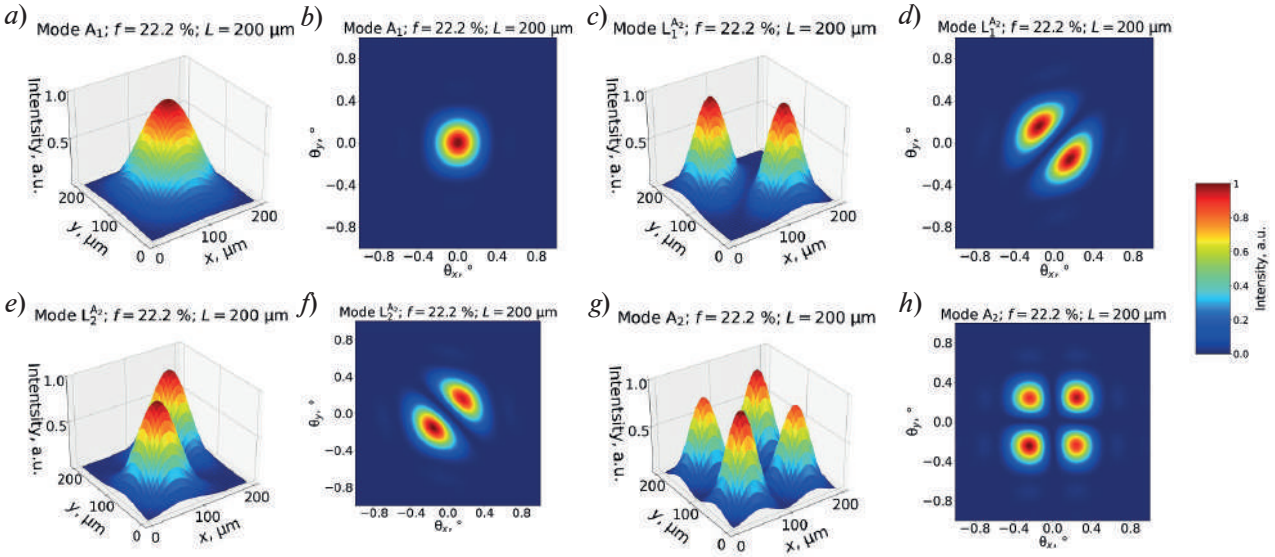

Fig. 2. Radiation intensities of group A resonator modes in near field for fundamental mode A_1 (*a*) and high-order modes $L_1^{A_2}$ (*c*), $L_2^{A_2}$ (*e*), A_2 (*g*) and in far field for A_1 (*b*), $L_1^{A_2}$ (*d*), $L_2^{A_2}$ (*f*), A_2 (*h*). $f = 22.2\%$, $L = 200$ μm

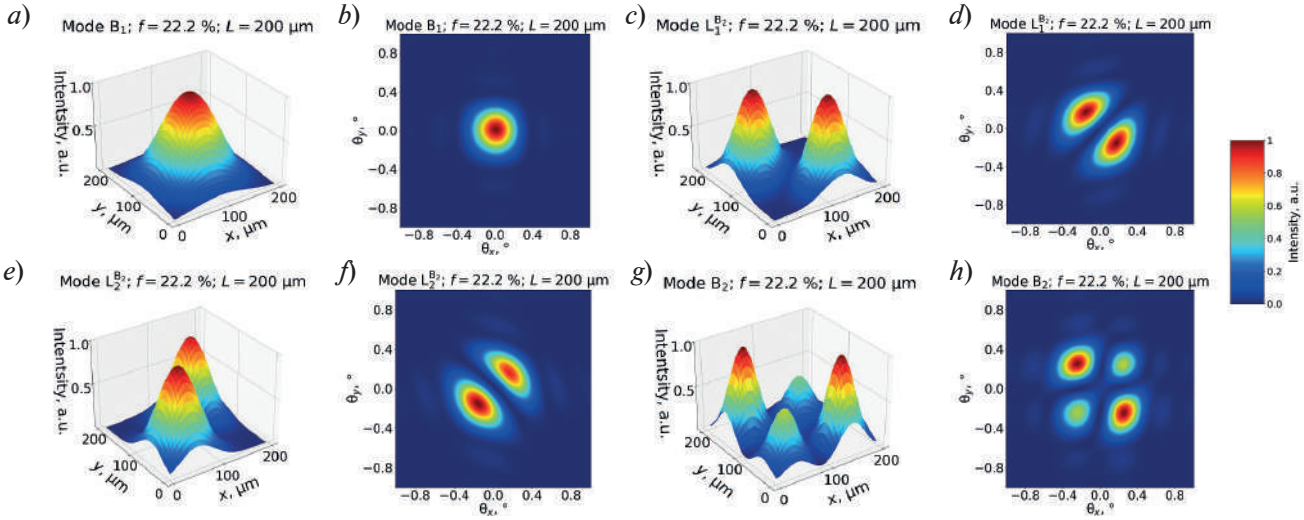

Fig. 3. Radiation intensities of group B resonator modes in near field for fundamental mode B_1 (*a*) and high-order modes $L_1^{B_2}$ (*c*), $L_2^{B_2}$ (*e*), B_2 (*g*) and in far field for B_1 (*b*), $L_1^{B_2}$ (*d*), $L_2^{B_2}$ (*f*), B_2 (*h*). $f = 22.2\%$, $L = 200$ μm

Using the A_1 mode, we will show the typical changes in the distribution of the radiation intensity of the modes with the change in the size of aperture. PC with holes in the shape of a RIT is characterized by an asymmetry in the intensity envelopes relative to the plane $y = L - x$, which is parallel to the triangle hypotenuse and perpendicular to the plane of the layer. This is especially noticeable at small cavity sizes: at $L = 50$ μm (Fig. 4, *a*) electromagnetic wave penetrates strongly into the boundaries $x = 0$ and $y = 0$ in comparison to $x = L$ and $y = L$. This leads to reduction in the symmetry of the intensity distribution in far field (Fig. 4, *d*). Increase of resonator length leads to enhancing symmetry of intensity distribution in near and far field (Fig. 4, *b*, *c*, *e*, *f*),

because of propagating in plane of PC layer wave manages to fully interact with PC holes, that also provides improvement of resonator properties. Besides this, increase of the radiation aperture leads to narrowing of the output beam in far field: at L = 50 μm, full width at half maximum FWHM = 1.33°, at L = 200 μm, FWHM = 0.35°, at L = 400 μm, FWHM = 0.17°. A similar situation is observed for mode B_1.

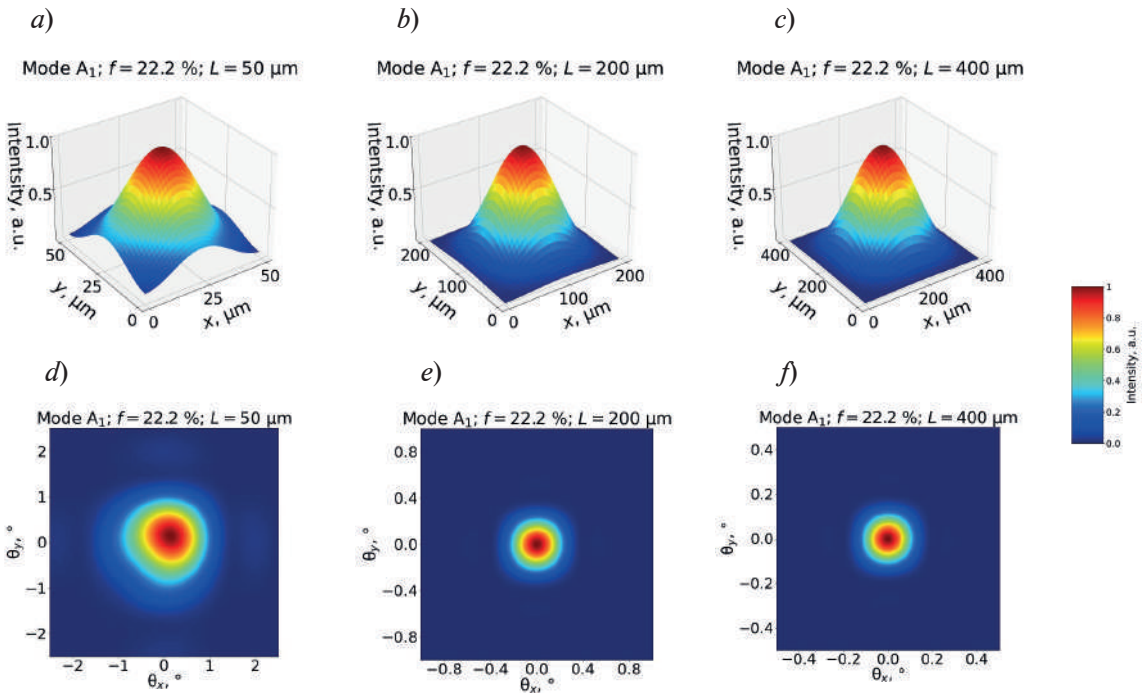

Fig. 4. Radiation intensity distributions of mode A_1 in near field at L = 50 μm (*a*), L = 200 μm (*b*), L = 400 μm (*c*) and in far field at L = 50 μm (*d*), L = 200 μm (*e*), L = 400 μm (*f*)

However, increase of the cavity length leads to weakening of mode discrimination, which is shown in the dependence of resonator modes optical losses on cavity length at Fig. 5, *a*. Thus, mode selection has a value of 100 cm^{-1} at L = 50 μm, and 4 cm^{-1} at L = 400 μm. Meeting the threshold generation condition for several modes will lead to a loss of single-mode operation, and the generation of high-order modes will lead to a significant increase in the divergence of the output beam (Fig. 5, *b*), as well as to loss of the beam pattern symmetry. It is also important to note that a change of the lowest threshold mode ($A_1 \rightarrow B_1$) occurs at L = 140 μm.

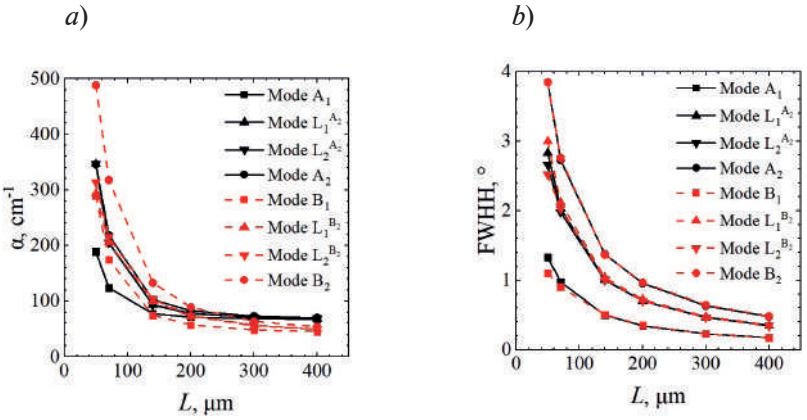

Fig. 5. Resonator modes optical losses dependence on cavity length (*a*). Beam divergence angle dependence on radiation aperture (*b*)

Conclusion

We have made theoretical calculations of dependences of radiation pattern on cavity length for SEL with resonator based on square lattice PC. The results show that growth of the radiation aperture leads to decrease of beam divergence angle, along with improvement of pattern symmetry. However, this also provides weakening of mode composition selection, as a result, single-mode operation is lost. Based on the results we can suggest optimal cavity length for studied heterostructure, which saves single-mode operation, but provides small beam divergence, specifically at $L = 200$ μm mode discrimination has large enough value of 14 cm^{-1}, and threshold mode B_1 radiation has beam divergence angle of 0.35°.

REFERENCES

1. **Shashkin I.S. et al.,** Light characteristics of narrow-stripe high-power semiconductor lasers (1060 nm) based on asymmetric AlGaAs/GaAs heterostructures with a broad waveguide, Semiconductors. 54 (4) (2020) 408–413.

2. **Peng C.Y., Tsao K., Cheng H.T., Feng M., Wu C.H.,** Investigation of the current influence on near-field and far-field beam patterns for an oxide-confined vertical-cavity surface-emitting laser, Optics Express. 28 (2020) 30748–30759

3. **Imada M., Noda S., Chutinan A., Tokuda T., Murata M., Sasaki G.,** Coherent two-dimensional lasing action in surface-emitting laser with triangular-lattice photonic crystal structure, Appl. Phys. Lett. 75 (1999) 316–318.

4. **Noda S., Yokoyama M., Imada M., Chutinan A., Mochizuki M.,** Polarization mode control of two-dimensional photonic crystal laser by unit cell structure design, Science. 293 (2001) 1123–1125.

5. **Vurgaftman I., Meyer J.R.,** Design optimization for high-brightness surface-emitting photonic-crystal distributed-feedback lasers, IEEE J. Quantum Electron. 39 (2003) 689–700.

6. **Hirose K., Liang Y., Kurosaka Y., Watanabe A., Sugiyama T., Susumu Noda S.,** Watt-class high-power, high-beam-quality photonic-crystal lasers, Nature Photonics. 8 (2014) 406–411.

7. **Liang Y., Peng C. Sakai K., Iwahashi S., Noda S.,** Three-dimensional coupled-wave model for square-lattice photonic crystal lasers with transverse electric polarization: A general approach, Physical Review. 84 (2011) 195119.

8. **Oreshko I.V., Zolotarev V.V., Slipchenko S.O., Kazakova A.E., Pikhtin N.A.,** Resonators of IR lasers based on two-dimensional photonic crystals for organization of surface output of radiation, Semiconductors. 59 (2) (2025) 109–116.

9. **Liang Y., Peng C., Sakai K., Iwahashi S., Noda S.,** Three-dimensional coupled-wave analysis for square-lattice photonic crystal surface emitting lasers with transverse-electric polarization: finite-size effects, Optics Express. 20 (14) (2012) 15945–15961.

THE AUTHORS

NEKRASOV Aleksey S.
nekrasov.74as@gmail.com

ZOLOTAREV Vasily V.
zolotarev.bazil@mail.ioffe.ru

ORESHKO Ivan V.
ioreshko@mail.ioffe.ru

SLIPCHENKO Sergey O.
serghpl@mail.ioffe.ru
ORCID: 0000-0003-4851-3641

PIKHTIN Nikita A.
nike@hpld.ioffe.ru

Received 16.12.2025. Approved after reviewing 10.02.2026. Accepted 12.02.2026.

© Peter the Great St. Petersburg Polytechnic University, 2026

Conference paper
UDC 534-16
DOI: https://doi.org/10.18721/JPM.191.115

Band structure of PT-symmetric phononic crystals

Z.M. Yashkin ✉, M.V. Zakharchenko, G.F. Glinskii

St. Petersburg Electrotechnical University "LETI", St. Petersburg, Russia;
✉ a3691215@yandex.ru

Abstract. In the present paper, the theory of phononic crystals is generalized to the case of periodic media with anisotropic elastic properties, as well as to the PT-symmetric structures with gain and loss. An operator form of the equation for a stationary elastic wave in a crystal is proposed. A generalized condition of PT symmetry for systems with anisotropic elastic properties is obtained.

Keywords: phononic crystal, PT symmetry, exceptional points

Funding: The study was carried out within the project FSEE-2025-0007 (state assignment of the Ministry of Science and Higher Education of the Russian Federation 075-00003-25-00 dated 12.25.2024).

Citation: Yashkin Z.M., Zakharchenko M.V., Glinskii G.F., Band structure of PT-symmetric phononic crystals, St. Petersburg State Polytechnical University Journal. Physics and Mathematics. 19 (1.1) (2026) 92–97. DOI: https://doi.org/10.18721/JPM.191.115

This is an open access article under the CC BY-NC 4.0 license (https://creativecommons.org/licenses/by-nc/4.0/)

Конференционная статья
УДК 534-16
DOI: https://doi.org/10.18721/JPM.191.115

Зонная структура PT-симметричных фононных кристаллов

З.М. Яшкин ✉, М.В. Захарченко, Г.Ф. Глинский

Санкт-Петербургский государственный электротехнический университет «ЛЭТИ»
им. В. И. Ульянова (Ленина), Санкт-Петербург, Россия
✉ a3691215@yandex.ru

Аннотация. В настоящей работе теория фононных кристаллов обобщается на случай периодических сред с анизотропией упругих свойств, а также PT-симметричных структур с усилением и потерями. Предлагается операторная форма записи уравнения стационарной упругой волны в кристалле. Получено обобщенное условие PT-симметрии для систем с анизотропными упругими свойствами.

Ключевые слова: фононный кристалл, PT-симметрия, особые точки

Финансирование: Исследование проводилось в рамках проекта № FSEE-2025-0007 (государственное задание Министерства науки и высшего образования Российской Федерации № 075-00003-25-00 от 25.12.2024).

Ссылка при цитировании: Яшкин З.М., Захарченко М.В., Глинский Г.Ф., Зонная структура PT-симметричных фононных кристаллов // Научно-технические ведомости СПбГПУ. Физико-математические науки. 2026. Т. 19. № 1.1. С. 92–97. DOI: https://doi.org/10.18721/JPM.191.115

Статья открытого доступа, распространяемая по лицензии CC BY-NC 4.0 (https://creativecommons.org/licenses/by-nc/4.0/)

© Yashkin Z.M., Zakharchenko M.V., Glinskii G.F., 2026. Published by Peter the Great St. Petersburg Polytechnic University.

Introduction

Over the past decade, the properties of parity-time-symmetric (PT-symmetric) systems have been actively studied. Such systems are invariant under the parity (P) and time (T) reversal. The concept of PT symmetry is considered not only in quantum mechanics but also in continuum media theory. In particular, PT symmetry in the theory of elastic waves enables the study of various fundamental phenomena, such as one-way propagation [1], unidirectional sound focusing [2], and invisible sensing [3].

In this context, phononic crystals (PC) are crucial components of the implementation of these effects into the development of novel electronic devices. Most works in the field of PT-symmetric phononic crystals focus on the structures based on isotropic media [1, 4]. However, there is a lack of theoretical investigations of PT-symmetric systems based on semiconductor heterostructures, which often exhibit anisotropic elastic properties.

In the present paper, a general operator formalism for the analysis of elastic waves in a PC is proposed, which allows studying media with arbitrary anisotropy of elastic and mechanical properties. The developed theoretical approach is used to study the band structure of PT-symmetric phononic crystals, taking into account special cases of PT symmetry breaking.

Theory

In the framework of continuum mechanics, stationary elastic waves in crystals are described by the following equation:

$$\sum_{k,l,m} c_{iklm}(\mathbf{x}) \frac{\partial^2 u_m(\mathbf{x})}{\partial x_k \partial x_l} = -\omega^2 \mu(\mathbf{x}) u_i(\mathbf{x}), \tag{1}$$

where $c_{iklm}(\mathbf{x})$ is the component of the elasticity tensor, $u_i(\mathbf{x})$ is the complex amplitude of the displacement vector, $\mu(\mathbf{x})$ is the coordinate-dependent crystal density, ω is frequency of elastic waves. Note that considering the displacement field reality, the displacement vector components $\mathbf{u}(\mathbf{x}, t)$ can be expressed through the real part of the corresponding complex phasor $\mathbf{u}(\mathbf{x})e^{-i\omega t}$.

In the general case, a structure under study can be characterized by losses or gain. From a mathematical point of view, such properties of elastic media are described by the imaginary part of the elastic tensor $\tilde{\mathbf{C}}(\mathbf{x})$, which can be represented as:

$$\tilde{\mathbf{C}}(\mathbf{x}) = \tilde{\mathbf{C}}'(\mathbf{x}) + i\tilde{\mathbf{C}}''(\mathbf{x}),$$

where $\tilde{\mathbf{C}}'(\mathbf{x})$ and $\tilde{\mathbf{C}}''(\mathbf{x})$ are its real and imaginary parts, respectively. Note that the complex parameters of the analyzed systems naturally arise when considering time (or spatial) dispersion effects. However, when the components of the elastic tensor change slightly over a given frequency range, it is sufficient to use their constant values. Such a way of description of elastic properties is widely used in the theory of PT-symmetric phononic crystals, where gain and loss are engineered artificially and maintained under certain experimental conditions [1, 2, 4].

Taking into account space inversion and time reversal, we can write a generalized PT symmetry condition for crystal density and elasticity tensor coordinate dependencies:

$$\mu(\mathbf{x}) = \mu(-\mathbf{x}),\ \tilde{\mathbf{C}}(\mathbf{x}) = \tilde{\mathbf{C}}^*(-\mathbf{x}).$$

Note that time reversal reduces to complex conjugation [1].

It can be shown that conventional Eq. (1) is a special case of the following operator equation, written in the coordinate representation:

$$(\hat{\mathbf{s}} \cdot \hat{\mathbf{k}})^+ \hat{c} (\hat{\mathbf{s}} \cdot \hat{\mathbf{k}}) |u\rangle = \omega^2 \hat{\mu} |u\rangle. \tag{2}$$

Here $\hat{\mathbf{s}}$ is the polarization operator, $\hat{\mathbf{k}}$ is the wave vector operator, $\hat{c}$ and $\hat{\mu}$ are the operators of the elasticity and density of the crystal, respectively, $|u\rangle$ is a vector in a complex Hilbert space that describes a displacement field. A similar approach was successfully developed in the theory of photonic crystals [5].

© Яшкин З.М., Захарченко М.В., Глинский Г.Ф., 2026. Издатель: Санкт-Петербургский политехнический университет Петра Великого.

To prove the equivalence of Eqs. (1) and (2), it is necessary to write the operator equation in a certain basis. Consider a set of states "of phonon" $|i, \mathbf{x}\rangle$ with a certain coordinate $\mathbf{x}$ and elastic wave polarization i ($i = x, y, z$). These states form a basis that satisfies the conditions of orthonormality and completeness:

$$\langle i, \mathbf{x} | k, \mathbf{x}' \rangle = \delta(\mathbf{x} - \mathbf{x}')\delta_{ik}, \langle i, l; \mathbf{x} | k, m; \mathbf{x}' \rangle = \delta(\mathbf{x} - \mathbf{x}')\delta_{ik}\delta_{lm},$$
$$\sum_i \int_V d\mathbf{x} | i, \mathbf{x} \rangle \langle i, \mathbf{x} | = 1, \sum_{i,l} \int_V d\mathbf{x} | i, l; \mathbf{x} \rangle \langle i, l; \mathbf{x} | = 1, \quad (3)$$

where V is the volume.

Using this basis set, we can define the vector $|u\rangle$ in coordinate representation:

$$|u\rangle = \sum_i \int_V d\mathbf{x} | i, \mathbf{x} \rangle \langle i, \mathbf{x} | u \rangle = \sum_i \int_V d\mathbf{x} | i, \mathbf{x} \rangle u_i(\mathbf{x}).$$

The matrix elements of the operators in Eq. (2) are determined as follows:

$$\langle i, k; \mathbf{x} | \hat{c} | l, m; \mathbf{x}' \rangle = c_{iklm}(\mathbf{x})\delta(\mathbf{x} - \mathbf{x}'), \langle i, \mathbf{x} | \hat{\mu} | k, \mathbf{x}' \rangle = \mu(\mathbf{x})\delta(\mathbf{x} - \mathbf{x}')\delta_{ik},$$
$$\langle i, \mathbf{x} | \hat{\mathbf{k}} | k, \mathbf{x}' \rangle = -i[\nabla_{\mathbf{x}}\delta(\mathbf{x} - \mathbf{x}')]\delta_{ik}, \langle i, l; \mathbf{x} | \hat{\mathbf{s}} | k, \mathbf{x}' \rangle = \mathbf{s}_{il,k}\delta(\mathbf{x} - \mathbf{x}'),$$

where $\mathbf{s}_{il,k}$ are the matrix elements written through the Clebsch–Gordan coefficients [6].

Using expressions (2), (3), it can be shown that:

$$\langle i, k; \mathbf{x} | \hat{c} \left(\hat{\mathbf{s}} \cdot \hat{\mathbf{k}} \right) | u \rangle = \sum_l \int_V d\mathbf{x}' \langle i, k; \mathbf{x} | \hat{c} \left(\hat{\mathbf{s}} \cdot \hat{\mathbf{k}} \right) | l, \mathbf{x}' \rangle \langle l, \mathbf{x}' | u \rangle = \sigma_{ik},$$

$$\langle i; \mathbf{x} | \left(\hat{\mathbf{s}} \cdot \hat{\mathbf{k}} \right)^+ | \sigma \rangle = \sum_{l,m} \int_V d\mathbf{x}' \langle i; \mathbf{x} | \left(\hat{\mathbf{s}} \cdot \hat{\mathbf{k}} \right)^+ | l, m; \mathbf{x}' \rangle \langle l, m; \mathbf{x}' | \sigma \rangle = \sum_l \frac{\partial \sigma_{il}}{\partial x_l},$$

where σ_{ik} is the component of the mechanical stress tensor and $|\sigma\rangle$ is the corresponding state vector in the complex Hilbert space, describing a mechanical stress field.

Using the relation between the mechanical stress tensor and the strain tensor [6], Eq. (1) can be written in the following form:

$$\sum_k \frac{\partial \sigma_{ik}}{\partial x_k} = -\mu\omega^2 u_i.$$

Thus, Eq. (2) in the coordinate representation reduces to Eq. (1).

By introducing auxiliary vectors $|\tilde{u}\rangle = \hat{\mu}^{1/2} |u\rangle$, we can reduce Eq. (2) to the eigenvalue problem for a non-Hermitian operator:

$$\hat{D} | \tilde{u} \rangle = \omega^2 | \tilde{u} \rangle.$$

Here, we introduced a "dynamical" operator $\hat{D} = \hat{\mu}^{-1/2} (\hat{\mathbf{s}} \cdot \hat{\mathbf{k}})^+ \hat{c} (\hat{\mathbf{s}} \cdot \hat{\mathbf{k}}) \hat{\mu}^{-1/2}$, whose eigenvalues are squared eigenfrequencies.

A phononic crystal is a translationally invariant system with periodically changing elastic properties. In this case, it is convenient to use states with a certain wave vector and polarization as a basis $|i, \mathbf{b} + \mathbf{k}\rangle$ ($\mathbf{b}$ is the reciprocal lattice vector of the PC, $\mathbf{k}$ – the wave vector, taking values in the corresponding superlattice Brillouin zone). Set of states $|i, \mathbf{b} + \mathbf{k}\rangle$ is also considered orthonormal and complete.

The corresponding matrix elements of the operators in Eq. (2) are defined as:

$$\langle i, l; \mathbf{b} + \mathbf{k} | \hat{c} | k, m; \mathbf{b}' + \mathbf{k}' \rangle = c_{iklm}(\mathbf{b} - \mathbf{b}')\delta_{\mathbf{kk}'}, \langle i, \mathbf{b} + \mathbf{k} | \hat{\mu} | l, \mathbf{b}' + \mathbf{k}' \rangle = \mu(\mathbf{b} - \mathbf{b}')\delta_{il}\delta_{\mathbf{kk}'},$$
$$\langle i, \mathbf{b} + \mathbf{k} | \hat{\mathbf{k}} | l, \mathbf{b}' + \mathbf{k}' \rangle = (\mathbf{b} + \mathbf{k})\delta_{\mathbf{bb}'}\delta_{\mathbf{kk}'}\delta_{il}, \langle i, l; \mathbf{b} + \mathbf{k} | \hat{\mathbf{s}} | m, \mathbf{b}' + \mathbf{k}' \rangle = \mathbf{s}_{il,m}\delta_{\mathbf{bb}'}\delta_{\mathbf{kk}'}, \quad (4)$$

where $c_{iklm}(\mathbf{b} - \mathbf{b}')$ and $\mu(\mathbf{b} - \mathbf{b}')$ are the Fourier transforms of the components of the elastic tensor and the crystal density, respectively.

Expressions (4) allow determining the matrix of the operator $\hat{D}$, which is diagonal in indices $\mathbf{k}$ and $\mathbf{k}'$ and has a block-diagonal structure, where each block is a matrix of smaller dimension, corresponding to a certain value of the vector $\mathbf{k}$. As a consequence, the operator Eq. (2) can be represented as the following matrix equation:

$$D(\mathbf{k})\tilde{\mathbf{u}}_j(\mathbf{k}) = \omega_j^2(\mathbf{k})\tilde{\mathbf{u}}_j(\mathbf{k}).$$

Herein $D(\mathbf{k})$ is the matrix of the operator $\hat{D}$, and $\tilde{\mathbf{u}}_j(\mathbf{k})$ are the corresponding eigenvectors.

Thus, the problem of determining the band structure of a phononic crystal is reduced to the problem of determining the eigenvalues $\omega_j^2(\mathbf{k})$ and eigenvectors $\tilde{\mathbf{u}}_j(\mathbf{k})$ of a non-Hermitian matrix. It should be noted that in a non-Hermitian problem, the eigenvectors are not orthogonal, but are related by the conditions of biorthonormality and completeness to the solution of the adjoint problem for eigenvalues and eigenvectors [7].

To determine the spatial distribution of the displacement field, it is necessary to consider $\tilde{\mathbf{u}}_j(\mathbf{k})$ in the basis $|i, \mathbf{x}\rangle$, which is related to the basis $|i, \mathbf{b} + \mathbf{k}\rangle$ by the inverse Fourier transform:

$$u_{i,j}(\mathbf{x};\mathbf{k}) = \frac{1}{\sqrt{\Omega}}\sum_{\mathbf{b}} e^{i\mathbf{b}\mathbf{x}} u_{\mathbf{b}i,j}(\mathbf{k}).$$

Here Ω is the volume of a unit cell. Components $u_{\mathbf{b}i,j}(\mathbf{k})$ form respective vectors $\mathbf{u}_j(\mathbf{k})$, which are related to the eigenvectors $\tilde{\mathbf{u}}_j(\mathbf{k})$ of the matrix $D(\mathbf{k})$ by the following formula:

$$\mathbf{u}_j(\mathbf{k}) = \mu^{-1/2}\tilde{\mathbf{u}}_j(\mathbf{k}),$$

where the matrix μ is defined through the matrix elements (4).

Results and Discussion

The theory developed was used to analyze the band structure and the displacement fields of a one-dimensional PT-symmetric anisotropic PC. The studied structure is schematically shown in Fig. 1. The values of the elasticity tensor components were taken from [8, 9].

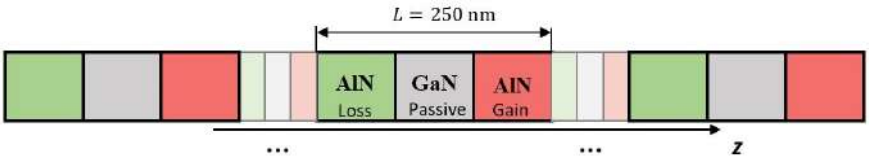

Fig. 1. One-dimensional PC consisting of AlN/GaN layers. The PC period is L = 250 nm. Passive regions are marked in gray, regions characterizing wave amplification are marked in red, and attenuation is marked in green

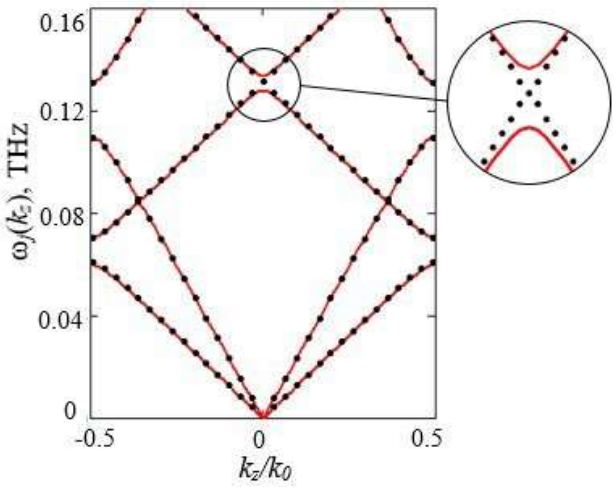

Fig. 2. Band structure of passive PC (red line) and PT-symmetric PC (black dotted line ($\gamma = 2$))

The energy loss and gain in AlN cells are characterized by the following imaginary components of the elasticity tensor: $c_{11}'' = c_{44}'' = \pm\gamma \cdot 10^{10}$ Pa (where "+" denotes a cell with loss, "–" denotes a cell with gain). Fig. 2 shows the calculated band structure of the fully passive 1D AlN/GaN PC (without gain and loss), as well as a PT-symmetric 1D PC with active elementary cells.

As can be seen from Fig. 2, the band structures for the passive PC and the PT-symmetric PC slightly differ quantitatively. However, a coalescence of the dispersion branches can be observed for the latter case. Fig. 3, *a* shows the spatial distribution of the displacement fields for a PC with PT symmetry and its violation (Fig. 3, *b*).

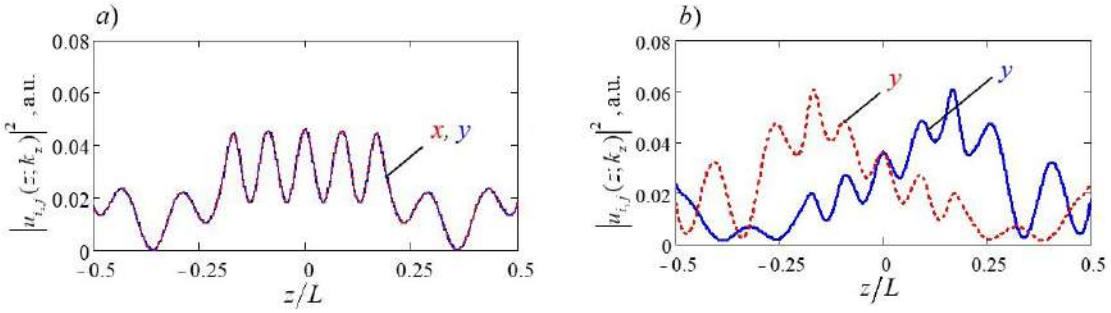

Fig. 3. Squared modulus of displacement fields at $k_z = 0.25k_0$, $j = 21$, $i = x$ (red dotted line), and at $j = 22$, $i = y$ (blue line), PT-symmetric case ($\gamma = 6$) (*a*); squared modulus of the displacement fields at $k_z = 0.25k_0$, $j = 21$, $i = y$ (red dotted line), and at $j = 22$, $i = y$ (blue line), case of PT symmetry breaking ($\gamma = 7$) (*b*). $k_0 = 2\pi/L$.

One of the characteristic features of PT-symmetric systems is the presence of exceptional points, corresponding to singularities in the dependence of frequency on the system parameters. Fig. 4 shows the dependencies of the imaginary frequency component for two modes $j = 21$, 22 on the parameter γ.

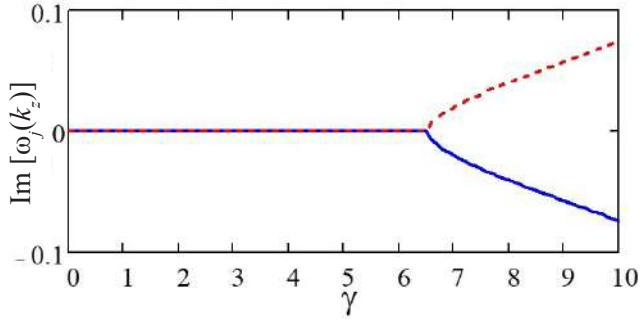

Fig. 4. Dependences of imaginary frequency component for two modes $j = 21$ (red dotted line) and $j = 22$ (blue line) on the parameter γ, for $k_z = 0.25k_0$

Fig. 4 shows an exceptional point for $\gamma \approx 6.5$, corresponding to the broken PT symmetry. This explains that when $\gamma = 6$ (Fig. 3, *a*) the amplitudes of the waves in the regions with gain and loss are equal, while for the case $\gamma = 7$ (Fig. 3, *b*) such symmetry of the eigenstates cannot be observed.

Conclusion

The paper develops a new theoretical approach for the analysis of the band structure of the phononic crystal. A generalized operator form of the equation of a stationary elastic wave in a crystal is proposed. It is shown that the problem of determining the band structure and eigenmodes of a PC is reduced to a matrix problem of finding eigenvalues and eigenvectors. This approach allows analyzing the PCs with arbitrary anisotropy of elastic properties. A generalized condition for PT-symmetric systems with anisotropic elastic properties was obtained. The proposed method was used to calculate the band structure and the spatial distribution of the displacement field of the one-dimensional PT-symmetric PC and to analyze the system's behavior near the exceptional points. This theory can be further developed to study systems with temporal and spatial dispersion of elastic properties, analogous to the operator formalism of macroscopic electrodynamics [7].

Acknowledgments

This study was supported by the State assignment for the Saint Petersburg Electrotechnical University "LETI" (theme No. FSEE-2025-0007).

REFERENCES

1. **Xuefeng Z., Hamidreza R., Chengzhi S., Jie Z., Xiang Z.,** PT-Symmetric Acoustics, Physical Review X. 4 (3) (2014) 031042.

2. **Tuo L., Xuefeng Z., Fei C., Shanjun L., Jie Z.,** Unidirectional wave vector manipulation in two-dimensional space with an all-passive acoustic parity-time-symmetric metamaterials crystal, Phys. Rev. Lett. 120 (12) (2018) 124502.

3. **Fleury, R., Sounas, D., Alù, A.,** An invisible acoustic sensor based on parity-time symmetry, Nature Communications. 6 (2015) 5905.

4. **Hang Y., Xin Z., Yuechang L., Yuanwei Y., Fugen W., Degang Z.,** Novel acoustic flat focusing based on the asymmetric response in parity-time-symmetric phononic crystals, Scientific Reports. 9 (2019) 10048.

5. **Glinskii G.F.,** Photonic crystals based on media with arbitrary anisotropy of permittivity and permeability, Tech. Phys. 64 (3) (2019) 293–301.

6. **Glinskii G.F.,** Semiconductors and Semiconductor Nanostructures: Symmetry and Electron States (in Russian), Tekhnolit, St. Petersburg. (2008).

7. **Zakharchenko M.V., Glinskii G.F.,** Propagation and scattering of electromagnetic waves Biorthogonal electrodynamics, Physica Scripta. 100 (4) (2025) 045212.

8. **Kazan M., Moussaed E., Nader R., Masri P.,** Elastic constants of aluminum nitride, Physica Status Solidi (C). 4 (1) (2007) 204–207.

9. **Yamaguchi M., Yagi T., Azuhata T., Sota T., Suzuki K., Chichibu S., Nakamura S.,** Brillouin scattering study of gallium nitride: elastic stiffness constants, Journal of Physics: Condensed Matter. 9 (1) (1997) 241.

THE AUTHORS

YASHKIN Zakhar M.
a3691215@yandex.ru
ORCID: 0009-0003-0633-0596

ZAKHARCHENKO Mikhail V.
mikhailvzakh@gmail.com
ORCID: 0000-0003-4970-9021

GLINSKII Gennadii F.
genaglinskii@mail.ru
ORCID: 0000-0002-4952-9664

Received 12.12.2025. Approved after reviewing 02.03.2026. Accepted 09.03.2026.

© Peter the Great St. Petersburg Polytechnic University, 2026

Conference paper
UDC 535.37, 535.33
DOI: https://doi.org/10.18721/JPM.191.116

Room temperature microlasers based on quasi-planar geometry

A.V. Babichev [1]✉, Ya.N. Kovach [1], A.S. Dragunova [2], I.S. Makhov [2], N.V. Kryzhanovskaya [2], Yu.M. Zadiranov [1], Yu.A. Salii [1], M.M. Kulagina [1], M.A. Bobrov [1], A.P. Vasiliev [1], S.A. Blokhin [1], N.A. Maleev [2], L.Ya. Karachinsky [3], I.I. Novikov [3], A.Yu. Egorov [3]

[1] Ioffe Institute, St. Petersburg, Russia;
[2] National Research University Higher School of Economics, St. Petersburg branch, St. Petersburg, Russia;
[3] ITMO University, St. Petersburg, Russia
✉ a.babichev@mail.ioffe.ru

Abstract. The planar microcavity structure was grown using molecular-beam epitaxy. Single-mode lasing was observed at a wavelength of 960 nm for pillars with a diameter of 15 μm. At 300 K, the lasing threshold was approximately 30 mW. Increasing the pump power to 2.7 times the threshold power resulted in a mode energy shift of approximately 1 meV. This shift in the mode energy position corresponds to approximately 12 degrees of laser heating.

Keywords: molecular-beam epitaxy, micropillar cavity, gallium arsenide, InGaAs, Stransky-Krastanow growth mode

Funding: The work of A.V. Babichev, Ya.N. Kovach, A.S. Dragunova, A.P. Vasil'ev, and S.A. Blokhin was supported by the grant of the Russian Science Foundation (project no. 22-19-00221-П), https://rscf.ru/project/22-19-00221/ in the part of MBE epitaxy, and the study of photoluminescence spectra. The work of I.S. Makhov and N.V. Kryzhanovskaya was supported by the project of the Basic Research Program at the HSE University (project no. HSE-BR-2025-069) in the part of the analysis of the spectra of the test structure.

Citation: Babichev A.V., Kovach Ya.N., Dragunova A.S., Makhov I.S., Kryzhanovskaya N.V., Zadiranov Yu.M., Salii Yu.A., Kulagina M.M., Bobrov M.A., Vasil'ev A.P., Blokhin S.A., Maleev N.A., Karachinsky L.Ya., Novikov I.I., Egorov A.Yu., Room temperature microlasers based on quasi-planar geometry, St. Petersburg State Polytechnical University Journal. Physics and Mathematics. 19 (1.1) (2026) 98–104. DOI: https://doi.org/10.18721/JPM.191.116

This is an open access article under the CC BY-NC 4.0 license (https://creativecommons.org/licenses/by-nc/4.0/)

Конференционная статья
УДК 535.37, 535.33
DOI: https://doi.org/10.18721/JPM.191.116

Микролазеры на основе квази-планарной геометрии, работающие при комнатной температуре

А.В. Бабичев [1]✉, Я.Н. Ковач [1], А.С. Драгунова [2], И.С. Махов [2], Н.В. Крыжановская [2], Ю.М. Задиранов [1], Ю.А. Салий [1], М.М. Кулагина [1], М.А. Бобров [1], А.П. Васильев [1], С.А. Блохин [1], Н.А. Малеев [1], Л.Я. Карачинский [3], И.И. Новиков [3], А.Ю. Егоров [3]

[1] Физико-технический институт им. А.Ф. Иоффе РАН, Санкт-Петербург, Россия;
[2] Национальный исследовательский университет "Высшая школа экономики", Санкт-Петербургский филиал, Санкт-Петербург, Россия;
[3] Университет ИТМО, Санкт-Петербург, Россия;
✉ a.babichev@mail.ioffe.ru

© Babichev A.V., Kovach Ya.N., Dragunova A.S., Makhov I.S., Kryzhanovskaya N.V., Zadiranov Yu.M., Salii Yu.A., Kulagina M.M., Bobrov M.A., Vasil'ev A.P., Blokhin S.A., Maleev N.A., Karachinsky L.Ya., Novikov I.I., Egorov A.Yu., 2026. Published by Peter the Great St. Petersburg Polytechnic University.

Аннотация. Гетероструктура планарного микрорезонатора была выращена методом молекулярно-пучковой эпитаксии. Продемонстрирована одномодовая генерация на длине волны 960 нм для микролазеров с диаметром 15 мкм. При температуре 300 K порог генерации составлял приблизительно 30 мВт. Превышение пороговой мощности в 2.7 раза привело к сдвигу положения энергии кванта, соответствующей длине волны генерации, около 1 мэВ. Данное смещение положения энергии кванта соответствует нагреву лазера около 12 градусов.

Ключевые слова: молекулярно-пучковая эпитаксия, микрорезонатор, арсенид галлия, InGaAs, режим роста Странского-Крастанова

Финансирование: Работа А.В. Бабичева, Я.Н. Ковача, А.С. Драгуновой, А.П. Васильева и С.А. Блохина выполнена при финансовой поддержке Российского научного фонда (проект № 22-19-00221-П), https://rscf.ru/project/22-19-00221/ в части эпитаксии методом молекулярно-пучковой эпитаксии и исследования спектров фотолюминесценции. Работа И.С. Махова и Н.В. Крыжановской выполнена при финансовой поддержке Программы фундаментальных исследований НИУ ВШЭ (проект № HSE-BR-2025-069) в части анализа спектров фотолюминесценции тестовых структур.

Ссылка при цитировании: Бабичев А.В., Ковач Я.Н., Драгунова А.С., Махов И.С., Крыжановская Н.В., Задиранов Ю.М., Салий Ю.А., Кулагина М.М., Бобров М.А., Васильев А.П., Блохин С.А., Малеев Н.А., Карачинский Л.Я., Новиков И.И., Егоров А.Ю. Микролазеры на основе квази-планарной геометрии, работающие при комнатной температуре // Научно-технические ведомости СПбГПУ. Физико-математические науки. 2026. Т. 19. № 1.1. С. 98–104. DOI: https://doi.org/10.18721/JPM.191.116

Статья открытого доступа, распространяемая по лицензии CC BY-NC 4.0 (https://creativecommons.org/licenses/by-nc/4.0/)

Introduction

Reservoir computing (RC) is one of the effective ways to implement neuromorphic computing due to its ability to efficiently learn through linear regression and classification. Compared with the electrical implementation of the RC, its optical implementation is promising due to its large scalability and large speed. In particular, RC based on diffractively coupled (DC) laser arrays made it possible to realize gigahertz speeds. In this case, the system bandwidth is determined by the internal dynamics of the lasers and the roundtrip time for light to pass through the external optics (~nanoseconds).

Current-injected vertical-cavity surface-emitting lasers (VCSELs) [1 – 4] and optically pumped micropillar cavity lasers [5 – 9] can serve as laser sources that provide DC. Both of these types of vertical microcavity lasers provide the vertical emission and array fabrication required for DC operation. The current-injected VCSEL array with a quantum wells (QWs) active region allows for diffractive coupling to be realized at room temperature [1], but the maximum element size in the array does not exceed 24 [1], which is due to the large pitch of the lasers on the substrate (≥80 μm [5]). In addition, the emission wavelength of individual current-injected VCSELs varies, and this can hardly be compensated due to wavelength tuning induced by the injection current [5]. Optically pumped microlasers with an active region based on quantum dots (QDs) provide a small element pitch (≤10 μm) and enable DC via injection locking, but do not provide lasing at room temperature. The emission wavelength of individual optically pumped microlasers can be precisely compensated by adjusting the pillar diameter [5]. As a result, it is possible to fabricate dense, spectrally homogeneous arrays of microlasers required for RC [5].

The low operating temperatures of optically pumped micropillar cavity lasers are due to optical absorption in mirrors at the pump wavelength and the low material gain of the active regions. The use of active regions based on QWs, whose gain is significantly larger than that of QDs, in the fabrication of microlasers is very limited. Due to the small diameter of the pillar cavity, large non-radiative surface recombination limits the possibility of continuous-wave (CW) operation of the QWs-based microlaser even at low-temperatures. In contrast, the tight confinement of charge

© Бабичев А.В., Ковач Я.Н., Драгунова А.С., Махов И.С., Крыжановская Н.В., Задиранов Ю.М., Салий Ю.А., Кулагина М.М., Бобров М.А., Васильев А.П., Блохин С.А., Малеев Н.А., Карачинский Л.Я., Новиков И.И., Егоров А.Ю., 2026. Издатель: Санкт-Петербургский политехнический университет Петра Великого.

carriers in QDs reduces this effect. The use of mirrors based on GaAs/$Al_{0.9}Ga_{0.1}As$ layers, as well as an active region based on InGaAs QDs makes it possible to implement lasing action at 130 K for a microlaser with a diameter of 5 μm [10], which was the maximum operating temperature for micropillar lasers based on GaAs/$Al_{0.9}Ga_{0.1}As$ mirrors. In fact, strong optical absorption in the output mirror layers (GaAs) at the pump wavelength limits the power-conversion efficiency (PCE) to about 3%. Using resonant pumping of the wetting layer (WL) states (pumping in the range of 905–922 nm [10]) allows to mitigate the absorption in the output mirror layers. At the same time, due to the extremely small thickness of the WL, the absorption of the active region is negligible, resulting in a PCE value of less than one percent [10].

To implement laser operation at elevated temperatures, low absorbing (at the pump wavelength) mirrors based on $Al_{0.2}Ga_{0.8}As/Al_{0.9}Ga_{0.1}As$ layers were invented [11]. These low-absorption mirrors allow the PCE to be increased by approximately ten times (up to ~30% [11,12]). Increasing the number of QDs layers from one [11] to three allows for compensation of the increase in internal optical loss with increasing temperature. In this case, the maximum operating temperature does not exceed 220 K [6, 7]. For practical application of micropillar cavity lasers, it is necessary to ensure operation at room temperature.

This paper discusses the first results of studies of micropillar cavity lasers operating at room temperature, which was the main goal of the study.

Materials and Methods

The growth of a planar cavity structure was carried out using molecular-beam epitaxy (MBE). The optical length of the GaAs microcavity was one wavelength divided by the refractive index (1 λ microcavity). The microcavity was formed by distributed Bragg reflectors based on Al0.2Ga0.8As/$Al_{0.9}Ga_{0.1}As$ layers. Compared with previous microcavities based on $Al_{0.2}Ga_{0.8}As/Al_{0.9}Ga_{0.1}As$ mirrors (based on 35 and 27 pairs in the bottom and top mirrors [7]), the modelled quality factor (Q-factor) of the cold cavity (excluding the absorption of the active region) increased more than twofold. The number of pairs in the bottom and top mirrors was 35 and 31, respectively. Three layers of QDs were used as the active region. QDs were self-assembled from $In_{0.5}Ga_{0.5}As$ using Stranski-Krastanov growth method and located in the center of the cavity, at the optical field node. Compared to the previous [7], changing the growth conditions eliminates vertical alignment of QDs. This leads to an increase in the material gain of the active region [13]. To fabricate the micropillar cavities, a dry etching process was performed through a mask of reflowed photoresist.

For optical characterization, the samples were placed in an optical cryostat (Cryostation® s50, Montana Instruments). The temperature of samples during the study was fixed at 300 K. A semiconductor laser diode with a wavelength of 808 nm was used for optical pumping in CW mode. For optical pumping, a 20× objective (Mitutoyo M Plan Apo NIR) with a focal spot size of 4 μm was used. The reduction in the pumping spot size (pumping the central part of the pillar) compared to previous ones [6, 7, 11], allows for lateral heat extraction and minimizing heating of the active region. An SR-500i spectrograph (Andor Shamrock) was used to collect spectra at different pump powers. A diffraction grating with 1200 slits per millimeter limits the spectral resolution to 0.05 nm.

Results and Discussion

Single-mode emission was observed at a wavelength of 960 nm for a pillar with a diameter of 15 μm. To analyze the input-output (I-O) characteristic, the luminescence peak was fitted at different pump powers. The pseudo-Voigt function was used to determine the integrated intensity and linewidth in analogy with [11]. A superlinear (S-shaped) increase in the I-O characteristic (on a double logarithmic scale) was demonstrated, which, along with the narrowing of the luminescence peak (the Full Width at Half Maximum, FWHM, decreases from 0.2 to 0.05 nm, see Fig. 1, *a*), confirms the transition to lasing in microlaser with a diameter of 15 μm. To determine the lasing threshold and the Q-factor at threshold pump power, the I-O characteristic was fitted using an expression determined by solving the rate equations [10, 14]: $P_{pump}(P_{out}) = A\gamma/\beta[BP_{out}(1 + \xi)(1 + \beta BP_{out})/(1 + BP_{out}) - \beta\xi BP_{out}]$, where P_{pump} and P_{out} are the pump and output power, A and B are the input and output scaling factors, β is the fraction of the total spontaneous emission coupled to the lasing mode (spontaneous emission factor) [14]. The dimensionless factor ξ can be determined by: $\xi = n_0\beta/\gamma\tau_{sp}$, where n_0 is the exciton number at transparency threshold, τ_{sp} is the spontaneous

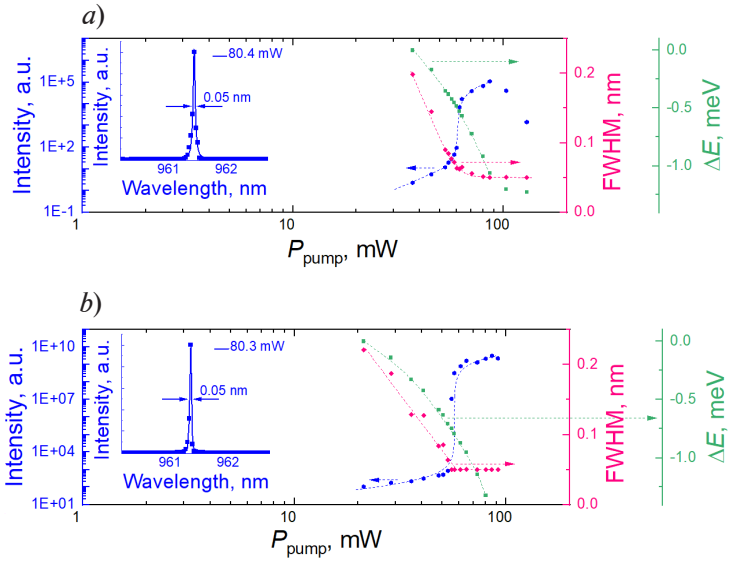

Fig. 1. Integrated intensity (left *Y*-axis), linewidth, and mode energy shift (right *Y*-axes) obtained at different pump powers. The dots on the panels correspond to experimental data, the dashed blue lines to intensities, the dashed red lines to linewidths, and dashed green lines to mode energy shifts. Panel (*b*) shows results for a pillar whose position on the substrate is shifted by 2760 μm compared to the pillar shown in panel (*a*).

The insets show the lasing spectrum at a pump power of 80.4 mW (panel *a*) and 80.3 mW (panel *b*)

emission lifetime, and γ is the cavity decay rate. To determine the value of γ, one can use the expression $\gamma = 2\pi v_L/Q$, where v_L is the lasing frequency and Q is the quality-factor determined at threshold pump power. To fit the *I-O* characteristic, $\tau_{sp} = 1$ ns can be used [10]. The value of n_0 can be determined from the QDs density and the effective size of the optical aperture as mentioned previously [5] and is equal to 22500. When fitting the *I-O* characteristics, β-factor was used as a fitting parameter and the value of ξ was fixed at 1.8. The latter was determined by specifying the values of γ, τ_{sp} and n_0. The best-fit value of the spontaneous emission factor in the laser mode is $7.5 \cdot 10^{-4}$%. The results of the fitting are shown in Fig. 1 (dotted *S*-shaped line on the left *Y* axis). Assuming that the mean photon number in the mode is unity at the threshold [14] ($BP_{out} = 1$), the lasing threshold P_{th} can be extracted from the reduced expression: $P_{th} = A\gamma/2\beta[\xi(1 - \beta) + 1 + \beta]$. Using this expression, the lasing threshold is determined, which is 32 mW. The Q-factor at threshold pump power is 4400. A further increase in the pump power leads to an increase in the Q-factor to at least 19300 (see Fig. 1, *a*, right *Y*-axis), which is limited by the spectral resolution of the monochromator used. It also should be noted that the deviation from *S*-type *I-O* characteristic is observed at pump power more than 86 mW, which may be caused by extreme heating of the sample. To assess this issue, mode energy shift (ΔE) analysis was previously used [6, 7, 11]. If there is no additional heating, at low pump power, band filling and the plasma effect cause a blue shift in the mode energy. A further increase in pump power leads to a blue shift caused by an increase in the free carrier density [11]. Conversely, if thermal heating is present, then with increasing pump power the thermal effect dominates over others, causing a red shift of the mode energy. A similar behavior of the mode energy as a function of the pump power (red shift) is demonstrated in the examined pillar (see Fig. 1, right *Y*-axis). Increasing the pump power from 37 to 86 mW results in a red shift of the mode energy above 1 meV. Based on the mode energy shift as a function of temperature (T) [7], a rough estimate of sample heating can be made. At low temperatures, the $\Delta E/\Delta T$ dependence is nonlinear; at elevated temperatures, it can be approximated by a linear fit with a slope of ~0.08 meV/K. Taking this value into account, the heating of the microcavity laser is approximately 12 degrees at a pump power of 86 mW.

To study the spectral homogeneity over the substrate surface, the output characteristics of a micropillar laser were investigated, the position of which on the substrate was shifted by 2760 μm compared to the position of the micropillar described above and shown in Fig. 1, *a*. The pillar diameter was similar to the previous one (15 μm). A clear *S*-shaped *I-O* characteristic (on a double logarithmic scale) was also demonstrated, which, together with the reduction of FWHM

from 0.22 to 0.05 nm (see Fig. 1, *b*), confirms the laser action. The lasing threshold extracted from the rate-equations analysis is 29 mW. The small difference between the lasing threshold and the similar value discussed above (32 mW) may be associated with a change in the magnitude of the gain to cavity detuning, which varies across the substrate due to variations in the thickness of the epitaxial layers across the substrate. A spectral nonuniformity of 29 meV along the radius of a 2-inch wafer was previously reported for a planar cavity structure grown by metal-organic vapor phase epitaxy (MOVPE) [5], which is associated with a thickness variation of approximately 2%. In contrast, for the planar microcavity grown by the MBE, the thickness change is less than one percentage, resulting in a resonance energy shift that is 7 times smaller [12] compared to its MOVPE-grown counterpart. As a result, this is the main reason for the low difference in the lasing threshold across the substrate surface. The lasing wavelength just above the threshold is 960.46 nm for the second micropillar, which differs from the similar value discussed above by approximately 0.21 nm (279 μeV). A resonance mode variation of approximately 1 meV along a 64×64 μm^2 array with a standard deviation of 342 μeV was previously reported [4]. As a result, a resonance difference of approximately 280 μeV, achieved in an experiment with a shift along the substrate of ~2.8 mm, demonstrates the potential for fabricating highly uniform arrays of QDs micropillars required for RC using the MBE growth method.

For comparative analysis with previous studies, it should be noted that the maximum operating temperature of lasers with low-absorption mirrors (based on $Al_{0.2}Ga_{0.8}As/Al_{0.9}Ga_{0.1}As$ layers) and microcavities grown by MBE and MOVPE is 220 [7] and 200 K [6]. Further increase in the operating temperature is limited by thermal heating of the sample, which occurs until the lasing threshold is reached. To address this issue, a pumping scheme with a point focus in the central region of the pillar was implemented, allowing for additional lateral heat dissipation, similar to VCSELs with a buried tunnel junction [2, 3]. Furthermore, the *Q*-factor of the vertical microcavity more than doubled, and the material gain increased due to the absence of vertical positioning of the vertically stacked QDs layers. As a result, optimization of the optical pumping method and design optimization will make it possible to operate microcavity lasers at room temperature.

Conclusion

Optically pumped microlasers operating at room temperature are needed for the development of quantum photonics, integrated photonic circuits [6] and reservoir computing [5]. This work demonstrates the possibility of operating micropillar cavity lasers at room temperature. At the same time, doubling the pump power above the lasing threshold results in sample heating by more than 10 degrees. Further research will focus on analyzing pulse characteristics to minimize sample heating.

Recently, a photonic-defect cavity was used to achieve operation at room temperature [6]. While the bottom mirror is semiconductor-based, the top mirror is entirely dielectric. The thermal conductivity (κ) of SiN_x (the high-refractive index material in the pair) is approximately 2.5 times lower than that of $Al_{0.2}Ga_{0.8}As$. Moreover, the κ value of SiO_x (the low-refractive index material in the pair) is approximately 58 times lower than that of $Al_{0.9}Ga_{0.1}As$. These facts limit the heat dissipation through a dielectric mirror compared to its semiconductor counterpart. To demonstrate the practical application potential of the photonic defect cavity, further analysis of the heating (mode energy shift) is necessary.

The concept of a photonic-defect cavity based on entirely semiconductor mirrors could become an alternative to micropillar cavities but involves a two-step epitaxy process. In fact, before epitaxy of the top mirror, it is necessary to develop epitaxial layers for overgrowing the etched mesa. Two-step epitaxy of semiconductor mirrors on GaAs substrates was previously achieved [15], demonstrating the potential of a photonic defect cavity based on semiconductor quasi-planar geometry.

REFERENCES

1. **Pflüger M., Brunner D., Heuser T., Lott J. A., Reitzenstein S., Fischer I.,** Experimental reservoir computing with diffractively coupled VCSELs, Optics Letters. 49 (9) (2024) 2285–2288.

2. **Babichev A.V., Kovach Y.N., Blokhin S.A., Karachinsky L.Y., Novikov I.I., Egorov A.Y., Tian S.-C., Bimberg D.,** Long-wavelength VCSELs with buried tunnel junction: design optimization, JPhys Photonics. 7 (3) (2025) 032001.

3. **Babichev A., Blokhin S., Gladyshev A., Karachinsky L., Novikov I., Blokhin A., Bobrov M., Kovach Y., Kuzmenkov A., Nevedomsky V., Maleev N., Kolodeznyi E., Voropaev K., Vasilyev A., Ustinov V., Egorov A., Han S., Tian S.-C., Bimberg D.,** Impact of device topology on the performance of high-speed 1550 nm wafer-fused VCSELs, Photonics. 10 (6) (2023) 660.

4. **Blokhin S.A., Bobrov M.A., Blokhin A.A., Kuzmenkov A.G., Maleev N.A., Ustinov V.M., Kolodeznyi E.S., Rochas S.S., Babichev A.V., Novikov I.I., Gladyshev A.G., Karachinsky L.Ya., Denisov D.V., Voropaev K.O., Ionov A.S., Egorov A.Yu.,** Analysis of the internal optical losses of the vertical-cavity surface-emitting laser of the spectral range of 1.55 μm formed by a plate sintering technique, Optics Spectroscopy. 127 (1) (2019) 140–144.

5. **Heuser T., Grose J., Holzinger S., Sommer M. M., Reitzenstein S.,** Development of highly homogenous quantum dot micropillar arrays for optical reservoir computing, IEEE Journal of Selected Topics in Quantum Electronics. 26 (1) (2020) 1–9.

6. **Gaur K., Tripathi S., Laudani F., Barua A., Limame I., Koulas-Simos A., Rodt S., Reitzenstein S.,** Photonic-defect cavities as next-generation room-temperature microlasers: a comparative study with micropillars, Laser & Photonics Reviews. 19 (18) (2025) e00533.

7. **Babichev A., Makhov I., Kryzhanovskaya N., Blokhin A., Zadiranov Y., Salii Y., Kulagina M., Bobrov M., Vasil'ev A., Blokhin S., Maleev N., Tchernycheva M., Karachinsky L., Novikov I., Egorov A.,** Lasing of quantum-dot micropillar lasers under elevated temperatures, IEEE Journal of Selected Topics in Quantum Electronics. 31 (5) (2025) 1–8.

8. **Limame I., Shih C.-W., Koulas-Simos A., Pietsch J., Roche L. J., Plattner M., Koltchanov A., Rodt S., Reitzenstein S.,** Diameter-dependent whispering gallery mode lasing effects in quantum dot micropillar cavities, Optics Express. 32 (18) (2024) 31819–31829.

9. **Babichev A., Makhov I., Kryzhanovskaya N., Troshkov S., Zadiranov Y., Salii Y., Kulagina M., Bobrov M., Vasil'ev A., Blokhin S., Maleev N., Karachinsky L., Novikov I., Egorov A.,** Low-threshold surface-emitting whispering-gallery mode microlasers, IEEE Journal of Selected Topics in Quantum Electronics. 31 (2) (2025) 1–8.

10. **Andreoli L., Porte X., Heuser T., Große J., Moeglen-Paget B., Furfaro L., Reitzenstein S., Brunner D.,** Optical pumping of quantum dot micropillar lasers, Optics Express. 29 (6) (2021) 9084–9097.

11. **Shih C.-W., Limame I., Krьger S., Palekar C.C., Koulas-Simos A., Brunner D., Reitzenstein S.,** Low-threshold lasing of optically pumped micropillar lasers with $Al_{0.2}Ga_{0.8}As/Al_{0.9}Ga_{0.1}As$ distributed Bragg reflectors, Applied Physics Letters. 122 (15) (2023) 151111.

12. **Babichev A.V., Nikitina E.V., Karachinsky L.Ya., Novikov I.I., Egorov A.Yu.,** Planar micropillar cavity structure with enhanced power-conversion efficiency. In: Proceedings of the 2024 International Conference on Electrical Engineering and Photonics (EExPolytech), Saint Petersburg, Russia, 17 – 18 October 2024; Proc. IEEE. 2024. 266–269.

13. **Bimberg D., Grundmann M., Ledentsov N.N.,** Quantum Dot Heterostructures, John Wiley & Sons, New Jersey, United States. (1999).

14. **Bjork G., Yamamoto Y.,** Analysis of semiconductor microcavity lasers using rate equations, IEEE Journal of Quantum Electronics. 27 (11) (1991) 2386–2396.

15. **Egorov A.Y., Karachinsky L.Y., Novikov I.I., Babichev A.V., Berezovskaya T.N., Nevedomskiy V.N.,** Metamorphic distributed Bragg reflectors for the 1440–1600 nm spectral range: Epitaxy, formation, and regrowth of mesa structures, Semiconductors. 49 (10) (2015) 1388–1392.

THE AUTHORS

BABICHEV Andrey V.
a.babichev@mail.ioffe.ru
ORCID: 0000-0002-3463-4744

KOVACH Yakov N.
yakovachyakov@gmail.com
ORCID: 0000-0003-4858-4968

DRAGUNOVA Anna S.
anndra@list.ru
ORCID: 0000-0002-0181-0262

MAKHOV Ivan S.
imahov@hse.ru
ORCID: 0000-0003-4527-1958

KRYZHANOVSKAYA Natalia V.
nataliakryzh@gmail.com
ORCID: 0000-0002-4945-9803

ZADIRANOV Yuriy M.
Zadiranov@mail.ioffe.ru

SALII Yulia A.
Guseva.Julia@mail.ioffe.ru

KULAGINA Marina M.
Marina.Kulagina@mail.ioffe.ru

BOBROV Mikhail A.
bobrov.mikh@gmail.com
ORCID: 0000-0001-7271-5644

VASIL'EV Alexey P.
Vasiljev@mail.ioffe.ru
ORCID: 0000-0002-2181-5300

BLOKHIN Sergey A.
blokh@mail.ioffe.ru
ORCID: 0000-0002-5962-5529

MALEEV Nikolay A.
maleev@beam.ioffe.ru
ORCID: 0000-0003-2500-1715

KARACHINSKY Leonid Ya.
leonid.karachinsky@connector-optics.com
ORCID: 0000-0002-5634-8183

NOVIKOV Innokenty I.
innokenty.novikov@itmo.ru
ORCID: 0000-0003-1983-0242

EGOROV Anton Yu.
anton.egorov@connector-optics.com
ORCID: 0000-0002-0789-4241

Received 28.11.2025. Approved after reviewing 19.02.2026. Accepted 20.02.2026.

© Peter the Great St. Petersburg Polytechnic University, 2026

Conference paper
UDC 621.373.8
DOI: https://doi.org/10.18721/JPM.191.117

Analysis of the low-frequency noise of 89X nm-range single-mode VCSELs

M.A. Bobrov [1]✉, S.A. Blokhin [1], Ya.N. Kovach [1], A.A. Blokhin [1], N.A. Maleev [1], A.G. Kuzmenkov [1], M.N. Marchiy [1], A.P. Vasil'ev [2]

[1] Ioffe Institute, St. Petersburg, Russia;
[2] Submicron Heterostructures for Microelectronics, Research & Engineering Center, St. Petersburg, Russia
✉ bma@mail.ioffe.ru

Abstract. This paper presents the results of experimental investigations of low-frequency relative intensity noise and phase noise of single-mode 89X nm-range vertical-cavity surface-emitting lasers (VCSELs) with different photon lifetimes. The lasers are based on a hybrid vertical microcavity design with carrier injection through intracavity contact layers and composite Bragg gratings. Analysis of the low-frequency amplitude noise of the VCSELs showed that the noise spectrum in the frequency range from 100 Hz to 10 kHz has a 1/*f*-noise trend, transitioning to white noise at frequencies above 10 kHz. The dependence of the amplitude noise on the laser's optical power has a W-shaped form. An increase in temperature leads to growth in both amplitude and phase noise, both at a fixed operating current and at comparable optical power of laser radiation. In the frequency range of 1–100 kHz, the achieved amplitude noise level does not exceed −120 dB/Hz. Meanwhile, in the 10–100 kHz frequency range, the phase noise level saturates at $0.6–1.1 \cdot 10^9$ Hz^2/Hz (depending on temperature and optical power) for devices with a characteristic photon lifetime of ~ 8.5 ps. The obtained results allow the use of the developed VCSELs in compact quantum sensors of various types.

Keywords: vertical cavity surface emitting laser, relative intensity noise, amplitude noise, phase noise, frequency noise, quantum sensors

Funding: Research was supported in part by the Ministry of Science and Higher Education of the Russian Federation (project reference number FFUG-2025-0006).

Citation: Bobrov M.A., Blokhin S.A., Kovach Y.N., Blokhin A.A., Maleev N.A., Kuzmenkov A.G. Marchiy M.N., Vasil'ev A.P., Analysis of the low-frequency noise of 89X nm-range single-mode VCSELs, St. Petersburg State Polytechnical University Journal. Physics and Mathematics. 19 (1.1) (2026) 105–110. DOI: https://doi.org/10.18721/JPM.191.117

This is an open access article under the CC BY-NC 4.0 license (https://creativecommons.org/licenses/by-nc/4.0/)

Конференционная статья
УДК 621.373.8
DOI: https://doi.org/10.18721/JPM.191.117

Исследование низкочастотных шумов одномодовых вертикально-излучающих лазеров диапазона 89X нм

М. А. Бобров [1]✉, С. А. Блохин [1], Я. Н. Ковач [1], А. А. Блохин [1], Н. А. Малеев [1], А. Г. Кузьменков [1], М. Н. Марчий [1], А. П. Васильев [2]

[1] Физико-технический институт им. А.Ф. Иоффе РАН, Санкт-Петербург, Россия;
[2] Научно-технологический центр микроэлектроники и субмикронных гетероструктур РАН, Санкт-Петербург, Россия
✉ bma@mail.ioffe.ru

© Bobrov M.A., Blokhin S.A., Kovach Y.N., Blokhin A.A., Maleev N.A., Kuzmenkov A.G. Marchiy M.N., Vasil'ev A.P., 2026. Published by Peter the Great St. Petersburg Polytechnic University.

Аннотация. В работе приведены результаты экспериментальных исследований низкочастотных шумов относительной интенсивности и фазовых шумов одномодовых вертикально-излучающих лазеров спектрального диапазона 89X нм с различными временами жизни фотонов в резонаторе на основе гибридной конструкции вертикального микрорезонатора с инжекцией носителей заряда через внутрирезонаторные контактные слои и композиционные брэгговские решетки (ВИЛ). Анализ низкочастотных амплитудных шумов ВИЛ показал, что спектр шумов в частотном диапазоне от 100 Гц до 10 кГц имеет вид 1/*f*-шума, а при частотах выше 10 кГц переходит в белый шум. Зависимость амплитудных шумов от оптической мощности лазера имеет W-образный вид. Повышение температуры ведет к росту амплитудных и фазовых шумов как при фиксированном рабочем токе, так и сравнимой оптической мощности излучения лазера. В частотном диапазоне 1–100 кГц достигнутый уровень амплитудных шумов не превышает −120 Дб/Гц, тогда как в диапазоне частот 10–100 кГц уровень фазовых шумов насыщается на уровне $0{,}6–1{,}1\cdot10^9$ Гц^2/Гц (в зависимости от температуры и оптической мощности) для приборов с характерным временем жизни фотонов в резонаторе ~ 8,5 пс. Полученные результаты позволяют использовать разработанные ВИЛ в компактных квантовых сенсорах различного типа.

Ключевые слова: вертикально-излучающий лазер, шумы относительной интенсивности, амплитудные шумы, фазовые шумы, частотные шумы, квантовые сенсоры

Финансирование: Исследования выполнены при частичной поддержке Министерства науки и высшего образования Российской Федерации (FFUG-2025-0006).

Ссылка при цитировании: Бобров М.А., Блохин С.А., Ковач Я.Н., Блохин А.А., Малеев Н.А., Кузьменков А.Г., Марчий М.Н., Васильев А.П. Исследование низкочастотных шумов одномодовых вертикально-излучающих лазеров диапазона 89X нм // Научно-технические ведомости СПбГПУ. Физико-математические науки. 2026. Т. 19. № 1.1. С. 105–110. DOI: https://doi.org/10.18721/JPM.191.117

Статья открытого доступа, распространяемая по лицензии CC BY-NC 4.0 (https://creativecommons.org/licenses/by-nc/4.0/)

Introduction

VCSELs are a promising type of injection laser for use in compact atomic sensors based on alkali metals (quantum frequency standards, quantum magnetometers, and gyroscopes) [1]. These lasers must meet a specific set of obligatory requirements: precise tuning of the radiation wavelength to the line of atomic transitions of alkali metals in the gas cell, single-mode generation, emission linear polarization in a fixed direction, small spectral linewidth, high speed at low operating currents, low phase and amplitude noise, and the ability to operate at elevated temperatures. In the overwhelming majority of studies devoted to VCSELs operating in the 79X nm [2 – 4] and 89X nm [5 – 7] spectral ranges, attention is primarily focused on the issues of stabilizing the polarization state of the radiation, ensuring the required optical power in single-mode regime, and/or laser response time at a given temperature. However, the issue of analyzing the relative intensity noise (RIN, amplitude noise) and phase noise (frequency noise) in the low-frequency region has received very little attention.

This paper presents the results of experimental studies of the RIN and phase noise of single-mode polarization-stable VCSELs operating in the 89X nm spectral range (hereinafter, 89X nm-range VCSELs), implemented within the framework of a hybrid design of a vertical microcavity with carrier injection through intracavity contact layers and composite Bragg gratings. The influence of temperature and photon lifetime on the noise characteristics of the VCSEL is considered.

Materials and Methods

The studied single-mode 89X nm VCSELs are implemented based on a previously proposed design with intracavity contacts, an optical resonator with InGaAs/AlGaAs quantum wells as the

© Бобров М.А., Блохин С.А., Ковач Я.Н., Блохин А.А., Малеев Н.А., Кузьменков А.Г., Марчий М.Н., Васильев А.П., 2026. Издатель: Санкт-Петербургский политехнический университет Петра Великого.

active region, and a diamond-shaped oxide current aperture. A more detailed description of the aforementioned VCSEL design is provided in [8]. Variation of the photon lifetime in the resonator was achieved by controlling the output mirror losses through modification of the top dielectric distributed Bragg reflector (DBR) reflectivity (by varying the number of DBR layer pairs and/or the thickness of the phase-matching layer). Details of the method for determining the photon lifetime are presented in [12].

Investigations of the 89X nm VCSELs relative intensity noise (RIN) were performed using a digital lock-in amplifier (SRS SR830 Lock-In Amplifier) operating in a mode measuring the noise power spectral density within a 1 Hz bandwidth at a specified frequency offset from the carrier. To improve the signal-to-noise ratio, low-noise components were used in the measurement setup, including a Hamamatsu S3584 photodetector and a transimpedance amplifier. To account for the nonlinearity of the electrical path and transimpedance amplifier, the corresponding frequency-dependent transfer function was measured. The use of a low-noise power supply with an additional low-pass filter minimized the contribution of technical noise. The noise level was calculated by subtracting the thermal noise, measured in the absence of an optical signal, from the total noise RMS signal, calculated based on the time-averaged in-phase and quadrature noise components, followed by normalization to the transfer function. Variation of the frequency offset from the carrier frequency yielded the frequency dependence of the amplitude noise, while the operating current and the laser temperature were additionally changed to obtain RIN dependence on output optical power or temperature.

Phase noise measurements of the 89X nm VCSELs were conducted using an optical frequency discriminator which converted laser frequency fluctuations into intensity fluctuations. A gas cell containing the cesium isotope ^{133}Cs vapors and buffer gas N_2 was used as an optical frequency discriminator. The linear part of the cell's absorption profile ensured proportional conversion of frequency noise into amplitude noise. The gas cell parameters were chosen to ensure not only complete conversion of phase noise into amplitude noise (discriminator slope), but also the complete dominance of the converted phase noise contribution over the direct contribution of the laser's amplitude noise. A wide-aperture lens was introduced into the optical setup to form a low divergent beam. In order to measure laser phase noise, individual 89X nm VCSEL chips, mounted in TO packages, were tuned to the edge of the gas cell's absorption line to the point of maximum discriminator slope. The position of this point was determined by the maximum of the detected amplitude noise. The procedure for recording such amplitude noise is similar to the methodology described above. It was carried out in an analogous manner – variation of the frequency offset from the carrier frequency and measurement of the noise power spectral density in a 1 Hz bandwidth yielded the frequency dependence of the phase noise.

Results and Discussion

Fig. 1 shows the current-optical power characteristics of 89X nm-range VCSELs with a selectively-oxidized current aperture diameter of 2.5 μm and different photon lifetimes in the resonator, selected for the investigation of noise properties. It is evident that an increase in the photon lifetime in the resonator leads to a reduction in the current threshold value and a decrease in the differential efficiency. Analysis of the emission spectra and polarization state showed that the devices operate in a single-mode lasing regime with a side-mode suppression ratio (SMSR) exceeding 30 dB and a fixed polarization direction with an orthogonal polarization suppression ratio (OPSR) above 17 dB at operating currents up to ~3.2–3.4 mA (the current range corresponding to a multimode lasing regime is highlighted in gray).

Fig. 2, *a* shows the RIN dependence on optical power at different detection frequencies, using Laser 4 as an example. The dependence of the amplitude noise on the laser's output optical power exhibits a W-shaped form. Specifically, as the output optical power increases in the spontaneous emission regime, an initial decrease in the RIN level is observed, followed by a sharp increase in noise as the laser approaches threshold. In the stimulated emission regime, a pronounced drop in RIN is evident, reaching a local minimum (which slightly exceeds the shot noise level) which is consistent with the results reported in [7, 9]. However, for optical powers exceeding 0.5 mW, this trend reverses despite the continued increase in optical power. An increase in the laser temperature does not fundamentally alter the characteristic behavior of the RIN; however, it leads to an increase in the RIN level both at a given output optical power and at a fixed operating current

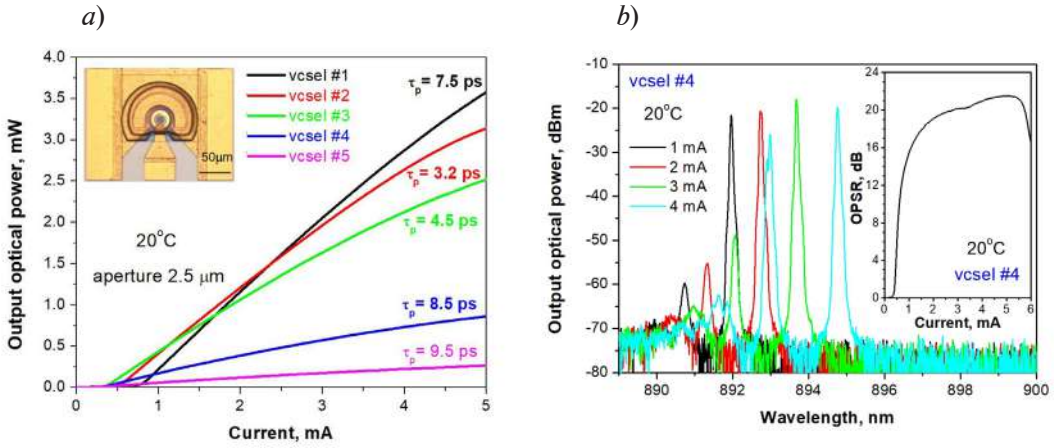

Fig. 1. Evolution of output optical power as functions of current (*a*) and optical spectra for different operating currents (*b*) measured at 20 °C, the inset in panel (*b*) shows the OPSR

(see Fig. 2, *b*). This observed behavior could be attributed to both thermal effects due to laser self-heating and the noise from higher-order transverse modes at elevated operating currents. Nevertheless, in the frequency range of 1–100 kHz, the RIN level does not exceed –120 dB/Hz. This result correlates with findings from studies on single-mode, polarization-stable 89X nm VCSELs with a classical vertical microcavity design [7, 9].

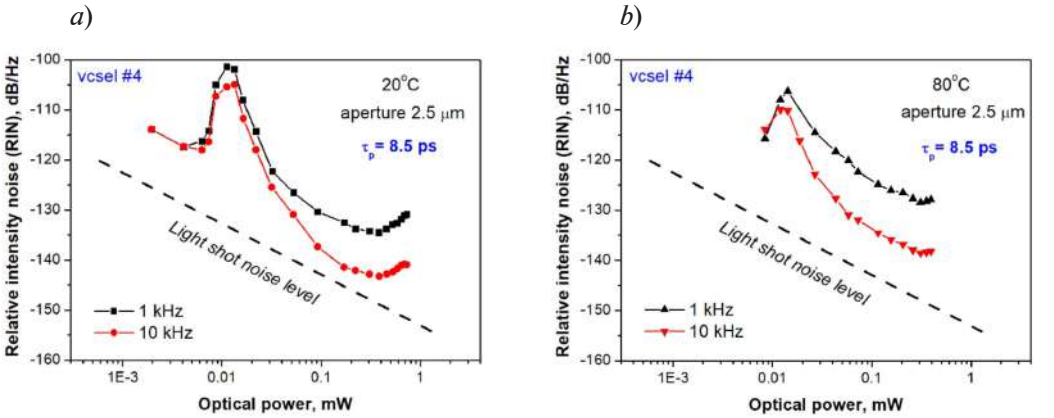

Fig. 2. RIN noise as a function of output optical power for VCSEL 4 with a 2.5 μm current oxide aperture, measured at 20 °C (*a*) and 80 °C (*b*).
The dashed straight line shows the calculated shot noise level as a function of the detected radiation level

Fig. 3, *a* shows a RIN as a function of photon lifetime in the resonator for single-mode 89X nm-range VCSELs. The devices featured a characteristic selectively-oxidized current aperture size of 2.5 μm and were measured at a temperature of 20°C with a fixed output optical power of 0.3 mW. The characteristic behavior of the laser's RIN in the low-frequency region follows a $1/f$ noise (flicker noise) trend with a roll-off rate of ~11 dB/decade, transitioning to white noise at frequencies above 10 kHz. The level of this white noise significantly exceeds the detectable shot noise level of the photodetector. With an increase in photon lifetime from 1.7 ps to 8.5 ps, a reduction in the amplitude noise of the 89X nm VCSELs is observed: the white noise level decreases from –130 dB/Hz to –145 dB/Hz. However, a further increase in photon lifetime above 9.5 ps leads to an increase in amplitude noise. This observation can be explained by the fact that to maintain the specified output optical power level (~0.3 mW) with a sharp drop in differential efficiency, a significant increase in the operating current is required. Narrow-aperture VCSELs are characterized by stronger self-heating of the active region (higher internal laser temperature) compared to broad-aperture lasers at comparable output power levels, due to their higher thermal resistance. This increased self-heating leads to the observed rise in RIN.

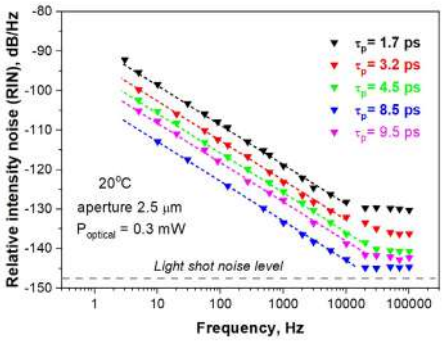

Fig. 3. Frequency dependences of RIN for a VCSEL with a 2.5 μm current oxide aperture and different photon lifetimes, all measured at an output optical power of 0.3 mW and a temperature of 20 °C.

The dashed horizontal line shows the calculated shot noise level corresponding to a detected optical power of 0.3 mW

Direct measurement of phase noise across a wide range of operating currents and output optical powers presents a non-trivial challenge, and in the case of employing the method of laser frequency fluctuation conversion into intensity fluctuations using an optical frequency discriminator, it is not feasible. The issue is that the emission wavelength of the laser under investigation must coincide with the absorption wavelength of the chosen optical discriminator. Fig. 4, *a* illustrates the influence of photon lifetime on the phase noise for 89X nm-range VCSELs with a 2.5 μm characteristic selectively-oxidized current aperture size. The characteristic behavior of the phase noise in the 1–1000 Hz frequency range follows a $1/f$ noise trend, whereas in the 10–100 kHz frequency range, saturation occurs at a level of $0.5–1.1 \cdot 10^7$ Hz^2/Hz, depending on the degree of current exceeding the threshold current. This result correlates with findings reported in [7, 9]. A reduction in the photon lifetime within the resonator leads to an expected increase in the phase noise level, which correlates well with the data from direct measurements of the spectral linewidth of 89X nm VCSELs using a scanning Fabry–Pérot interferometer [8]. The reason is that the white phase noise is closely related to the instantaneous fundamental laser linewidth; however, since the phase noise spectrum in a real laser is enriched by flicker noise, the integral of the phase noise spectral density contains information about the actual laser linewidth [10]. Fig. 4, *b* shows the frequency dependence of the phase noise for a device with a characteristic selectively-oxidized current aperture size of 2.5 μm and a photon lifetime of ~8.5 ps, measured at a laser temperature of 60°C. The fundamental characteristic behavior of the phase noise does not change with increasing temperature; however, an additive increase in noise is observed. This correlates well with the broadening of the spectral linewidth of 89X nm VCSELs with rising temperature [11]. Consequently, the white phase noise at frequencies above 10 kHz reaches a level of $0.6–1.1 \cdot 10^9$ Hz^2/Hz.

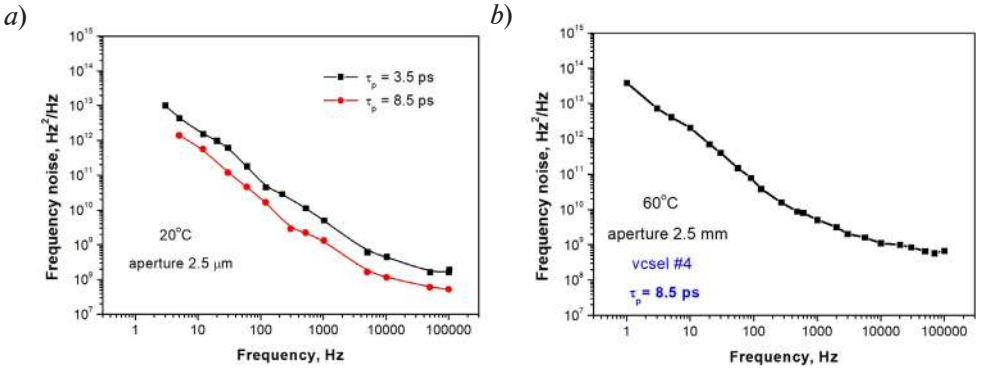

Fig. 4. Frequency dependences of phase noise for 89X nm-range VCSELs with a 2.5 μm characteristic current oxide aperture: influence of the VCSEL photon lifetime at a measurement temperature of 20 °C (*a*); influence of the measurement temperature for the VCSEL with a photon lifetime of 8.5 ps at 60 °C (*b*)

Conclusion

Thus, a comprehensive study of the amplitude and phase noise of an 89X nm-range VCSEL with intracavity contacts was conducted. Increasing temperature leads to an increase in the amplitude and phase noise levels. Increasing the cavity lifetime reduces the amplitude and phase noise levels, but a sharp drop in differential efficiency ultimately leads to an increase in internal temperature and, consequently, an increase in both noise levels.

REFERENCES

1. **Kitching J.,** Chip-scale atomic devices, Appl Phys Rev. 5 (3) (2018) 031302.

2. **Zhang J. Ning Y., Zhang J., Zhang X., Zeng Y., Wang L.,** 795 nm VCSELs for 87Rb based miniaturized atomic clock, Opt. Precis. Eng. 22 (1) (2014) 50–57.

3. **Zhou Y., Jia Y., Zhang X., Zhang J., Liu Z., Ning Y., Wang L.,** Large-aperture single-mode 795 nm VCSEL for chip-scale nuclear magnetic resonance gyroscope with an output power of 4.1 mW at 80 °C, Opt. Express. 30 (6) (2022) 8991.

4. **Fu Q., Sun Y., Yu S., Wang A., Yin J., Zhao Y., Dong J.,** Low Threshold Current and Polarization-Stabilized 795 nm Vertical-Cavity Surface-Emitting Lasers, Nanomaterials. 13 (6) (2023) 1120.

5. **Zhang J., Zhang X., Zhu H., Zhang J., Ning Y., Qin L., Wang L.,** High-temperature operating 894.6nm-VCSELs with extremely low threshold for Cs-based chip scale atomic clocks, Opt. Express. 23 (11) (2015) 14763.

6. **Ii X., Zhou Y., Zhang X., Zhang J., Zeng Y., Ning Y., Wang L.,** High-power single-mode 894 nm VCSELs operating at high temperature (>2 mW @ 365 K), Appl. Phys. B. 128 (1) (2022) 16.

7. **Gruet F., Al-Samaneh A., Kroemer E., Bimboes L., Miletic D., Affolderbach C., Wahl D., Boudot R., Mileti G., and Michalzik R.,** Metrological characterization of custom-designed 8946 nm VCSELs for miniature atomic clocks, Opt. Express. 21 (5) (2013) 5781.

8. **Blokhin S.A., Kovach Ya.N., Bobrov M.A., Blokhin A.A., Maleev N.A., Kuzmenkov A.G., Zadiranov Yu.M., Kulagina M.M., Guseva Yu.A., Vasil'ev A.P., Ustinov V.M.,** Vertical-cavity surfaceemitting lasers for compact atomic sensors, St. Petersburg State Polytechnical University Journal. Physics and Mathematics. 16 (3.2) (2023) 16–22.

9. **Kroemer E., Rutkowski J., Maurice V., Vicarini R., Hafiz M.A., Gorecki C., Boudot R.,** Appl. Opt. 55 (31) (2016) 8839.

10. **Di Domenico G., Schilt S., Thomann P.,** Simple approach to the relation between laser frequency noise and laser line shape, Appl. Opt. 49 (25) (2010) 4801.

11. **Kovach Ya.N., Blokhin S.A., Bobrov M.A., Blokhin A.A., Maleev N.A., Vasil'ev A.P.,** Temperature influence on the spectral linewidth of 89X nm single-mode VCSELs, St. Petersburg State Polytechnical University Journal. Physics and Mathematics. 18 (1.1) (2025) 128–133.

12. **Westbergh P., Gustavsson J., Kugel B., Haglund A., Larsson A.,** Impact of photon lifetime on high-speed VCSEL performance, IEEE Journal of Selected Topics in Quantum Electronics. 17 (6) (2012) 1603–1613.

THE AUTHORS

BOBROV Mikhail A.
bma@mail.ioffe.ru
ORCID: 0000-0001-7271-5644

BLOKHIN Selgey A.
blokh@mail.ioffe.ru
ORCID: 0000-0003-4858-4968

KOVACH Yakov N.
J-n-kovach@mail.ioffe.ru
ORCID: 0000-0002-0048-7514

BLOKHIN Alexey A.
Aleksey.Blokhin@mail.ioffe.ru
ORCID: 0000-0002-3449-8711

MALEEV Nikolay A.
maleev@beam.ioffe.ru
ORCID: 0000-0003-2500-1715

KUZMENKOV Alexander G.
kuzmenkov@mail.ioffe.ru
ORCID: 0000-0002-7221-0117

MARCHIJ Mariya N.
M.N.Marchij@mail.ioffe.ru

VASIL'EV Alexey P.
Vasiljev@mail.ioffe.ru
ORCID: 0000-0002-2181-5300

Received 16.12.2025. Approved after reviewing 03.03.2026. Accepted 13.03.2026.

© Peter the Great St. Petersburg Polytechnic University, 2026

Conference paper
UDC 53
DOI: https://doi.org/10.18721/JPM.191.118

Illumination and temperature dependence of optical interactions in multijunction solar cells

P.D. Kornienko [1]✉, V.S. Epoletov [1], S.A. Levina [1], V.R. Larionov [1], M.A. Mintairov [1], M.V. Nakhimovich [1], M.Z. Shvarts [1]

Ioffe Institute, St. Petersburg, Russia

✉ p.d.kornienko@mail.ioffe.ru

Abstract. Optical interactions in multijunction solar cells result from radiative charge carrier recombination in a wide-bandgap subcell, which generates additional photocurrent in a narrower-bandgap subcell via photovoltaic conversion of the emitted photons. This paper proposes a method for the experimental determination of the optical interactions efficiency, including the measurement of its limiting (saturation) value, γ_S. The method was tested on triple-junction GaInP/GaAs/Ge solar cells. The parameter γ_S was recorded at ultra-high current densities through the *p–n* junction, achieved using small-area samples and specialized equipment. The relationship between the obtained values and the properties of the semiconductor structure is discussed, including the temperature dependence of the radiative recombination efficiency (luminescence intensity).

Keywords: multijunction solar cells, optical interactions, electroluminescence intensity, saturation current

Citation: Kornienko P.D., Epoletov V.S., Levina S.A., Larionov V.R., Mintairov M.A, Nakhimovich M.V., Shvarts M.Z., Illumination and temperature dependence of optical interactions in multijunction solar cells, St. Petersburg State Polytechnical University Journal. Physics and Mathematics. 19 (1.1) (2026) 111–116. DOI: https://doi.org/10.18721/JPM.191.118

This is an open access article under the CC BY-NC 4.0 license (https://creativecommons.org/licenses/by-nc/4.0/)

Конференционная статья
УДК 53
DOI: https://doi.org/10.18721/JPM.191.118

Зависимость оптических взаимодействий в каскадных солнечных элементах от освещенности и температуры

П.Д. Корниенко ✉, В.С. Эполетов, С.А. Левина, В.Р. Ларионов, М.А. Минтаиров, М.В. Нахимович, М.З. Шварц

Физико-технический институт им. А.Ф. Иоффе РАН, Санкт-Петербург, Россия

✉ p.d.kornienko@mail.ioffe.ru

Аннотация. Оптические взаимодействия в многопереходных солнечных элементах являются следствием процесса излучательной рекомбинации носителей заряда в широкозонном субэлементе с соответствующей этому генерацией дополнительного фототока в более узкозонном субэлементе при фотоэлектрическом преобразовании излученных фотонов. В статье предложена методика экспериментального определения эффективности оптических взаимодействий, включающая регистрацию ее предельного значения γ_S. Методика апробирована на трехпереходных солнечных элементах GaInP/GaAs/Ge. Регистрация параметра γ_S осуществлялась при сверхвысоких плотностях тока через *p–n*-переход, что достигалось использованием малоразмерных образцов и специализированного оборудования. Обсуждается связь полученных значений со свойствами полупроводниковой структуры, в том числе зависимость эффективности излучательной рекомбинации (интенсивности люминесценции) от температуры.

© Kornienko P.D., Epoletov V.S., Levina S.A., Larionov V.R., Mintairov M.A, Nakhimovich M.V., Shvarts M.Z., 2026. Published by Peter the Great St. Petersburg Polytechnic University.

Ключевые слова: многопереходные солнечные элементы, оптические взаимодействия, интенсивность электролюминесценции, ток насыщения

Ссылка при цитировании: Корниенко П.Д., Эполетов В.С., Левина С.А., Ларионов В.Р., Минтаиров М.А., Нахимович М.В., Шварц М.З. Зависимость оптических взаимодействий в каскадных солнечных элементах от освещенности и температуры // Научно-технические ведомости СПбГПУ. Физико-математические науки. 2026. Т. 19. № 1.1. С. 111–116. DOI: https://doi.org/10.18721/JPM.191.118

Статья открытого доступа, распространяемая по лицензии CC BY-NC 4.0 (https://creativecommons.org/licenses/by-nc/4.0/)

Introduction

The record conversion efficiencies demonstrated by multijunction (MJ) solar cells (SCs) based on A_3B_5 semiconductor compounds make them particularly attractive for both space and specialized terrestrial applications [1, 2]. MJ SCs with record-breaking efficiency are based on high-quality direct-bandgap semiconductors (e.g., GaAs, GaInP), where radiative recombination of charge carriers dominates. Radiation generated in a wide-bandgap (WB) subcell can be absorbed in an adjacent narrower-bandgap (NB) subcell that is in an optical contact with it. This process of optical interaction results in the generation of an additional luminescence-induced photocurrent in the radiation-receiving subcell.

Radiative recombination in a WB subcell – and consequently, the optical interactions (OI) it initiates – occurs when a portion of the photogenerated carriers recombine within the *p–n* junction instead of being extracted into the external circuit. This situation is realized under a mismatch (difference) in the photocurrents of the subcells, which can arise either during device operation or be intentionally created to study the characteristics of an MJ SC. Correctly assessing the influence of OI is an important practical task, as this effect introduces systematic artifacts into the measured spectral quantum efficiency dependencies of MJ SCs [3, 4]. Moreover, a numerical description of OI can serve as a tool for determining the internal properties of the heterostructure. In this work, the model from Ref. [5] is chosen to describe OI. Its fundamental equation can be written as:

$$\gamma = \gamma_S \frac{J_{rd}}{4J_{pn}}\left(1-\sqrt{1+\frac{4J_{pn}}{J_{rd}}}\right)^2, \quad (1)$$

where γ_S and J_{rd} are two physically meaningful model parameters: the limiting OI efficiency and the current boundary between the recombination and diffusion sections of the current-voltage (*I–V*) characteristic of the emitting *p–n* junction, respectively.

According to the two-diode model, the current through the *p–n* junction J_{pn} is defined as the sum of the diffusion (diode ideality factor $A = 1$) and recombination ($A = 2$) components:

$$J_{pn} = J_1 + J_2 = J_{01}\left[\exp\left(\frac{qV}{kT}\right)-1\right] + J_{02}\left[\exp\left(\frac{qV}{2kT}\right)-1\right], \quad (2)$$

where V is the applied voltage, k is the Boltzmann constant, T is the temperature in kelvins, J_{01} and J_{02} are the diffusion and recombination reverse saturation currents, respectively.

The OI efficiency γ is defined for a pair of adjacent subcells. Consider a case where a WB subcell generates an excess photocurrent J_W under external broad-spectrum illumination, while a NB subcell generates a lower photocurrent J_{N0}. The luminescent radiation from the WB *p–n* junction propagates through the monolithic MJ SC structure and is absorbed by the NB subcell, increasing its current to a value J_N. Under the short-circuit condition of the NB subcell, the total output current of the MJ SC in a general case is given by J_N. Consequently, the current through the emitting *p–n* junction can be expressed as [5]:

$$J_{pn} = J_W - J_N. \quad (3)$$

© Корниенко П.Д., Эполетов В.С., Левина С.А., Ларионов В.Р., Минтаиров М.А., Нахимович М.В., Шварц М.З., 2026. Издатель: Санкт-Петербургский политехнический университет Петра Великого.

From here on the OI efficiency will be defined as the ratio of the luminescence-induced current J_L to the excess current in the WB subcell's *p–n* junction:

$$\gamma = \frac{J_N - J_{N0}}{J_W - J_N} = \frac{J_L(J_{pn})}{J_{pn}}. \quad (4)$$

The key parameter for describing OI is its limiting efficiency γ_S, which is attained under the condition $J_1 >> J_2$. The second model parameter, J_{rd}, defines the point where $J_1 = J_2$, referred to above (see expression (1)) as the current boundary between the recombination and diffusion sections of the dark *I–V* characteristic of the emitting *p–n* junction [5]:

$$J_{rd} = \frac{J_{02}^2}{J_{01}}. \quad (5)$$

Previous experimental studies of OI in MJ SCs [5, 6] were conducted in the range of low current densities through the *p–n* junction, where direct observation of the OI efficiency reaching its saturation mode is not feasible. Consequently, the experimental data were approximated using expression (1) (or its analogues), which involves fitting both parameters (γ_S and J_{rd}) simultaneously, thereby reducing the accuracy of their estimation. This work presents a method for the direct experimental determination of the parameter γ_S.

Materials and Methods

The study of OI was performed using GaInP/GaAs/Ge triple-junction SC. To operate under ultra-high current density conditions, small-area (~0.4 mm²) devices were fabricated (the SC configuration was comparable in size with laser power converter [7]).

The experiment was based on recording the *I–V* curves under different ratios of photocurrents generated by the subcells of the MJ SC. This was achieved using lasers with emission wavelengths corresponding to the spectral sensitivity ranges of the subcells (532 nm, 810 nm, and 1064 nm). The laser radiation was delivered to the MJ SC through an optical fiber with a beam combiner and attached terminal optical homogenizer. To prevent overheating of the SC, a pulsed laser operation mode was employed. The sample was fixed on a thermostabilized platform with a Peltier unit monitored by a temperature controller.

According to the principles governing the *I–V* curves formation of MJ SCs [8, 9], when the bottom (Ge) subcell exhibits a sharply rising characteristic under reverse bias, the resulting dependence features two horizontal sections (Fig. 1, *b*): the first "plateau" corresponds to the short-circuit current of the middle subcell, and the second to that of the bottom subcell. This allows the current of the bottom subcell to be determined directly from the MJ SC *I–V* curve, which simplifies the methodology for tracing the OI efficiency (such methods typically require the synchronous measurement of photogenerated currents from individual subcells).

As a result of selective (external) illumination of the top, middle, and bottom subcells, the photocurrents $I_{top}^{ext}, I_{mid}^{ext}$ and I_{bot}^{ext} are generated, respectively. Depending on the applied voltage, V_1 or V_2 (see Fig. 1), current flows through the *p–n* junctions of the subcells, initiating electroluminescence. Part of this emitted radiation induces a photocurrent in the adjacent subcell. Consequently, the photocurrent of the radiation-receiving subcell consists of two components: the current I^{ext} induced by the external radiation and the current $I^L = \gamma \cdot I^{pn}$ induced by OI.

To find the induced currents, two operating regimes are analyzed (see Fig. 1). When the middle subcell is biased in short-circuit point (Fig. 1, *a*), the resulting absorption of luminescence from the GaInP *p–n* junction augments the photocurrent in the GaAs subcell: $I'_{mid} = I_{mid}^{ext} + I_{mid}^{L}$. Similarly, a current $I'_{bot} = I_{bot}^{ext} + I_{bot}^{L}$ is recorded under the short-circuit condition of the Ge (bottom) subcell. Consequently, even when $I_{bot}^{ext} = 0$, the measured photocurrent is non-zero due to electroluminescence from the WB *p–n* junctions.

To determine the OI efficiency, it is necessary to compare the currents generated by each subcell at different points on the $I-V$ characteristic [8]. The current through the emitting (GaInP) *p–n* junction could be written as:

$$I_1^{pn} = I_{top}^{ext} - I'_{mid}, \quad (6a)$$

$$I'_{mid} = I_{mid}^{ext} + \gamma^{tm} \cdot I_1^{pn}, \quad (6b)$$

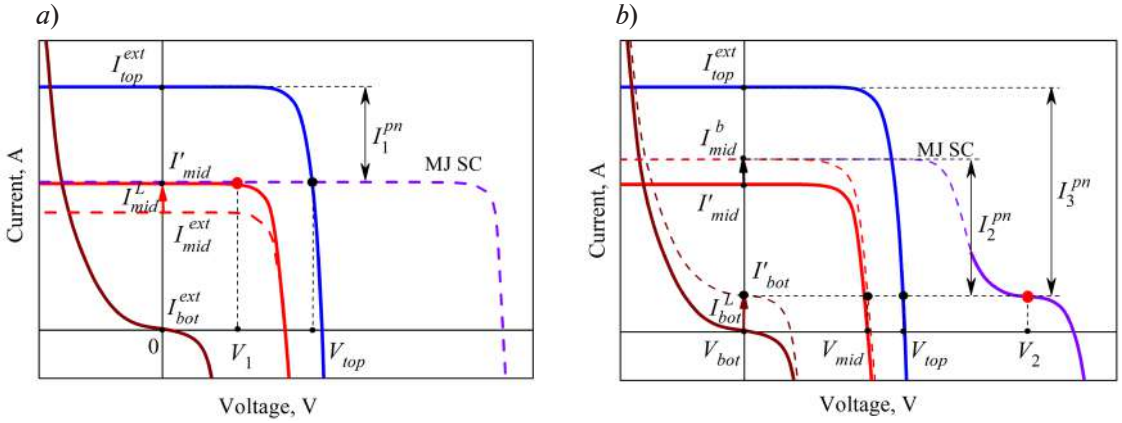

Fig. 1. $I-V$ curves of the subcells with the middle (*a*) and bottom (*b*) subcell under the short-circuit condition.
The lines "MJ SC" correspond to the total $I-V$ curve of the MJ SC

where γ^{tm} is the OI efficiency for the GaInP–GaAs subcell pair.

It should be noted that all currents appearing in equations (6) can be measured experimentally, enabling the calculation of the parameter γ^{tm}. To obtain I_{top}^{ext}, it is sufficient to record the total I–V curve of the MJ SC under conditions where $I_{mid}^{ext} > I_{top}^{ext}$ and $I_{bot}^{ext} > I_{top}^{ext}$. To identify I_{mid}^{ext} the current at the first plateau of the I–V curve is measured under a condition of photocurrent balance between the top and middle subcells: $I_{mid}^{ext} = I_{top}^{ext}$. In this balanced state, both subcells are effectively short-circuited, ensuring $I_{mid}^{L} = 0$.

When the second plateau on the I–V curve is recorded (see Fig. 1, *b*), the Ge subcell operates under the short-circuit condition, generating a current I'_{bot}. In this regime, the current of the middle subcell differs from its value I'_{mid}, extracted from the total I–V characteristic in the previously discussed case (Fig. 1, *a*). During the transition from middle-subcell to bottom-subcell current limitation, the middle subcell current increases to a new value, denoted here as I_{mid}^{b}. A cascade optical interaction is observed: the Ge subcell becomes coupled to both upper WB p–n junctions. The currents through these emitting junctions are given by:

$$I_2^{pn} = I_{mid}^{b} - I'_{bot}, \tag{7a}$$

$$I_3^{pn} = I_{top}^{ext} - I'_{bot}. \tag{7b}$$

The corresponding addition to the current of the middle subcell can be expressed as:

$$I_{mid}^{b} - I'_{mid} = \gamma^{tm} \cdot I_3^{pn}, \tag{7c}$$

while the total current of the bottom subcell is:

$$I'_{bot} = I_{bot}^{ext} + \gamma^{mb} \cdot I_2^{pn}, \tag{7d}$$

where γ^{mb} is the OI efficiency for the GaAs-Ge pair.

Thus, following the reasoning applied to the group of equations (6), all currents appearing in expressions (7) can be obtained experimentally, which enables the parameter γ^{mb} to be found.

Results and Discussion

Fig. 2, *a* presents the OI efficiency values for the GaInP-GaAs and GaAs-Ge pairs over a current density range of 20 to 60 A/cm^2. All experimental data points were obtained using the methodology described above. Achieving high current densities through the p–n junction enables observation of the saturation region of the function $\gamma(J_{pn})$, where the condition $J_1 >> J_2$ is met and the value of γ remains constant. The limiting OI efficiency values for the sample under study (i.e. for the certain multijunction heterostructure) can be estimated as $\gamma_S^{tm} \approx 0.1$ and $\gamma_S^{mb} \approx 0.6$.

The data presented in Fig. 2, *a* were acquired at room temperature. To identify the reasons for the lower OI efficiency in the GaInP-GaAs pair compared to the GaAs-Ge, the temperature

dependences of the electroluminescence intensity from the respective emitting *p–n* junctions were investigated (Fig. 2, *b*). For GaAs, as expected, the electroluminescence intensity – and consequently the parameter γ_S – increases with decreasing temperature, which is attributed to a reduction in the non-radiative recombination rate. In contrast, and consistent with the study in [10], GaInP exhibits an inverse anomalous trend: at low temperatures, a region is observed where the electroluminescence intensity increases with rising temperature, followed by a gradual decline. This behavior is presumably due to the thermal activation energy of the dominant non-radiative recombination center being lower than that of the radiative recombination channel.

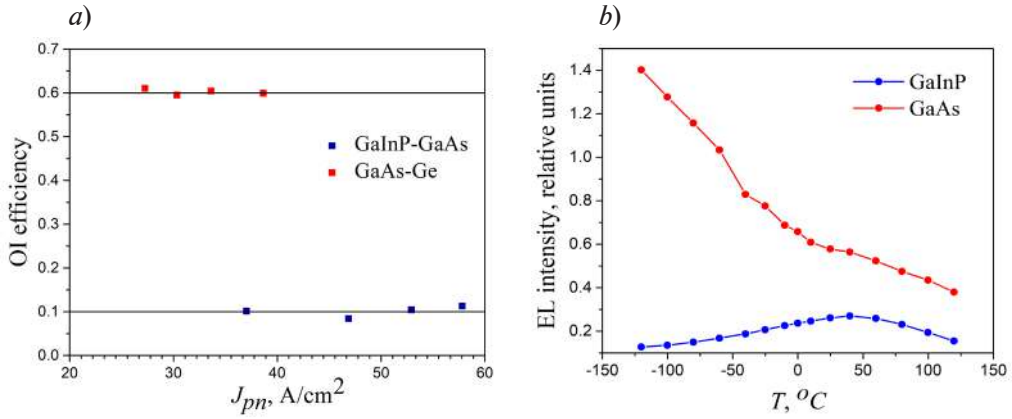

Fig. 2. Dependence of the OI efficiency on the current through the emitting *p–n* junction (*a*) and temperature dependences of the electroluminescence (EL) intensity from the emitting *p–n* junctions (*b*)

Based on the experimental data, the values of the parameter J_{rd} were determined for the GaInP and GaAs *p–n* junctions (Table 1). For comparison, this parameter was also calculated for a reference sample with an identical internal structure but a larger junction area (S_{pn}). The discrepancy observed for the top (GaInP) subcell may be attributed to an increased density of surface defects in the sample of larger size.

Table 1

J_{rd} values for the emitting *p–n* junctions

Subcell	J_{rd} value	
	$S_{pn} = 0.4$ mm^2	$S_{pn} = 4$ mm^2
GaInP	0.4	0.92
GaAs	0.51	0.51

Conclusion

An experimental methodology for determining the efficiency of optical interaction between subcells over a wide range of currents through the emitting *p–n* junctions has been developed and implemented. Applied to triple-junction GaInP/GaAs/Ge solar cells, this method yielded the values of the limiting optical interaction efficiency γ_S and the characteristic current J_{rd}.

Temperature dependences of the electroluminescence intensity from the emitting junctions were investigated. The GaInP subcell exhibits an anomalous temperature dependence, which may be attributed to the thermalization of non-radiative recombination centers in the material and the presence of surface states.

The parameters obtained for multijunction solar cells using this methodology, particularly the limiting optical interaction efficiency, can be employed to improve the accuracy of theoretical modeling and to mitigate the adverse influence of measurement artifacts that arise during the recording of spectral responsivity dependencies.

REFERENCES

1. **Green M.A., Dunlop E.D., Yoshita M., Kopidakis N., Bothe K., Siefer G., Hinken D., Rauer M., Hohl-Ebinger J., Hao X.,** Solar cell efficiency tables (Version 66), Progress in Photovoltaics: Research and Applications. 32(7) (2024) 425–441.

2. **Mejía Escobar M.A., Algora C.,** Surveying the potential of flexible and high-specific-power photovoltaic assemblies and arrays for space applications, Joule. 9(11) (2025) 102194.

3. **Li J.-J., Lim S.H., Allen C.R., Ding D., Zhang Y.-H.,** Combined Effects of Shunt and Luminescence Coupling on External Quantum Efficiency Measurements of Multijunction Solar Cells, IEEE Journal of Photovoltaics. 1(2) (2011) 225–230.

4. **Barrigyn E., Espinet-González P., Contreras Y., Rey-Stolle I,** Why can't I measure the external quantum efficiency of the Ge subcell of my multijunction solar cell? AIP Conference Proceedings. 1679 (2015) 050002.

5. **Shvarts M.Z., Mintairov M.A., Emelyanov V.M., Evstropov V.V., Lantratov V.M., Timoshina N.Kh.,** Method for direct measurements of luminescent coupling efficiency in concentrator MJ SCs, AIP Conference Proceedings. 1556 (2013) 147–150.

6. **Allen C.R., Lim S.H., Li J.-J., Zhang Y.-H.,** Simple method for determining luminescence coupling in multi-junction solar cells, Proceedings of 37th IEEE Photovoltaic Specialists Conference (PVSC). (2011) 000452–000453.

7. **Kalyuzhnyy N.A., Malevskaya A.V., Mintairov S.A., Mintairov M.A., Nakhimovich M.V., Salii R.A., Shvarts M.Z., Andreev V.M.,** Photovoltaic AlGaAs/GaAs devices for conversion of high-power density laser (800–860 nm) radiation, Sol. Energy Mater. Sol. Cells. 262 (2023) 112551.

8. **Levina S.A., Emelyanov V.M., Filimonov E.D., Mintairov M.A., Shvarts M.Z., Andreev V.M.,** Cascade optical coupling and quantum efficiency measurements of MJ SCs, Solar Energy Materials and Solar Cells. 180 (2018) 233–241.

9. **Levina S.A., Filimonov E.D., Mintairov M.A., Shvarts M.Z.,** Multijunction solar cells with pronounced optical coupling: Single wavelength laser biasing approach at quantum efficiency measurements, AIP Conference Proceedings. 2012 (2018) 100003.

10. **Shvarts M.Z., Emelyanov V.M., Mintairov M.A., Evstropov V.V., Timoshina N. Kh.,** Temperature influence on luminescent coupling efficiency in concentrator MJ SCs, AIP Conference Proceedings. 1679 (2015) 120003.

THE AUTHORS

KORNIENKO Polina D.
p.d.kornienko@mail.ioffe.ru
ORCID: 0009-0006-8993-4142

MINTAIROV Mikhail A.
mamint@mail.ioffe.ru
ORCID: 0000-0002-3481-477X

EPOLETOV Vadim S.
Vadep@mail.ioffe.ru
ORCID: 0009-0004-3925-6289

NAKHIMOVICH Mariia V.
NMar@mail.ioffe.ru
ORCID: 0009-0005-4371-1077

LEVINA Svetlana A.
levina@mail.ioffe.ru
ORCID: 0000-0003-4554-3300

SHVARTS Maxim Z.
shvarts@scell.ioffe.ru
ORCID: 0000-0002-2230-7770

LARIONOV Valeri R.
larion@scell.ioffe.ru

Received 14.12.2025. Approved after reviewing 05.02.2026. Accepted 05.02.2026.

© Peter the Great St. Petersburg Polytechnic University, 2026

Conference paper
UDC 629.7.064.56
DOI: https://doi.org/10.18721/JPM.191.119

Prospects of hybrid bifacial four-junction solar cell for concentrating photovoltaics

K.K. Prudchenko [1]✉, E.V. Kontrosh [1], I.A. Tolkachev [1], S.N. Abolmasov [2], V.S. Kalinovskii [1], E.I. Terukov [1,2]

[1] Ioffe Institute, St. Petersburg, Russia;
[2] R&D center for thin film technologies in energetics, St. Petersburg, Russia
✉ prudchenkokk@mail.ioffe.ru

Abstract. A hybrid monolithic four-junction solar cell composed of GaInP/Ga(In)As/Ge electricity-generating linear arrays arranged in an *n*-α-Si:H/(*p*)*c*-Si:(Ga)/*p*-a-Si:H bifacial photoactive heat-dissipating substrate was investigated as part of a concentrator photovoltaic module. The module provides a specific power output ≤ 500 W/m^2 (AM0, 1367 W/m^2) at the beginning of life, taking into account the converted the Earth albedo. The damage coefficient of effective diffusion length for minority charge carriers in the photoactive heat-dissipating substrate has been determined as $K_L = 1 \cdot 10^{-11}$ at 1 MeV electron fluence up to $1 \cdot 10^{15}$cm^{-2}. The anticipated lifespan of the monolithic hybrid four-junction solar cell in the module on geostationary orbit is projected to be ≤ 15 years. Accounting for the albedo effects, it does not only increase the generated electrical power but also reduces thermal stress on the spacecraft's solar panel.

Keywords: hybrid four-junction solar cell, concentrator photovoltaic module, albedo of the Earth, GaInP/Ga(In)As/Ge electricity-generating linear arrays, bifacial photoactive heat dissipating substrate, damage coefficient, geostationary orbit

Citation: Prudchenko K.K., Kontrosh E.V., Tolkachev I.A., Abolmasov S.N., Kalinovskii V.S., Terukov E.I., Prospects of hybrid bifacial four-junction solar cell for concentrating photovoltaics, St. Petersburg State Polytechnical University Journal. Physics and Mathematics. 19 (1.1) (2026) 117–122. DOI: https://doi.org/10.18721/JPM.191.119

This is an open access article under the CC BY-NC 4.0 license (https://creativecommons.org/licenses/by-nc/4.0/)

Конференционная статья
УДК 629.7.064.56
DOI: https://doi.org/10.18721/JPM.191.119

Перспективы двухстороннего четырехпереходного гибридного солнечного элемента для концентраторной фотовольтаики

К.К. Прудченко [1]✉, Е.В. Контрош [1], И.А. Толкачев [1], С.Н. Аболмасов [2], В.С. Калиновский [1], Е.И. Теруков [1, 2]

[1] Физико-технический институт им. А.Ф. Иоффе РАН, Санкт-Петербург, Россия;
[2] ООО «НТЦ тонкопленочных технологий в энергетике», Санкт-Петербург, Россия
✉ prudchenkokk@mail.ioffe.ru

Аннотация. Монолитный гибридный четырехпереходный солнечный элемент на основе GaInP/Ga(In)As/Ge электрогенерирующих линеек и *n*-α-Si:H/(*p*)c-Si:(Ga)/*p*-α-Si:H двухстороннего фотоактивного теплоотводящего основания был исследован в составе концентраторного фотоэлектрического модуля. Концентраторный фотоэлектрический модуль для солнечных батарей нового поколения способен обеспечить в начале срока службы удельную мощность ≤ 500 Вт/м^2 (AM0, 1367 Вт/м^2) с учётом альбедо Земли. Определён «эффективный» коэффициент деградации диффузионной длины неосновных носителей заряда фотоактивного теплоотводящего основания $K_L = 1 \cdot 10^{-11}$. Ожидаемый срок службы гибридного

© Prudchenko K.K., Kontrosh E.V., Tolkachev I.A., Abolmasov S.N., Kalinovskii V.S., Terukov E.I., 2026. Published by Peter the Great St. Petersburg Polytechnic University.

четырехпереходного солнечного элемента в составе модуля составит ≤ 15 лет на геостационарной орбите. Учёт альбедо Земли позволяет не только увеличить вырабатываемую электрическую мощность, но и снизить тепловую нагрузку на солнечную батарею космического аппарата.

Ключевые слова: гибридный четырехпереходный солнечный элемент, концентраторный фотоэлектрический модуль, альбедо Земли, GaInP/Ga(In)As/Ge электрогенерирующие линейки, двухстороннее фотоактивное теплоотводящее основание, коэффициент деградации, геостационарная орбита

Ссылка при цитировании: Прудченко К.К., Контрош Е.В., Толкачев И.А., Аболмасов С.Н., Калиновский В.С., Теруков Е.И. Перспективы двухстороннего четырехпереходного гибридного солнечного элемента для концентраторной фотовольтаики // Научно-технические ведомости СПбГПУ. Физико-математические науки. 2026. Т. 19. № 1.1. С. 117–122. DOI: https://doi.org/10.18721/JPM.191.119

Статья открытого доступа, распространяемая по лицензии CC BY-NC 4.0 (https://creativecommons.org/licenses/by-nc/4.0/)

Introduction

The presented research aims to enhance concentrated photovoltaic module (CPVM) based on three-junction GaInP/GaAs/Ge solar cells (SCs). An increase in specific electrical power in radiation-exposed environments could be achieved by employing a hybrid (concentrator-planar) four-junction (4-J) SC with bifacial photosensitivity. The development of a bifacial hybrid 4-J SC involves monolithic bonding a GaInP/Ga(In)As/Ge SC with a silicon heterojunction (SHJ) *n*-α-Si:H/(*p*)*c*-Si:(Ga)/*p*-α-Si:H SC, serving as a photoactive heat-dissipating substrate (PHDS), utilizing vacuum soldering techniques. It was motivated by two key factors: firstly, the exceptionally high conversion efficiencies achieved by SHJ SCs with gallium-doped *p*-type substrates, reaching over 26% under standard terrestrial sunlight conditions (1000 W/m², AM1.5) [1]; secondly, addressing the challenge posed by radiation-induced performance degradation of SHJ SCs, where efficiency loss remains below 30% (at a fluence of 1 MeV electrons of $1 \cdot 10^{15}$ cm^{-2}) under space environmental conditions (1367 W/m^2, AM0) [2]. Enhanced specific electrical power in bifacial hybrid 4-J SCs is achieved not only through improvements in the efficiency of GaInP/Ga(In)As/Ge SCs, but also by converting reflected scattered solar radiation into usable energy by the SHJ PHDS, including contributions from Earth's albedo [3, 4]. It should be noted that such hybrid systems maintain functionality even under conditions of misalignment relative to the Sun greater than ±2° [4].

To determine the operational lifetime of CPVM on geostationary Earth orbit (GEO), the degradation extent of a 4-J hybrid SC resulting from radiation exposure was assessed by evaluating the damage coefficient of minority carrier diffusion length. In 4-J hybrid SC, radiation hardness will be constrained by the silicon subcell due to lower absorption coefficient and electron/hole mobilities compared to III-V semiconductor materials. A fluence of 1 MeV electrons equivalent to $1 \cdot 10^{15}$ cm^{-2} corresponds to nonionizing radiation effects accumulated in GEO environment over a period of 15 years [5].

Materials and Methods

Investigations were carried out on a CPVM (Fig. 1), representing an elementary cell upon which the solar panel is built. The photovoltaic component of the CPVM is mounted onto a carbon fiber supporting frame. It ensures reduction of specific weight characteristics of the solar panel down to 2 kg/m^2. Moreover, it successfully passes all necessary ground tests simulating mechanical stresses encountered in outer space, such as thermal cycling, vibration, and shock impacts. On the front side of the assembly, a paired linear Fresnel lens concentrator (LC) with a focal distance of 32 mm, an optical area of 50 mm × 100 mm, and an efficiency of 90% is located. On the backside, a bifacial 4-J hybrid SC (Fig. 2, *a*) is positioned. Ohmic contacts for the 4-J SC were established by installing two electricity-generating linear arrays (EGLAs) with a size of 54 mm × 104 mm × 0.15 mm on the bifacial *n*-α-Si:H/(*p*)c-Si:(Ga)/*p*-a-Si:H

© Прудченко К.К., Контрош Е.В., Толкачев И.А., Аболмасов С.Н., Калиновский В.С., Теруков Е.И., 2026. Издатель: Санкт-Петербургский политехнический университет Петра Великого.

SHJ PHDS. These components were assembled using a specialized vacuum-brazing technique performed on the R200C (Savtech, Russia) machine [6]. Each EGLA consists of 18 thinned GaInP/Ga(In)As/Ge SCs with dimensions 5.6 mm × 6.4 mm, with thickness reduced to 80 μm. Additionally, the CPVM design includes an optical reflector system (indicated by 4 and 6 in Fig. 1, *a*) aimed at further improving the device performance.

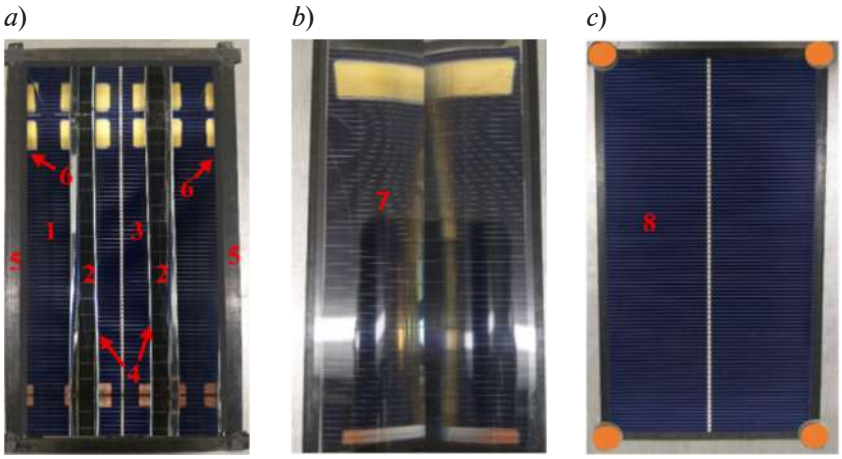

Fig. 1. Photographs of the CPVM with a bifacial 4-J hybrid SC: front side without LC (*a*), front side with LC (*b*), and rear side (*c*); (1) corresponds to bifacial 4-J hybrid SC, (2) to GaInP/Ga(In)As/Ge EGLA, (3) to SHJ PHDS, (4) to side reflectors, (5) to carbon fiber composite support frame, (6) to reflectors on frame walls, (7) to paired linear Fresnel LC, (8) to rear side of the hybrid SC in CPVM

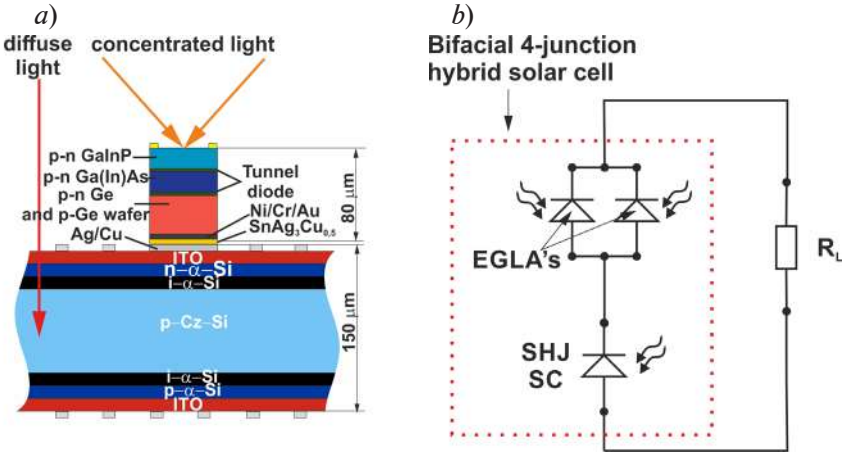

Fig. 2. Schematic representation of the bifacial 4-J hybrid SC structure (*a*) and schematic electric connection diagram of GaInP/Ga(In)As/Ge EGLAs with SHJ PHDS in CPVM (*b*), where R_L denotes the load resistance

To evaluate radiation hardness, *n*-α-Si:H/(*p*)c-Si:(Ga)/*p*-a-Si:H SHJ SCs with an area of 1 cm^2, and a resistivity ranging between (1.5–4.0) Ω·cm, were manufactured. Samples were irradiated by 1 MeV electrons with fluences ranging from $2.5 \cdot 10^{14}$ to $1 \cdot 10^{15}$ cm^{-2}. Details regarding the irradiation conditions are provided in Ref. [2]. Before and after electron irradiation, both dark and light current-voltage characteristics (*I–V* curves) were measured. Dark *I–V* curves of the SHJ SCs were acquired at room temperature using a high-precision source-measurement unit. Light *I–V* curves of the SHJ SCs with an active optical area of 0.9 cm^2, as well as those of the CPVM and individual circuit elements (Fig. 2, *b*), were recorded under collimated simulated solar illumination (AM0, 1367 W/m^2) at room temperature.

Results and Discussion

Figure 3 shows light *I–V* curves for the studied CPVM under normal incidence of collimated light beam (AM0, 1367 W/m^2), illustrating the interconnection layout (Fig. 2, *b*) optimized

for photocurrent matching between EGLAs and the SHJ PHDS to maximize power output, considering the albedo effect. Further refinement of the CPVM design is needed for more precise alignment. Two parallel-connected EGLAs provide open-circuit voltage values of 2.84 V and generate a specific electrical power of 396 W/m^2 at an efficiency of 29% (Fig. 3, curves 1,1'). Meanwhile, the SHJ PHDS converts diffuse radiation, due to albedo, thus generating additional electrical power (Fig. 3, curves 3,3'). Thus, the bifacial 4-J hybrid SC integrated into the CPVM and matched in terms of photocurrent delivers a specific power output of 489 W/m^2 at an efficiency of 29.3% and an open-circuit voltage of 3.5 V (Fig. 3, curves 2,2'). The power increase of the CPVM equipped with bifacial 4-J hybrid SC amounts to 19% at the beginning of life without adding complexity, weight, and cost to the overall concentrator module structure. Accounting for the influence of albedo not only enhances the generated electrical power but also alleviates thermal loading on the satellite's solar panel.

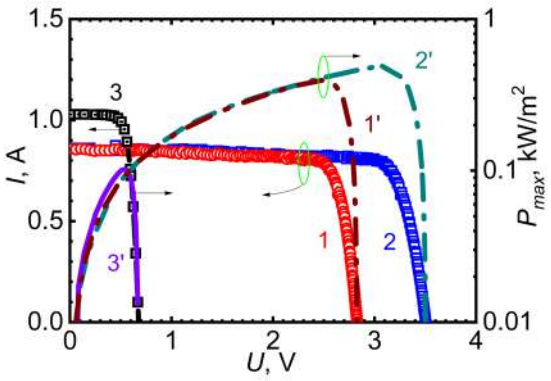

Fig. 3. Light I–V (curves 1–3) and calculated P_{max}-V (curves 1′–3′) characteristics measured under simulated solar illumination (AM0, 1367 W/m^2) with LC efficiency of ~90%: 1, 1′ correspond to only parallel-connected GaInP/Ga(In)As/Ge EGLA; 2, 2′ to bifacial 4-J hybrid SC with parallel-connected EGLA with SHJ PHDS connected in series, accounting for albedo; 3, 3′ to SHJ Si PHDS with albedo

The evaluation of the CPVM's operational lifetime on GEO is based on determining its radiation hardness when exposed to 1 MeV electrons with fluences up to $1\cdot10^{15}$ cm^{-2}. Since the limiting component of the CPVM structure is the SHJ PHDS, the analysis of radiation hardness focuses on this element. Given the substantial decrease in the external quantum efficiency into long-wave region [2], we assume that the crystalline silicon substrate degrades predominantly. Under electron fluences up to $1\cdot10^{15}$ cm^{-2}, where processes related to the removal of majority charge carriers play a secondary role [7], the principal indicator of degradation is the reduction in minority carrier diffusion length due to defect introduction (recombination centers). This reduction is characterized by the damage coefficient of diffusion length, which is defined by Equation (1):

$$\frac{1}{L_{eff}^{\ 2}} - \frac{1}{L_0^{\ 2}} = K_L \phi, \tag{1}$$

where L_0 and L_{eff} are the the effective diffusion lengths of minority charge carriers before and after irradiation, Φ is the fluence of 1 MeV electrons, K_L is the damage coefficient of the diffusion length of minority charge carriers. Since the SHJ PHDS represents a p–i–n heterostructure consisting of amorphous/crystalline silicon, the pre-irradiation "effective" diffusion length for the PHDS was assumed to be approximately 1100 μm in calculations [8]. As demonstrated in Ref. [9], the damage coefficient K_L is correlated with saturation currents through Eqs. (2) and (3):

$$J_{0r\phi} = J_{0r0}(K_L L_0^{\ 2}\phi + 1)\sqrt{\frac{p_0}{p_0 - R_c\phi}}, \tag{2}$$

$$J_{0d\phi} = J_{0d0}\sqrt{K_L L_0^{\ 2}\phi + 1}\,\frac{p_0}{p_0 - R_c\phi}, \tag{3}$$

where J_{0r0}, $J_{0r\Phi}$ and J_{0d0}, $J_{0d\Phi}$ are the saturation currents for the recombination and diffusion mechanisms of dark current flow before and after irradiation, respectively, p_0 is the dopant concentration, R_c is the removal rate of the majority charge carriers from crystalline silicon doped with Ga, equal to 0.04 cm^{-1} [10]. Saturation currents corresponding to conduction mechanisms are derived from fitting experimental data of the forward branches of dark I–V curves, according to equation (4) [11]:

$$j_t = J_{0t}\left[\exp\left(\frac{U - jR_s}{A_t\varepsilon}\right) - 1\right] + J_{0r}\left[\exp\left(\frac{U - jR_s}{A_r\varepsilon}\right) - 1\right] + J_{0d}\left[\exp\left(\frac{U - jR_s}{A_d\varepsilon}\right) - 1\right], \quad (4)$$

where J_{0t} (with $A_t > 2$), J_{0r} ($A_r = 2$), J_{0d} ($A_d = 1$) – the saturation currents for tunnel-trap, recombination, and diffusion current mechanisms, respectively, A_i is the diode ideality factors; U is the bias voltage; R_s is the series resistance of the cell structure, $\varepsilon = kT/q$ is the characteristic potential, k is the Boltzmann's constant, q is the electron charge, and T is the temperature.

By substituting the calculated saturation currents values (Table 1) into equations (2) and (3), the damage coefficient for the SHJ PHDS was determined as $K_L = 1 \cdot 10^{-11}$. For comparison, the coefficients K_L have been reported as follows: $6 \cdot 10^{-11}$ for boron-doped Back Surface Field (BSF) SCs and $4 \cdot 10^{-11}$ for gallium-doped BSF SCs [10, 12]. As for emerging Passivated Emitter Rear Cell (PERC) SCs, the value of K_L is estimated at $5 \cdot 10^{-11}$ [13].

Table 1

Parameters of the dark *I*–*V* curve fitting for SHJ solar cells using Equation (4)

Fluence, cm^{-2}	A_t	J_{0t}, A/cm^2	J_{0r}, A/cm^2	J_{0d}, A/cm^2	R_s, $\Omega \cdot cm^2$
0	3.17	$2.86 \cdot 10^{-6}$	$1 \cdot 10^{-9}$	$4.4 \cdot 10^{-14}$	2.71
$2.5 \cdot 10^{14}$	3.2	$3.86 \cdot 10^{-6}$	$3 \cdot 10^{-8}$	$1 \cdot 10^{-12}$	2.14
$5 \cdot 10^{14}$	3.79	$6.88 \cdot 10^{-6}$	$5.92 \cdot 10^{-8}$	$2 \cdot 10^{-12}$	2.61
$1 \cdot 10^{15}$	4	$9.09 \cdot 10^{-6}$	$1.19 \cdot 10^{-7}$	$2.47 \cdot 10^{-12}$	2.67

Conclusion

The possibility of using a bifacial hybrid four-junction solar cell in concentrated photovoltaic module has been explored. A hybrid four-junction solar cell composed of GaInP/Ga(In)As/Ge electricity-generating linear arrays and a photoactive heat-dissipating substrate made of *n*-α-Si:H/(*p*)c-Si:(Ga)/*p*-α-Si:H, incorporating Earth's albedo into the concentrated photovoltaic module, demonstrates the capability to deliver electrical power up to 500 W/m^2 with an efficiency of 29.3%. The operational lifetime of a concentrated photovoltaic module integrated into solar panels on geostationary Earth orbit is restricted by the radiation hardness of the silicon photoactive heat-dissipating substrate, characterized by a damage coefficient of minority carrier diffusion length, $K_L = 1 \cdot 10^{-11}$. This value is smaller than that found in state-of-the-art silicon solar cells used in space applications, such as Back Surface Field solar cells, as well as promising Passivated Emitter Rear Cell solar cells. We estimate that the service life of a solar panel based on concentrated photovoltaic module with a bifacial hybrid four-junction solar cell on geostationary Earth orbit may reach up to 15 years.

REFERENCES

1. **Ru X., Yang M., Wang Y., Wang J., Xue C., Yin S., Hong C., Peng F., Qu M., Lu J., Fang L., Xie T., Li Z., Xu X.,** Development of *p*-type Silicon Heterojunction Solar Cells with 26.6% Efficiency. In: 2023 IEEE 50th Photovoltaic Specialists Conference (PVSC), San Juan, Puerto Rico, USA. (2023) 1–3.

2. **Kalinovskii V.S., Terukov E.I., Prudchenko K.K., Bazeley A.A., Kontrosh E.V., Tolkachev I.A., Titov A.A.,** Investigation of radiation resistance of heterostructure silicon solar cells, Technical Physics Letters. 49 (8) (2023) 55–57.

3. **Delleur A.M., Kerslake T.W.,** Electrical performance of the international space station US photovoltaic array during bifacial illumination. In: Proceedings of the 37th intersociety energy conversion engineering conference, Washington, USA. (2002) 39–44.

4. **Kalinovskii V.S., Kontrosh E.V., Ionova E.A., Pavlova E.G., Koksharov E.G., Andreev V.M.,** Study of Misorientation Characteristics of Hybrid Solar Cell-Doubled Linear Lens Concentrator System. AIP Conference Proceedings. 2550 (1) (2022) 030002.

5. **Salzberger M., Rutzinger M., Nömayr C., Lugli P., Zimmermann C.G.,** Progress in Photovoltaics. 26 (2018) 317–323.

6. **Glazov A.L., Kalinovskii V.S., Muratikov K.L.,** Heat transfer through soldered and bonded joints of multilayer semiconductor devices studied by laser photothermal beam-deflection method, International Journal of Heat and Mass Transfer. 120 (2018) 870–878.

7. **Yamaguchi M., Taylor S.J., Matsuda S., Kawasaki O.,** Mechanism for the anomalous degradation of Si solar cells induced by high fluence 1 MeV electron irradiation, Applied Physics Letters. 68 (22) (1996) 3141–3143.

8. **Stefani Vicari B., Kim M., Wright M., Soeriyadi A., Andronikov D., Nyapshaev I., Abolmasov S., Emtsev K., Abramov A., Hallam B.,** Stability study of silicon heterojunction solar cells fabricated with gallium- and boron-doped silicon wafers, Solar RRL. 5 (9) (2021) 2100406.

9. **Taylor S.J., Yamaguchi M., Yamaguchi T., Watanabe S., Ando K., Matsuda S., Hisamatsu T., Kim S.I.,** Comparison of the effects of electron and proton irradiation on silicon diodes, Journal of Applied Physics. 83 (9) (1998) 4620–4627.

10. **Khan A., Yamaguchi M., Ohshita Y., Dharmaraso N., Araki K., Khanh V.T., Itoh H., Ohshima T., Imaizumi M., Matsuda S.,** Strategies for Improving Radiation Tolerance of Si Space Solar Cells, Solar Energy Materials and Solar Cells. 75 (1–2) (2003) 271–276.

11. **Andreev A.A., Andreev V.M., Kalinovsky V.S., Pokrovsky P.V., Terukov E.I.,** Evaluation of the Conversion Efficiency of Thin-Film Single-Junction (a-Si:H) and Tandem (μc-Si:H + a-Si:H) Solar Cells by Analysis of the Experimental Dark and Load Current-Voltage (I–V) Characteristics, Semiconductors. 46 (2012) 929–936.

12. **Yamaguchi M., Khan A., Taylor S.J., Imaizumi M., Hisamatsu T., Matsuda S.,** A Detailed Model to Improve the Radiation-Resistance of Si Space Solar Cells, IEEE Transactions on Electron Devices. 46 (10) (1999) 2133–2138.

13. **Yamaguchi M., Lee K.H., Araki K., Kojima N., Okuno Y., Imaizumi M.,** Analysis for Nonradiative Recombination Loss and Radiation Degradation of Si Space Solar Cells, Progress in Photovoltaics: Research and Applications. 29 (2021) 98–108.

REFERENCES

PRUDCHENKO Kseniia K.
prudchenkokk@mail.ioffe.ru
ORCID: 0000-0003-4437-2984

ABOLMASOV Sergey N.
S.Abolmasov@hevelsolar.com
ORCID: 0000-0002-8877-8372

KONTROSH Evgeniy V.
kontrosh@mail.ioffe.ru
ORCID: 0000-0003-1812-3714

KALINOVSKII Vitaliy S.
vitak.sopt@mail.ioffe.ru
ORCID: 0000-0003-4858-7544

TOLKACHEV Ivan A.
TolkachevIA@mail.ioffe.ru
ORCID: 0000-0001-8202-7087

TERUKOV Evgeniy I.
eug.terukov@mail.ioffe.ru
ORCID: 0000-0002-4818-4924

Received 17.12.2025. Approved after reviewing 09.02.2026. Accepted 20.02.2026.

© Peter the Great St. Petersburg Polytechnic University, 2026

Conference paper
UDC 621.315.592
DOI: https://doi.org/10.18721/JPM.191.120

Modeling the current-voltage characteristics and optimizing the laser-powered photovoltaic converters with a spot-type rear contact

A.D. Malevskaya ✉, M.A. Mintairov, V.V. Evstropov, D.A. Malevsky, A.V. Malevskaya, S.A. Mintairov, N.A. Kalyuznyy

Ioffe Institute, St. Petersburg, Russia
✉ anmalevskaya@mail.ioffe.ru

Abstract. A method for comprehensively modeling the current-voltage characteristics of laser-powered photovoltaic converters (PVCs) with spot-type rear contact is proposed. The method accounts for both optical losses caused by shading of the photoactive region and electrical losses caused by radial current spreading to the spot-type rear contacts. A balance between these factors is achieved at specific values of the diameter of spots and distance between contacts, which could be determined using the proposed method. The geometric parameters of the rear contacts (diameter and spot pitch) were optimized to maximize the laser radiation conversion efficiency of the AlGaAs/GaAs PVCs.

Keywords: photovoltaic converters, spot-type contact, current spreading, current-voltage characteristics

Citation: Malevskaya A.D., Mintairov M.A., Evstropov V.V, Malevsky D.A., Malevskaya A.V., Mintairov S.A., Kalyuznyy N.A., Modeling the current-voltage characteristics and optimizing the laser-powered photovoltaic converters with a spot-type rear contact, St. Petersburg State Polytechnical University Journal. Physics and Mathematics. 19 (1.1) (2026) 123–128. DOI: https://doi.org/10.18721/JPM.191.120

This is an open access article under the CC BY-NC 4.0 license (https://creativecommons.org/licenses/by-nc/4.0/)

Конференционная статья
УДК 621.315.592
DOI: https://doi.org/10.18721/JPM.191.120

Моделирование вольт-амперных характеристик и оптимизация фотоэлектрических преобразователей лазерного излучения с точечным тыльным контактом

А.Д. Малевская ✉, М.А. Минтаиров, В.В. Евстропов, Д.А. Малевский, А.В. Малевская, С.А. Минтаиров, Н.А. Калюжный

Физико-технический институт им. А.Ф. Иоффе РАН, Санкт-Петербург, Россия
✉ anmalevskaya@mail.ioffe.ru

Аннотация. В работе предложена методика комплексного моделирования вольт-амперных характеристик фотоэлектрических преобразователей (ФЭП) лазерного излучения с точечным тыльным контактом. Методика позволяет учесть как оптические потери, связанные с затенением фотоактивной области, так и электрические потери, обусловленные радиальным растеканием тока к тыльным точечным контактам. Баланс между этими факторами достигается при определённых значениях диаметра и расстояния между контактами, которые могут быть определены с помощью предложенного метода. Проведена оптимизация геометрических параметров тыльных точечных контактов (диаметр и шаг) с целью максимизации эффективности преобразования AlGaAs/GaAs ФЭП.

Ключевые слова: фотоэлектрические преобразователи, точечный тыльный контакт, растекание тока, вольт-амперные характеристики

© Malevskaya A.D., Mintairov M.A., Evstropov V.V, Malevsky D.A., Malevskaya A.V., Mintairov S.A., Kalyuznyy N.A., 2026. Published by Peter the Great St. Petersburg Polytechnic University.

Ссылка при цитировании: Малевская А.Д., Минтаиров М.А., Евстропов В.В., Малевский Д.А., Малевская А.В., Минтаиров С.А., Калюжный Н.А. Моделирование вольт-амперных характеристик и оптимизация фотоэлектрических преобразователей лазерного излучения с точечным тыльным контактом // Научно-технические ведомости СПбГПУ. Физико-математические науки. 2026. Т. 19. № 1.1. С. 123–128. DOI: https://doi.org/10.18721/JPM.191.120

Статья открытого доступа, распространяемая по лицензии CC BY-NC 4.0 (https://creativecommons.org/licenses/by-nc/4.0/)

Introduction

The development of highly efficient photovoltaic converters (PVCs) for laser radiation (LR) requires finding a compromise between minimizing optical losses and reducing electrical contact resistance [1 – 4]. In conventional PVCs and solar cells, only the front contact design requires optimization with this viewpoint. However, PVCs with record-breaking conversion efficiencies for monochromatic radiation [5] as well as high-power (200–500 W/cm^2) laser radiation [6] with $\lambda = 800–850$ nm were developed recently. In such PVCs the epitaxial AlGaAs/GaAs heterostructure is separated from the growth-wafer and transferred to a carrier-substrate with a metal reflector on its surface. The embedded rear metal reflector offers several advantages to the PVC. The reflector returns recombination radiation to the active region and allows decreasing the thickness of the absorber materials without loss of charge carrier collection that leads to high conversion efficiency. However, such a PVC design also requires optimizing optical and resistive losses for the rear contact.

A promising geometry for this purpose is the use of spot-type rear contact, which is effectively used in the light-emitting diodes produced by lift-off techniques [7]. However, the spot-type contact caused an increase in series resistance associated with the radial spreading of current to the spots. Today, there are no universal methods for taking into account both optical and electrical losses for quantitatively estimating the influence of spot-type contact geometry on the current-voltage characteristics (*I–V* curves) of the PVC.

The aim of the work is to develop a method that combines the calculation of optical and electrical parameters for creating the optimal design for a spot-type rear contact. The method is based on two- [8] and three-parameter [9] tube models, which was successfully used to analyze solar cells with a solid rear contact and a finger-pitched front contact construction.

Materials and Methods

The proposed method for modeling a solar cell with a spot-type rear contact consists of several sequential stages. The first stage is the evaluation of the optical parameters. Replacing a solid rear contact with a spot-type contact affects the PVC's spectral sensitivity and saturation current. The changes in these parameters are calculated using linear interpolation between experimental data obtained for samples with different spot-type rear configuration.

Based on the adjusted parameters, such as spectral sensitivity, photogenerated current, dark saturation currents, the generation part of *I–V* curve is calculated. Such *I–V* curve describes the behavior of the *p–n* junction without taking into account ohmic losses according to equation (1):

$$J = J_g - \sum \left[J_{0,j} \exp\left(\frac{qV}{A_j kT} \right) - 1 \right], \quad (1)$$

Next, the losses on the front contact grid are taken into account using the method described in [9], in which a distributed equivalent circuit describing the part of the structure from the upper layer to the emitter is considered. The *I–V* curve of the PVC taking into account the resistance of top part PVC (from top contact-layer to the emitter) is calculated by using equation (2):

© Малевская А.Д., Минтаиров М.А., Евстропов В.В., Малевский Д.А., Малевская А.В., Минтаиров С.А., Калюжный Н.А., 2026. Издатель: Санкт-Петербургский политехнический университет Петра Великого.

$$J = J_g - \sum\left[J_{0,tr,j} \exp\left(\frac{q\left[V - j \cdot R\right]}{A_j kT} \right) \right], \tag{2}$$

where J is the current density, J_g is the photogenerated current, V is the applied voltage, k is the Boltzmann constant, T is the temperature, q is the electron charge, $J_{0,tr,j}$ is the saturation currents for current tubes, R is the resistance.

This *I–V* curve is used to calculate the *I–V* curve which takes into account current spreading to the spot-type rear contacts. The equation was arrived assuming that the lower part of the *I–V* curve structure (from rear contact-layer to the base layer) could be divided into repeating triangular fragments between the contacts (Fig. 1). Each fragment is divided into m parts, in which the current flows along n parallel current tubes. The resistance of the i-th current tube in the jth part is calculated (as in [9]) by equation (3):

$$R = R_V \cdot n + R_L \cdot i, \tag{3}$$

where R_V is the vertical resistance is usually determined by the properties of the substrate material on which the PC epitaxial structure is grown, $R_{L_{i,j}} = \left[\left(\frac{D}{2} \right)^2 + \left(\frac{D}{2} \cdot j \right)^2 \right] \cdot \frac{R_{sheet}}{w}$ is the lateral resistance depends on the tube number, $w = D/4m$ is the tube thickness, D is the distance between contacts, R_{sheet} is the sheet resistance. The equation for $R_{L_{i,j}}$ is obtained by analogy with the calculations given in [8]. The *I–V* curve calculation can be performed using a similar procedure proposed in [9]: the number of parts ***m*** and the number of tubes ***n*** are selected, the resistances R_V and R_L, are calculated, and the resistances of the tubes $R_{i,j}$, are determined, then the *I–V* curve for the all current tubes are calculated. Summation of the all the tube *I–V* curves allow obtaining the complete PVC *I–V* curve.

The model discussed above was applied to search for the optimal parameters of the spot-type rear contacts of AlGaAs/GaAs PVC. The epitaxial heterostructure (Fig. 2) of PVC was grown by the metal-organic vapor phase epitaxy.

To study the influence of contact grid parameters on resistive losses, three PVC samples based on the epitaxial heterostructure (Fig. 2) were fabricated and studied. The only variable parameter were the finger pitches of the front contact: 140 μm (sample A), 180 μm (sample B), and 220 μm (sample C). The spot-type rear of all samples were the same with d = 10 μm and D = 75 μm.

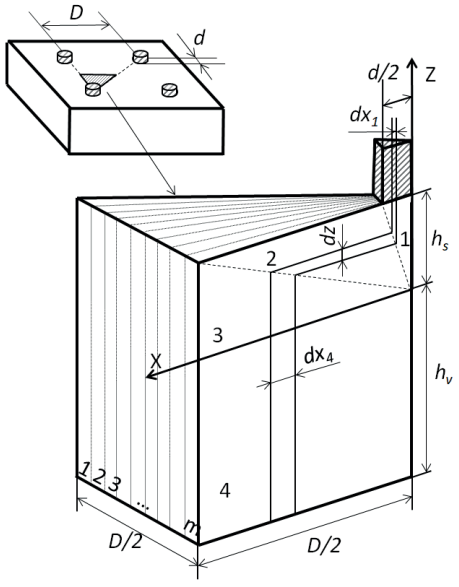

Fig. 1. Schematic representation of the model of radial current spreading in lower part of PVC with the spot-type rear contacts

To demonstrate the contribution of each modeling step, Fig. 3 shows the *I–V* curves for sample A, obtained taking into account various components of ohmic losses. The initial *I–V* curve (curve 1, blue line) is calculated based on experimental *I–V* curve without taking into account resistive losses by Eq. (1). At the next step of the model procedure, the resistive losses caused by spreading between the fingers of the front contact are taken into account (curve 2, orange line) according to Eq. (2). The radial spreading of current between the spot-type rear contacts further increases the resistive losses. The final simulated *I–V* curve (curve 3, green line) demonstrates good agreement with the experimental data (curve 4, red dots) and allows determining the parameters of PVCs (Table 1).

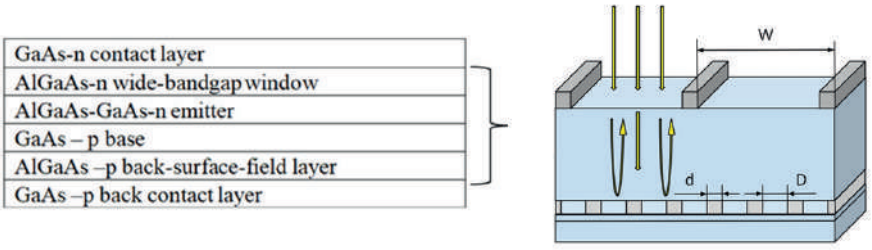

Fig. 2. Schematic representation of the AlGaAs/GaAs PVC epitaxial heterostructure

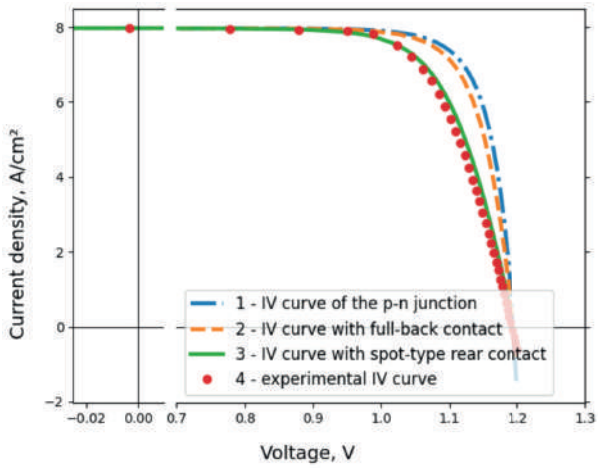

Fig. 3. *I–V* curve of PVC at various stages of modeling: 1 corresponds to the non-resistive *I–V* curve of the *p–n* junction, 2 to the *I–V* curve taking into account losses on the front contact grid, 3 to the *I–V* curve with additional consideration of current spreading to spot-type rear contacts, 4 to the experimental *I–V* curve

Table 1

Parameters of contact grid templates and modeling parameters

	Sample A $W = 140$ μm	Sample B $W = 180$ μm	Sample C $W = 220$ μm
J_{01}, A/cm²	$4.42 \cdot 10^{-20}$	$5.88 \cdot 10^{-20}$	$5.41 \cdot 10^{-20}$
J_{02}, A/cm²	$2.63 \cdot 10^{-10}$	$2.46 \cdot 10^{-10}$	$2.64 \cdot 10^{-10}$
finger-pitched front contact			
R_{Sheet}, Ohm·cm²	11.93	12.03	11.96
R_V, Ohm·cm²	0.0		
ρ_{Me}, Ohm·mm²/cm	$1.6 \cdot 10^{-6}$		
spot-type rear contacts			
R_{Sheet}, Ohm·cm²	11.98	12.00	11.99

Notations. W is the pitch of the front contact fingers, J_{01} and J_{02} are the saturation currents with ideality factors $A = 1$ and $A = 2$, RV is the vertical resistance of the structure, ρ_{Me} is the specific resistance of the contact finger, R_{Sheet} – sheet resistance.

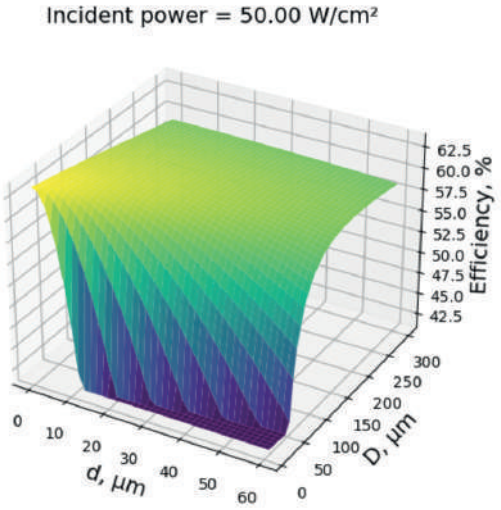

Fig. 4. Dependencies of the efficiency of laser radiation conversion (λ = 800–850 nm) at an incident power of 50 W/cm2 on the spot diameter (*d*) and intercontact distance (*D*) of spot-type rear contact for AlGaAs/GaAs PVC

To optimize the contact geometry, the proposed method is applied to PVC as a number of iterations. A series of calculations is performed for an array of spot-type rear contact diameters and intercontact distance values. For each variant, the conversion efficiency is determined. Analysis of the resulting dependence allows identifying the optimal values that lead to a balance between optical and electrical losses. The method was applied to an AlGaAs/GaAs PVC with an finger pitches of front contact of W = 140 μm. The calculation results are shown in Fig. 4. It was found that the optimal parameters for a high incident power of P_{inc} = 50 W/cm^2 are the following. Obtained parameters allows increasing the efficiency of laser radiation conversion (λ = 800–850 nm) by 1.2% due to the changing intercontact distance D from 75 to 17.4 μm and spot diameter from d = 10 to 2 μm.

Conclusion

A method for comprehensive modeling and optimization of photovoltaic converters with spot-type rear contact was developed, based on a modified tube model. The method allows quantitatively accounting for the competing effects: shading of the back side of the photovoltaic converter by the spot-type contacts and increase in the series resistance due to radial current spreading between spots. An iterative calculation of the photoconversion efficiency for an AlGaAs/GaAs PVC was performed by varying the parameters of the spot-type rear contact. It is shown that the optimal parameters (spot diameter of 2 μm and intercontact distance of 17 μm) allow increasing the efficiency by 1.2% compared to the case of a sample with a spot diameter of 10 μm and an intercontact distance of 60 μm, which exhibited an efficiency of 62.0% [6]. Thus, the proposed method provides a tool for the rear contact design of high-efficiency photovoltaic converters with embedded metal reflectors.

Conflict of interest

The authors declare that they have no conflict of interest.

REFERENCES

1. **Handy R.J.,** Theoretical analysis of the series resistance of a solar cell. Solid-State Electron. 10 (8) (1967) 765–775.

2. **Gessert T.A., Li X., Coutts T.J.,** Practical guidelines for grid metallization in photovoltaic solar cell research. Sol. Cells. 30 (1-4) (1991) 459–472.

3. **Liu M., Römer U., Ekins-Daukes N.J., Lennon A.,** Optical analysis of light management for finger designs in CPV systems. Prog. Photovolt. Res. Appl. 30 (10) (2022) 1219–1227.

4. **Blakers A.W.,** Shading losses of solar-cell metal grids. J. Appl. Phys. 71 (10) (1992) 5237–5241.

5. **Helmers H., Lopez E., Hohn O., Lackner D., Schon J., Schauerte M. et al.,** 68.9% efficient GaAs-Based photonic power conversion enabled by photon recycling and optical resonance. Phys. Status Solidi Rapid Res. Lett. 15 (2021).

6. **Kalyuzhnyy N.A., Malevskaya A.V., Mintairov S.A., Mintairov M.A., Nakhimovich M.V., Salii R.A., Shvarts M.Z., Andreev V.M.,** Photovoltaic AlGaAs/GaAs devices for conversion of high-power density laser (800–860 nm) radiation. Sol. Energy Mater. Sol. Cells. 262 (2023).

7. **Malevskaya A.V., Kalyuzhnyy N.A., Soldatenkov F.Y., Levin R.V., Salii R.A., Malevskii D.A., Pokrovskii P.V., Larionov V.R., Andreev V.M.,** Technical Physics. 68 (1) (2023) 161.

8. **Mintairov M.A., Evstropov V.V., Mintairov S.A., Timoshina N.Kh., Shvarts M.Z., Kalyuzhnyy N.A.,** On Current Spreading in Solar Cells: a Two-Parameter Tube Model. Semiconductors. 50 (7) (2016) 987–992.

9. **Malevskaya A.D., Mintairov M.A., Evstropov V.V., Malevskiy D.A., Kalyuzhnyy N.A.,** Three-parameter tube model of current spreading in solar cells. Semiconductors. 10 (2024) 573.

THE AUTHORS

MALEVSKAYA Anastasia D.
anmalevskaya@mail.ioffe.ru
ORCID: 0009-0008-5664-6130

MALEVSKAYA Aleksandra V.
amalevskaya@mail.ioffe.ru
ORCID: 0000-0003-4018-6631

MINTAIROV Mikhail M.
mamint@mail.ioffe.ru
ORCID: 0000-0002-3481-477X

MINTAIROV Sergei A.
mamint@mail.ioffe.ru
ORCID: 0000-0002-6176-6291

EVSTROPOV Valery V
vvevstropov@gmail.com
ORCID: 0000-0001-7158-0426

KALYUZNYY Nikolay A.
Nickk@mail.ioffe.ru
ORCID: 0000-0001-8443-4663

MALEVSKY Dmitry A.
dmalevsky@scell.ioffe.ru
ORCID: 0000-0002-9337-4137

Received 15.12.2025. Approved after reviewing 30.01.2026. Accepted 06.02.2026.

© Peter the Great St. Petersburg Polytechnic University, 2026

Conference paper
UDC 621.315.592
DOI: https://doi.org/10.18721/JPM.191.121

Optimization of AlGaN/GaN heterostructures for high-electron mobility transistors

D.S. Arteev [1,2]✉, A.V. Sakharov [1,2], A.E. Nikolaev [1,2], E.E. Zavarin [1,2], S.N. Rodin [1,2], A.F. Tsatsulnikov [1,2]

[1] Ioffe Institute, St. Petersburg, Russia;
[2] Submicron Heterostructures for Microelectronics, Research & Engineering Center, RAS, St. Petersburg, Russia
✉ ArteevDS@mail.ioffe.ru

Abstract. We theoretically study AlGaN/AlN/GaN heterostructures aimed at optimizing the AlGaN barrier for GaN-based high-electron-mobility transistors (HEMTs). Self-consistent Poisson–Schrödinger calculations combined with semi-empirical transport modeling are used to evaluate the two-dimensional electron gas (2DEG) concentration, sheet resistance, and saturation drain current as functions of barrier thickness and aluminum mole fraction. Technologically relevant constraints, including unintentional Ga incorporation, 2DEG-density-dependent mobility and saturation velocity, and the critical thickness of AlGaN coherently strained to GaN, are taken into account. Well-defined optimal barrier thicknesses minimize the sheet resistance to R_S ~ 250 Ω/□, while the saturation drain current increases with barrier thickness and Al content, limited by strain-induced cracking. The results provide practical guidance for barrier design in GaN-based HEMTs.

Keywords: GaN, AlGaN, HEMT, two-dimensional electron gas, Poisson–Schrödinger equations, sheet resistance, critical thickness

Citation: Arteev D.S., Sakharov A.V., Nikolaev A.E., Zavarin E.E., Rodin S.N., Tsatsulnikov A.F., Optimization of AlGaN/GaN heterostructures for high-electron mobility transistors, St. Petersburg State Polytechnical University Journal. Physics and Mathematics. 19 (1.1) (2026) 129–133. DOI: https://doi.org/10.18721/JPM.191.121

This is an open access article under the CC BY-NC 4.0 license (https://creativecommons.org/licenses/by-nc/4.0/)

Конференционная статья
УДК 621.315.592
DOI: https://doi.org/10.18721/JPM.191.121

Оптимизация гетероструктур AlGaN/GaN для транзисторов с высокой подвижностью электронов

Д.С. Артеев [1,2]✉, А.В. Сахаров [1,2], А.Е. Николаев [1,2], Е.Е. Заварин [1,2], С.Н. Родин [1,2], А.Ф. Цацульников [1,2]

[1] Физико-технический институт им. А. Ф. Иоффе РАН, Санкт-Петербург, Россия;
[2] НТЦ Микроэлектроники РАН, Санкт-Петербург, Россия
✉ ArteevDS@mail.ioffe.ru

Аннотация. В работе теоретически исследуются гетероструктуры AlGaN/AlN/GaN с целью оптимизации барьерного слоя AlGaN для транзисторов с высокой подвижностью электронов на основе GaN. Для оценки концентрации двумерного электронного газа (2ДЭГ), слоевого сопротивления и насыщенного тока стока в зависимости от толщины барьера и мольной доли алюминия применялось численное решение самосогласованной системы уравнений Пуассона–Шрёдингера в сочетании с полуэмпирическим моделированием транспорта. Учтены технологические ограничения, такие как непреднамеренное встраивание атомов Ga, зависимость

© Arteev D.S., Sakharov A.V., Nikolaev A.E., Zavarin E.E., Rodin S.N., Tsatsulnikov A.F., 2026. Published by Peter the Great St. Petersburg Polytechnic University.

подвижности и насыщенной скорости 2ДЭГ от его концентрации, а также критическая толщина AlGaN, напряженного относительно GaN. Найдена оптимальная толщина барьерного слоя, обеспечивающая минимальное слоевое сопротивление R_S ~ 250 Ω/□, в то время как насыщенный ток стока увеличивается с ростом толщины барьера и содержания алюминия, но ограничен растрескиванием слоя из-за механических напряжений. Полученные результаты представляют практические рекомендации по проектированию барьерного слоя в транзисторах на основе GaN.

Ключевые слова: GaN, AlGaN, транзистор, двумерный электронный газ, уравнения Пуассона–Шрёдингера, слоевое сопротивление, критическая толщина

Ссылка при цитировании: Артеев Д.С., Сахаров А.В., Николаев А.Е., Заварин Е.Е., Родин С.Н., Цацульников А.Ф. Оптимизация гетероструктур AlGaN/GaN для транзисторов с высокой подвижностью электронов // Научно-технические ведомости СПбГПУ. Физико-математические науки. 2026. Т. 19. № 1.1. С. 129–133. DOI: https://doi.org/10.18721/JPM.191.121

Статья открытого доступа, распространяемая по лицензии CC BY-NC 4.0 (https://creativecommons.org/licenses/by-nc/4.0/)

Introduction

High-electron-mobility transistors (HEMTs) based on III-nitride heterostructures are finding increasing use in modern electronics. Gallium nitride, with its unique combination of properties such as a wide bandgap, high electron saturation velocity, high breakdown electric field strength, and relatively high electron mobility [1], offers superior performance compared with silicon and conventional III-V semiconductors. These advantages, particularly in terms of breakdown voltage and thermal stability, make GaN especially suitable for high-power applications.

In GaN-channel heterostructures, the AlGaN barrier layer is a critical element. Conventional designs typically employ a barrier layer with a thickness of 20–30 nm and an aluminum mole fraction of 20–30%, which provides a good balance of performance and reproducibility in metalorganic vapor phase epitaxy (MOVPE) production. However, increasing performance demands on electronic components are driving the development of novel heterostructure architectures. For example, operation at higher frequencies requires heterostructures with thinner barrier layers. For some applications, low sheet resistance is crucial, while for others, high operating current is desired, necessitating optimization of the barrier layer's thickness and composition while accounting for practical technological constraints.

In this paper, we analyze the effect of AlGaN barrier thickness and Al mole fraction in AlGaN/AlN/GaN heterostructures, taking into account technologically relevant constraints.

Materials and Methods

A typical HEMT heterostructure, consisting of a thick GaN channel, a thin (~1 nm) AlN interlayer, and an $Al_xGa_{1-x}N$ barrier of variable Al mole fraction x and thickness d was selected as the model system. The GaN layer was assumed to be fully relaxed, while both the interlayer and the barrier were treated as elastically strained to the GaN lattice. The two-dimensional electron gas (2DEG) concentration N in the channel of the heterostructures was obtained through a numerical self-consistent solution of the coupled 1D Poisson and Schrödinger equations [2] using a predictor-corrector approach for faster convergence [3]. Spontaneous and piezoelectric polarization, as well as a position-dependent electron effective mass were taken into account. All calculations were performed for room temperature, and background doping was assumed to be negligible in comparison with polarization-induced charge. Any underlying buffer layers that might be present were also disregarded due to their minimal direct effect on the 2DEG characteristics.

Unintentional incorporation of Ga atoms into subsequently grown Al-containing layers is a well-known effect in epitaxial growth of HEMT heterostructures, particularly in MOVPE, where Al mole fraction in nominally binary AlN interlayer can be as low as ~0.45 instead of ~1 [4, 5].

© Артеев Д.С., Сахаров А.В., Николаев А.Е., Заварин Е.Е., Родин С.Н., Цацульников А.Ф., 2026. Издатель: Санкт-Петербургский политехнический университет Петра Великого.

However, it is still unclear whether the measured mole fraction reflects "true" atomic distribution or it is simply a measurement artifact due to poor spatial resolution or surface roughness [6]. For our heterostructures, the nominally 1-nm-thick AlN interlayer was estimated to be ~1.5 nm $Al_{0.65}Ga_{0.35}N$, so we used these values in calculations. The Al mole fraction in the AlGaN barrier layer was also limited to a maximum value $x = 0.65$.

The calculation of 2DEG mobility that accounts for multiple occupied subbands and all relevant carrier-scattering mechanisms can be computationally demanding. Moreover, such calculations often fail to reproduce the experimentally observed mobility-density dependences a priori [7]. For this reason, the dependence of the 2DEG mobility μ on the 2DEG concentration N was approximated using empirical fits based on the highest experimentally measured mobilities obtained for our heterostructures. This semi-empirical approach implicitly accounts for dominant (intrinsic, unavoidable, as we believe) density-dependent scattering mechanisms and has previously demonstrated good predictive capability in our earlier studies [8, 9], where the predictions were experimentally verified. The dependence of the 2DEG saturation velocity $v_{sat}(N)$ on the 2DEG density N was taken from [10].

In addition, the mechanical stability of the AlGaN barrier layer was considered. Due to the smaller in-plane lattice constant of AlN compared to GaN, an AlGaN film grown on GaN experiences tensile strain. As the layer thickness increases, the elastic strain energy accumulates, and once this energy exceeds a critical threshold, the layer may relax through the formation of surface cracks. The corresponding critical thickness d_{cr} for crack initiation was estimated using the Griffith fracture criterion [11].

Results and Discussion

The calculated values of the 2DEG concentration N for various Al mole fraction x and barrier thickness d, combined with the mobility dependence $\mu(N)$, were used to obtain the sheet resistance $R_S = (e \cdot N \cdot \mu)^{-1}$, shown in Fig. 1, *a*. These results reveal well-defined optimal thickness values over a wide compositional range $x > 0.30$ in terms of minimal sheet resistance $R_S \approx 250$ Ω/□ (the red dashed line in Fig. 1, *a*). These optima result from a trade-off between increasing 2DEG concentration and the accompanying reduction in mobility at high carrier densities. The optimal thickness values remain below the critical thickness (solid black lines in Fig. 1) for all Al mole fractions. It should be noted that for the barrier layers with the Al mole fractions $x > 0.54$, the optimal thickness falls below 2 nm, and when the 2DEG is located very close to the surface, additional scattering mechanisms, such as remote surface roughness scattering [12] or scattering by charged surface states [13] may become significant. These effects are not considered in the present study; however, they do not appear to be inevitable and can be mitigated through proper optimization of the growth process.

The saturation drain current was estimated as $I_D = e \cdot N \cdot v_{sat}$. This expression is appropriate for the high-field (velocity-saturation) regime, where the electron drift velocity approaches the saturation limit, such as at sufficiently high drain voltage. The resulting values of I_D as a function of Al mole fraction x and barrier thickness d are shown in Fig. 1, *b*. As one can see, in contrast to R_S, the saturation drain current does not exhibit an optimum with respect to x and d. Instead, it increases monotonically with increasing barrier thickness and Al mole fraction, indicating a 'more is better' behavior, despite the reduced saturation velocity for the high 2DEG density. In practice, however, this trend is constrained by the strain accumulated in the AlGaN layer, which limits the maximum achievable thickness and Al content before cracking. At the same time, when considering barrier layers with thicknesses equal to the critical value, a thinner barrier with a higher Al mole fraction provides a higher drain current than a thicker barrier with a lower Al mole fraction. Under these conditions, the maximum saturation drain current achievable for AlGaN/GaN-based transistors grown by MOVPE technology is ~2.6 A/mm for $_x = 0.65$. This value should be regarded as a rough upper-limit estimate, since the model used does not account for several phenomena that may limit the drain current, such as self-heating, source and drain contact resistance, short-channel transport effects, etc.

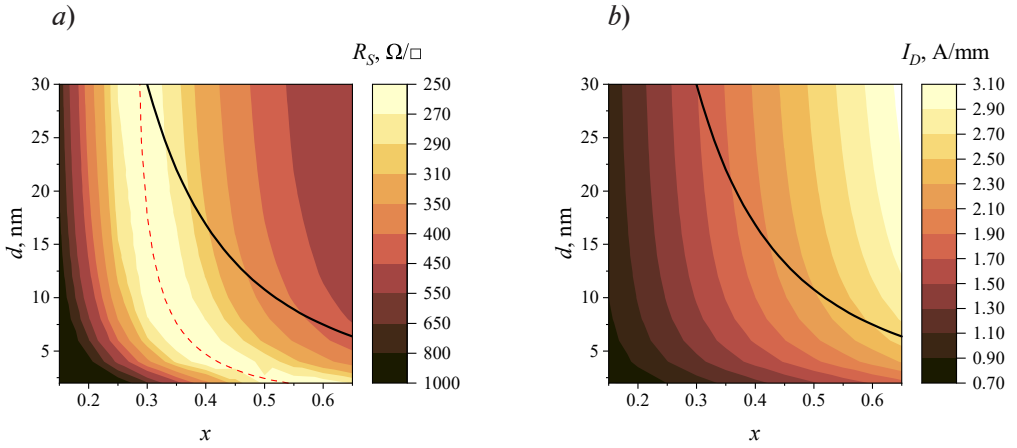

Fig. 1. Dependence of sheet resistance R_S (*a*) and saturation drain current I_D (*b*) on the Al mole fraction *x* and thickness d of $Al_xGa_{1-x}N$ barrier layer.
The black solid line represents the critical thickness of the AlGaN layer coherently strained to GaN. The red dashed line indicates the minimal sheet resistance of ~250 Ω/□

Conclusion

In this work, we analyzed the influence of AlGaN barrier thickness and aluminum mole fraction on the transport properties of AlGaN/AlN/GaN heterostructures under technologically relevant constraints. Self-consistent Poisson–Schrödinger simulations combined with semi-empirical transport modeling revealed well-defined optimal barrier thicknesses that minimize the sheet resistance to ~250 Ω/□ over a range of Al compositions, while the saturation drain current increases monotonically with increasing Al mole fraction and barrier thickness. It was also shown that higher Al content is favorable for achieving a high saturation drain current, and the achievable values are ultimately constrained by strain-induced critical thickness limitations. The presented results provide practical guidelines for optimizing AlGaN barrier design in GaN-based high-electron-mobility transistors.

REFERENCES

1. **Arteev D.S., Sakharov A.V., Zavarin E.E., et al.,** Stress Analysis of GaN-Based Heterostructures on Silicon Substrates, Semiconductors. 2 (2024) 99–102.

2. **Arteev D.S., Sakharov A.V., Lundin W.V., et al.,** Influence of AlN/GaN interfacial non-idealities on the properties of two-dimensional electron gas in AlGaN/AlN/GaN heterostructures, J. Phys. Conf. Ser. 1 (2021) 012202.

3. **Trellakis A., Galick A.T., Pacelli A., Ravaioli U.,** Iteration scheme for the solution of the two-dimensional Schrцdinger-Poisson equations in quantum structures, J. Appl. Phys. 12 (1997) 7880–7884.

4. **Yamada A., Ishiguro T., Kotani J., et al.,** Origin of unintentional gallium incorporation into AlN spacer layer grown by metalorganic vapor phase epitaxy, Phys. Status Solidi B. 2 (2017) 1600496.

5. **Mazumder B., Kaun S. W., Lu J., et al.,** Atom probe analysis of AlN interlayers in AlGaN/AlN/GaN heterostructures, Appl. Phys. Lett. 11 (2013) 111603.

6. **Yunin P.A., Drozdov Yu.N., Drozdov M.N., et al.,** Quantitative SIMS depth profiling of Al in AlGaN/AlN/GaN HEMT structures with nanometer-thin layers, Surf. Interface Anal. 2 (2017) 117–121.

7. **Farvacque J.-L., Bougrioua Z., Carosella F., Moerman I.,** Free carrier mobility in AlGaN/GaN quantum wells, J. Phys. Condens. Matter. 48 (2002) 13319.

8. **Arteev D.S., Sakharov A.V., Nikolaev A.E., et al.,** 2DEG-based multilayer AlGaN/GaN heterostructures with lowered sheet resistance, St Petersburg State Polytech. Univ. J. Phys. Math. 1.1 (2023) 380–384.

9. **Arteev D.S., Sakharov A.V., Nikolaev A.E., et al.,** Sheet resistance of AlGaN/GaN heterostructures with barriers of increased Al content, St. Petersburg State Polytechnical University Journal. Physics and Mathematics. 18 (1.1) (2025) 46–51.

10. **Bajaj S., Shoron O.F., Park P.S., et al.,** Density-dependent electron transport and precise modeling of GaN high electron mobility transistors, Appl. Phys. Lett. 15 (2015) 153504.
11. **Floro J.A., Follstaedt D.M., Provencio P., et al.,** Misfit dislocation formation in the AlGaN/GaN heterointerface, J. Appl. Phys. 12 (2004) 7087–7094.
12. **Cao Y., Xing H., Jena D.,** Polarization-mediated remote surface roughness scattering in ultrathin barrier GaN high-electron mobility transistors, Appl. Phys. Lett. 22 (2010) 222116.
13. **Chen F., Wang X.,** Charged surface states scattering in AlGaN/GaN heterostructures, Phys. E Low-Dimens. Syst. Nanostructures. (2017) 21–23.

THE AUTHORS

ARTEEV Dmitri S.
ArteevDS@mail.ioffe.ru
ORCID: 0000-0003-4447-8789

ZAVARIN Evgenii E.
EZavarin@mail.ioffe.ru
ORCID: 0000-0001-8380-3172

SAKHAROV Alexei V.
Val@beam.ioffe.ru
ORCID: 0000-0002-9976-999X

RODIN Sergey N.
s_rodin77@mail.ru
ORCID: 0000-0003-2236-8642

NIKOLAEV Andrey E.
Aen@mail.ioffe.ru
ORCID: 0000-0001-6522-4484

TSATSULNIKOV Andrey F.
Andrew@beam.ioffe.ru
ORCID: 0000-0002-5078-8946

Received 15.12.2025. Approved after reviewing 05.02.2026. Accepted 12.02.2026.

© Peter the Great St. Petersburg Polytechnic University, 2026

Conference paper
UDC 621.315.592
DOI: https://doi.org/10.18721/JPM.191.110

Hybridization between the plasmonic modes of a graphene square screened by a metal gate and the Fabry–Pérot resonances in barrier layer

K.V. Mashinsky [1]✉, V.V. Popov [1], D.V. Fateev [1,2]

[1] Kotelnikov Institute of Radio Engineering and Electronics of the RAS (Saratov Branch), Saratov, Russia
[2] Saratov State University, Saratov, Russia
✉ konstantin-m92@yandex.ru

Abstract. Hybridization of fundamental and higher plasmonic modes of a graphene square screened by a metal back gate with the Fabry–Pérot resonances in barrier layer is predicted. We show that the absorption cross-section of higher plasmon modes in a screened graphene square is greater than that in the unscreened structure by an order of magnitude.

Keywords: graphene, plasmon, Fabry–Pérot resonance, terahertz

Funding: This study was funded by Russian Science Foundation grant number 22-19-00611-П.

Citation: Mashinsky K.V., Popov V.V., Fateev D.V., Hybridization between the plasmonic modes of a graphene square screened by a metal gate and the Fabry–Pérot resonances in the barrier layer, St. Petersburg State Polytechnical University Journal. Physics and Mathematics. 19 (1.1) (2026) 64–68. DOI: https://doi.org/10.18721/JPM.191.110

This is an open access article under the CC BY-NC 4.0 license (https://creativecommons.org/licenses/by-nc/4.0/)

Конференционная статья
УДК 621.315.592
DOI: https://doi.org/10.18721/JPM.191.110

Гибридизация между плазмонными модами графенового квадрата, экранированного металлическим затвором, и резонансами Фабри–Перо в барьерном слое

К.В. Машинский [1]✉, В.В. Попов [1], Д.В. Фатеев [1, 2]

[1] Саратовский филиал Института радиотехники и электроники им. В.А. Котельникова РАН, г. Саратов, Россия
[2] Саратовский государственный университет, г. Саратов, Россия
✉ konstantin-m92@yandex.ru

Аннотация. Предсказана гибридизация основной и высших плазмонных мод графенового квадрата, экранированного нижним металлическим затвором, с резонансами Фабри–Перо в барьерном слое. Показано, что сечение поглощения высших плазмонных мод в экранированном графене возрастает на порядок величины по сравнению с соответствующими значениями в неэкранированной структуре.

Ключевые слова: графен, плазмон, резонанс Фабри-Перо, терагерц

Финансирование: Исследование поддержано Российским научным фондом (проект № 22-19-00611-П).

Ссылка при цитировании: Машинский К.В., Попов В.В., Фатеев Д.В. Гибридизация между плазмонными модами графенового квадрата, экранированного металлическим затвором, и резонансами Фабри–Перо в барьерном слое // Научно-технические ведомости СПбГПУ. Физико-математические науки. 2026. Т. 19. № 1.1. С. 64–68. DOI: https://doi.org/10.18721/JPM.191.110

Статья открытого доступа, распространяемая по лицензии CC BY-NC 4.0 (https://creativecommons.org/licenses/by-nc/4.0/)

© Mashinsky K.V., Popov V.V., Fateev D.V., 2026. Published by Peter the Great St. Petersburg Polytechnic University.

Introduction

Unique properties of graphene, such as a gapless linear energy spectrum [1] and high electron mobility at room temperature [2], become particularly evident when exciting terahertz (THz) plasmons [3] in graphene nanostructures. Plasmons in graphene exhibit strong electric field localization and open up a range of new nonlinear effects [3]. It is possible to create THz-emitting devices based on plasmons in active graphene [4] using charge carrier inversion in graphene [5] and the emergence of drift instabilities [6].

All of this makes the study of THz plasmons in graphene promising for development of detectors, sensors and amplifiers of THz waves [3].

Only a few plasmonic effects have been discovered in spatially confined two-dimensional (2D) electron systems. In particular, the electromagnetic retardation leads to a decrease in the resonant frequencies of plasmonic excitations in 2D electron stripes [7]. It has also been proposed to use edge plasmons in confined graphene structures to achieve stronger localization of the THz field below the diffraction limit [8]. The lowest plasmonic modes in square 2D electron systems placed in an external magnetic field were studied experimentally and theoretically in [9].

For the theoretical description of plasmonic effects in transistor graphene structures, the quasi-electrostatic approach is typically used [10, 11], making it possible to estimate both the frequencies of plasmonic resonances and the possibility of their electrical tuning. However, within the quasi-electrostatic approximation, it is impossible neither to describe the retardation effects of electromagnetic fields, nor to solve problems of the excitation of 2D plasmons by electromagnetic waves and the emission of electromagnetic waves by 2D plasmons.

A clear advantage of the finite-difference time-domain (FDTD) method is its applicability for analyzing the plasmonic effects in complex structures containing the resonators of various geometric shapes [12, 13]. However, FDTD calculations were unable to explain experimental data on 2D plasmon resonances in graphene nanoribbons [14]. The intrinsic problem of the FDTD method arises from large differences in the scales of subwavelength plasmonic elements and of the entire structure, the latter typically significantly exceeds the wavelength of the electromagnetic wave.

In this paper, we study the hybridization of fundamental and higher plasmon modes of a graphene square screened by a metal back gate with the Fabry–Pérot resonances in the barrier layer by using a self-consistent electromagnetic approach.

Materials and Methods

The structure consists of a graphene square with a side $w = 1$ μm separated from the metal back gate by a barrier layer of boron nitride of thickness d with a dielectric constant $\varepsilon_2 = 4.5$ (Fig. 1, *a*). The metal gate is located on the surface of the dielectric medium with a dielectric constant $\varepsilon_3 = 4.5$. A plane monochromatic THz wave with the electric field polarized along one side of the graphene square is normally incident onto graphene from free space ($\varepsilon_1 = 1$). The Fermi energy of charge carriers in graphene is 150 meV, its momentum scattering time is 2 ps which corresponds to carrier mobility about 10^7 cm^2/V·s at room temperature [15].

The study was conducted within the framework of the self-consistent electromagnetic approach based on the integral equation method [16, 17]. This approach includes several steps. First, Maxwell's equations and electromagnetic boundary conditions are Fourier transformed. In the next step, the integral equations for the components of oscillating current densities in x- and y-directions in graphene are formulated. Third, these integral equations are solved using the Galerkin method, which transforms the system of two integral equations into an infinite system of linear algebraic equations for the coefficients of the current density expansion over the Legendre polynomials. Finally, the infinite system of linear algebraic equations is truncated to achieve the desired level of the solution convergence and numerically solved. The calculated coefficients of the current density expansion make it possible to calculate the absorption cross-section of the structure, determine the electromagnetic fields in any point of the structure, and find the spatial distribution of charge density oscillations in graphene. To evaluate the efficiency of plasmon excitation in graphene, the absorption cross-section (as the ratio of the average absorbed power

© Машинский К.В., Попов В.В., Фатеев Д.В., 2026. Издатель: Санкт-Петербургский политехнический университет Петра Великого.

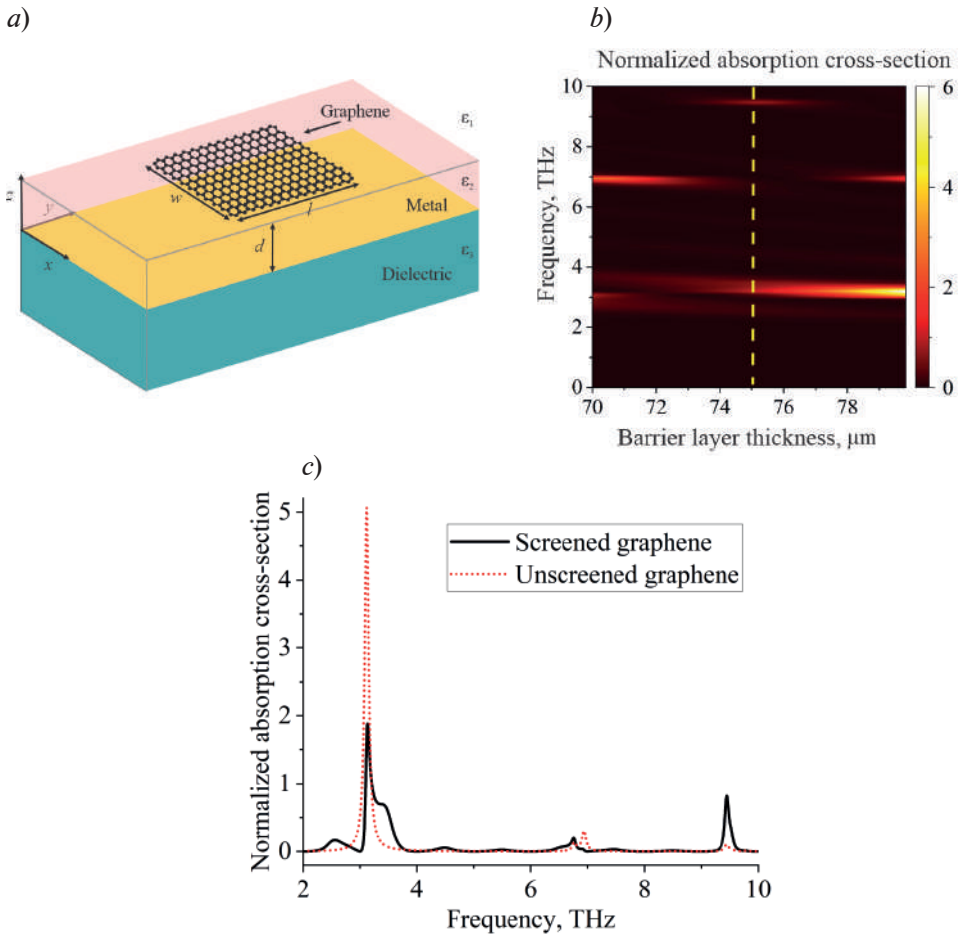

Fig. 1. Studied structure (*a*); absorption cross-section (normalized to the geometric area of graphene square) spectra as a function of barrier layer thickness (*b*); normalized absorption cross-section of unscreened graphene (red dotted line) and screened graphene with barrier layer thickness $d = 75$ μm (black solid line; the third resonance amplification mode at a frequency of 9.5 THz) (*c*)

to the average energy flux density of the incident wave), normalized to the area of graphene, is used in the work.

Results and Discussion

The dependence of calculated normalized absorption cross-section spectra on barrier layer thickness demonstrates the fundamental plasmon resonance with large dipole moment (at a frequency of about 3 THz) and the series of higher plasmon resonances with smaller dipole moment (at frequencies of about 7 THz and 9.5 THz) (Fig. 1, *b*) [18]. Due to the smaller dipole moment of higher plasmon modes, they are much more weakly coupled to the external THz wave. Using a structure with a thick dielectric barrier whose thickness is comparable to the wavelength of THz wave, it is possible to observe Fabry–Pérot resonances in the barrier layer at frequencies $\omega = \pi(2m-1)/(2\sqrt{\varepsilon_0\mu_0\varepsilon_2 d})$, here m is an integer. Fig. 1, *b* shows the Fabry–Pérot resonances in the dielectric barrier layer due to their interaction with plasmon resonances. The frequencies of plasmon resonances do not depend on d for such distances between the graphene and the metal screen, since the plasmon wavelength is significantly shorter than d. The cross-section of the absorption spectrum of Fig. 1, *b* at $d = 75$ μm is shown in Fig. 1, *c* (black solid line). Fig. 1, *c* (black solid line) also shows the main plasmon resonance (3 THz) and two higher resonances at frequencies at 7 and 9.5 THz, as well as a set of Fabry–Pérot resonances. Hybridization of plasmon resonances and Fabry–Pérot resonances occurs if the barrier layer thickness is comparable with the wavelength of incident THz wave in medium 2. In the constructive interference regime, more power of incident THz wave is converted into plasmons in the graphene, increasing the plasmon absorption cross-section. This plasmon 'pumping' effect significantly increases the efficiency of

interaction of THz radiation not only with the fundamental but also with higher plasmon modes (Fig. 1, *c* (black solid line)). The interference of plasmon modes in the graphene layer and Fabry–Pérot modes in the barrier layer allows selective enhancement of higher plasmon modes and, thus, a significant increase in the localization of the plasmon electric field. The absorption cross-section of high plasmon modes in screened graphene square is increased by an order of magnitude compared to that in the unscreened structure (Fig. 1, *c* (red dotted line)).

The Fabry–Pérot resonances of electromagnetic wave in the barrier layer can be used not only to enhance but also to weaken parasitic plasmonic resonances, for example, to create narrow-band radiation sources.

Conclusion

In this work, we predict hybridization between the fundamental and higher plasmonic modes of a graphene square screened by a metal back gate and the Fabry–Pérot resonances in the barrier layer. The anticrossing effect of plasmon and Fabry–Pérot resonances makes it possible to create structures which may enhance or weaken any plasmon resonance, especially the higher ones.

Acknowledgments

This study was founded by the Russian Science Foundation, Grant # 22-19-00611-П.

REFERENCES

1. **Otsuji T., Boubanga Tombet S.A., Satou A., Fukidome H., Suemitsu M., Sano E., Popov V., Ryzhii M., Ryzhii V.,** Graphene-based devices in terahertz science and technology, Journal of Physics D: Applied Physics. 45 (30) (2012) 303001.

2. **Mayorov A.S., Gorbachev R.V., Morozov S.V., Britnell L., Jalil R., Ponomarenko L.A., Blake P., Novoselov K.S., Watanabe K., Taniguchi T., Geim A.K.,** Micrometer-scale ballistic transport in encapsulated graphene at room temperature, Nano Letters. 11 (6) (2011) 2396–2399.

3. **Han J.W.,** Progress of terahertz nonlinearities on graphene plasmonic structures, Current Applied Physics. 74 (2025) 44–53.

4. **Boubanga Tombet S., Knap W., Yadav D., Satou A., But D.B., Popov V.V., Gorbenko I.V., Kachorovskii V., Otsuji T.,** Room-Temperature Amplification of Terahertz Radiation by Grating-Gate Graphene Structures, Physical Review X. 10 (3) (2020) 31004.

5. **Ryzhii V.,** Negative dynamic conductivity of graphene with optical pumping, Journal of Applied Physics. 101 (8) (2007) 083114.

6. **Moiseenko I.M., Fateev D.V., Popov V.V.,** Dissipative drift instability of plasmons in a single-layer graphene, Physical Review B. 109 (4) (2024) L041401.

7. **Kukushkin I.V., Muravev V.M., Smet J.H., Hauser M., Dietsche W., Von Klitzing K.,** Collective excitations in two-dimensional electron stripes: Transport and optical detection of resonant microwave absorption, Physical Review B. 73 (2006) 113310.

8. **Nikitin A.Y., Guinea F., García-Vidal F.J., Martín-Moreno L.,** Edge and waveguide terahertz surface plasmon modes in graphene microribbons, Physical Review B. 84 (2011) 161407(R).

9. **Zarezin A.M., Mylnikov D., Petrov A.S., Svintsov D., Gusikhin P.A., Kukushkin I.V., Muravev V.M.,** Plasmons in a square of two-dimensional electrons, Physical Review B. 107 (2023) 075414.

10. **Rakheja S., Sengupta P.,** Gate-voltage tunability of plasmons in single-layer graphene structures - Analytical description, impact of interface states, and concepts for terahertz devices, IEEE Transactions on Nanotechnology. 15 (2016) 113.

11. **Ryzhii V., Ryzhii M., Shur M.S., Mitin V., Satou A., Otsuji T.,** Resonant plasmonic terahertz detection in graphene split-gate field-effect transistors with lateral p-n junctions, Journal of Physics D: Applied Physics. 49 (2016) 315103.

12. **Zhou F., Wang Y., Zhang X., Wang J., Liu Z., Luo X., Zhang Z., Gao E.,** Dynamically adjustable plasmon-induced transparency and switching application based on bilayer graphene metamaterials, Journal of Physics D: Applied Physics. 54 (2021) 054002.

13. **Lorente-Crespo M., Ballesteros G.C., Mateo-Segura C., García-Meca C.,** Edge-plasmon whispering-gallery modes in nanoholes, Physical Review Applied. 13 (2020) 1.

14. **Zhao W., Zhao S., Li H., Wang S., Zhang S., Huang K., Qiu H., Chen J., Li Z., Luo Y., Gao P., Wang Y., Bao W., Gao P., Bai X., Wang J.,** Nanoimaging of low-loss plasmonic waveguide modes in a graphene nanoribbon. Nano Letters, 21 (7) (2021) 3106–3111.

15. **Domaretskiy D., Wu Z., Nguyenet V.H., Hayward N., Babich I., Li X., Nguyen E., Barrier J., Indykiewicz K., Wang W., Gorbachev R.V., Xin N., Watanabe K., Taniguchi T., Hague L., Fal'ko V.I., Grigorieva I.V., Ponomarenko L.A., Berdyugin A.I., Geim A.K.,** Proximity screening greatly enhances electronic quality of graphene, Nature. 644 (2025) 646–651.

16. **Mashinsky K.V., Popov V.V., Fateed D.V.,** Complete electromagnetic consideration of plasmon mode excitation in graphene rectangles by incident terahertz wave, Scientific Reports. 14 (2024) 7546.

17. **Fateev D.V., Polischuk O.V., Mashinsky K.V.,** Calculation plasmon resonances in the structure of a graphene rectangular resonator located above a homogeneous graphene sheet, RENSIT. 18 (1) (2026) 115–122.

18. **Polischuk O.V., Fateed D.V., Popov V.V.,** Terahertz plasmon modes excitation in a graphene square microcavity, RENSIT. 16 (3) (2024) 367–372.

THE AUTHORS

MASHINSKY Konstantin V.
konstantin-m92@yandex.ru
ORCID: 0000-0002-0724-6391

POPOV Vyacheslav V.
popov_slava@yahoo.co.uk
ORCID: 0000-0003-1303-6443

FATEEV Denis V.
fateevdv@yandex.ru
ORCID: 0000-0003-1406-5385

Received 15.12.2025. Approved after reviewing 23.03.2026. Accepted 24.03.2026.

© Peter the Great St. Petersburg Polytechnic University, 2026

Conference paper
UDC 538.9
DOI: https://doi.org/10.18721/JPM.191.122

Response times of two-dimensional photodetectors limited by intrinsic resistance and capacitance

I.V. Safonov ✉, D.A. Svintsov

Moscow Institute of Physics and Technology (National Research University), Dolgoprudny, Russia

✉ safonov.iv@phystech.edu

Abstract. Most contemporary architectures of photodetectors based on two-dimensional materials include global gates for carrier density control and local *p–n* junctions in the channel. We study the dependence of photocurrent in such detectors on the light modulation frequency, fully taking into account the effects of distributed resistance and gate-channel capacitance. The decay of photocurrent with modulation frequency governs the response time. We find that the maximum modulation frequency is largely determined by the position of light-sensitive junction with respect to the middle of the channel. Largest modulation frequency is achieved for junctions in immediate vicinity of either source or drain contacts, while fast roll-off of the modulation characteristic is observed for junction in the middle of the channel.

Keywords: two-dimensional materials, photodetectors, high-frequency photoresponse, distributed electronic circuits

Funding: This study was funded by Russian Science Foundation grant number 21-79-20225-P. The research of Safonov I.V. was supported by the Foundation for the Advancement of Theoretical Physics and Mathematics "BASIS" (grant No.24-1-5-118-1).

Citation: Safonov I.V., Svintsov D.A., Response times of two-dimensional photodetectors limited by intrinsic resistance and capacitance, St. Petersburg State Polytechnical University Journal. Physics and Mathematics. 19 (1.1) (2026) 134–140. DOI: https://doi.org/10.18721/JPM.191.122

This is an open access article under the CC BY-NC 4.0 license (https://creativecommons.org/licenses/by-nc/4.0/)

Конференционная статья
УДК 538.9
DOI: https://doi.org/10.18721/JPM.191.122

Время отклика двумерных фотодетекторов, ограниченное собственными сопротивлением и ёмкостью

И.В. Сафонов ✉, Д.А. Свинцов

Московский физико-технический институт (национальный исследовательский университет), г. Долгопрудный, Россия

✉ safonov.iv@phystech.edu

Аннотация. Большинство современных фотодетекторов на основе двумерных материалов имеют глобальные затворы для управления плотностью носителей заряда и локальные *p–n*-переходы в канале. Мы изучаем зависимость фототока в таких детекторах от частоты модуляции света, полностью учитывая влияние распределенного сопротивления и распределенной емкости затвор-канал. Спад фототока с частотой модуляции определяет время отклика. Мы показываем, что максимальная частота модуляции в значительной степени определяется положением светочувствительного перехода относительно середины канала. Наибольшая частота модуляции достигается для переходов, расположенных в непосредственной близости от контактов истока или стока, в то время как быстрый спад модуляционной характеристики наблюдается для перехода, расположенного в середине канала.

Ключевые слова: двумерные материалы, фотодетекторы, высокочастотный фотоотклик, распределенные электрические цепи

© Safonov I.V., Svintsov D.A., 2026. Published by Peter the Great St. Petersburg Polytechnic University.

Финансирование: Исследование было профинансировано Российским научным фондом в рамках гранта № 21-79-20225-П. Работа Сафонова И.В. выполнена при поддержке Фонда развития теоретической физики и математики "БАЗИС" (грант № No.24-1-5-118-1).

Ссылка при цитировании: Сафонов И.В., Свинцов Д.А. Время отклика двумерных фотодетекторов, ограниченное собственными сопротивлением и ёмкостью // Научно-технические ведомости СПбГПУ. Физико-математические науки. 2026. Т. 19. № 1.1. С. 134–140. DOI: https://doi.org/10.18721/JPM.191.122

Статья открытого доступа, распространяемая по лицензии CC BY-NC 4.0 (https://creativecommons.org/licenses/by-nc/4.0/)

Introduction

Photodetectors based on two-dimensional (2D) materials feature ultrafast response and possibility of tuning via electrical gating [1]. Response times can be divided into intrinsic times governing the formation of local photocurrent, and extrinsic times governing the formation of voltage and current in an electronic circuit. The intrinsic times in most 2D photodetectors are very short. In graphene, where photovoltage is generated via thermoelectric effect, the intrinsic time is that of carrier thermalization [2]. The latter is estimated as hundreds of femtoseconds. In 2D electron systems based on quantum wells, photocurrent generation via plasmon drag is often dominant [3]. The intrinsic time of such effect is that of momentum relaxation, on the order of 1–10 picoseconds in high-quality heterostructures [4].

We study the response time of gated 2D photodetectors vs. their structural parameters: channel resistance, channel length, gate-channel capacitance and position of the light-sensitive junction. We theoretically consider the photocurrent response I_{ph} to the radiation with modulation frequency f_{mod} and show that $I_{ph}(f_{\mathrm{mod}})$ drops with frequency. We show that the maximum frequency depends strongly on the position of light-sensitive junction with respect to source and drain contacts, and find that structures with photocurrent generation in the immediate vicinity of the metal leads are superior to those with junction in the mid-channel.

Materials and Methods

Short intrinsic photoresponse implies that it can be easily masked by circuit effects, i.e. by resistive and capacitive delays. The truly external delays are minimized by matching the photodetectors with coplanar lines. However, many photodetectors have their own channel resistance and internal capacitances: the capacitance between source and drain contacts, and capacitance of the channel with respect to the gate, as shown in Fig. 1, *a*. The distributed character of resistance and capacitance in 2D detectors makes the question about *RC*-limited response time complex. Despite the existence of several circuit models of gated photodetectors [5, 6], it is not yet understood which resistance and capacitance govern the response time and maximum modulation frequency.

Currently, there exist two main approaches for radiation detection with 2D materials. The first one lies in the electrical induction of *n*- and *p*-type regions within the channel via application of opposite voltages to the split gates [7 – 9]. The gate-induced *p–n* junction is generally located in the middle of the channel, and the photocurrent $j_{ph}(x)$ is generated locally at the junction, Fig. 1, *b*. The second approach lies in deposition of metal contacts with dissimilar work function [10, 11], Fig. 1, *c*. Carrier diffusion between metals and 2D channel leads to the formation of *p–i–n* doping profile. The photocurrent $j_{ph}(x)$ in such architecture is generated in the immediate vicinity of metal leads. In some rare situations, like bulk photovoltaic [12] or photon drag effects [13], the photocurrent is generated in 2D channel uniformly, Fig. 1, *d*.

We consider the photoresponse of 2D detector with channel of length L, source and drain contacts located at $x = 0$ and $x = L$, respectively. The detector is globally gated, and the gate-channel separation is $d << L$. The emerging photocurrent I_{ph} is measured between source and drain contacts. We model I_{ph} at the circuit level without specifying the microscopic origin of the photoresponse. More precisely, we present the overall current density $j(x)$ as a sum of photocurrent $j_{ph}(x)$ and drift current $-\sigma dV/dx$, where σ is the conductivity of 2D material and V is the local voltage in the channel:

© Сафонов И.В., Свинцов Д.А., 2026. Издатель: Санкт-Петербургский политехнический университет Петра Великого.

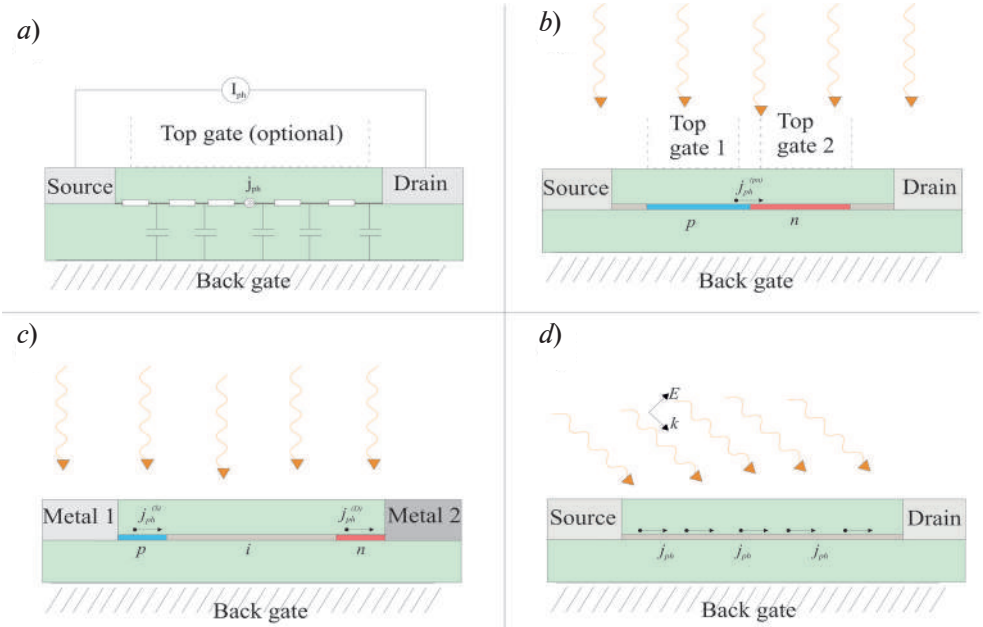

Fig.1. Schematic of the gated photodetector with 2D channel and its equivalent distributed *RC* circuit with localized photocurrent source (*a*); possible physical realizations of 2D photodetectors (*b*, *c*), fitting the scheme of panel (*a*): detector with *p*–*n* junction induced by split gate (b), detector with *p*–*i*–*n* junction due to dissimilar metal contacts (*c*), detector based on photon drag effect (*d*)

$$j(x) = j_{ph}(x) - \sigma \frac{dV}{dx}. \tag{1}$$

The role of drift current is especially clear for localized distribution of photocurrent density, i.e., for characteristic width of the function $j_{ph}(x)$ well below the source-drain separation L. The local electric field dV/dx in this case builds up in the regions where $j_{ph}(x)$ is zero, such that the total current becomes spatially uniform. For time-independent illumination, requiring the spatial uniformity of the current, we find

$$I_{ph,dc} = \frac{1}{L}\int_0^L j_{ph}(x)\,dx, \tag{2}$$

i.e., the global photocurrent is the spatial average of local photocurrents.

The photoresponse to the modulated radiation is far less trivial. We consider the harmonic variations of local photocurrent $j_{ph}(x, t) = j_{ph}(x)e^{-i\omega t}$, where $\omega = 2\pi f_{\text{mod}}$ is the modulation frequency. The buildup of local electric potential is now not instantaneous and governed by the continuity equation:

$$-i\omega\rho(x) + \frac{d}{dx}\left(j_{ph}(x) - \sigma\frac{dV}{dx}\right) = 0, \tag{3}$$

where $\rho(x)$ is the local charge density in the channel. We link the charge density $\rho(x)$ and electric potential $V(x)$ via Poisson's equation. For 2D channels with proximate gates, the Poisson's equation can is solved in the local capacitance approximation:

$$\rho(x) = C_A\left[V(x) - V_G\right], \tag{4}$$

where $C_A = \varepsilon\varepsilon_0/d$ is the gate-to-channel capacitance per unit area, and V_G is the gate voltage. Considering the smallness of photo-induced voltage and potential as compared to their dc values, we write $\rho(x) = \text{CAV(x)}$. The final equation for distribution of photoinduced potential becomes

$$V(x) + \frac{1}{q_p^2}\frac{d^2V(x)}{dx^2} = \frac{1}{i\omega C_A}\frac{dj_{ph}(x)}{dx}; \tag{5}$$

In the regime of photocurrent measurement, its boundary conditions are $V(0) = V(L) = 0$. Above, $q_p = \sqrt{i\omega C_A/\sigma}$ is the complex parameter governing the spatial propagation of electric potential. In the low-frequency regime, the conductivity $\sigma \equiv \sigma dc$ is real, and the parameter q_p is

complex, $q_p = e^{i\pi/4}\sqrt{\omega C_A/\sigma_{dc}}$. In such situations the spreading of potential is diffusive. Similar equation has been adopted in earlier papers [14, 15] for the analysis of plasmon-assisted resonant photoresponse of detectors.

Determination of photocurrent I_{ph} in external circuit for time-dependent response is based on Shockley–Ramo theorem. It states that I_{ph} is the weighted average of local currents

$$I_{ph} = \int_0^L g(x)\, j(x)\, dx, \tag{6}$$

where the weight function $g(x)$ is the electric field in the channel created by unity voltage between source and drain. In the case of proximate gates considered here, the source-drain electric field is strongly screened by the gate, and persists only in the immediate vicinity of lateral contacts, $g(x) \approx [\delta(x) + \delta(x - L)]/2$ [16]. The current measured I_{ph} in such case is the average of local currents at the source and drain:

$$I_{ph} = -\sigma\left(\left.\frac{dV}{dx}\right|_{x=0} + \left.\frac{dV}{dx}\right|_{x=L}\right). \tag{7}$$

Eq. (6) is readily solved for arbitrary spatial dependence of $j_{ph}(x)$, and current in external circuit is symbolically presented as

$$I_{ph} = \frac{1}{2}\int_0^L \frac{\sin\left[q_p x\right] - \sin\left[q_p (L - x)\right]}{\sin\left[q_p L\right]} \frac{dj_{ph}}{dx}\, dx. \tag{8}$$

The frequency dependence of photocurrent is fully encoded in parameter $q_p(\omega) = e^{i\pi/4}\sqrt{\omega C_A/\sigma_{dc}}$. The wave vector $q_p(\omega)$ can be presented as $q_p(\omega) = e^{i\pi/4}\sqrt{\omega RC}/L$, where R is the total channel resistance and C is the total gate-channel capacitance. Thus, Eq. (8) generalizes the concept of *RC*-delay to the detectors with distributed resistance and capacitance.

Results and Discussion

To highlight the dependence of response time and maximum modulation frequency on localization of light-sensitive junction, we adopt the box-shaped model of photocurrent

$$j_{ph}(x) = j_{ph}^{(0)}\theta\left[x - \left(x_{ph} - w/2\right)\right]\theta\left[\left(x_{ph} + w/2\right) - x\right].$$

Physically, the light-sensitive junction has length w, centered at x_{ph}, and generates constant photocurrent $j_{ph}^{(0)}$. The model describes all three setups of Fig. 1, *b*, *c*, *d* via appropriate choice of x_{ph} and w. Plugging the model photocurrent distribution into expression (8), we find the current in external circuit:

$$I_{ph}(\omega) = j_{ph}^{(0)} \sin\left(\frac{q_p w}{2}\right)\left[\cos\left(q_p x_{ph}\right)\cot\left(\frac{q_p L}{2}\right) + \sin\left(q_p x_{ph}\right)\right]. \tag{9}$$

Eq. (9) is our central result. Figure 2 shows the computed dependences of I_{ph} on modulation frequency at various junction positions x_{ph} and small junction width $w = L/20$. The model parameters are adequate for contemporary graphene detectors, $L = 10$ μm, $d = 100$ nm, $\sigma^{-1} = 100$ Ohm, $\varepsilon = 4$. We observe that the frequency roll-off of the photocurrent is fastest when the junction is positioned in the middle of the channel, and becomes slower as the junction gets closer to the source. The dependence $I_{ph}(\omega)$ is symmetric with respect to the mid-channel, i.e. the frequency roll-off is identical for $x_{ph} = x_0$ and $x_{ph} = L - x_0$. The computed dependence supports our intuition about the propagation of photovoltage signals in distributed photodetectors. If the photocurrent is generated away from the source and drain, it takes a long time for the signal propagation to the contacts, therefore the maximum modulation frequency is low. On the contrary, for signal generated in immediate vicinity of either contact, the *RC*-limited response time is very short. Only a small fraction of channel resistance and gate-channel capacitance contributes to the apparent *R* and *C*. For very small separations between junction and the contact (case $x_{ph} = L/5$ in Fig. 2), the photocurrent can even initially grow with frequency.

At very high frequencies the photocurrent eventually decays according to the asymptotic law

$$I_{ph}(\omega) = j_{ph}^{(0)} \frac{q_p w}{2} \exp\left(-\frac{|q_p|}{\sqrt{2}} \min\left\{ x_{ph}, L - x_{ph} \right\} \right). \quad (10)$$

The maximum modulation frequency $f_{\text{mod}}^{\max}$, i.e., the frequency at which the photodetector response drops by e times, is given by

$$f_{\text{mod}}^{\max} = \frac{1}{\pi RC} \frac{L}{\min\left\{ x_{ph}, L - x_{ph} \right\}}. \quad (11)$$

An intuitive interpretation of (11) is the following: only a fraction of total resistance and capacitance located between the light-sensitive junction metal contact is relevant to the RC-delay of the distributed photodetector.

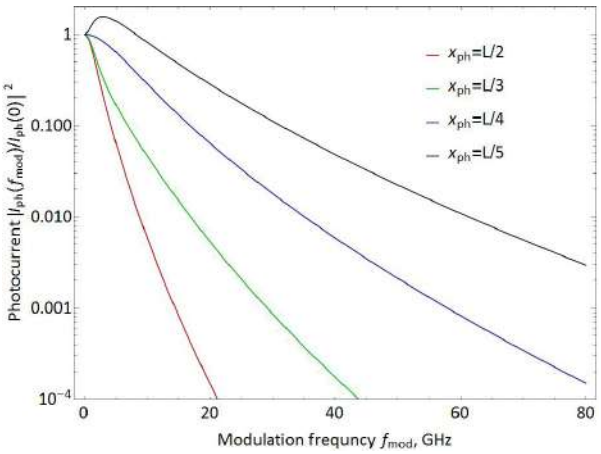

Fig. 2. Dependence of photocurrent on modulation frequency $f_{\text{mod}} = \omega/2\pi$ computed with Eq. (9) for different positions of the light-sensitive junction x_{ph}. Detector parameters are channel length L=10 μm, gate-channel separation d = 100 nm, gate dielectric constant ε = 4, channel resistivity σ^{-1} = 100 Ohm.

Finally, we discuss the limitations of our model. First of all, it is based on local capacitance approximation which is valid for proximate gates $|q_p|d << 1$. This assumption is best fulfilled at low frequencies, particularly, for the parameters of Fig. 2 and f_{mod} =10 GHz we estimate $|q_p|^{-1} \approx 700$ nm, which is well above the distance to the gate. Attempting to go beyond the local capacitance approximation, one can replace Eq. (4) with the full Poisson's equation taking into account realistic geometry of the source, drain and gate contacts. For certain simple arrangements of contacts, it can be solved with conformal mapping techniques [25].

Another approximation of our model is the harmonic approximation to the modulated local photocurrent $j_{ph}(x, t) = j_{ph}(x)e^{-i\omega t}$. Such approximation can be valid if only the modulation frequency is well below the radiation frequency, $f_{\text{mod}} << f_{\text{rad}}$. The assumption can be restrictive for sub-terahertz detectors considered for future wireless communications [12], where f_{rad} = 100–300 GHz. The applicability of our model is limited to tens of gigahertz in that case. For optical fiber detectors (λ = 1.55 μm, $f_{\text{rad}} \approx 200$ THz), the applicability of the model is very broad and definitely covers the contemporary achievable modulation frequencies.

Conclusion

We generalized the concept of RC delay to the photodetectors based on 2D materials with global gates and local light-sensitive p–n junctions. We shown that 'proper' resistance and capacitance governing the maximum modulation frequency and the response time are those of the part of the channel between light-sensitive p–n junction and most proximate contact (either source or drain). We derived a general expression for the frequency roll-off of the photoresponse valid at arbitrary light modulation frequencies and arbitrary distribution of the photocurrent within the channel.

Acknowledgments

The work was supported by the grant 21-79-20225-P of the Russian Science Foundation. The author acknowledges helpful discussions with Viacheslav Muravev on the technology of high-frequency measurements of photodetectors. Ilya Safonov thanks Vladimir Potanin via the Center for Neurophysics and Neuromorphic Technologies for financial support. The research of Safonov I.V. was supported by the Foundation for the Advancement of Theoretical Physics and Mathematics "BASIS" (grant No.24-1-5-118-1).

REFERENCES

1. **Rogalski A., Kopytko M., Martyniuk P.,** Two-dimensional infrared and terahertz detectors: Outlook and status, Applied Physics Reviews. 6 (2019) 021316.

2. **Tielrooij K.J., Massicotte M., Piatkowski L., Woessner A., Ma Q., Jarillo-Herrero P., van Hulst N.F., Koppens F.H.L.,** Generation of photovoltage in graphene on a femtosecond timescale through efficient carrier heating, Nature Nanotechnology. 10 (2015) 437–443.

3. **Kurita Y., Ducournau G., Coquillat D., Satou A., Kobayashi K., Boubanga-Tombet S.A., Yadav D., Watanabe T., Wang F., Taniguchi T., Lupien C., Lefebvre B., Meziani Y.M., Knap W., Mitura G., Inoue T., Suemitsu T., Otsuji T.,** Ultrahigh sensitive sub-terahertz detection by InP-based asymmetric dual-grating-gate high-electron-mobility transistors and their broadband characteristics, Applied Physics Letters. 104 (2014) 251114.

4. **Muravev V.M., Solov'ev V.V., Fortunatov A.A., Tsydynzhapov G.E., Kukushkin I.V.,** On the response time of plasmonic terahertz detectors, JETP Letters. 103 (2016) 792–797.

5. **Coquillat D., Nadar S., Dyakonova N., Varani L., Knap W., Blin S., Pénarier A., Torres J., Avignon E.F.R.,** High-Speed Room Temperature Terahertz Detectors Based on InP Double Heterojunction Bipolar Transistors, International Journal of High Speed Electronics and Systems. 25 (2016) 1640011.

6. **Rudin S., Rupper G., Shur M.,** Ultimate response time of high electron mobility transistors, Journal of Applied Physics. 117 (2015) 174502.

7. **Castilla S., Terrйs B., Autore M., Viti L., Li J., Nikitin A. Y., Vangelidis I., Watanabe K., Taniguchi T., Vitiello M. S., Hillenbrand R., Tielrooij K. J., Koppens F. H. L.,** Plasmonic antenna coupling to hyperbolic phonon-polaritons for sensitive and fast mid-infrared photodetection with graphene, Nature Communications. 11 (2020) 4872.

8. **Titova E., Mylnikov D., Kashchenko M., Safonov I., Zhukov S., Dzhikirba K., Novoselov K. S., Bandurin D. A., Alymov G., Svintsov D.,** Ultralow-noise Terahertz Detection by p–n Junctions in Gapped Bilayer Graphene, ACS Nano. 17 (2023) 8223–8229.

9. **Soundarapandian K.P., Miao J., Wei Y., Zhang Y., Feng L., Peng Y., Chen Z., Sun B., Yang R., Chen J., Wang Z., Chen X., Wang H.M., Yan F., Fu X., Yu G., Wang N., Shi Y., Wu Z., Zhang Y., Hu Z., Wang H.,** High-Speed Graphene-based Sub-Terahertz Receivers enabling Wireless Communications for 6G and Beyond, arXiv preprint. (2024).

10. **Koepfli S.M., Baumann M., Ryser A., Valenta J., Chatzopoulos I., Emboras A., Leuthold J.,** Metamaterial graphene photodetector with bandwidth exceeding 500 gigahertz, Science. 380 (2023) 1169–1174.

11. **Wei J., Xu C., Dong B., Qiu C. W., Lee C.,** Mid-infrared semimetal polarization detectors with configurable polarity transition, Nature Photonics. 15 (2021) 614–620.

12. **Otteneder M., Hubmann S., Lu X., Kozlov D.A., Golub L.E., Watanabe K., Taniguchi T., Efetov D.K., Ganichev S.D.,** Terahertz Photogalvanics in Twisted Bilayer Graphene Close to the Second Magic Angle, Nano Letters. 20 (2020) 7152–7158.

13. **Karch J., Olbrich P., Schmalzbauer M., Ivchenko E.L., Wurstbauer U., Weiss D., Brida D., Unterrainer K., Ganichev S.D.,** Dynamic Hall Effect Driven by Circularly Polarized Light in a Graphene Layer, Physical Review Letters. 105 (2010) 227402.

14. **Dyakonov M., Shur M.,** Detection, mixing, and frequency multiplication of terahertz radiation by two-dimensional electronic fluid, IEEE Transactions on Electron Devices. 43 (1996) 380–387.

15. **Ryzhii V., Shur M.S.,** Resonant terahertz detector utilizing plasma oscillations in two-dimensional electron system with lateral Schottky junction, Japanese Journal of Applied Physics. 45 (2006) L1118–L1120.

16. **Svintsov D.,** Exact Solution for Driven Oscillations in Plasmonic Field-Effect Transistors, Physical Review Applied. 10 (2018) 024037.

17. **Ryzhii V., Khrenov G.,** High-Frequency Operation of Lateral Hot-Electron Transistors, IEEE Transactions on Electron Devices. 42 (1995) 166–171.

THE AUTHORS

SAFONOV Ilya V.
safonov.iv@phystech.edu
ORCID: 0000-0002-7292-6131

SVINTSOV Dmitry A.
svintcov.da@mipt.ru
ORCID: 0000-0001-7443-0685

Received 09.12.2025. Approved after reviewing 02.02.2026. Accepted 02.02.2026.

© Peter the Great St. Petersburg Polytechnic University, 2026

Conference paper
UDC 53.083
DOI: https://doi.org/10.18721/JPM.191.123

Time-resolved measurement of resistance

S.Ya. Vassilyev [1, 2] ✉, V.S. Khrapai [1], E.S. Tikhonov [1]

[1] Osipyan Institute of Solid State Physics RAS, Chernogolovka, Russia;
[2] Moscow Institute of Physics and Technology (National Research University), Dolgoprudny, Russia
✉ servassilyev@gmail.com

Abstract. This article discusses and implements a method for measuring sharp jumps in sample resistance with time resolution of 100 ns at a temperature of 4.2 K using the ATF-55143 transistor as an example. The operating principle of the circuit, calibration, and accounting for parasitic capacitance are described.

Keywords: time-resolved measurements, radio frequency measurements, resistance change

Citation: Vassilyev S.Ya., Khrapai V.S., Tikhonov E.S., Time-resolved measurement of resistance, St. Petersburg State Polytechnical University Journal. Physics and Mathematics. 19 (1.1) (2026) 141–145. DOI: https://doi.org/10.18721/JPM.191.123

This is an open access article under the CC BY-NC 4.0 license (https://creativecommons.org/licenses/by-nc/4.0/)

Конференционная статья
УДК 53.083
DOI: https://doi.org/10.18721/JPM.191.123

Измерение сопротивления образцов с разрешением по времени

С.Я. Васильев [1, 2] ✉, В.С. Храпай [1], Е.С. Тихонов [1]

[1] Институт Физики Твердого Тела им. Ю.А. Осипьяна РАН, г. Черноголовка, Россия;
[2] Московский физико-технический институт (национальный исследовательский университет), г. Долгопрудный, Россия
✉ servassilyev@gmail.com

Аннотация. В статье рассматривается и реализуется метод измерения резких скачков сопротивления образцов с разрешением по времени в 100 нс при температуре 4.2 К на примере транзистора ATF-55143. Описывается принцип работы схемы, калибровка и учёт паразитной ёмкости.

Ключевые слова: время-разрешенные измерения, радиочастотные измерения, изменение сопротивления

Ссылка при цитировании: Васильев С.Я., Храпай В.С., Тихонов Е.С. Измерение сопротивления образцов с разрешением по времени // Научно-технические ведомости СПбГПУ. Физико-математические науки. 2026. Т. 19. № 1.1. С. 141–145. DOI: https://doi.org/10.18721/JPM.191.123

Статья открытого доступа, распространяемая по лицензии CC BY-NC 4.0 (https://creativecommons.org/licenses/by-nc/4.0/)

© Vassilyev S.Ya., Khrapai V.S., Tikhonov E.S., 2026. Published by Peter the Great St. Petersburg Polytechnic University.

Introduction

Accurate measurements of sample resistance with high time resolution are a highly demanded task in the field of solid-state physics. A well-established, high-speed resistance measurement method can be used to study samples that change their resistance during the experiment. This method can be used to monitor fast processes in solid-state physics, which occur in microseconds or less. For example, such a method could be used to read the state of a charge sensor on a semiconductor platform for fast quantum calculations [1]. The motivation for this work comes from a paper [2] on the suppression of superconductivity in superconducting islands in Al-InAs nanowires by transport current. The results of this study suggest that the destruction of superconductivity in such islands occurs abruptly at certain bias voltages with a characteristic relaxation time of the order of μs. The ultimate goal of the present work is to create an electrical circuit capable of operating at low temperatures, rapidly changing the voltage on the sample and maintaining it constant for several microseconds, while also ensuring current measurement with time resolution of at least 100 ns. Circuit tuning in this study was performed using a commercial Agilent ATF-55143 low noise enhancement mode pseudomorphic high electron mobility transistor. Abrupt changes of resistance in response to fast gate modulation in this study mimic the resistance switches in nanowires caused by superconducting transition.

Materials and Methods

To use the transistor in the experiment and adjust its resistance, the resistance dependence on gate voltage must be measured. A four-terminal circuit was used to measure the sample resistance and eliminate the wiring contribution and high-impedance load [3]. The resistance R of the transistor for different voltage U_g applied to its gate was extracted from the current–voltage characteristics shown in Fig. 1, *a*. To minimize the experimental uncertainty, 15 measurements were performed for each gate voltage value, and the average value was taken. The obtained dependence of R on U_g is given in Fig. 1, *b*. This dependence is later used for tuning the time-resolved resistance measurement method.

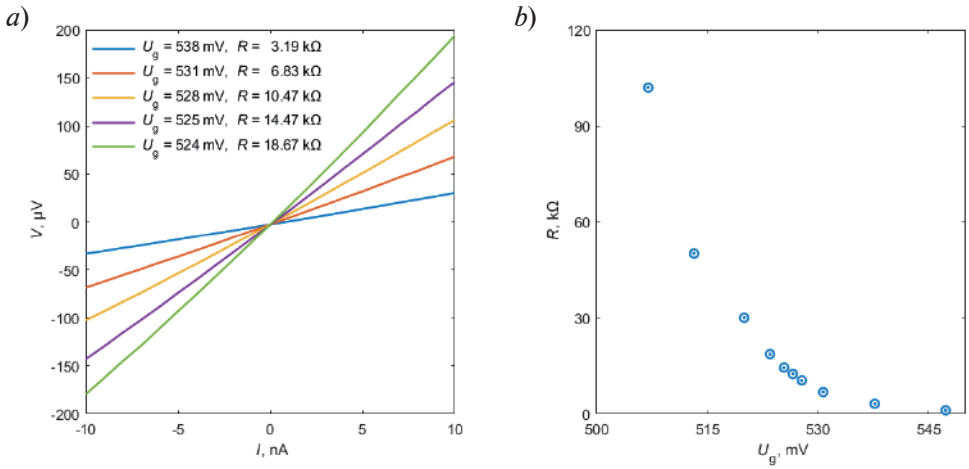

Fig. 1. Transistor I–V characteristics for various gate voltages (*a*); transistor resistance dependence on the applied gate voltage (*b*)

The detailed electrical circuit of the experiment is shown in Fig. 2. In addition to the four-terminal circuit, the circuit also includes components required in time-resolved measurements: resistors (R_0) for impedance-matching of the coaxial cable to prevent signal reflection [4]; capacitors (C_1) in the AC path for decoupling the DC and AC currents; resistors (R_1) as a high-impedance load; grounded capacitors (C_2) in the DC circuit for filtering interference; resistor (R_2) to create a current source. The inevitable stray capacitance (C_s) is also shown in the scheme and will be considered later.

© Васильев С.Я., Храпай В.С., Тихонов Е.С., 2026. Издатель: Санкт-Петербургский политехнический университет Петра Великого.

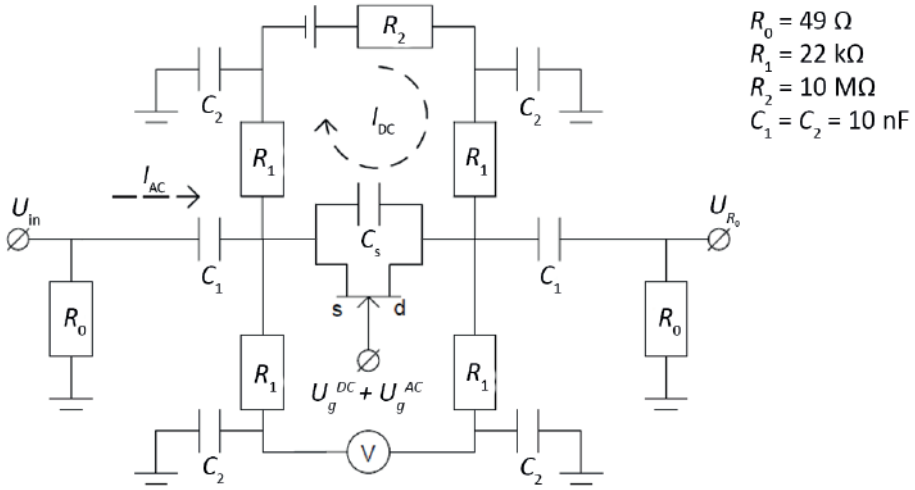

Fig. 2. Electrical diagram with the sample, radio-frequency components and four-terminal DC measurement layout

The radio-frequency (RF) measurement scheme is presented in Fig. 3. The measurement is performed by sending a square-wave signal from the AFG 3021B RF arbitrary function generator to the input and reading the signal from the circuit's output using Keysight DSOX1204G oscilloscope. Three stages of high-frequency amplifiers were used to bring the signal to the oscilloscope. The response time of the amplifiers was increased to a few microseconds with the help of extra capacitors between the stages (200 nF – 2 μF). Additional low-pass (15 MHz) filter was also used in the output circuit to reduce noise in the output signal. The sample and the first amplifier are placed in the cryostat at a temperature of 4.2 K.

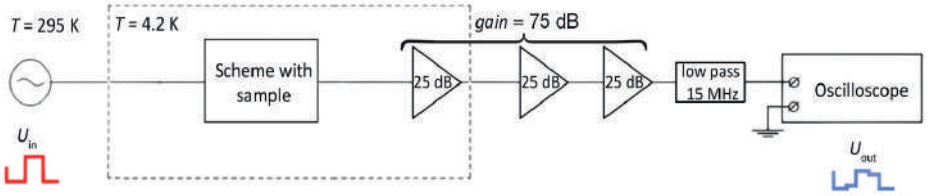

Fig. 3. Electrical diagram of the time-resolved resistance measurement

The signal is received relative to R_0 = 49 Ω resistance. Therefore, the sample resistance R and R_0 create a voltage divider, which can be seen in Fig. 2. Thus, the dependence of the ratio of the input voltage U_{in} and output voltage U_{out} on R can be written using the formula for a voltage divider. Considering gain from amplifiers:

$$\frac{U_{out}}{U_{in}} = gain \cdot \frac{U_{R_0}}{U_{in}} = gain \cdot \frac{R_0}{R + R_0}. \quad (1)$$

Note that Eq. (1) is valid on time scales much shorter than the charging time of the capacitors in Fig. 2, which depends both on the sample resistance and the load resistances R_1. In our experiment the charging time falls in the microsecond range for $R > 1$ kΩ. Under this condition, Eq. (1) can be simplified in this way:

$$u = r \cdot gain, \quad (2)$$

where $u = U_{out}/U_{in}$, $r = |R_0/ (Z_{\|} + R_0)|$ and gain is the total voltage gain of the amplifiers. Note that here we have taken into account the stray capacitance, which is connected in parallel to the sample. The effective impedance of the sample is thus $Z_{\|} = R \parallel Z_S$, where the stray impedance Z_S is the imaginary impedance of the stray capacitance.

Results and Discussion

As the transistor resistance can be controlled, Eq. (2) can be tested for a set of R values. The 100 kHz square-wave with 158 μV (peak-to-peak) input signal U_{in} is sent to the sample. The output signal does not decay noticeably during half-period for $R > 10$ kΩ, so its U_{out} values can be correctly determined. For smaller R the capacitors charge faster and the time decay of the signal becomes visible, as seen in Fig. 4. For simplicity, the value of U_{out} for such signals is taken as the signals' maximum value.

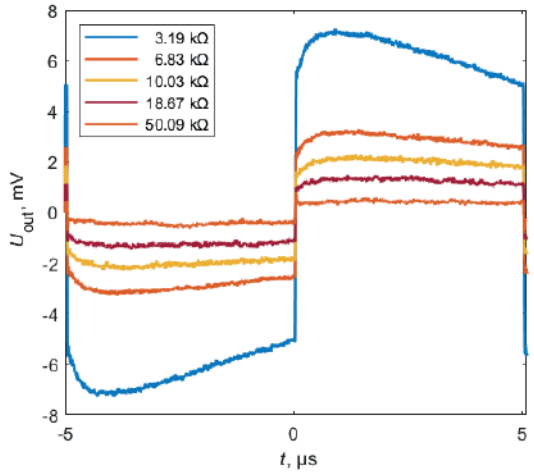

Fig 4. Measured output signal amplitude U_{out} as a function of t. Different colors correspond to different sample resistances R displayed in the legend. Input AC amplitude U_{in} = 158 μV (peak-to-peak)

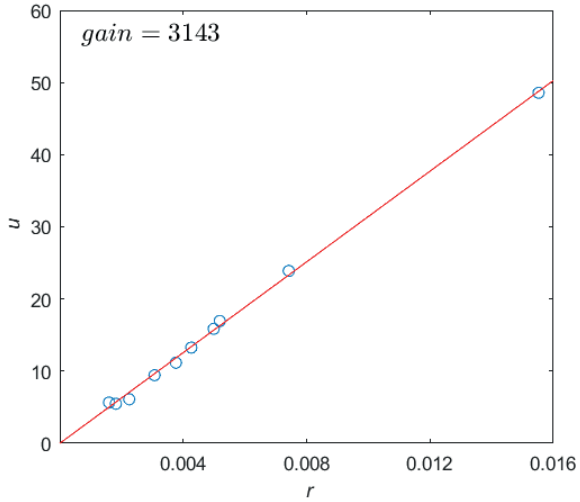

Fig. 5. Dependence of u on r for U_{in} = 158 μV (peak-to-peak). The data is obtained from a calibration shown in Fig. 4. The slope of the fitted line corresponds to the *gain*

Fig. 5 shows the obtained dependence $u(r)$ according to Eq. (2). The dependence is linearized taking the stray impedance $|Z_S|$= 32.91 kΩ. This data allows obtaining a total gain of the setup, which equals *gain* = 3143. This value corresponds to approximately 70 dB and is smaller than the total gain 75 dB of the amplifiers calibrated independently. Most likely, the discrepancy comes from cable losses.

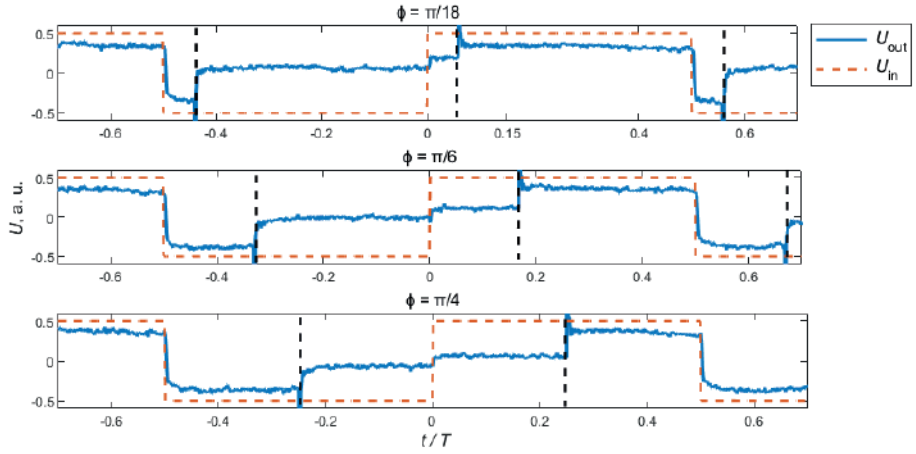

Fig. 6. Output signal amplitude U_{out} changing in time for different phase shifts between the square-wave signals applied to the input terminal and to the transistor. U_{in} = 158 μV (peak-to-peak). U_g^{AC} = 30 mV (peak-to-peak). The time axis is shown relative to the input signal period T = 10 μs. Black dashed lines mark the time instances of the resistance switches mediated by the signal at the transistor gate

Finally, we have used the setup for the time-resolved resistance measurement. Applied input voltage U_{in} remains the same. The constant voltage $U_g^{DC} = 270$ mV is applied to the gate of the transistor (see Fig. 2) to make its resistance on the order of 10 kΩ. Note that the gate voltage characteristics changed in this experiment as compared to Fig. 1 owing to uncontrollable switching of the transistor state at low temperature. In addition, a square wave signal $U_g^{AC} = 30$ mV (peak-to-peak) at the frequency of input signal U_{in} with a phase delay ϕ relative to it was sent to the transistor gate. This leads to abrupt changes in the transistor resistance, which is then detected as sudden switches in the output voltage. An example of the experiment is shown in Fig. 6. The time axis on the graphs is shown relative to the input signal period $T = 10$ μs, to compare it with the phase delay ϕ of the gate-voltage signal (vertical dashed lines). As expected, the time delay of switches mediated by the gate-voltage follows the value of ϕ.

Conclusion

As a result of this work, a setup for detecting abrupt resistance switches in the sample was assembled and configured. The achieved time resolution of the method is limited by the 15 MHz low-pass filter (Fig. 3) and, according to the datasheet, does not exceed 100 ns. Such a resolution is enough for the purpose of measurement of the superconducting switching time in floating superconducting islands in Al-InAs nanowires, which is expected to be in the microsecond range.

REFERENCES

1. **Razmadze D., Sabonis D., Malinowski F.K., Mйnard G.C., Pauka S., Nguyen H., Van Zanten D.M., O'Farrell E.C., Suter J., Krogstrup P., Kuemmeth F., Marcus C.M.,** Radio-Frequency Methods for Majorana-Based Quantum Devices: Fast Charge Sensing and Phase-Diagram Mapping, Phys. Rev. Applied. 11 (2019) 064011.

2. **Shpagina E.V., Tikhonov E.S., Ruhstorfer D., Koblmüller G., Khrapai V.S.,** Fate of the superconducting state in floating islands of hybrid nanowire devices, Phys. Rev. B. 109 (2024) L140501.

3. **Kozhevnikov A.Yu., Egorova E.V.,** Measuring Specific Resistivity with a Four-Probe Method and Electrical Resistivity with a Four-Contact Device, Journal of Advances in Modern Radio Electronics. 3 (2019) 1–5 (in Russian).

4. **Traficante D.D.,** Impedance: What it is, and why it must be matched, Concepts in Magnetic Resonance. 1 (2) (1989) 73–92.

THE AUTHORS

VASSILYEV Sergey Ya.
servassilyev@gmail.com
ORCID: 0009-0003-9339-9865

KHRAPAI Vadim S.
dick@issp.ac.ru
ORCID: 0000-0002-1053-9654

TIKHONOV Evgeny S.
tikhonov@issp.ac.ru
ORCID: 0000-0003-0632-2564

Received 12.12.2025. Approved after reviewing 19.02.2026. Accepted 04.03.2026.

© Peter the Great St. Petersburg Polytechnic University, 2026

Novel materials

Conference paper
UDC 538.958
DOI: https://doi.org/10.18721/JPM.191.124

Investigation of self-hybridized waveguide exciton-polaritons in the two-dimensional antiferromagnet CrSBr at room temperature

I.E. Kalantaevskii ✉, T.D. Gorelkina, V.A. Kravtsov

ITMO University, St. Petersburg, Russia

✉ i.kalantaevskii@metalab.ifmo

Abstract. The interaction between light and excitons in van der Waals materials offers new avenues for exploring strong coupling in quantum systems. Exciton-polaritons, arising from the coherent hybridization of excitons and photons, provide a unique platform for studying collective interactions, optical anisotropy, and tunable responses in low-dimensional structures. This work investigates the self-hybridization of photonic and excitonic modes in a waveguide based on the two-dimensional antiferromagnetic semiconductor CrSBr. Using angle-resolved photoluminescence and numerical modeling, we demonstrate that the pronounced anisotropy of exciton localization along the crystallographic *b*-axis leads to strong interaction with the waveguide mode. The observed anticrossing of dispersion curves is quantitatively described by a coupled oscillator model with a coupling strength of ~185 meV, providing direct evidence for the formation of self-hybridized exciton-polaritons. In the orthogonal polarization, no such interaction occurs, and only directional waveguide emission is detected. These findings pave the way for miniaturized polaritonic devices based on van der Waals magnets, where light matter interaction can be controlled by both waveguide geometry and magnetic order.

Keywords: two-dimensional semiconductors, exciton-photon coupling, self-hybridization, angle-resolved photoluminescence

Funding: The research was supported by the Russian Science Foundation grant No. 25-72-20030.

Citation: Kalantaevskii I.E., Gorelkina T.D., Kravtsov V.A., Investigation of self-hybridized waveguide exciton-polaritons in the two-dimensional antiferromagnet CrSBr at room temperature, St. Petersburg State Polytechnical University Journal. Physics and Mathematics. 19 (1.1) (2026) 146–150. DOI: https://doi.org/10.18721/JPM.191.124

This is an open access article under the CC BY-NC 4.0 license (https://creativecommons.org/licenses/by-nc/4.0/)

Конференционная статья
УДК 538.958
DOI: https://doi.org/10.18721/JPM.191.124

Исследование самогибридизованных волноводных экситон-поляритонов в двумерном антиферромагнетике CrSBr при комнатной температуре

И.Э. Калантаевский ✉, Т.Д. Горелкина, В.А. Кравцов

Университет ИТМО, Санкт-Петербург, Россия

✉ i.kalantaevskii@metalab.ifmo

Аннотация. Взаимодействие света с экситонами в ван-дер-ваальсовых материалах открывает новые пути для исследования сильной связи в квантовых системах. Экситон-поляритоны, возникающие при когерентной гибридизации экситонов и фотонов, представляют собой уникальную платформу для изучения коллективных взаимодействий, оптической анизотропии и управляемых откликов в низкоразмерных структурах. В данной работе исследована самогибридизация фотонной и

© Kalantaevskii I.E., Gorelkina T.D., Kravtsov V.A., 2026. Published by Peter the Great St. Petersburg Polytechnic University.

экситонной мод в волноводе на основе двумерного антиферромагнитного полупроводника CrSBr. Методами спектроскопии угло-разрешённой фотолюминесценции и численного моделирования продемонстрировано, что выраженная анизотропия экситонной локализации вдоль кристаллографической оси *b* приводит к сильному взаимодействию с волноводной модой. Наблюдаемое антипересечение дисперсионных кривых количественно описано моделью связанных осцилляторов с энергией связи ~185 мэВ, что прямо подтверждает образование самогибридизованных экситон-поляритонов. В перпендикулярной поляризации подобное взаимодействие отсутствует, и регистрируется только направленная волноводная эмиссия. Полученные результаты открывают перспективы создания миниатюрных поляритонных устройств на основе ван-дер-ваальсовых магнитов, в которых взаимодействие света с веществом может контролироваться как геометрией волновода, так и магнитным порядком.

Ключевые слова: двумерные полупроводники, экситон-фотонная связь, самогибридизация, угло-разрешённая фотолюминесценция

Финансирование: Работа выполнена при поддержке гранта РНФ № 25-72-20030/.

Ссылка при цитировании: Калантаевский И.Э., Горелкина Т.Д., Кравцов В.А., Исследование самогибридизованных волноводных экситон-поляритонов в двумерном антиферромагнетике CrSBr при комнатной температуре // Научно-технические ведомости СПбГПУ. Физико-математические науки. 2026. Т. 19. № 1.1. С. 146–150. DOI: https://doi.org/10.18721/JPM.191.124

Статья открытого доступа, распространяемая по лицензии CC BY-NC 4.0 (https://creativecommons.org/licenses/by-nc/4.0/)

Introduction

The interaction between light and excitons in van der Waals semiconductors has established these materials as a versatile platform for strong light–matter coupling and polaritonic phenomena [1 – 3]. In particular, materials combining a high refractive index, strong in-plane optical anisotropy, and large excitonic oscillator strength are especially attractive for realizing waveguide-based and cavity-free polariton systems operating at room temperature [4 – 6]. Chromium sulfide bromide (CrSBr) has recently emerged as a unique two-dimensional semiconductor in this context. Owing to its large refractive index and pronounced birefringence, CrSBr supports strongly confined optical modes with polarization-dependent dispersion, while simultaneously hosting robust excitons with large binding energies and strong oscillator strength [7].

Optical studies have demonstrated that the excitonic response of CrSBr dominates the dielectric function along one crystallographic axis, leading to extreme optical anisotropy and highly directional light propagation [8]. This combination of high-index dielectric response and strong excitonic resonances enables efficient hybridization between excitons and confined photonic modes, giving rise to a variety of polaritonic phenomena. Recent works have reported waveguide and cavity exciton polaritons in CrSBr, including strong and ultrastrong coupling regimes, polarization-selective polariton modes, and self-hybridized exciton–photon states arising from the intrinsic optical properties of the material [9 – 11]. More broadly, strong excitons in van der Waals semiconductors have enabled nonlinear polariton effects and, in suitably engineered systems, signatures of polariton Bose–Einstein condensation [12, 13].

Despite the rapid progress in understanding exciton polaritons in CrSBr, the behavior of these hybrid modes within the light cone remains largely unexplored. This regime is particularly important because it governs the interplay between guided near-field excitations and radiative far-field modes, and is directly relevant for the design of integrated polaritonic devices. Understanding how strong excitonic resonances in CrSBr hybridize with waveguide modes in this regime is therefore essential for developing compact, room-temperature polariton platforms based on anisotropic van der Waals semiconductors.

© Калантаевский И.Э., Горелкина Т.Д., Кравцов В.А., 2026. Издатель: Санкт-Петербургский политехнический университет Петра Великого.

Results and Discussion

This article investigates a waveguide based on the two-dimensional van der Waals magnetic semiconductor CrSBr. A multilayer CrSBr sample was prepared by mechanical exfoliation from a bulk crystal and subsequently dry-transferred onto a SiO_2 substrate patterned with cylindrical pedestals etched using hydrofluoric acid. The thickness of the CrSBr layer, which governs the formation of a single optical waveguide mode, was controlled and verified via atomic force microscopy.

The waveguide layer thickness was selected based on simulations of the guided mode within the material, ensuring its spectral proximity to the exciton resonance at approximately 1.3 eV. The mode distribution, calculated using the transfer matrix method, is shown in Fig. 1, *a*. To understand the waveguide mode formation, we took refractive index data from the work of our colleagues [7] (inset in Fig. 1, *a*). The results reveal a strong localization of the excitonic resonance along the *b*-axis.

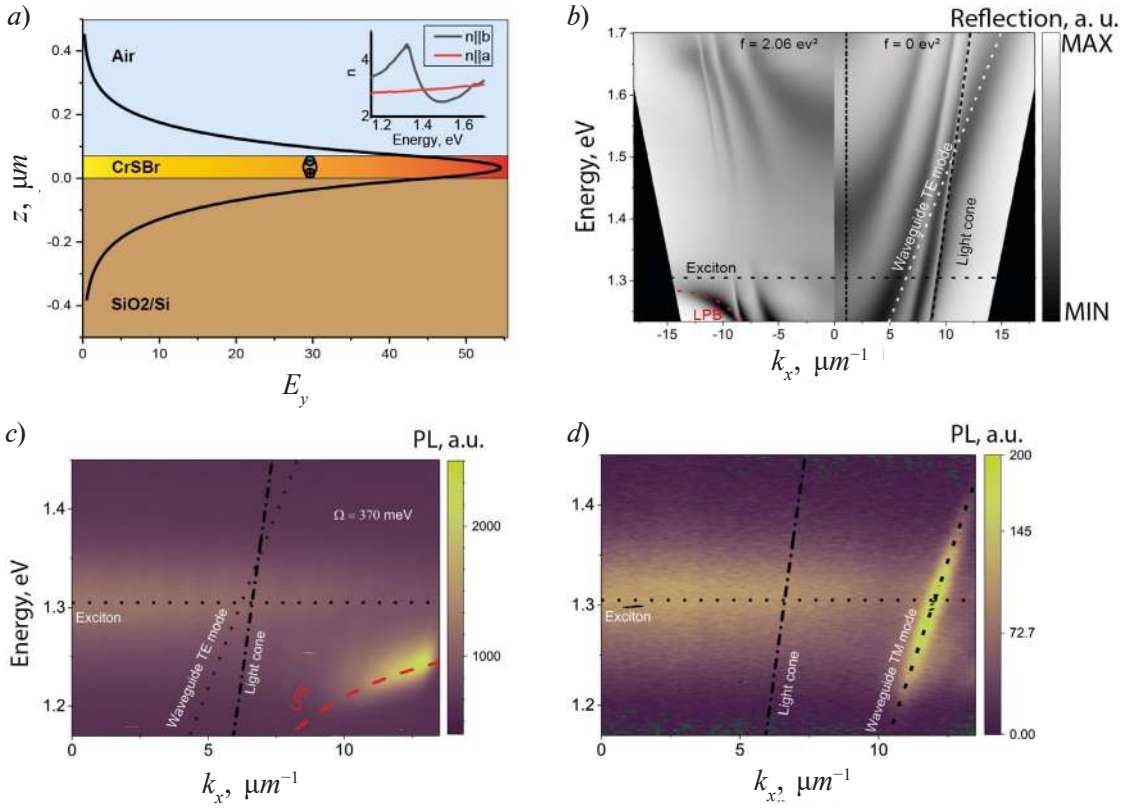

Fig. 1. Schematic representation of the sample (*a*);
transfer matrix method results for oscillator strength 2.06 eV2 and 0 eV2 (*b*);
angle-resolved photoluminescence spectra for TE (*c*) and TM (*d*)

First, we conducted a simulation of waveguide modes. We used the refractive index data featuring the exciton resonance, fitted it, and extracted an oscillator strength of 2.06 eV^2. Subsequently, we simulated reflectance spectra in the presence of a high index GaP layer for two cases: using the measured refractive index and using a background refractive index (~3.4) without the excitonic resonance. The simulation results are shown in Fig. 1, *b*. The figure shows the calculated reflection spectra. The figure is divided into two parts, which differ in the strength of the exciton resonance oscillator. The figure on the right shows a waveguide mode with an exciton resonance oscillator strength equal to zero. The white dotted line shows the dispersion of the waveguide mode, the black horizontal dotted line shows the position of the exciton resonance, the oblique black dotted line labeled with a grid cone shows the boundary of the wave vectors freely propagating into the open space. The red dotted line on the left side of the drawing shows the lower polariton branch. A clear anticrossing between the photonic and waveguide modes within the excitonic resonance region is observed, indicative of self-hybridized exciton-polaritons.

Following this, we conducted a series of angle-resolved photoluminescence experiments using a solid immersion lens. Measurements were performed in an Otto geometry with a high-index GaP solid immersion lens [14]. This configuration, combined with a high-aperture objective, enabled access to large wavevectors beyond the light cone ~16 μm^{-1}. Data were acquired for two orthogonal polarizations.

Fig. 1, *c* clearly shows the anticrossing between the waveguide and excitonic modes. Fitting this dispersion with a coupled oscillator model yields a coupling strength of ~185 meV and Rabi splitting of ~370 meV, which indicates that there is a strong coupling. In contrast, Fig. 1, *d* shows no anticrossing; instead, the photoluminescence is coupled directly into the transverse magnetic (TM) waveguide mode. The difference in behavior indicates the essential role of polarization properties and symmetry of modes in the interaction process.

To better understand the formation of exciton polaritons and their relationship to the waveguide mode in the material, angle-resolved reflectance measurements were performed on samples with different thicknesses. Fig. 2, *a* shows the measured angle-resolved reflectance maps for various thicknesses. It can be observed that the polariton branches shift to lower energies with decreasing thickness. Numerical simulations were also conducted for the measured thicknesses; Fig. 2, *b* shows a similar behavior of the waveguide polariton modes. Unlike the experiment, where the low-energy part exhibits weak contrast due to the spectral sensitivity of the silicon CCD detector, the simulation provides a clearer picture. For the two largest thicknesses, the lower polariton branch becomes visible. In general, the observed and modeled data show that the selection of the sample thickness can control the position of the polariton dispersion.

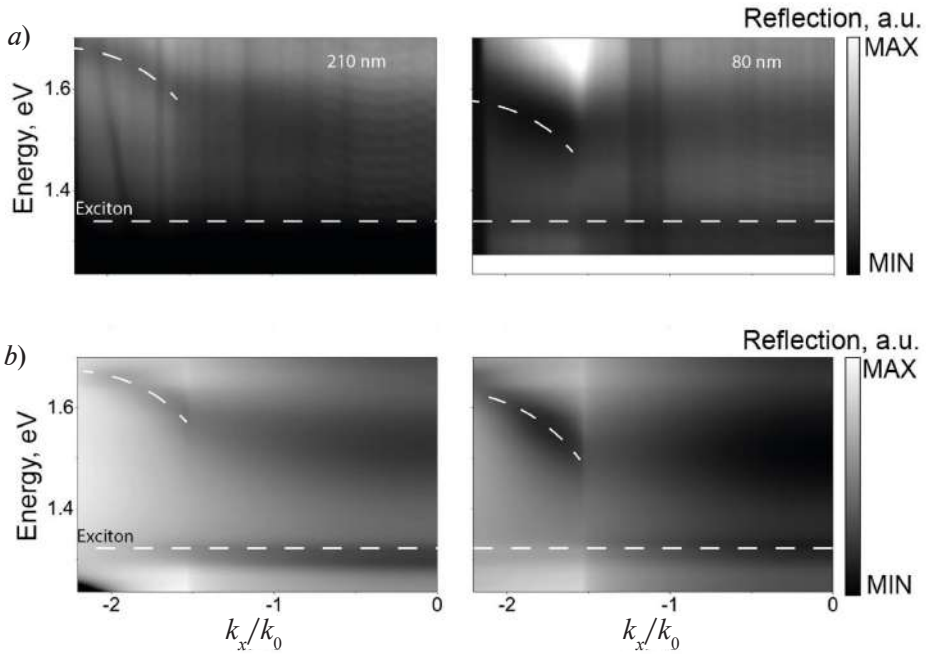

Fig. 2. Experimental angle-resolved reflectance maps for thicknesses of 210 and 80 nm (*a*); angle-resolved reflectance maps obtained using the Transfer Matrix Method (TMM) for the same thicknesses (*b*)

Conclusion

Our study directly demonstrates the formation of guided polaritons below the light line in a CrSBr-based waveguide, achieving strong light-matter coupling (~185 meV) mediated by the material's intrinsic optical anisotropy. This waveguide geometry provides a robust, cavity-free platform for polariton generation and control. Furthermore, by varying the waveguide thickness, we achieve tuning of the polariton branches, highlighting an additional degree of freedom for device design. These results establish CrSBr as a promising material platform for integrated, tunable polaritonics operating at room temperature.

REFERENCES

1. **Basov D.N., Fogler M.M., García de Abajo F.J.,** Polaritons in van der Waals materials, Science. (354) (2016).
2. **Low T., et al.,** Polaritons in layered two-dimensional materials, Nature Materials. (16) (2017) 182–194.
3. **Wang G., et al.,** Excitons in atomically thin transition metal dichalcogenides, Reviews of Modern Physics. (90) (2018) 021001.
4. **Hu F., et al.,** Imaging exciton–polariton transport in $MoSe_2$ waveguides, Nature Photonics. (11) (2017) 356–360/
5. **Flatten L.C., et al.,** Room-temperature exciton–polaritons with two-dimensional WS_2, Scientific Reports. (6) (2016) 33134.
6. **Liu X., et al.,** Strong light–matter coupling in two-dimensional atomic crystals, Nature Photonics. (9) (2015) 30–34.
7. **Ermolaev G. et al.,** Giant optical anisotropy in CrSBr from giant exciton oscillator strength, arXiv preprint arXiv:2509.18866. (2025).
8. **Zhang X., et al.,** Excitonic negative refraction mediated by magnetic orders. (2024).
9. **Wang T., et al.,** Magnetically-dressed CrSBr exciton-polaritons in ultrastrong coupling regime, Nature Communications.14 (1) (2025)5966.
10. **Li Q., et al.,** Magnetic exciton-polariton with strongly coupled atomic and photonic anisotropies, arXiv preprint arXiv:2306.11265. (2023).
11. **Lin K., et al.,** Strong exciton–phonon coupling as a fingerprint of magnetic ordering in van der Waals layered CrSBr, ACS nano. 18 (4) (2024) 2898–2905.
12. **Adak P.Ch., et al.,** Directional Flow of Confined Polaritons in CrSBr, Advanced Materials. (2025) 12557.
13. **Han B., et al.,** Exciton-polariton condensate in the van der Waals magnet CrSBr. arXiv preprint arXiv:2501.18233. (2025).
14. **Pidgayko D., et al.,** Direct imaging of isofrequency contours of guided modes in extremely anisotropic all-dielectric metasurface., ACS Photonics. 6 (2) (2018) 510–515.

THE AUTHORS

KALANTAEVSKII Ivan E.
i.kalantaevskii@metalab.ifmo.ru
ORCID: 0009-0003-7746-1753

GORELKINA Tatiana D.
tatiana.gorelkina@metalab.ifmo.ru

KRAVTSOV Vasily A.
vasily.kravtsov@metalab.ifmo.ru
ORCID: 0000-0002-3555-1027

Received 15.12.2025. Approved after reviewing 21.01.2026. Accepted 31.03.2026.

© Peter the Great St. Petersburg Polytechnic University, 2026

Conference paper
UDC 535.015
DOI: https://doi.org/10.18721/JPM.191.125

Second harmonic generation in iodine quasi-2D halide perovskite crystals

E.V. Sapozhnikova [1,2], D.A. Semyonov [1]✉, S.S. Anoshkin [1], D.A. Tatarinov [1,2], G.A. Verkhogliadov [2], A.P. Pushkarev [1,2]

[1] ITMO University, St. Petersburg, Russia;
[2] Skolkovo Institute of Science and Technology, Moscow, Russia;
✉ dmitrii.semenov@metalab.ifmo.ru

Abstract. Layered quasi-two-dimensional halide perovskites have attracted significant attention as exceptional materials for nonlinear optics and photonics applications due to their remarkable photophysical properties. The incorporation of quasi-2D spacer ligands into the halide perovskite framework induces alterations in the crystal structure and leads to changing its properties due to quantum confinement effects. Notably, certain crystal structures may exhibit a lack of center symmetry, facilitating the observation of second harmonic generation. Furthermore, the optical properties of halide perovskite crystals can vary dramatically based on the composition of the quasi-2D spacers. In this study, we investigate the second harmonic generation signal of two compositions: $PEA_2MAPb_2I_7$ and a novel methyl-substituted PEA derivative, $MePEA_2MAPb_2I_7$. Our results reveal distinct second-harmonic generation characteristics for both compositions and demonstrate enhanced stability in MePEA-based crystals. This work contributes to the understanding of the relationship between crystal composition and nonlinear optical behavior in quasi-2D perovskites, paving the way for future advancements in photonic applications.

Keywords: quasi-2D halide perovskites, second harmonic generation, photoluminescence, non-linear optics

Funding: The work was supported by the Russian Science Foundation (Project No. 25-22-00278, https://rscf.ru/project/25-22-00278/).

Citation: Sapozhnikova E.V., Semyonov D.A., Anoshkin S.S., Tatarinov D.A., Verkhogliadov G.A., Pushkarev A.P., Second harmonic generation in iodine quasi-2D perovskite crystals, St. Petersburg State Polytechnical University Journal. Physics and Mathematics. 19 (1.1) (2026) 151–155. DOI: https://doi.org/10.18721/JPM.191.125

This is an open access article under the CC BY-NC 4.0 license (https://creativecommons.org/licenses/by-nc/4.0/)

Конференционная статья
УДК 535.015
DOI: https://doi.org/10.18721/JPM.191.125

Генерация второй гармоники в йодовых квазидвумерных галогенидных перовскитных кристаллах

Е.В. Сапожникова [1,2], Д.А. Семёнов [1]✉, А.С. Аношкин [1], Д.А. Татаринов [1,2], Г.А. Верхоглядов [2], А.П. Пушкарёв [1, 2]

[1] Университет ИТМО, Санкт-Петербург, Россия;
[2] Сколковский институт науки и технологий, Москва, Россия;
✉ dmitrii.semenov@metalab.ifmo.ru

Аннотация. В данной работе исследуется генерация второй гармоники в квазидвумерных перовскитных йодовых кристаллах для получения стабильного сигнала во времени. Мы сравниваем различные квазидвумерные лиганды и изучаем их влияние на нелинейные эффекты в синтезированных кристаллах.

© Sapozhnikova E.V., Semyonov D.A., Anoshkin S.S., Tatarinov D.A., Verkhogliadov G.A., Pushkarev A.P., 2026. Published by Peter the Great St. Petersburg Polytechnic University.

Ключевые слова: квазидвумерные галогенидные перовскиты, генерация второй гармоники, фотолюминесценция, нелинейная оптика

Финансирование: Работа выполнена при поддержке Российского фонда науки (проект No. 25-22-00278, https://rscf.ru/project/25-22-00278/).

Ссылка при цитировании: Сапожникова Е.В., Семёнов Д.А., Аношкин С.С., Татаринов Д.А., Верхоглядов Г.А., Пушкарёв А.П., Генерация второй гармоники в йодовых квазидвумерных галогенидных перовскитных кристаллах // Научно-технические ведомости СПбГПУ. Физико-математические науки. 2026. Т. 19. № 1.1. С. 151–155. DOI: https://doi.org/10.18721/JPM.191.125

Статья открытого доступа, распространяемая по лицензии CC BY-NC 4.0 (https://creativecommons.org/licenses/by-nc/4.0/)

Introduction

Quasi-two-dimensional (quasi-2D) halide perovskites are a unique class of materials characterized by the incorporation of organic spacer cations into the bulk halide perovskite framework [1]. An increasing number of research highlights the significant influence of the chemical composition of these organic spacers on the optical and structural properties of quasi-2D perovskite systems [2 – 4]. Notably, the choice of organic spacer can affect nonlinear optical phenomena, such as second harmonic generation (SHG). Since SHG requires the absence of an inversion center in the crystal structure, any modifications to the orientation or symmetry resulting from alterations to the spacer can substantially impact the efficiency of the nonlinear optical response.

Recent studies have demonstrated SHG in various iodine-based quasi-2D perovskite crystals, including those incorporating *n*-butylammonium (BA) [5], phenethylammonium (PEA) [2], and various chiral ligand-based structures [4]. However, the intensity and stability of SHG in these iodine-based crystals remain relatively low. In this work, we investigate SHG in a novel methyl-substituted PEA-based [6] single crystal, $MePEA_2MAPb_2I_7$ and compare its SHG characteristics with those of the more commonly studied $PEA_2MAPb_2I_7$ crystal.

Materials and Methods

$MePEA_2MAPb_2I_7$ and $PEA_2MAPb_2I_7$ solutions were synthesized using stoichiometric mixtures of 0.3 mmol PbI2 (> 99.999 %) and 0.3 mmol MePEAI or PEAI (> 99.9 %) and 0.3 mmol MAI (> 99.9 %) in dimethyl sulfoxide. The solutions were prepared and stored in an inert atmosphere of a nitrogen-filled glove box. Each solution was deposited between two glass substrates that were pressed together and remained heated up to 60 °C for further crystal growth. Bright-field, dark-field and luminescent images of the structures were taken on an Axio Imager A2m optical microscope (Carl Zeiss SMT), optical pumping was performed using a 350 nm wavelength UV lamp. SHG spectra were measured on a Labram spectrometer with optical pumping by a TEMA femtosecond pulsed laser (λ = 1045 nm) and a frequency of 70 MHz through a NIR 50x (NA = 0.42) objective.

Results and Discussion

In this study, we investigate quasi-2D halide perovskite single crystals with the general formula $L_2MA_{(n-1)}Pb_nI_{(3n+1)}$, where MA represents methylammonium, Pb denotes lead, I is an iodine, L is either PEA or MePEA ligand as the organic spacer, and n indicates the number of perovskite layers separated by these organic spacers from other perovskite layers [1]. Specifically, we focus on the quasi-2D perovskite phases with n = 2, namely $PEA_2MAPb_2I_7$ and $MePEA_2MAPb_2I_7$, which were synthesized from precursor solutions held between substrate glasses at a temperature of 60 °C.

For our experiments, we selected a series of perovskite crystals exhibiting similar photoluminescence (PL) spectra. Fig. 1, *a*, *b*, c shows the optical microscopy images of the crystals obtained in bright-field, fluorescence and dark-field modes, respectively, for $MePEA_2MAPb_2I_7$ (upper row) and $PEA_2MAPb_2I_7$ (lower row). The PL spectra for both compositions normalized

© Сапожникова Е.В., Семёнов Д.А., Аношкин С.С., Татаринов Д.А., Верхоглядов Г.А., Пушкарёв А.П., 2026. Издатель: Санкт-Петербургский политехнический университет Петра Великого.

by the maximum of the most intense signal for MePEA are illustrated in Fig. 1, *d*, revealing a PL peak around 580 nm. This peak is consistent with the characteristics of the quasi-2D perovskite phase with $n = 2$, thereby confirming the composition of the synthesized crystals.

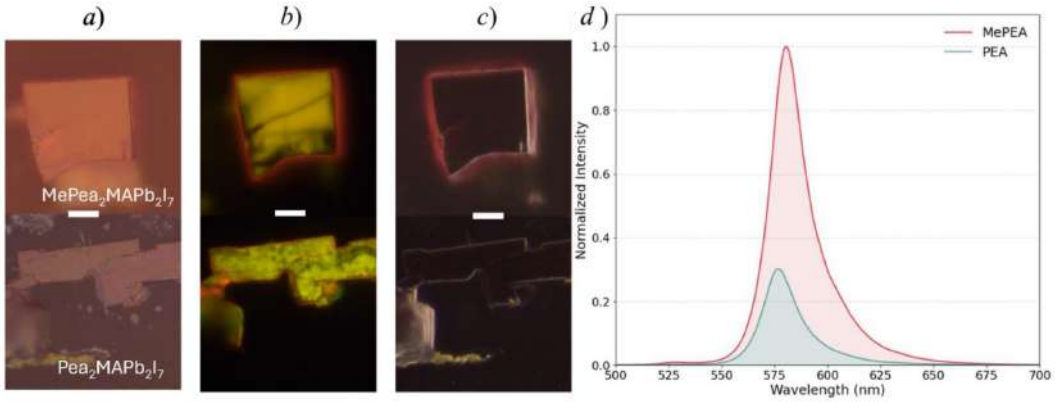

Fig.1. Bright-field (*a*), fluorescent (*b*) and dark-field (*c*) images of quasi-2D perovskite crystals with a scale bar of 10 microns, the upper row is $MePEA_2MAPb_2I_7$, the lower row is $PEA_2MAPb_2I_7$; PL spectra of $PEA_2MAPb_2I_7$ and $MePEA_2MAPb_2I_7$ crystals of the same phase group at the same pump fluence (*d*)

Upon excitation with a 1045 nm femtosecond laser, both samples exhibited SHG and two-photon photoluminescence (2PL). As is known, SHG is the second-order nonlinear process and thus the SHG intensity should have quadratic dependency on the incident pump power. The slopes of the measured power-intensity correlations were estimated to be 1.74 and 1.76 for $PEA_2MAPb_2I_7$ and $MePEA_2MAPb_2I_7$, respectively, which is close to quadratic law (Fig. 2, *a*, *b*), proving the occurrence of SHG. The SHG threshold was estimated to be 0.4 mJ/cm^2 for both compositions. The intensity of the SHG signal for both methyl-substituted and usual PEA-based crystals were obtained at the same pump power and normalized to the most intense signal value (Fig. 2, *c*, *d*). The difference in intensity of normalized signal may be attributed to different thickness of structures, as it was previously reported in other works [3].

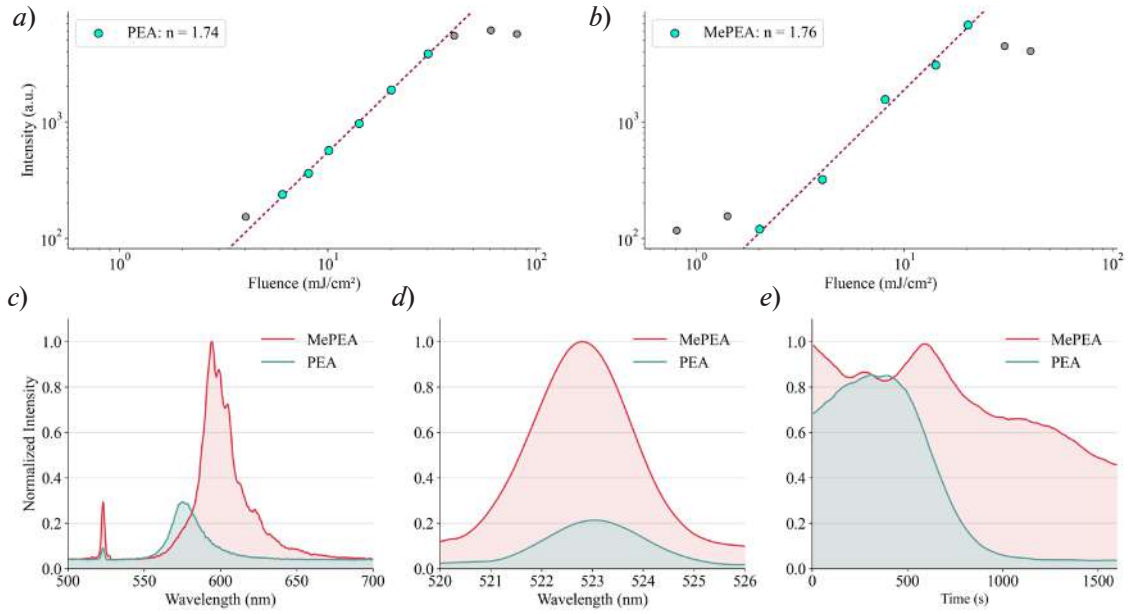

Fig.2. Dependence of the SHG peak intensity on the optical pump power in a logarithmic scale for the composition $PEA_2MAPb_2I_7$ (*a*) and $MePEA_2MAPb_2I_7$ (*b*); 2PL spectra with SHG peak for compositions $PEA_2MAPb_2I_7$ and $MePEA_2MAPb_2I_7$, at low fluence (1.2 mJ/cm^2) (*c*); SHG spectra for $MePEA_2MAPb_2I_7/PEA_2MAPb_2I_7$ crystals at the same pump fluence (6 mJ/cm^2) (*d*); temporal dependency of SHG peak intensity under continuous pump fluence (6 mJ/cm^2) (*e*)

In addition, for the $MePEA_2MAPb_2I_7$ crystal, the 2PL spectra presented a non-uniform shape compared to $PEA_2MAPb_2I_7$ (Fig. 2, *c*). Such a shape, with multiple peaks in the 2PL spectra, might be attributed to the impact from other phases with n ranging from 3 to 6, however the $n = 2$ peak remains dominant. Thus, the exact role of additional methyl group on quasi-2D crystal phase formation and their SHG intensity remains under discussion, and additional structural characterization is required.

To compare the SHG stability of both compositions, the SHG intensity was measured under continuous excitation at 6 mJ/cm^2 incident fluence for 1600 seconds (Fig. 2, *e*). It was revealed that the SHG signal disappeared after 1000 s for the $PEA_2MAPb_2I_7$ crystal, whereas the SHG signal for MePEA-based crystal remained by the end of the measurements. During the continuous optical pump, the perovskite crystal degradation is mainly attributed to the heating of sample and additional oxidation or adsorption of water molecules from the air. Previously, it was established that MePEA-based perovskite films demonstrated better structural stability against polar solvents exposure compared to regular PEA-based structures [7]. Thus, MePEA may also impact the temporal stability of the SHG signal in $MePEA_2MAPb_2I_7$ crystals as it provides better structural stability.

Conclusion

In conclusion, our research demonstrates the occurrence of SHG in both $MePEA_2MAPb_2I_7$ and $PEA_2MAPb_2I_7$ compositions. Notably, the MePEA-based quasi-2D perovskite crystal exhibits enhanced stability compared to its PEA-based counterpart. Specifically, the operational half-lifetime at 6 mJ/cm^2 incident fluence for SHG intensity in the MePEA-based crystal is approximately twice as long, measuring 25 minutes compared to 12.5 minutes for the PEA-based crystal. These findings prove the significant relationship between organic spacer composition and the stability of SHG in iodine-based perovskite crystals. Consequently, this work contributes valuable insights toward the development of quasi-2D perovskite materials for advanced photonic applications.

Acknowledgments

The work was supported by the Russian Science Foundation (Project No. 25-22-00278, https://rscf.ru/project/25-22-00278/).

REFERENCES

1. **Chen Y., et al.,** 2D Ruddlesden–Popper perovskites for optoelectronics. Advanced Materials. 30 (2018) 1703487.

2. **Morrow D.J., et al.,** Disentangling second harmonic generation from multiphoton photoluminescence in halide perovskites using multidimensional harmonic generation. The Journal of Physical Chemistry Letters. 11 (2020) 6551–6559.

3. **Wei W., et al.,** Regulating second-harmonic generation by van der Waals interactions in two-dimensional lead halide perovskite nanosheets. Journal of the American Chemical Society. 141 (2019) 9134–9139.

4. **Li J., et al.,** Regulating Second-Harmonic Generation in 2D Chiral Perovskites Through Achiral Organic Spacer Cation Alloying Strategy. Laser & Photonics Reviews. 19 (2025) 2401379.

5. **Stoumpos C.C., et al.,** Ruddlesden–Popper hybrid lead iodide perovskite 2D homologous semiconductors. Chemistry of Materials. 28 (2016) 2852–2867.

6. **Alahbakhshi M., et al.,** Highly efficient quasi 2D blue perovskite electroluminescence leveraging a dual ligand composition. Advanced Functional Materials. 33 (2023) 2214315.

7. **Verkhogliadov G.A., et al.,** Phase control of quasi-2D halide perovskite by post-treatment and antisolvent treatment techniques, St. Petersburg State Polytechnical University Journal Physics and Mathematics. 18 (2025) 263–267.

THE AUTHORS

SAPOZHNIKOVA Elizaveta V.
e.sapozhnikova@metalab.ifmo.ru
ORCID: 0009-0000-2732-6711

SEMYONOV Dmitrii A.
dmitrii.semenov@metalab.ifmo.ru

ANOSHKIN Sergey S.
sergey.anoshkin@metalab.ifmo.ru
ORCID: 0000-0003-4552-3991

TATARINOV Dmitry A.
dmitry.tatarinov@metalab.ifmo.ru
ORCID: 0000-0002-4825-9041

VERKHOGLIADOV Grigorii A.
g.Verkhogliadov@skoltech.ru
ORCID: 0000-0002-6222-5526

PUSHKAREV Anatoly P.
an.pushkarev@skoltech.ru
ORCID: 0000-0002-1793-6812

Received 15.12.2025. Approved after reviewing 10.03.2026. Accepted 17.03.2026.

© Peter the Great St. Petersburg Polytechnic University, 2026

Conference paper
UDC: 53.093
DOI: https://doi.org/10.18721/JPM.191.126

The role of charge carrier diffusion in halide perovskite luminophores with memory for optical computing

A.A. Ekgardt [1]✉, A.A. Marunchenko [2], E.V. Sapozhnikova [1,3], G.A. Verkhogliadov [3], A.P. Pushkarev [1,3]

[1] ITMO University, St. Petersburg, Russia;
[2] Lund University, Lund, Sweden;
[3] Skolkovo Institute of Science and Technology, Moscow, Russia;
✉ aleksei.ekgardt@metalab.ifmo.ru

Abstract. The optical elements that can combine memory and signal modulation have become a topic of interest in the field of neuromorphic computing systems. In particular, the optical analogue of a memristor called memlumor exhibits promising features in which the change of the output luminescence depends not only on the excitation light signal but also on the state of the material. Metal halide perovskite luminophores are considered to be suitable for memlumor implementation as they exhibit modulation of photoluminescence due to the interaction of structure defects with the environment and previous interactions, thereby possessing memory. Luminescence in perovskite materials is described via Shockley–Reed–Hall model which takes into account charge carriers dynamics in the structure. Additionally, the diffusion of charge carriers also plays a key role and highly depends on memlumor's size. This paper explores the perovskite memlumor's functionality based on their characteristic size to identify optimal parameters and suitable designs for future optical neuromorphic computing architectures.

Keywords: neuromorphic systems, memlumors, metal halide perovskites, photoluminescence, charge carrier diffusion, quantum yield, time-resolved photoluminescence, Shockley–Read–Hall model, optical computing systems

Funding: The work was supported by the Russian Science Foundation (project 25-29-00520, https://rscf.ru/project/25−29−00520/).

Citation: Ekgardt A.A., Marunchenko A.A., Sapozhnikova E.V., Verkhogliadov G.A., Pushkarev A.P., The role of charge carrier diffusion in halide perovskite luminophores with memory for optical computing, St. Petersburg State Polytechnical University Journal. Physics and Mathematics. 19 (1.1) (2026) 156−161. DOI: https://doi.org/10.18721/JPM.191.126

This is an open access article under the CC BY-NC 4.0 license (https://creativecommons.org/licenses/by-nc/4.0/)

Конференционная статья
УДК: 53.093
DOI: https://doi.org/10.18721/JPM.191.126

Роль диффузии носителей заряда в галогенидных перовскитных люминофорах с памятью для оптических вычислений

А.А. Экгардт [1]✉, А.А. Марунченко [2], Е.В. Сапожникова [1,3], Г.А. Верхоглядов [1,3], А.П. Пушкарев [1,3]

[1] Университет ИТМО, Санкт-Петербург, Россия;
[2] Университет Лунда, г. Лунд, Швеция;
[3] Сколковский институт науки и технологий, Москва, Россия;
✉ aleksei.ekgardt@metalab.ifmo.ru

Аннотация. Оптические элементы, сочетающие функции памяти и модуляции сигнала, вызывают значительный интерес в области нейроморфных вычислительных систем. В частности, оптический аналог мемристора – мемлюмор. Он обладает

© Ekgardt A.A., Marunchenko A.A., Sapozhnikova E.V., Verkhogliadov G.A., Pushkarev A.P., 2026. Published by Peter the Great St. Petersburg Polytechnic University.

перспективными свойствами: выходной сигнал люминесценции зависит не только от возбуждающего светового сигнала, но и от текущего состояния материала. Металлогалогенидные перовскитные люминофоры подходят для реализации мемлюморов, поскольку демонстрируют модуляцию фотолюминесценции за счет взаимодействия структурных дефектов с окружающей средой, учитывая при этом историю предыдущих воздействий, что обеспечивает эффект памяти. Люминесценцию в перовскитах описывает модель Шокли–Рида–Холла, учитывающая динамику носителей заряда. Кроме того, диффузия носителей заряда играет ключевую роль и сильно зависит от размеров мемлюмора. В статье исследуется функциональность перовскитных мемлюморов в зависимости от их характерных размеров для определения оптимальных параметров и подходящих элементов для будущих оптических нейроморфных вычислительных архитектур.

Ключевые слова: нейроморфные системы, мемлюморы, металлогалогенидные перовскиты, фотолюминесценция, диффузия носителей заряда, квантовый выход, время-разрешенная фотолюминесценция, модель Шокли–Рида–Холла, оптические вычислительные системы

Финансирование: Работа выполнена при поддержке Российского фонда науки (проект 25-29-00520, https://rscf.ru/project/25-29-00520/).

Ссылка при цитировании: Экгардт А.А., Марунченко А.А., Сапожникова Е.В., Верхоглядов Г.А., Пушкарев А.П. Роль диффузии носителей заряда в галогенидных перовскитных люминофорах с памятью для оптических вычислений // Научно-технические ведомости СПбГПУ. Физико-математические науки. 2026. Т. 19. № 1.1. С. 156–161. DOI: https://doi.org/10.18721/JPM.191.126

Статья открытого доступа, распространяемая по лицензии CC BY-NC 4.0 (https://creativecommons.org/licenses/by-nc/4.0/)

Introduction

The von Neumann architecture, which is used in the vast majority of most modern computers, faces significant limitations in performance and energy efficiency, especially when applied to artificial intelligence and large-scale data processing tasks [1]. An alternative approach, such as optical neuromorphic computing architectures inspired by biological neural networks, are attracting increasing attention. A key component in such systems is the memlumor [2], a device that combines memory functionality with photoluminescence, enabling optical neuromorphic computing. Metal halide perovskites considered to be a promising material for memlumors due to their high charge carrier mobility, high photoluminescent quantum yield and simple synthesis methods [3]. Memory effects in perovskite materials occur on time scales ranging from milliseconds to minutes due to their photochemical activity under the influence of light. Furthermore, the thickness and lateral dimensions of the elements are important for maximizing photoluminescence and for the memlumor's operation itself, as in perovskites the carrier diffusion length exceeds several microns [4]. When excitation light is focused on an array of small elements linked together or a large bulk element of the material, the carriers quickly spread throughout the sample, which modulates the carrier concentration on the plane and thus inevitably influences the formation of the luminescence signal [5]. The focus of this work is to estimate the influence of memlumor's size on its functionality. For this purpose, two types of experiments are carried out: an experiment with wide uniform illumination and multiple perovskite $CsPbBr_3$ crystals of different effective sizes (from 100 nm to 1000 nm), as well as time-resolved luminescence at different pulse repetition rates and perovskite $MAPbBr_3$ films of different thicknesses (from 70 nm to 450 nm).

Materials and Methods

To produce $CsPbBr_3$ microcrystals the initial solution was synthesized using mixtures of 0.3 mmol CsBr and 0.3 mmol $PbBr_2$ in dimethyl sulfoxide. The solution was spin-coated onto a glass substrate at 6000 rpm spin cycle, which was later heated up to 70 °C in a Petri dish filled with 180 ml of isopropanol. The 0.32 ml of solution was then drop-cast onto a substrate and remained heated for 10 minutes in order to facilitate the crystal growth.

© Экгардт А.А., Марунченко А.А., Сапожникова Е.В., Верхоглядов Г.А., Пушкарев А.П., 2026. Издатель: Санкт-Петербургский политехнический университет Петра Великого.

A series of $MAPbBr_3$ solutions (0.4 M, 0.6 M, 0.8 M, 1 M, 1.5 M) were prepared and spin-coated onto a glass substrate at 3000 rpm spin cycle for 40 seconds in order to create polycrystalline perovskite films with various thickness (70 nm, 170 nm, 200 nm, 240 nm and 450 nm).

Scanning electron microscopy (SEM) and atomic force microscopy (AFM) were used to analyze the structure's size, providing precise determination of linear dimensions and morphology. Photoluminescent images of crystals were obtained on an Axio Imager.A2m (Carl Zeiss SMT) optical microscope. Image processing was performed using the ImageJ and Gwyddion software packages, and numerical modeling of charge carrier dynamics was carried out using a Shockley–Read–Hall model with diffusion, allowing for comparison between experimental and theoretical results. The time-resolved photoluminescence (TRPL) measurements were performed using a TEMA femtosecond pulse laser with a wavelength of 350 nm and frequency of 10–200 kHz and 100 nJ/cm^2 fluence.

Results and Discussion

Images of the $CsPbBr_3$ crystal were obtained on a photoluminescent microscope and PL of each crystal was estimated according to pixel intensity. SEM was used to measure the exact size of the crystals and evaluate their shape (Fig. 1, *a*). The study of photoluminescent properties of CsPbBr3 microcrystals depending on their linear size (in the range of 100–1000 nm) showed that the integral value of photoluminescence remains almost unchanged (Fig. 1, *b*), while the quantum yield decreases inversely proportional to the square of the size (Fig. 1, *c*). As the linear size increases, the computational density also decreases inversely proportional to the square of the size (Fig. 1, *d*).

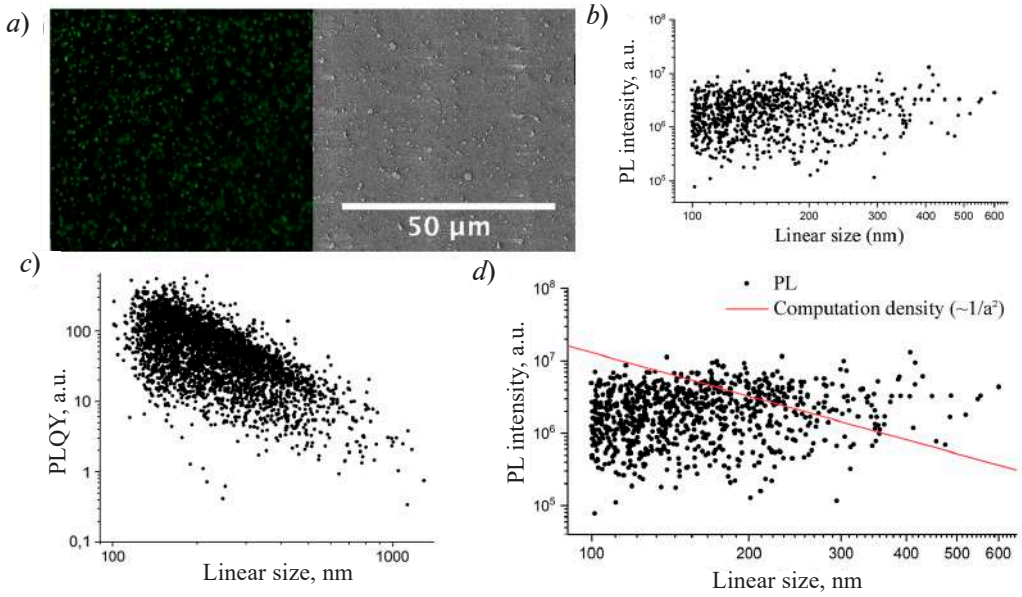

Fig. 1. Fluorescent (left) and SEM (right) images of the same area of $CsPbBr_3$ crystals (*a*); dependence of the photoluminescence intensity on the linear size of the crystal (*b*); dependence of the photoluminescence quantum yield on the linear size of the crystal (*c*); dependence of the photoluminescence intensity and computation density on the linear size of the crystal (*d*)

For $MAPbBr_3$ films with thicknesses of 70–450 nm, the charge carrier dynamics was evaluated using TRPL method that allows measuring the lifetime of nonradiative and radiative processes in structure and estimate charge carrier density. The resulting TRPL kinetics (Fig. 2, *a*) exhibit two components of lifetime: a fast one (Fig. 2, *b*) (on the order of nanoseconds), associated with diffusion, and a slow one (in the range from 10 to 100 nanoseconds).

The description of luminescence in $MAPbBr_3$ films is carried out using the Shockley–Reed–Hall model that also consider the charge carrier diffusion and memlumor formalism (1).

$$\begin{cases} \dfrac{d}{dt}\big(n(t)\big) = g(t) - k_r n(t)\, p(t) - k_t\big(N_t - n_t(t)\big) n(t) + D_n \cdot \dfrac{\partial^2 n}{\partial z^2}, \\ \dfrac{d}{dt} n_t(t) = k_t\big(N_t - n_t(t)\big) n(t) - k_n n_t(t)\, p(t), \\ \dfrac{d}{dt}\, p(t) = g(t) - k_r n(t)\, p(t) - k_n n_t(t)\, p(t) + D_p \cdot \dfrac{\partial^2 p}{\partial z^2}, \\ PL = k_r n(t)\, p(t) - PLQY\big(\vec{X}(t), I(t), t\big) \cdot I(t), \end{cases} \quad (1)$$

where $g(t)$ is the photogeneration rate of charge carriers, $I(t)$ is the pumping intensity (input signal), k_r is the constant of the rate of radiative recombination, N_t is the concentration of electron traps (defects), k_t is the constant rate of electron capture, k_n is the constant rate of trap release as a result of nonradiative recombination of trapped electrons with free holes, D_n and D_p are the diffusion coefficients for electrons and holes, respectively. This model considers the processes of photoexcitation ($g(t)$), photoluminescence (radiative recombination) ($k_r n(t)p(t)$), electron trap capture ($k_t(N_t - n_t(t))n(t)$) and trap release during nonradiative recombination ($k_n n_t(t)p(t)$).

Numerical modeling using Shockley–Read–Hall theory with added charge carrier diffusion and memlumor formalism confirmed that the fast component is associated with diffusion as it becomes more prominent with the increase of film thickness. (Fig. 2, *c*, *d*).

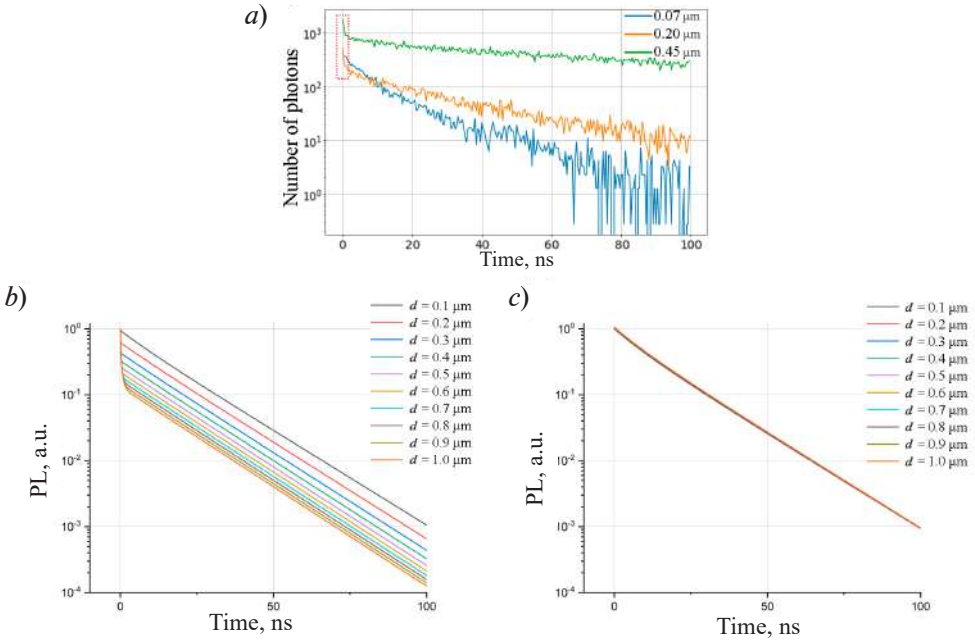

Fig. 2. TRPL kinetics for $MAPBBr_3$ films with thicknesses of 0.07 μm, 0.20 μm, 0.45 μm at a pump frequency of 30 kHz. TRPL experimental result (red frame is the fast component of luminescence attenuation associated with diffusion) (*a*); TRPL numerical modeling, obtained according to a diffusion-adjusted model (*b*); model without diffusion for a material with a thickness from 0.1 μm to 1 μm (*c*)

To further evaluate the role of charge carrier diffusion in memlumors based on metal halide perovskite films, it is necessary to look at the functionality of memlumors, namely, the modulation of the luminescence quantum yield depending on the pulse repetition rate of pump signal. As the film's thickness increases, the quantum yield also increases, while the luminescence peak decreases (Fig. 3, *a*, *b*, *c*). Due to the release time of traps (in order of tens to hundreds of microseconds) they do not have time to release themselves in the interval between pulses. As a result, more free holes remain, and, accordingly, photoluminescence also increases. After integrating the area under the decay curves for samples of different thicknesses curves for the modulation of the quantum yield were obtained (Fig. 3, *d*). Thus, it is revealed that the modulation is maximized for a 70 nm thick sample and minimized for a 450 nm one, suggesting that diffusion negatively

affects modulation. It can be seen from the TRPL kinetics that the role of diffusion increases with the increasing thickness, however, it is difficult to separate its effect on the quantum yield from the effect of the defect factor, which requires further quantitative studies.

The results indicate a preference for using independent elements with minimized diffusion to create high-density memlumor arrays, comparable in density to modern transistor circuits (up to 10^{10} cm^{-2}).

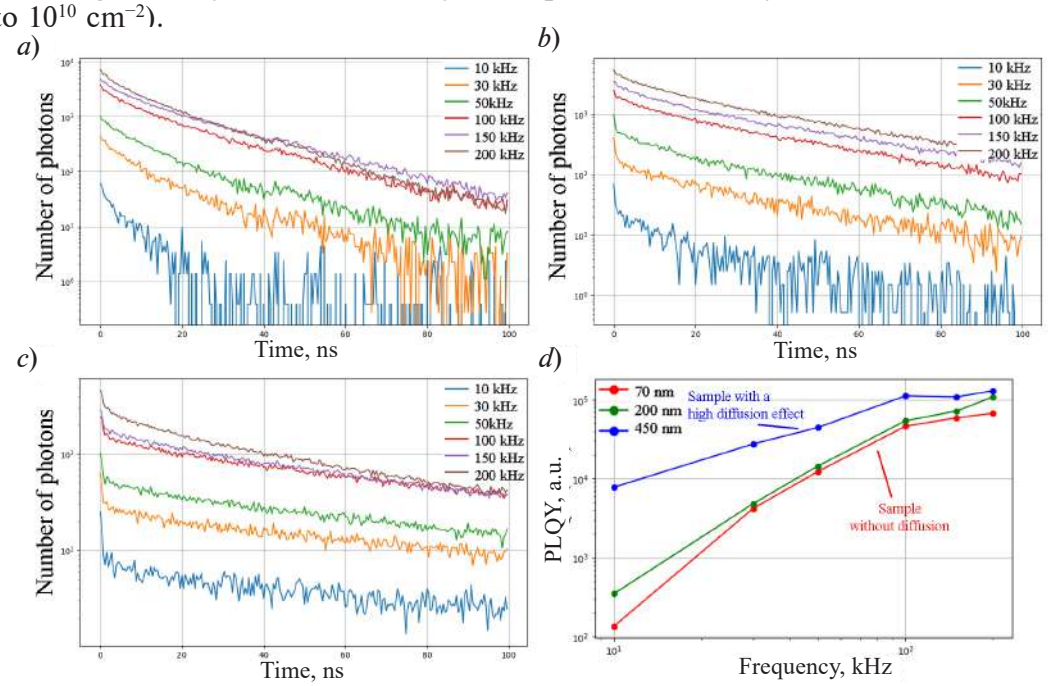

Fig. 3. TRPL kinetics measured at various repetition rates (10–200 kHz) for films with a thickness of 70 nm (*a*); 200 nm (*b*); 450 nm (*c*); dependence of the photoluminescence quantum yield on the pulse repetition rate for films with thicknesses of 70, 200 and 450 nm (*d*)

Conclusion

This work demonstrates the potential of metal halide perovskites for developing energy-efficient optical neuromorphic systems based on memlumors. Experimental and theoretical studies confirmed the influence of charge carrier diffusion on luminescent properties and highlighted the importance of minimizing diffusion for increasing element density. The results indicate the preference for using independent elements with minimal diffusion to create high-density memlumor arrays. The obtained data can be used to design new architectures for optical computing systems and high-density memlumor arrays with high performance and energy efficiency.

Acknowledgments

The work was supported by the Russian Science Foundation (project 25-29-00520, https://rscf.ru/project/25-29-00520/).

REFERENCES

1. **Merolla P.A., Arthur J.V., Alvarez–Icaza R. et al.,** A million spiking–neuron integrated circuit with a scalable communication network and interface. Science. 345 (2014) 668–673.

2. **Marunchenko A., Kumar J., Kiligaridis A. et al.,** Memlumor: A Luminescent Memory Device for Energy–Efficient Photonic Neuromorphic Computing. ACS Energy Letters. 9 (2024) 2075–2082.

3. **Pushkarev A.P., Korolev V.I., Markina D.I. et al.,** A Few–Minute Synthesis of CsPbBr3 Nanolasers with a High Quality Factor by Spraying at Ambient Conditions. ACS Applied Materials & Interfaces. 11 (2019) 1040–1048.

4. **Stranks S.D., Eperon G.E., Grancini G. et al.,** Electron–Hole Diffusion Lengths Exceeding 1 Micrometer in an Organometal Trihalide Perovskite Absorber. Science. 342 (2013) 341–344.

5. **Marunchenko A., Kumar J., Kiligaridis A. et al.,** Charge Trapping and Defect Dynamics as Origin of Memory Effects in Metal Halide Perovskite Memlumors. The Journal of Physical Chemistry Letters. 15 (2024) 6256–6265.

THE AUTHORS

EKGARDT Alexey A.
aleksei.ekgardt@metalab.ifmo.ru

MARUNCHENKO Aleksandr A.
a.marunchenko@metalab.ifmo.ru
ORCID: 0000-0002-0616-2524

SAPOZHNIKOVA Elizaveta V.
e.sapozhnikova@metalab.ifmo.ru
ORCID: 0009-0000-2732-6711

VERKHOGLIADOV Grigorii A.
g.verkhogliadov@metalab.ifmo.ru
ORCID: 0000-0002-6222-5526

PUSHKAREV Anatoly P.
an.pushkarev@skoltech.ru
ORCID: 0000-0002-1793-6812

Received 15.12.2025. Approved after reviewing 26.02.2026. Accepted 26.02.2026.

© Peter the Great St. Petersburg Polytechnic University, 2026

Conference paper
UDC 535.3
DOI: https://doi.org/10.18721/JPM.191.127

Switching of Kerker effect from single Sb_2Se_3 nanoparticles

A.R. Kolesnikova ✉, A.D. Sinelnik, D.A. Litvinov

ITMO University, St. Petersburg, Russia

✉ anna.kolesnikova@metalab.ifmo.ru

Abstract. The Kerker effect is one of the fundamental concepts in nanophotonics for controlling scattered radiation from single nanoparticles. It is based on the interaction of electric and magnetic dipoles, which, as a result of interference, determine the directional pattern of scattered radiation. The implementation of this principle allows the creation of nanoantennas that effectively redirect radiation from other nanoscale sources. This work demonstrates the possibility of dynamically controlling the directional pattern of scattered radiation by using nanoparticles made of the phase-change material Sb_2Se_3. The "ON" and "OFF" modes of directional scattering are shown when the phase of the material changes. These results may open up a new path in the implementation of dynamically changing nanoantennas for applications in quantum cryptography and optical telecommunications.

Keywords: nanoparticles, phase change materials, Kerker effect

Funding: This work was supported by the Russian Science Foundation (project No. 25-79-10137).

Citation: Kolesnikova A.R., Sinelnik A.D., Litvinov D.A., Switching of Kerker effect from single Sb_2Se_3 nanoparticles, St. Petersburg State Polytechnical University Journal. Physics and Mathematics. 19 (1.1) (2026) 162–167. DOI: https://doi.org/10.18721/JPM.191.127

This is an open access article under the CC BY-NC 4.0 license (https://creativecommons.org/licenses/by-nc/4.0/)

Конференционная статья
УДК 535.3
DOI: https://doi.org/10.18721/JPM.191.127

Переключение эффекта Керкера от одиночных наночастиц из Sb_2Se_3

А.Р. Колесникова ✉, А.Д. Синельник, Д.А. Литвинов

Университет ИТМО, Санкт-Петербург, Россия

✉ anna.kolesnikova@metalab.ifmo.ru

Аннотация. Эффект Керкера является одной из ключевых концепций современной нанофотоники для управления рассеянным излучением от одиночных наночастиц. Он основан на взаимодействии электрического и магнитного диполей, которые в результате интерференции определяют диаграмму направленности рассеянного излучения. Реализация данного принципа позволяет создавать наноантенны, эффективно перенаправляющие излучение от других наноразмерных источников. В данной работе демонстрируется возможность динамического управления диаграммой направленности рассеянного излучения за счет использования наночастиц из фазопеременного материала Sb_2Se_3. Показан режим «ВКЛ» и «ВЫКЛ» направленного рассеяния при смене фазы материала. Эти результаты могут открыть новой путь в реализации динамически изменяющихся наноантенн для приложений квантовой криптографии и оптической телекоммуникации.

Ключевые слова: наночастицы, фазопеременный материал, эффект Керкера

Финансирование: Работа выполнена при поддержке РНФ (проект № 25-79-10137).

© Kolesnikova A.R., Sinelnik A.D., Litvinov D.A., 2026. Published by Peter the Great St. Petersburg Polytechnic University.

Ссылка при цитировании: Колесникова А.Р., Синельник А.Д., Литвинов Д.А. Переключение эффекта Керкера от одиночных наночастиц из Sb2Se3 // Научно-технические ведомости СПбГПУ. Физико-математические науки. 2026. Т. 19. № 1.1. С. 162–167. DOI: https://doi.org/10.18721/JPM.191.127

Статья открытого доступа, распространяемая по лицензии CC BY-NC 4.0 (https://creativecommons.org/licenses/by-nc/4.0/)

Introduction

Controlling the direction of light propagation using nano-objects is a major achievement in modern nanophotonics. One way to achieve this control is by changing the directional pattern of scattered light from nanoparticles. This is possible due to the realization of the Kerker effect, in which interference occurs between magnetic and electric dipole moments. The Kerker effect was first described in 1983 when observing light scattering from a magnetic particle [1], but later this effect was generalized for non-magnetic particles as well. To date, it has been shown that the Kerker effect can be observed from various nano-objects, including metasurfaces and particles of arbitrary shape [2, 3]. However, as a rule, all implementations of the Kerker effect are static [4], that is, the scattering pattern can only change when the wavelength or size of the nanostructure changes. This imposes significant limitations on the use of nanoparticles as nanoantennas, as it is not possible to dynamically change the pattern.

One solution to the problem of dynamic light control could be the use of phase-change materials [5]. These are a class of materials that undergo a reversible phase transition from an amorphous to a crystalline state. Phase transitions in phase-change materials are realized under the action of a thermal stimulus, which can be created either directly by thermal heating or through the conversion of an electrical or optical pulse into local heat within the material. When the phase of the material changes, its optical and electrical properties also change dramatically. These materials are actively used to create reconfigurable metasurfaces and photonic structures that provide dynamic light control [6]. One of the promising materials in this class that can be used in photonics is Sb_2Se_3 (hereafter SbSe) [7]. This is a new wide-bandgap material with no losses in the near-IR range, which distinguishes it favorably from more well-known materials such as GST, AIST, and GeTe [8]. At the same time, the refractive index in both the amorphous and crystalline phases is close to that of silicon. This contributes to further compatibility with silicon photonics components.

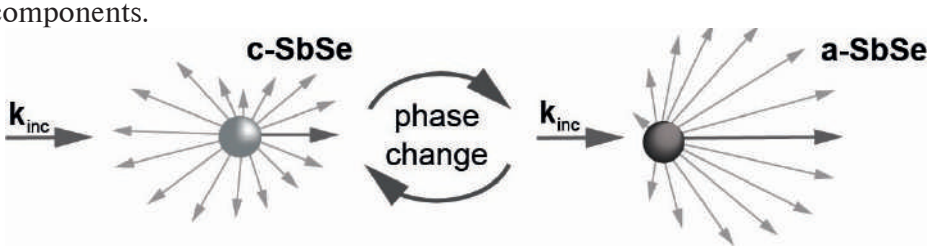

Fig.1. Schematic of the working principle of Huygens metaatom

In our work, we demonstrate the possibility of changing the light scattering diagram for SbSe nanoparticles by changing its phase (Fig. 1). We performed a theoretical calculation of light scattering spectra followed by multipole decomposition from nanoparticles with a diameter of 260–300 nm. We determined the dependence of the spectral position of resonances associated with the electric and magnetic dipole moments in the particle, as well as their spectral shift when the phase of the material changes. As a result of multipole decomposition, spectral regions were determined where electric and magnetic dipole moments of equal intensity are observed, i.e., regions where the Kerker effect can be observed. Finally, scattered light directionality diagrams were constructed, demonstrating the possibility of "ON" and "OFF" directional scattering when the phase of the material changes. These results can serve as a foundation for the creation of tunable nanoantennas for quantum and optical telecommunications applications and photonic computing circuits.

© Колесникова А.Р., Синельник А.Д., Литвинов Д.А., 2026. Издатель: Санкт-Петербургский политехнический университет Петра Великого.

Materials and Methods

The paper investigates light scattering by a single spherical nanoparticle (metaatom). The scattering cross-section (SCS) of a single metaatom can be expressed in terms of Mie theory:

$$C_{sca} = \frac{2\pi}{k^2}\sum_{n=1}^{\infty}(2n+1)\left(|a_n|^2 + |b_n|^2\right), \tag{1}$$

where is k_0 is the wavenumber in the surrounding medium, a_n and b_n are the Mie coefficients corresponding to the electric and magnetic multipole moments, respectively, and n is the order of multipole.

The Mie coefficients are expressed in terms of Riccati–Bessel functions:

$$\begin{aligned} a_n &= \frac{n_s\Psi_n(n_s x)\Psi'_n(x) - \Psi_n(x)\Psi'_n(n_s x)}{n_s\Psi_n(n_s x)\xi'_n(x) - \xi_n(x)\Psi'_n(n_s x)}, \\ b_n &= \frac{\Psi_n(n_s x)\Psi'_n(x) - n_s\Psi_n(x)\Psi'_n(n_s x)}{\Psi_n(n_s x)\xi'_n(x) - n_s\xi_n(x)\Psi'_n(n_s x)}, \end{aligned} \tag{2}$$

where ns is the refractive index of the sphere and the Riccati–Bessel functions are:

$$\Psi_n(x) = xj_n(x),\ \xi_n(x) = xh_n^{(1)}(x), \tag{3}$$

where $j_n(x)$ is the spherical Bessel function of the first kind, $h_n^{(1)}(x)$ is the spherical Hankel function of the first kind, x is the size parameter, defined as $x = k_0 r$ with r being the radius of the sphere.

To analyze the contribution of various multipole moments to the scattering of spherical nanoparticles, Cartesian electric and magnetic multipoles were calculated using the COMSOL Multiphysics software package (Electromagnetic Waves, Frequency Domain module).

Cartesian multipoles, defined by the polarization distribution inside the particle, are equivalent to spherical multipoles Mie for arbitrary shapes and spherical particles. The mathematical definition of electric and magnetic dipole moments in Cartesian representation was used in accordance with [9].

Electric dipole moment $\boldsymbol{p}$ in Cartesian form is as follows:

$$\boldsymbol{p} = \int \boldsymbol{P} j_0(kr)dV + \frac{k_0^2}{2}\int \frac{3(\boldsymbol{r}\cdot\boldsymbol{P}) - r^2\boldsymbol{P}}{(kr)^2} j_2(kr)dV, \tag{4}$$

where $\boldsymbol{P}$ is the polarization vector, r is the radius vector, k is the wavenumber in the particle, j_0 and j_2 are spherical Bessel functions.

Magnetic dipole moment $\boldsymbol{m}$:

$$\boldsymbol{m} = \frac{3i\omega}{2}\int \frac{\boldsymbol{r}\times\boldsymbol{P}}{kr} j_1(kr)dV. \tag{5}$$

The cross sections for the scattering of electric and magnetic dipoles were determined as:

$$C_{ED} = \frac{k_0^4}{6\pi\varepsilon_0^2|E_0|^2}\boldsymbol{p}^2, \tag{6}$$

$$C_{MD} = \frac{k_0^4}{6\pi\varepsilon_0^2|E_0|^2 c^2}\boldsymbol{m}^2, \tag{7}$$

where $|E_0|^2$ is the intensity of incident field.

Kerker conditions were used to analyze the radiation pattern. [1]. These conditions are given by:

$$C_{sca}^{\text{forward}} \propto |a_1 + b_1|^2, \tag{8}$$

$$C_{sca}^{\text{backward}} \propto |a_1 - b_1|^2. \tag{9}$$

The first condition ($a_1 = b_1$) corresponds to maximum forward scattering. The second condition ($a_1 = b_1$) leads to suppression of scattering in the forward direction and predominant backward scattering.

Results and Discussion

Let us consider the scattering cross section of a spherical particle in the amorphous and crystalline phases of a material when illuminated by a plane wave (the incident wave vector is directed along the x-axis). The research particle sizes were inves6tigated: radii R = 130 nm and R = 150 nm in the wavelength range 700–1000 nm. The choice of particle radii is due to the fact that the corresponding dipole resonances lie in the near-infrared and telecommunications range, which makes metaatoms applicable in telecommunications applications. The meta-atom is examined in air (n = 1), providing a universal approach to analysing its optical properties. As shown in the article on dielectric nanoparticles [10], the influence of the substrate on the spectral characteristics of the meta-atom depends on its optical properties. For weakly reflective substrates (for example, glass), the primary influence of the substrate is a change in the scattering cross-section amplitude, while the resonance shift remains insignificant. This approach allows us to identify the fundamental resonant characteristics of the material, and the influence of a specific substrate can subsequently be taken into account as a correction for given experimental conditions. In the amorphous phase, pronounced electric and magnetic dipole resonances are observed. The first-type Kerker effect occurs at 1030 nm for a particle with R = 130 nm and for a particle with R = 150 nm at a wavelength of 1393 nm. The scattering is collimated with the propagation of the incident radiation (Fig. 2). The coincidence of the phases of the electric and magnetic dipole moments in the amorphous phase at these wavelengths leads to preferential forward scattering and suppression of reflection. Thus, the amorphous phase exhibits the full behaviour of a Huygens metatom. A change in the particle radius leads to a shift in the spectral position of the electric and magnetic dipole resonances, and therefore also changes the position of their intersection, corresponding to the Kerker condition.

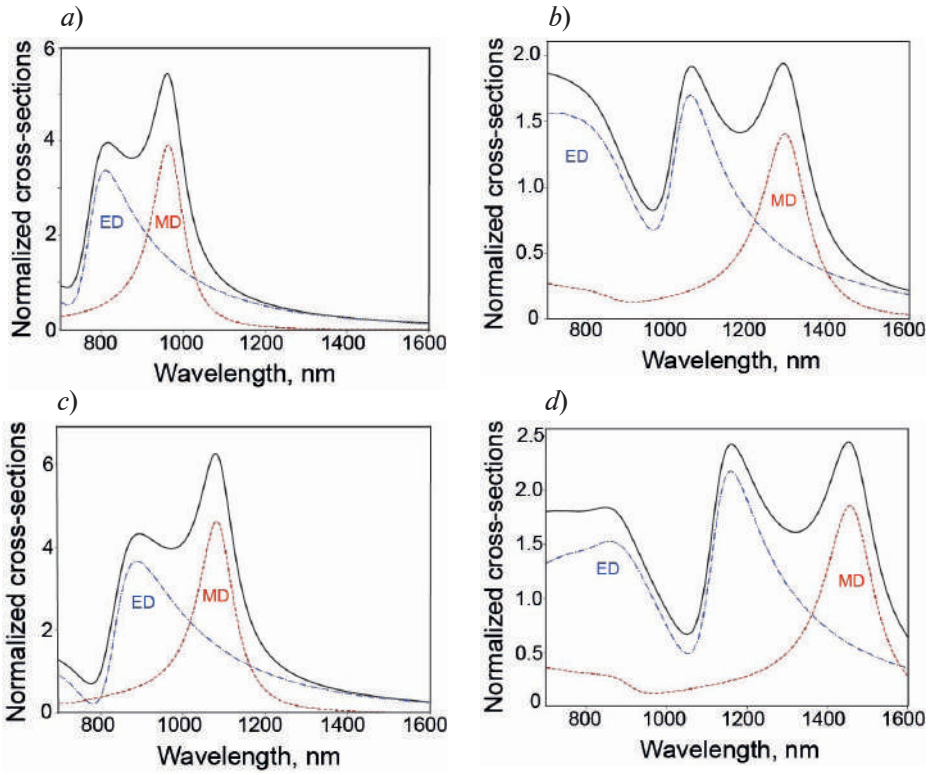

Fig.2. Scattering cross-sections and multipole decomposition for a spherical nanoparticle of (*a*) amorphous SbSe (R = 130 nm), (*b*) crystalline SbSe (R = 130 nm), (*c*) amorphous SbSe (R = 150 nm) and (*d*) crystalline SbSe (R = 150 nm). The spectra are normalized to the geometric section of the sphere

The transition to the crystalline state of the material is accompanied by an increase in the absorption of the material and a change in the phase of dipole oscillations. The change in the SbSe phase leads to significant changes in the scattering cross section. At wavelengths of 1030 and 1393 nm, there are no intersections between the electric and magnetic dipoles for the crystalline phase. The far-field scattering distribution at a wavelength of 1030 nm for a particle with a radius of 130 nm confirms these effects (Fig. 3).

These results highlight the potential of dynamic light control through phase state adjustment.

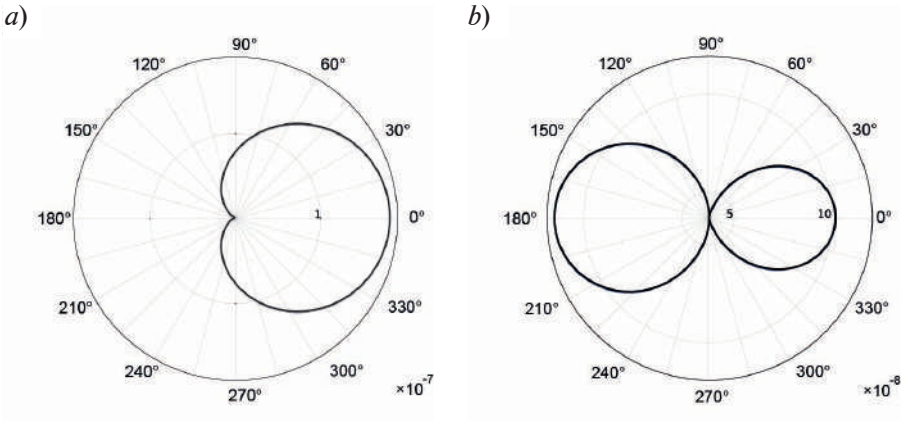

Fig.3. Far-field scattering patterns at wavelengths of 1030 nm, respectively from a single (*a*) amorphous SbSe nanoparticle and (*b*) crystalline SbSe nanoparticle

Conclusion

The work demonstrated that the Kerker effect is observed in the light scattering from a single SbSe nanoparticle. The possibility of dynamic changes in the spectral position of resonances in the scattering spectrum when the phase of the material changes was shown. The possibility of changing the direction of propagation of scattered radiation by changing the phase of SbSe has also been demonstrated. We are confident that the results obtained will find practical application in the creation of reconfigurable nanoantennas for telecommunications, cryptography, and photonic computing circuits.

REFERENCES

1. **Kerker M., Wang D.S., Giles C.L.,** Electromagnetic scattering by magnetic spheres, Journal of the Optical Society of America. 73 (6) (1983) 765–767.

2. **Liu W., Kivshar Y.S.,** Generalized Kerker effects in nanophotonics and meta optics, Optics Express. 26 (10) (2018) 13085–13105.

3. **Babicheva V.E., Evlyukhin A.B.,** Mie-resonant metaphotonics, Advances in Optics and Photonics. 16 (3) (2024) 539–658.

4. **Song I.H., Ki Y.G., Kim S.J., et al.,** Enhancing Antireflection Based on a Symmetry-Dependent Kerker Effect, Nano Letters. 24 (49) (2024) 15852–15860.

5. **Ding F., Yang Y., Bozhevolnyi S.I.,** Dynamic metasurfaces using phase-change chalcogenides, Advanced optical materials. 7 (14) (2019) 1801709.

6. **Korolev V., Sinelnik A.D., Rybin M.V., et al.,** Tunable high-order harmonic generation in GeSbTe nano-films, Nanophotonics. 13 (18) (2024) 3411–3419.

7. **Delaney M., Zeimpekis I., Lawson D., et al.,** A new family of ultralow loss reversible phase-change materials for photonic integrated circuits: Sb_2S_3 and Sb_2Se_3, Advanced Functional Materials. 30 (36) (2020) 2002447.

8. **Li, C., Pan, R., Gu, C., et al.,** Reconfigurable Micro/Nano-Optical Devices Based on Phase Transitions: From Materials, Mechanisms to Applications. Advanced Science. 11 (20) (2024) 2306344.

9. **Evlyukhin, A.B., Fischer, T., Reinhardt, C., Chichkov, B.N.,** Optical theorem and multipole scattering of light by arbitrarily shaped nanoparticles, Physical Review B. 94 (20) (2016) 205434.

10. **Miroshnichenko A.E., Evlyukhin A.B., Kivshar Y.S., Chichkov B.N.,** Substrate-induced resonant magnetoelectric effects for dielectric nanoparticles. Acs Photonics. 2 (10) (2015) 1423–1428.

THE AUTHORS

KOLESNIKOVA Anna R.
anna.kolesnikova@metalab.ifmo.ru
ORCID: 0009-0009-5457-4900

SINELNIK Artem D.
artem.sinelnik@metalab.ifmo.ru
ORCID: 0000-0003-2423-7945

LITVINOV Daniil A.
daniil.litvinov@metalab.ifmo.ru
ORCID: 0009-0007-0897-8993

Received 15.12.2025. Approved after reviewing 26.02.2026. Accepted 03.03.2026.

© Peter the Great St. Petersburg Polytechnic University, 2026

CONFERENCE ORGANIZERS AND SPONSORS

Organizers

Peter the Great St. Petersburg Polytechnic University (SPbPU)
Alferov University, Saint Petersburg
Ioffe Institute, Saint Petersburg
St. Petersburg State University
Russian-Armenian University, Yerevan

Sponsors

Ministry of Science and Higher Education of the Russian Federation (state assignment)
Tydex LLC, Saint Petersburg

Program Committee

M.M. Glazov, Ioffe Institute, St. Petersburg (*Chair*)
D.A. Firsov, Peter the Great St. Petersburg Polytechnic University (*Vice-Chair*)

V.F. Agekyan, St. Petersburg State University

I.A. Akimov, TU Dortmund University

V.Ya. Aleshkin, Istitute for Physics of Microstructures, Nizhny Novgorod

S.Yu. Verbin, St. Petersburg State University

A.E. Zhukov, Higher School of Economics, St. Petersburg

V.I. Zubkov, St. Petersburg Electrotechnical University "LETI", St. Petersburg

M.S. Kagan, Institute of Radioengineering and Electronics, Moscow

O.S. Komkov, St. Petersburg Electrotechnical University "LETI", St. Petersburg

V.P. Kochereshko, Ioffe Institute, St. Petersburg

H.A. Sarkisyan, Russian-Armenian University, Yerevan

D.R. Khokhov, Moscow State University

G.E. Cirlin, Alferov University, St. Petersburg

T.V. Shubina, Ioffe Institute, St. Petersburg

Organizing Committee

D.A. Firsov, Peter the Great St. Petersburg Polytechnic University (*Chair*)
M.Ya. Vinnichenko, Peter the Great St. Petersburg Polytechnic University (*Vice-Chair*)
N.Yu. Kharin, Peter the Great St. Petersburg Polytechnic University (*Secretary*)

E.V. Vladimirskaya, SPbPU
V.E. Gasumyants, SPbPU
D.A. Karaulov, SPbPU
V.P. Kochereshko, Ioffe Institute
G.A. Melentev, SPbPU
I.S. Mukhin, Alferov University
V.Yu. Panevin, SPbPU
H.A. Sarkisyan, Russian-Armenian University
R.V. Ustimenko, SPbPU
V.A. Shalygin, SPbPU

Journal

ST. PETERSBURG STATE POLYTECHNICAL UNIVERSITY JOURNAL: PHYSICS AND MATHEMATICS

Vol. 19, No. 1.1, 2026

Founder and publisher: Peter the Great St. Petersburg Polytechnic University

The journal is registered with the Federal Service for Supervision of Communications, Information Technology and Mass Media (Roskomnadzor).
Certificate ПИ ФС77-51457 issued 19.10.2012.

Editorial Office

Dr. Prof. *V.K. Ivanov*, Editor-in-Chief
Dr. Prof. *A.E. Fotiadi*, Deputy Editor-in-Chief
Dr. Prof.*V.V. Dubov*
Dr. Prof. *P.A. Karaseov*
Dr. Assoc. Prof. *V.M. Kapralova*
A.S. Kolgatina, translator
N.A. Bushmanova, editorial manager

All papers presented are final author versions
Peer review is under responsibility of the Program Committee

Phone +7 (812) 552-62-16

Website https://physmath.spbstu.ru/

E-mail: physics@spbstu.ru

Typesetting by *N.A. Bushmanova*

Published 15.05.2025. Format 60x84/8. Digital print.

Printer's sheets Print circulation 1000. Order ID .